ABSTRACT

HIGH RESOLUTION SOLAR OBSERVATIONS FROM FIRST PRINCIPLES TO APPLICATIONS

by
Angelo P. Verdoni

The expression "high-resolution observations" in Solar Physics refers to the spatial, temporal and spectral domains in their entirety. High-resolution observations of solar fine structure are a necessity to answer many of the intriguing questions related to solar activity. However, a researcher building instruments for high-resolution observations has to cope with the fact that these three domains often have diametrically opposed boundary conditions. Many factors have to be considered in the design of a successful instrument. Modern post-focus instruments are more closely linked with the solar telescopes that they serve than in past. In principle, the quest for high-resolution observations already starts with the selection of the observatory site.

The site survey of the Advanced Technology Solar Telescope (ATST) under the stewardship of the National Solar Observatory (NSO) has identified Big Bear Solar Observatory (BBSO) as one of the best sites for solar observations. In a first step, the seeing characteristics at BBSO based on the data collected for the ATST site survey are described. The analysis will aid in the scheduling of high-resolution observations at BBSO as well as provide useful information concerning the design and implementation of a thermal control system for the New Solar Telescope (NST). NST is an off-axis open-structure Gregorian-style telescope with a 1.6 m aperture. NST will be housed in a newly constructed 5/8-sphere ventilated dome. With optics exposed to the surrounding air, NST's open-structure design makes it particularly vulnerable to the effects of enclosure-related seeing. In an effort to mitigate these effects, the initial design of a thermal control system for the NST dome

is presented. The goal is to remediate thermal related seeing effects present within the dome interior. The THermal Control System (THCS) is an essential component for the open-telescope design of NST to work. Following these tasks, a calibration routine for the polarization optics for the Visible-light Imaging Magnetograph (VIM) is presented. VIM uses a set of two Liquid Crystal Variable Retarders (LCVRs) as the main components of its Stokes analyzer. Calibration of these components is a crucial step in providing reliable polarimetric measurements of the Sun using VIM. On 2007 July 15, using the Dunn Solar Telescope (DST) at the National Solar Observatory at Sacramento Peak (NSO/SP), New Mexico, the first polarimetric measurements using VIM were made. As a final step, illustrating an application of high-resolution solar observations, the results of a two-dimensional time-series acquired on 2006 June 11, using the DST at NSOP is presented. The data is used in a study of upflow events that are observed to occur in the Hα 656.3 nm and Na D_2 589.0 nm chromospheric absorption lines.

HIGH RESOLUTION SOLAR OBSERVATIONS FROM FIRST PRINCIPLES TO APPLICATIONS

by
Angelo P. Verdoni

A Dissertation
Submitted to the Faculty of
New Jersey Institute of Technology and
Rutgers, The State University of New Jersey – Newark
in Partial Fulfillment of the Requirements for the Degree of
Doctor of Philosophy in Applied Physics

Federated Physics Department

August 2009

APPROVAL PAGE

HIGH RESOLUTION SOLAR OBSERVATIONS FROM FIRST PRINCIPLES TO APPLICATIONS

Angelo P. Verdoni

8/5/09

Dr. Carsten Denker, Dissertation Advisor — Date
Research Professor of Physics, NJIT
Research Group Leader, Optical Solar Physics, Astrophysical Institute Potsdam

8/5/09

Dr. Dale E. Gary, Committee Member — Date
Professor of Physics, Director of Owens Valley Solar Array, NJIT

8/5/09

Dr. Haimin Wang, Committee Member — Date
Distinguished Professor of Physics, Associate Director of Center for
Solar-Terrestrial Research and Big Bear Solar Observatory, NJIT

8/5/09

Dr. Andrew Gerrard, Committee Member — Date
Associate Professor of Physics, NJIT

8/22/09

Dr. Camelia Prodan, Committee Member — Date
Assistant Professor of Physics, NJIT

8/5/09

Dr. Zhen Wu, Committee Member — Date
Professor of Physics, Department Chair, Rutgers University – Newark

BIOGRAPHICAL SKETCH

Author: Angelo P. Verdoni

Degree: Doctor of Philosophy

Date: August 2009

Undergraduate and Graduate Eduction:

- Doctor of Philosophy in Applied Physics,
  New Jersey Institute of Technology, Newark, New Jersey, 2009

- Bachelor of Science in Engineering Physics,
  University of Colorado at Boulder, Boulder, Colorado, 2003

Publications in Refereed Journals:

Denker, C., Deng, N., Rimmele, T. R., Tritschler, A. and Verdoni, A. P.: 2007, Field-Dependent Adaptive Optics Correction Derived with the Spectral Ratio Technique, *Solar Physics* **241/2**, 411–426.

Verdoni, A. P. and Denker, C.: 2007, The Local Seeing Environment at Big Bear Solar Observatory, *Publications of the Astronomical Society of the Pacific* **119**, 793-804.

McKenna, E., Jiuzhi, X., Verdoni, A. P., Yetzbacher, M., Fan, R. and Mickelson, A.: 2004, Kinetic model of irreversible photobleaching of dye-doped polymer waveguide materials, *Journal of Optical Society America B.* **21**, 1294–1301.

Hale, P.D., Clement, T.S., Coakley, K.J., Wang, C.M., DeGroot, D.C., and Verdoni, A.P.: 2000, Estimating the Magnitude and Phase Response of a 50 GHz Sampling Oscilloscope Using the "Nose-To-Nose" Method, *55th ARFTG Conf. Boston*, 35–42.

Publications in Conference Proceedings:

Denker, C. and Verdoni, A. P.: 2006, Integrating Seeing Measurements into the Operations of Solar Telescopes, *Proceedings of the SPIE* **6267**, 62670L.

Denker, C., Goode, P. R., Ren, D., Saadeghvaziri, M. A., Verdoni, A. P., Wang, H., Yang, G., Abramenko, V., Cao, W., Coulter, R., Fear, R., Nenow, J., Shoumko, S., Spirock, T. J., Varsik, J. R., Chae, J., Kuhn, J. R., Moon, Y., Park, Y. D. and Tritschler, A.: 2006, Progress on the 1.6-Meter New Solar Telescope at Big Bear Solar Observatory, *Proceedings of SPIE* **6267**, 62670A.

Verdoni, A. P.,Denker, C., Varsik, J. R., Shoumko, S., Nenow, J. and Coulter, R.: 2007, The Thermal Environment of the Fiber Glass Dome for the New Solar Telescope at Big Bear Solar Observatory, *Proceedings of the SPIE* **6689**, 6689-29.

Verdoni, A. P. and Denker, C.: 2006, The Thermal Control of the New Solar Telescope at Big Bear Observatory, *Proceedings of the SPIE* **6267**, 62670M.

Yang, G., Varsik, J. R., Shumko, S., Denker, C., Choi, S., Verdoni, A. P. and Wang, H.: 2006, The Telescope Control System of the New Solar Telescope at Big Bear Solar Observatory, *Proceedings of the SPIE* **6274**, 62741Y.

Conference Abstracts:

Deng, N., Choudhary, D. P., Denker, C., Verdoni, A. and Tritschler, A.: 2007, Three-Dimensional Structure of Evershed Flows, AAS/AAPT Joint Meeting, American Astronomical Society Meeting 210, #95.06.

Denker, C., Verdoni, A. P., Naqvi, M., Deng, N. and Tritschler, A.: 2007, Two-Dimensional Spectroscopy of Chromospheric and Photospheric Sunspot Fine-Structure, AAS/AAPT Joint Meeting, American Astronomical Society Meeting 210, #100.02.

Denker, C., Verdoni, A. P., Wöger, F., Tritschler, A., Rimmele, T. R., Kneer, F., Reardon, K., Sánchez-Andrade Nuño, B., Domínguez Cerdeña, I. and Puschmann, K.: 2007, Speckle Interferometry of Solar Adaptive Optics Imagery, DFG-NSF Astrophysics Research Conference on "Advanced Photonics in Application to Astrophysical Problems", Washington, DC.

Verdoni, A. P., Denker, C., Deng, N. and Tritschler, A.: 2007, Observations of Quiet Sun Chromosphere Dynamics, AAS/AAPT Joint Meeting, American Astronomical Society Meeting 210, #100.03.

To my family whose love, support and dedication made it possible for me to sail through the rough seas that lay ahead.

ACKNOWLEDGEMENT

Numerous people were involved in, and helped with the development of this thesis. The following is my appreciation and personal acknowledgement of all of their efforts.

I would first like to extend my gratitude and appreciation to all of the members of my thesis committee for their insightful and constructive input. I would also like to extend my gratitude to my advisor, Professor Carsten Denker for his insight and help in coordinating the content of this thesis. His discipline and scholarship have been a model for me to follow. I would like to acknowledge all of the faculty at the Center for Solar-Terrestrial Research for their help in providing me with answers, documentation and advise for all of my thesis related work.

A special thanks to Christine A. Oertel for making my life so much easier by smoothing out all of my administrative related responsibilities, organizing and hosting fantastic solar holiday parties and genuinely making my time here at NJIT more enjoyable.

My acknowledgement goes out to all of the faculty in the Applied Physics department at NJIT for their instruction, help, and guidance in all of my course work. I would particularly like to acknowledge Leslie Williams and Renee M. Crawley for their help in all departmental related matters.

A special thanks to all of the members of the National Solar Observatory at Sacramento Peak, New Mexico for all of their help in making observations and providing unparalleled hospitality. The observing staff at the Dunn Solar Telescope, Doug Gilliam and Joe Elrod, were extremely helpful in making our observing time at Sac Peak run seamlessly. Acknowledgement to all of the staff at BBSO for their support and collaboration. In regards to the seeing study and thermal control I acknowledge and extend my gratitude to John Varsik, Jeff Nenow, Tom Spirock, Randy Fear and Bill Marquette for all of their help.

The topographic map (Figure 2.1) was provided by the The National Map Project (`http://nationalmap.gov/`) of the U.S. Geological Survey.The ATST data was provided by the National Solar Observatory, which is operated by the Association of Universities for Research in Astronomy under a cooperative agreement with the National Science Foundation, for the benefit of the astronomical community. Many people have worked hard to lead the ATST site survey to a successful conclusion. Here, we would like to acknowledge the contributions of the BBSO staff, in particular R. J. Fear, J. Nenow, W. H. Marquette, and J. Varsik. We would like to thank Nathan Dalrymple for providing the initial programs to perform the thermal modeling of the primary mirror and Tom Spirock for providing some of the BBSO pictures. Work done for the thermal control system for the new solar telescope was supported by NSF under grants ATM 00-342560, ATM 00-86999, ATM 02-36945, IIS ITR 03-24816 and AST MRI 00-79482 and by NASA under grants NAG 5-12782 and NNG0-6GC81G.

TABLE OF CONTENTS

TABLE OF CONTENTS
(Continued)

Chapter Page

TABLE OF CONTENTS

(Continued)

LIST OF TABLES

Table **Page**

LIST OF FIGURES

Figure **Page**

Figure Page

Figure Page

Figure Page

Figure **Page**

Figure Page

Figure Page

Figure Page

Figure **Page**

LIST OF ACRONYMS

AFOSR	Air Force Office for Scientific Research
AO	Adaptive Optics
AOA	Adaptive Optics Associates
ATST	Advanced Technology Solar Telescope
BBMWD	Big Bear Municipal Water District
BBSO	Big Bear Solar Observatory
CAD	Computer Aided Design
CalTech	California Institute of Technology
CCD	Charge Coupled Device
CGH	Computer Generated Hologram
CMOS	Complex Metal-Oxide Semiconductor
DEC	Declination
DIMM	Differential Image Motion Monitor
DOT	Dutch Open Telescope
DST	Dunn Solar Telescope
ENSO	El Niño-Southern Oscillation
XML	Xtended Markup Language
FOV	Field-of-View
GMT	Giant Magellan Telescope
GUI	Graphical User Interface
ICE	Internet Communication Engine
ICOS	IC Optical Systems
IDL	Interactive Data Language
IfA	Institute for Astronomy (University of Hawaii)
HMI	Helioseismic and Magnetic Imager
HQ	Head Quarter
JOSO	Joint Organization for Solar Observations
KAO	Korean Astronomical Observatory
KIS	Kiepenheuer-Institut fr Sonnenphysik
LSST	Large Synoptic Survey Telescope

CHAPTER 1

INTRODUCTION

1.1 Overview

A tremendous amount of planning goes into the development and operation of modern large-aperture ground-based solar telescopes. From site selection and analysis of the local seeing environment to the detailed design and implementation of the post-focus instrumentation, the present day ground-based solar observatory is a considerable technological and scientific undertaking. Unlike their space-based counterparts, ground-based solar observatories must cope with the deleterious effects of the Earth's atmosphere that plague image quality and limit the performance of sensitive measurements such as solar polarimetry. Considerable advancements in Adaptive Optics (AO) technology and post-facto image reconstruction techniques such as Speckle Masking Imaging (SMI) have made ground-based observations of the Sun a less costly and an equally good alternative to space-based missions.

As an understanding of the processes that govern the Sun's dynamic behavior grows, the quest for observations with higher resolution becomes more apparent. Current projects, such as the Advanced Technology Solar Telescope (ATST) with a 4 m aperture, continue to test the technological limits and capabilities of modern day solar observatories. First principles demand that the proper choice for the location of a solar observatory is imperative. It is the job of the site survey to collect and analyze data that reflects whether or not a candidate site meets a given set of criteria. The impetus for developing those criteria is primarily based on the design of the telescope which in turn is governed by the scientific objectives of the community.

This thesis provides some of the major components necessary to realize modern high-resolution studies of the Sun using the 1.6 m New Solar Telescope (NST) (Goode

et al., 2000), at Big Bear Solar Observatory (BBSO) in Big Bear Lake, California. NST once complete, will be the largest ground based solar telescope. In Chapter 2 the characteristics and merits of BBSO as a high altitude lake-site observatory are discussed. The results of a statistical study conducted using data gathered during the Solar Site Survey Working Group (SSWG) assessment of BBSO as a candidate site for the location of ATST (Verdoni and Denker, 2007) are also presented. It is anticipated that the results from the study will provide some insight into the scheduling of high-resolution observations as well as provide information useful in the design of NST's THermal Control System (THCS).

In Chapter 3 NST's optical design, heat stop assembly, optical support structure, and control systems are discussed as well as the introduction of NST's suite of post-focus instrumentation. Chapters 4 and 5 are related to the preliminary design of the THCS (Verdoni and Denker, 2006; Verdoni *et al.*, 2007). Particular emphasis is given to the dome design and temperature probe experiments that verify the existence of a strong thermal gradient present inside of the dome. In Chapter 6 Adaptive Optics (AO) and Speckle Masking Imaging (SMI) techniques, commonly used in modern high-resolution observations of the Sun are discussed. In Chapter 7 a calibration method developed for the Stokes analyzer used by the Visible-light Imaging Magnetogram (VIM) is presented. To verify the success of the calibration method, the first polarimetric observations using VIM are also presented in Chapter 7. In conclusion, in Chapter 8 an example of an application of high-resolution solar observations is given, using a set of observations taken at the Dunn Solar Telescope (DST) at the National Solar Observatory/Sacramento Peak (NSO/SP), New Mexico. The observations consist of simultaneous images of a supergranular cell located in a quiet Sun region at disk center using VIM and a speckle camera.

1.2 Scientific Motivation

The science drivers for the construction of the large-aperture ground-based solar telescopes are many. One of the most pressing perhaps is an explanation of the dynamics and structure of small scale magnetic flux elements called "flux tubes". Zwaan (1981) states that flux tubes are a key ingredient in understanding solar magnetism. Small scale flux concentrations are certain to emerge in the solar photosphere. However, there is considerable debate regarding their magnetic field strength. On the other hand, there is little debate on the importance of these structures and the role they potentially play as channels of energy into higher layers of the solar atmosphere. Recent high-resolution space-based observations, such as those conducted using the Hinode Solar Optical Telescope (SOT), have observed the emergence of small scale magnetic flux element less than $2''$ in size (Centeno *et al.*, 2007). Using the spectro-polarimeter aboard Hinode, Centeno *et al.* (2007) presented the first observational evidence of a small scale emergent region and measured its longitudinal magnetic flux. With a 1.6 m clear aperture at a wavelength of 500 nm operating near the diffraction limit of the telescope, NST will have an angular resolution of approximately $0.065''$, corresponding to a length of 50 km on the solar surface. This is close to resolving a single flux tube or small agglomeration of flux tubes. Using VIM and the other post-focus NST instrument, the Infra-Red Imaging Magnetograph (IRIM) (Denker *et al.*, 2003b), spectro-polarimetric measurements could be made of small scale emergent flux regions. Other applications include (a) high-resolution, high cadence studies of solar activity such as flares, (b) the temporal evolution and sub arc-second structure of the magnetic region where the flare occurred, (c) magneto-convection in sunspots and (d) the study of potential heating mechanisms associated with the upper solar atmosphere (Goode *et al.*, 2003).

1.3 Seeing

Ground-based solar observations in the 21st century require a site with a large clear-time fraction, good sky transparency and excellent seeing conditions for extended periods of time. These characteristics lend themselves to the performance of high-resolution solar telescopes. From the onset of modern solar observations, site surveys have played an important role in effecting the location and design of solar observatories. A historic and very comprehensive solar site survey was conducted by George Ellery Hale at Mt. Wilson in California (Hale, 1905). The Mt. Wilson site was selected as the home for the famous 60-foot Tower Telescope. It was known at the time that ground layer heating was associated with image degrading seeing and the telescope was built on a tower with that in mind. To test the quality of Mt. Wilson, observations were made using a smaller telescope and image quality was determined through visual inspection.

In the 1970s, the Joint Organization for Solar Observations (JOSO) conducted a thorough search for potential sites using 40 cm telescopes as well as photoelectric seeing measurements to determine the seeing quality (Brandt and Wöhl, 1982). Another site survey that resulted in the selection of Big Bear Lake as the location for BBSO was conducted by the California Institute of Technology (Caltech, Zirin and Mosher, 1988). The survey conducted from 1965 to 1967 recognized the value of high-altitude lake site locations for observing the Sun. Similar to the Mt. Wilson survey, the Caltech study determined the quality of seeing by visual inspection of solar images developed on film. Advancements in technology and the development of site-survey related instrumentation has provided the means for a more quantitative approach to site selection. In Chapter 2 site-survey data collected at BBSO by the ATST SSWG is used in a statistical study of the local seeing conditions at Big Bear Lake.

1.4 Enclosure Related Seeing and Thermal Control

Considerable work has been done to understand and combat seeing and seeing related effects in solar and nighttime telescopes. In their enclosure-seeing report, the ATST Thermal Systems Group describes the types of thermal convection that arise in ventilated domes (Dalrymple *et al.*, 2004). For ventilated domes with a passive louver system such as in the NST dome, there are several convective effects that lead to enclosure related seeing. The most dominant form is the convection arising from exterior dome heating. It is costly to try and combat this effect. However, natural cooling caused by moderate to high-speed winds can lower the outside dome temperature and reduce the buoyant convection driven plumes due to the heated dome exterior. NST will not implement any active measures to control the natural convection from the dome shell heating such as air conditioning and or shell temperature regulation. The idea is to restrict convection to the "forced regime", which corresponds to the least impact type seeing in the enclosure (Dalrymple *et al.*, 2004). For the 20 m diameter ATST enclosure much larger wind speeds are required to move the convection to the forced regime than for the 10 m diameter BBSO dome, i.e., for a 4 m diameter mirror and a 20 m diameter enclosure the wind speed must be approximately 6 m s^{-1} to keep convection in the forced regime. The typical wind speed at BBSO is about 6 m s^{-1}. Therefore, the NST will almost always operate in the forced regime. In Chapter 4 the basic design of the THCS for NST is presented. The hierarchical structure of the THCS and a description of the THCS components are given. Chapter 5 carries further the development of the THCS and presents the results of experiments conducted using the 5/8-sphere dome louvers.

1.5 VIM: A Two-Dimensional Imaging Magnetograph

Solar magnetic field measurements are based on observing the polarization signal in a solar absorption line. In the presence of a sufficiently strong magnetic field, such

as those present in a sunspot ($\sim$ 1000 Gauss), a spectral line will be split into its respective Zeeman components. The effect is evident when looking at the intensity (Stokes I) profile of the spectral line. For weak fields, the effect is less evident and one must look at the polarization signal for information about the magnetic field. A solar polarimeter is an instrument that operates as a spectrometer and has in addition a set of polarization analyzing optics to discern between different states of polarization. VIM is one such instrument. It uses a Fabry-Pérot Interferometer (FPI) to scan the desired spectral line and a set of two LCVR to determine the state of polarization. In Chapter 7 a calibration method for the two LCVRs is presented along with the first polarimetric measurements obtained with VIM.

1.6 Quiet Sun Observations

Chapter 8 is a based on two-dimensional spectroscopic observations of a quiet Sun region at disk center made using VIM at the DST at NSO/SP on 2006 June 11. The telescope field was centered on a supergranular cell at disk center, and four 30-minute near simultaneous time-series were observed with a 600 nm broad band filter with a narrow band Hα 656.3 nm and NaD_2 589.0 nm interference filter (IF). The analysis of the data presented in Chapter 8 focuses on the occurrence of dynamic upflow events that occur in the solar atmosphere. Upflow events, such as the ones presented in Wang *et al.* (1998), have been observed in Hα line-wing (-0.05nm) filtergrams where they appear as dark rounded features with sizes of 2″–3″. In Chae *et al.* (1998) a close correlation between Hα upflow events and transition region explosive events was established. Upward velocities of 15–30 km s^{-1} are typical with lifetimes of 1–2min. Upflow events are thought low in the solar atmosphere in regions of magnetic diffusion. In a two-step magnetic reconnection model of presented in Chae *et al.* (1998), upflow events begin as a build up of a magnetic island that is formed as a result of slowly occurring magnetic reconnection in the photosphere.

A critical flux is reached provoking an instability that causes the island to move upwards with increasing velocity. The island is observed in Hα in the middle to upper chromosphere. In Chapter 8 application of the techniques used in Lee *et al.* (2000) are applied for studying upflow events in Hα using the Na D_2 data. The height of formation of the Na D_2 absorption line occurs at a lower altitude then Hα, thus allowing a unique view into the characteristics of upflow events in their nascent stages of development in the lower solar atmosphere.

CHAPTER 2

THE LOCAL SEEING ENVIRONMENT AT BIG BEAR SOLAR OBSERVATORY

2.1 Overview

The site survey for the Advanced Technology Solar Telescope (ATST) of the National Solar Observatory (NSO) was initiated in 2002 to find the best location for a 4-meter aperture solar telescope. At the end of a four year survey, three sites – Big Bear Solar Observatory (BBSO) in California, Mees Solar Observatory (MSO) on Haleakalā, Maui, Hawai'i, and Observatorio Roque de los Muchachos (ORM) on La Palma, Spain – were identified as excellent sites for high-resolution solar observations. MSO was ultimately chosen as the future ATST site. In this chapter a subset of the ATST site survey data focusing on the local seeing environment at BBSO is presented. Of particular interest are the seeing characteristics at a mountain lake-site observatory, its relation to the local environment and climate, and its implications for the 1.6-meter New Solar Telescope (NST) currently being built at BBSO. A close correlation of very good seeing conditions with the prevailing wind direction and speed is found. The observatory building, located at the end of a 300-meter causeway, is surrounded by the cool waters of Big Bear Lake, which effectively suppress the ground-layer seeing. Very good seeing conditions from sunrise to sunset are a unique feature of BBSO, which makes it ideally suited for synoptic observations and sustained high-resolution studies of solar activity and space weather.

2.2 Introduction

Ground-based solar observations in the 21st century require a site with a large clear-time fraction, good sky transparency and excellent seeing conditions for extended

periods of time. These characteristics lend themselves to the performance of high-resolution solar telescopes. From the onset of modern solar observations, site surveys have played an important role in effecting the location and design of solar observatories.

Starting in March 2002 and ending in August 2004 the National Solar Observatory conducted a thorough study of various sites (Hill *et al.*, 2004b,a, 2006; Lin and Penn, 2004; Socas-Navarro *et al.*, 2005) to place the ATST (Keil *et al.*, 2004; Rimmele *et al.*, 2005; Wagner *et al.*, 2006). Haleakalā on Maui, Hawai'i was selected as the future ATST site. Bradley *et al.* (2006) present a detailed study of weather data and nighttime seeing conditions for Haleakalā based in part on data from the Maui Space Surveillance System. They also study the dependence of seeing on wind characteristics. The ATST site survey has produced a wealth of seeing and climate data for all finalist sites, which will be of benefit (beyond the intended scope of the survey) for high-resolution solar observations and the operations solar telescopes at these locations.

BBSO is a lake-site observatory situated at an altitude of 2067 m in the San Bernardino mountains of Southern California. The Big Bear Lake follows the east-west orientation of Big Bear Valley. This orientation and the surrounding mountains channel the air flow and give rise to predominately westerly winds (Denker and Verdoni, 2006). Establishing the observatory was the result of a comprehensive site survey conducted in 1965 (Zirin and Mosher, 1988) by Caltech. Visual seeing estimates were derived for more than 30 sites throughout Southern California. By the end of the first year the survey had narrowed the field to the more promising sites: Big Bear Lake, Lake Elsinore, Mount Piños, and Lockwood Valley. In general, the survey determined that the best seeing conditions were encountered in the proximity of lakes or close to oceans. Over water, evaporation occurs simultaneously with cooling, which provides a natural temperature inversion and in turn limits local

variations of the refractive index resulting in good and stable seeing conditions. A large clear-time fraction coupled with good seeing conditions and feasibility of construction led to the final decision in favor of Big Bear Lake.

Around the same time as the Caltech site survey, solar physicists from 11 European countries joined to form (JOSO) in a concerted effort to find a suitable location to carry out solar observations of high quality in southern Europe (Brandt and Wöhl, 1982). By 1976 after a thorough survey of close to 40 sites, the organization had narrowed the choices to two islands in the Canaries – La Palma and Tenerife. The main difference between the two sites were the wind characteristics, i.e., wind speed and direction. The "Caldera Effect" at La Palma for easterly winds introduces local turbulence and deteriorates the seeing conditions. The nighttime seeing conditions at Observatorio del Roque de los Muchachos, La Palma were described in detail in Vernin and Munoz-Tunon (1994). The JOSO daytime seeing data, however, slightly favored Observatorio del Teide on Izaña, Tenerife.

The ATST site survey instrument suite consisted of a sky brightness monitor (Lin and Penn, 2004) and two instruments, the Shadow Band Ranger (ShaBaR) and the Solar-Differential Image Motion Monitor (S-DIMM), to measure the seeing characteristics (Beckers, 2001). The ShaBaR scintillometer data were used in two distinct inversion procedures to determine the height stratification of the atmospheric turbulence (Socas-Navarro *et al.*, 2005) with the S-DIMM measurements as boundary conditions for the ground-layer seeing. In addition, the scintillometer's DC signal was used as a proxy for the cloud-cover and clear-time fraction. In this study, only the S-DIMM data obtained at BBSO from 2002 March 3 until 2004 August 28 are used, since only site-specific seeing characteristics in the context of the future NST (Goode *et al.*, 2003; Denker *et al.*, 2006) are of interest. Furthermore, escaping the ground-layer seeing by placing the entrance aperture high above the ground is not an issue at BBSO, since the NST entrance aperture will be only 2 m higher than

the existing telescope and the seeing improvement with height is much less than the predictions for mountain and island sites (Socas-Navarro *et al.*, 2005). Therefore, the S-DIMM measurements obtained at a height of 8 m above the ground should be a fair representation of the seeing conditions under which the NST will operate (Denker and Verdoni, 2006).

In Section 2.2, some of the geographical and climatological features, which make BBSO a unique site for high-resolution studies of solar activity and space weather phenomena (Gallagher *et al.*, 2002) are presented. Instrument description and operation of the S-DIMM at BBSO are summarized in Section 2.3. The results of this study are presented in Section 2.4, where the seeing characteristics at BBSO, their relation to wind speed and direction, and the role of Big Bear Lake in effectively suppressing the ground-layer seeing are discussed. Section 2.5 provides a brief summary of the most important results and outlines some of the future work in the context of NST.

2.3 Local Climate and its Effects on Big Bear Lake

Big Bear Lake is an artificial reservoir in the San Bernardino Mountains (Figure 2.1) with a storage capacity of 90×10^6 m^3 and a surface area of 12 km^2. The lake is elongated in its east-west direction with a length of about 6 km and a width of about 2 km. The widest section of the lake is about 4 km. However, numerous bays and the lake's irregular shape result in a shore line over 33 km. The average depth is about 7 m with the deepest point located at the western end of the reservoir near the dam at 22 m. Towards the end of the drought season in late 2004, the lake level dropped to 5.3 m below full corresponding to a reduced storage volume of only 36.5×10^6 m^3. The surface area of the lake shrunk to an extend, where the shore line receded about 50 m beyond the observatory peninsula, i.e., the observatory was no longer surrounded by the lake. The lake level data are provided by the Big Bear

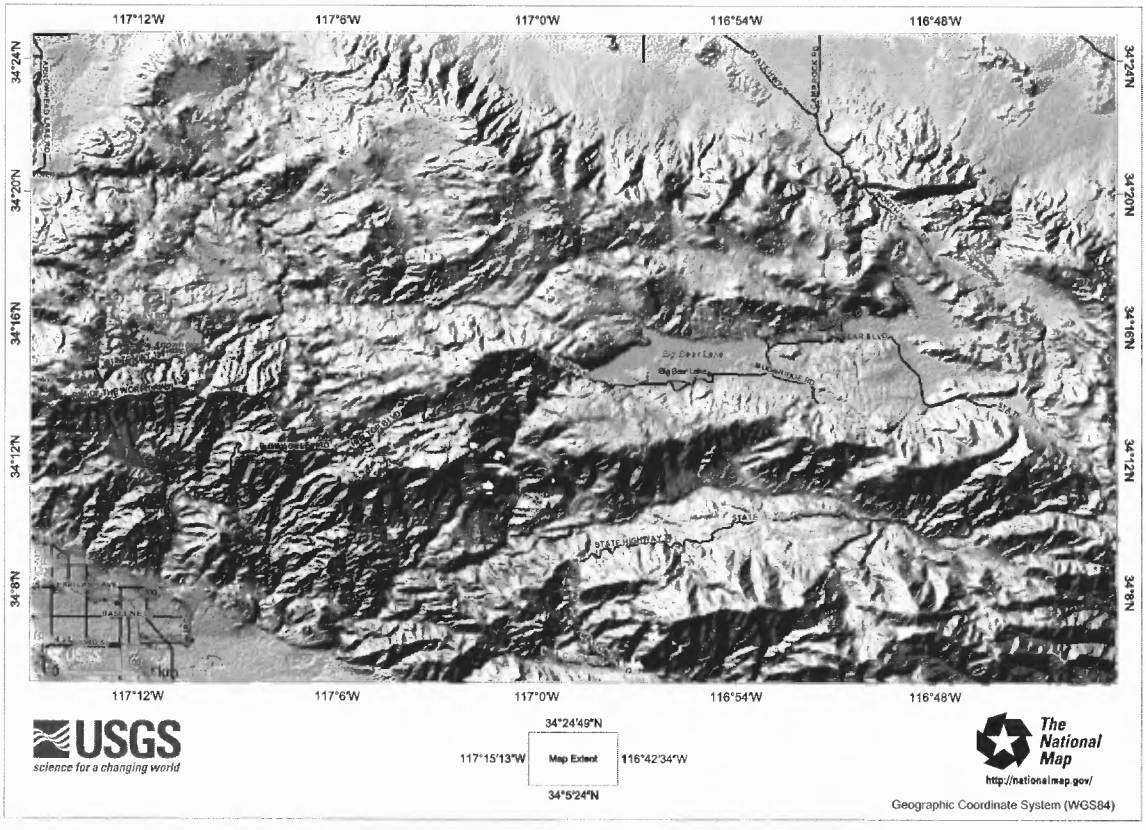

Figure 2.1 Topographical map (shaded relief) of Big Bear Lake and Big Bear Valley. BBSO is located at 116° 54.9′ West and 34° 15.2′ North.

Municipal Water District (BBMWD, `http://www.bbmwd.org/`) on a weekly basis a service to the public.

The San Bernardino Mountains receive most of their precipitation during the winter months. The lake is replenished in the spring by the run-off of the snow-packed mountains surrounding Big Bear Valley with minor contributions during the "monsoon season" in the summer. Figure 2.2 shows the lake level from 2000 to mid 2006. Evaporation in the summer and partial replenishment of the reservoir in the winter produce a characteristic step function, which is associated with a multi-year drought period in Southern California. The ATST site survey was carried out during the lowest lake levels. During a 14-day period with extreme precipitation, the lake rose by more than 5 m, which indicated the end of the drought period in 2005.

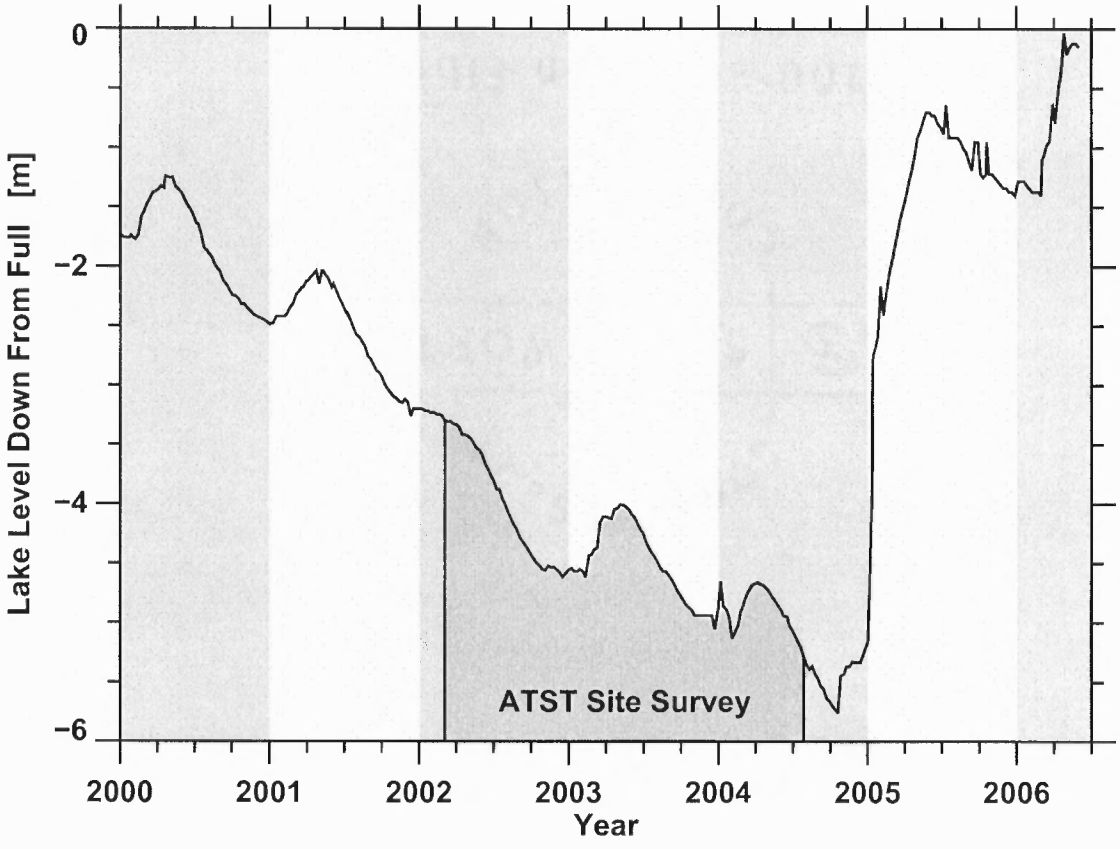

Figure 2.2 The level of Big Bear Lake from 2000 until mid-2006. The ATST site survey was conducted from March 2002 until August 2004 during an extended drought period in Southern California.

Precipitation in 2005 and 2006 has been above average and the lake was filled to capacity.

BBSO is located on a small island connected to the north shore of the lake by a 300-meter causeway (see Figure 2.3). Big Bear lake is situated at an altitude of 2067 m in the San Bernardino mountains of southern California. Geographically, the San Bernardino Mountain range is oriented in an east-west direction. This orientation allows for a predominantly westerly wind flowing along Big Bear Valley. The unique location of BBSO inside a mountain lake, which effectively suppresses the ground-layer seeing, raises one important issue. Even though the ATST site survey has been the most extensive survey of solar observing sites to date, its duration is

Figure 2.3 Big Bear Solar Observatory with ATST site survey test stand in 2002.

necessarily short compared to complex climate phenomena such as ocean-atmosphere interactions.

The El Niño-Southern Oscillation (ENSO) phenomenon, for example, is one of the strongest sources of climate variability in Southern California, which has been linked to the recent multi-year drought period in the south-western U.S. A detailed review of droughts and the paleoclimatic variability in the western U.S. has been presented by Woodhouse (2004). Periodic drought conditions are common and as the result of global climate change, the south-western U.S. is predicted to become dryer during both summer and winter seasons with more extreme temperature days and an increase in the severity of drought conditions (Hanson and Weltzin, 2000). Since climate prediction at regional scales are still in their infancy and past conditions might not be a good analogue for the future, the BBSO ATST results can only be interpreted as a snapshot of a range of seeing conditions. Similar connections between local climate may also exists for other sites covered in the ATST site survey. However, cost and feasibility have prohibited long-term studies of seeing characteristics so far.

2.4 Observations

Differential Image Motion Monitors (DIMMs) have been used by nighttime astronomers for years to study the seeing conditions of a particular site (e.g., Sarazin and Roddier, 1990). For nighttime observatories a typical DIMM instrument consists of two small pupils a fixed distance apart that image starlight onto a CCD or other detector. The images are optically separated on the CCD and the differential image motions are measured. The S-DIMM as presented in Beckers (2001) uses the differential motion between two images of the solar limb. The instrument was first presented by Liu and Beckers (2001) in a study of the seeing conditions at the Fuxian Lake Solar Station. The S-DIMM used in the ATST site survey consists of two apertures with a diameter of 45 mm. The apertures were covered with a reflecting foil to attenuate the incident light to approximately 10^{-5} transmission.

They are separated by 225 mm in the north-south direction. The apertures are placed on a 30 cm aperture telescope with a focal length of 2721 mm manufactured by Meade. A narrow slit is placed at a right angle across the solar limb. The limb is imaged separately on to a CCD detector and thus the differential motion is measured. The relation between the variance of the differential image motion and the Fried-parameter r_0 can be found in Sarazin and Roddier (1990). In the case of the S-DIMM, only the longitudinal variance can be used in determining the Fried parameter r_0. With daytime correlation time-scales being on the order of $\tau_0 \approx 40$ ms, the 10 s interval is long enough to yield reliable statistics used for determining the variances of the differential image motion.

The height of the test stand platform is 6 m above the causeway. The effective height of the seeing measurements is 8 m above ground taking into account telescope pier and the mount of the Meade telescope. The geodetic construction of the test stand allows only translational motions of the platform in the horizontal direction without any tilts. S-DIMM can be operated in wind speeds of up to 10 m/s. In

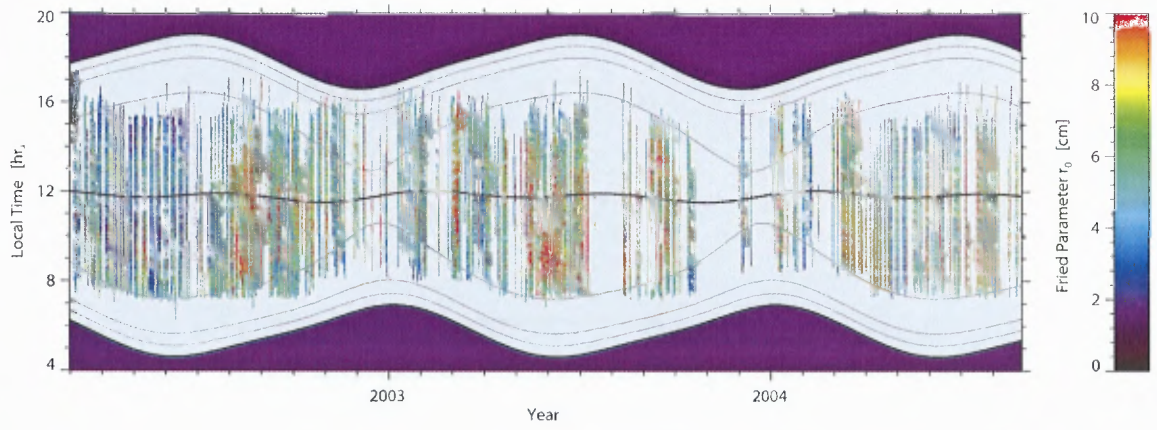

Figure 2.4 Rainbow color coded image of the Fried parameters r_0 obtained with S-DIMM. The color red corresponds to $r_0 \geqslant 10.0$ cm. Missing data points are displayed in light gray. The thick black lines represent sunrise, local noon, and sunset, respectively. The gray contours refer to air masses of 10, 5, and 2, respectively.

high wind conditions exceeding this threshold, the slit images can move off the CCD detector.

To aid the analysis, solar ephemeris including optical air mass computations were obtained from the Horizons On-Line Ephemeris System (`http://ssd.jpl.nasa.gov/horizons.cgi`, Giorgini *et al.*, 1996) provided by the Jet Propulsion Laboratory (JPL). The S-DIMM, ShaBaR, weather station, and ephemeris data are aggregated in one common data format. Since the seeing data was sampled at a cadence of 10 s for a period of 16 hours (from 4:00 am to 8:00 pm local time), each parameter was saved as a two-dimensional array with the observing day on one axis and the time of day on the other axis. The formatted data consisted of 910×5760 data points. Even though many data points do not contain any meaningful data (e.g., before sunrise and after sunset), this format enabled a straightforward merging of disparate data sets using standard logical operations. All data reduction was carried out in the Interactive Data Language (IDL) and the source code is available upon request.

The entire data set of S-DIMM Fried parameter measurements is summarized as a color image in Figure 2.4. In addition to indicators of sunrise, local noon, and

sunset (thick black lines), gray contour lines were added for air masses of 10, 5 and 2. Missing data values are presented in light gray. Most of the observations were obtained with air masses lower than 2. Only in the late afternoons during the winter months some measurements exist in the air mass regime between 2 and 5. Data points with air masses greater than 5 are completely absent.

The ATST seeing monitor is not a fully automated system. An observer had to start it every morning and shut it down in the (late) afternoon. Therefore, the ATST seeing data is biased by the site-specific observing profile. At BBSO, observing typically starts between 8:00 am and 9:00 am, which can easily be deduced from Figure 2.4. Even the switch to daylight savings time is clearly discernible. The seeing monitor was typically shut down between 4:00 pm and 6:00 pm. This bias towards observations during low air masses is quite different from the observing profiles at mountain sites. Here, the good seeing conditions in the early morning required an earlier start of the observations leading to a much larger number of observations with higher air masses.

The observing and error statistics of the BBSO seeing monitor are summarized in Table 2.1. The health status flags are represented in hexadecimal notation where each hexadecimal number corresponds to a particular error condition. Flag 2 is related to a read-out problem of the Meade telescope's right ascension position, which does not affect the seeing data. Flag 8 almost exclusively occurs when no light reaches the ShaBaR detectors, i.e., the instrument is stored in a protective weather cover but the weather station is still turned on to collect data. This data has to be excluded from the data analysis. In contrast to the approach in the SSWG report, data with Flag 10 were included, since their frequency distributions were very similar to the other ones included in the study. Since Flag 10 typically indicates high-wind conditions and BBSO is the windiest site in the ATST site survey, a large number of data points would have to be discarded otherwise.

Table 2.1 Health Status of All Seeing Monitor Subsystems

Flag	Data Points	Included	Error Condition
0x0000	253279	√	All seeing monitor subsystems are working.
0x0002	364789	√	Failed Meade.
0x0008	26074		Failed ShaBaR.
0x000a	475136		Failed ShaBaR/Meade.
0x0010	89486	√	Non-zero rail count (high wind).
0x0012	192624	√	Non-zero rail count (high wind) and failed Meade.
0x0014	8	√	Non-zero rail count (high wind) and failed weather station.
0x0018	867		Non-zero rail count (high wind) and failed ShaBaR.
0x001a	17093		Non-zero rail count (high wind) and failed ShaBaR/Meade.
0x0020	3533	√	Observing log entry.
0x0022	3664	√	Observing log entry and failed Meade.
0x0030	689	√	Observing log entry and non-zero rail count (high wind).
0x0032	1547	√	Observing log entry and non-zero rail count (high wind) and failed Meade.

NOTE.— Only measurements between sunrise and sunset are included. The data flags are: (0) good data, (1) failed video, (2) failed Meade, (4) failed weather station, (8) failed ShaBaR, (16) non-zero rail count (high wind), and (32) observing log entry. Since system events can occur simultaneously, the status flags are added numerically and are represented in hexadecimal notation. Data points with failed ShaBaR flags were excluded from the data analysis.

In summary, if the seeing monitor would have been operational every day from sunrise to sunset 4,070,000 individual measurements could have been obtained. However, the number of data entries for BBSO is about 1,430,000 (see Table 2.1). A substantial fraction of the missing data is related to the aforementioned observer profile. Other contributions are from complete system failures (July and November 2003) and bad weather conditions. Considering all data without a "failed ShaBaR" error flag about 910,000 data points could be used in this study. This number, however, is further reduced by about 60,000 data points, since some S-DIMM data were not properly transferred to the control computer. This led to periodically occurring Fried parameter values of $r_0 = 0.0$ cm. The signature of this are the thin gray horizontal bands in Figure 2.4.

In the final report (`http://atst.nso.edu/site/reports/RPT-0021.pdf`, Hill *et al.*, 2004b) of the SSWG, these missing values were replaced by a running average to have a better statistics for the comparison of S-DIMM and ShaBaR data. In this study, a more conservative approach is used and these values are dropped completely. In addition, all BBSO data was included in this study, whereas the time period covered in the SSWG report was restricted to a common time frame for the different sites (2002 July 18 to 2004 August 30). Since the treatment of missing data values and the instrument health status flags differs from the algorithms used in the SSWG report, the numerical results show some deviations. However, the overall agreement between the results is very good.

2.5 Results

2.5.1 General Seeing Characteristics

The most important parameters describing the seeing characteristics at BBSO are the Fried parameter r_0, the wind speed v, and the wind direction θ. The frequency

distributions discussed in this section include indiscriminately all valid data points of the entire site survey from from 2002 March 3 to 2004 August 28.

In Figure 2.5, the frequency distribution of the Fried parameter r_0 is shown. The mean, median, and 10th percentile of r_0 are 6.4 cm, 6.1 cm, and 10.1 cm, respectively. These values are indicated by vertical lines in Figure 2.5. Furthermore, a Fried parameter $r_0 > 7.0$ cm occurs during more than 37.3% of the time. The respective value for $r_0 > 12.0$ cm is 4.2%. Using the frequency distribution shown in Figure 2.5 as representative, observing times of 1166 and 130 hours are found for these thresholds of $r_0 > 7.0$ cm and $r_0 > 12.0$ cm. These blocks of observing time have already been corrected for the Clear Time Fraction (CTF)at BBSO. In Table 2 of the SSWG final report (Hill *et al.*, 2004b) two values of 0.712 and 0.714 are listed for the CTF. The latter value was obtained during the site survey of the Global Oscillation Network Group (GONG Hill *et al.*, 1994). In contrast to this study, the SSWG final report lists in Table 1 the number of hours with $r_0 > 7.0$ cm and $r_0 > 12.0$ cm at BBSO as 863 and 65, respectively.

The r_0 thresholds were used in the ATST site survey as benchmarks for comparing the various sites. The frequency distribution of the r_0 values can be approximated by a log-normal distribution (see e.g., Fried and Mevers, 1974)

$$f(r_0, \mu, \sigma) = \frac{1}{r_0 \sigma \sqrt{2\pi}} \exp\left(\frac{-(\ln r_0 - \mu)^2}{2\sigma^2}\right) \tag{2.1}$$

with a mean of $\mu = 1.8$ and a standard deviation of $\sigma = 0.5$ of r_0's logarithm. The expected value is $\mathrm{E}(r_0) = \exp(\mu + \sigma^2/2) = 6.8$ cm with variance $\mathrm{Var}(r_0) = \exp(\sigma^2 - 1)\exp(2\mu + \sigma^2) = 21.3$ cm^2 (corresponding to a standard deviation of 4.6 cm). Since a significant number of r_0 values cluster close to 0.0 cm, the log-normal distribution cannot be used to fit the entire population. Therefore, a Gaussian

$$g(r_0, \mu, \sigma) = \frac{1}{\sigma \sqrt{2\pi}} \exp\left(\frac{-(r_0 - \mu)^2}{2\sigma^2}\right) \tag{2.2}$$

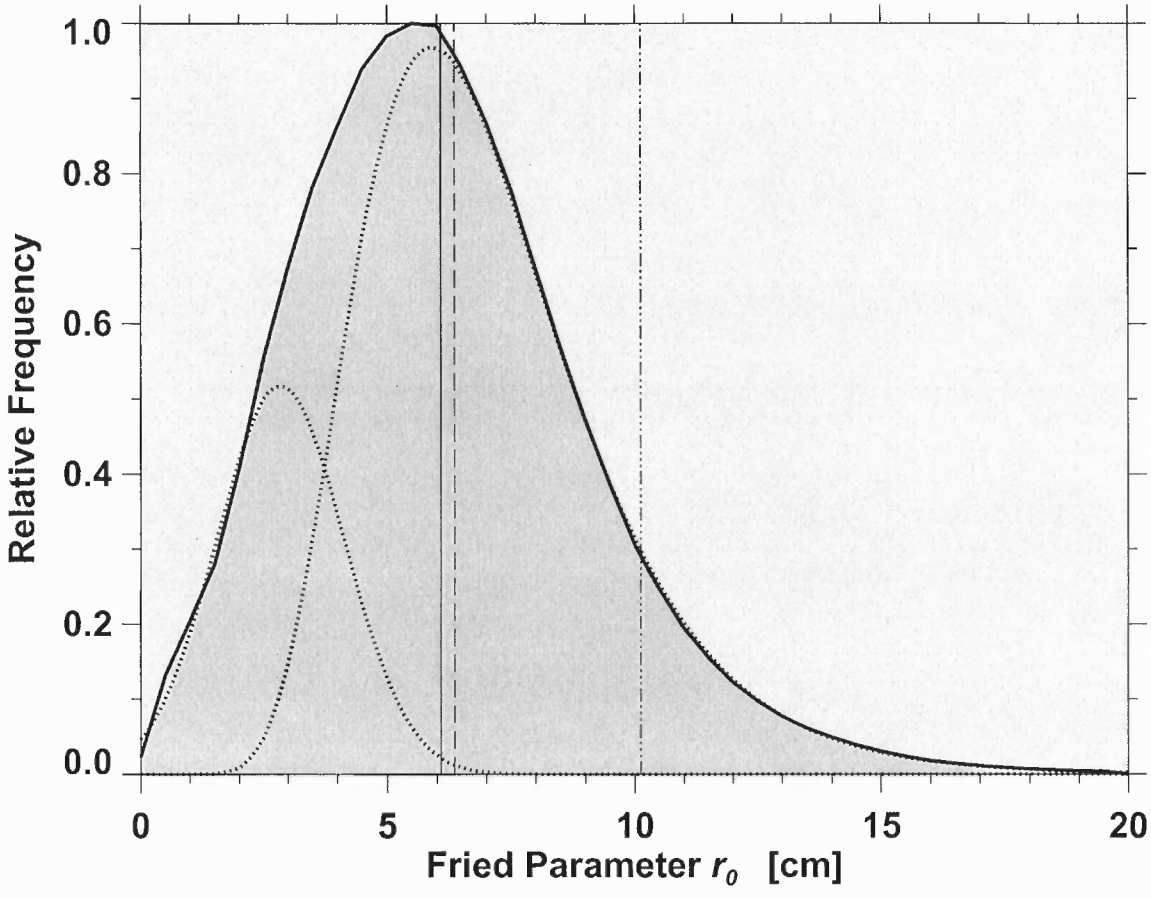

Figure 2.5 Histogram of the Fried parameter r_0. The vertical lines represent the mean (solid), median (dashed), and 10th percentile values of the Fried parameter r_0, respectively. The dotted curves (from left to right) represent the normal and log-normal distribution fits, respectively.

with a mean r_0 of $\mu = 2.8$ cm and a corresponding standard deviation of $\sigma = 1.3$ cm was added. Other fits, including two Gaussians or two log-normal distributions, led to unsatisfactory results. This might be an indication of the presence of two different seeing regimes. A similar problem was found in fitting the wind speed distribution (see Figure 2.6), where an additional Gaussian was required to account for the low wind speed population. Indeed, the two different r_0 distribution could be a signature of the changeover from the gentle mountain downslope winds at night to the more forceful daytime winds traversing Big Bear Lake.

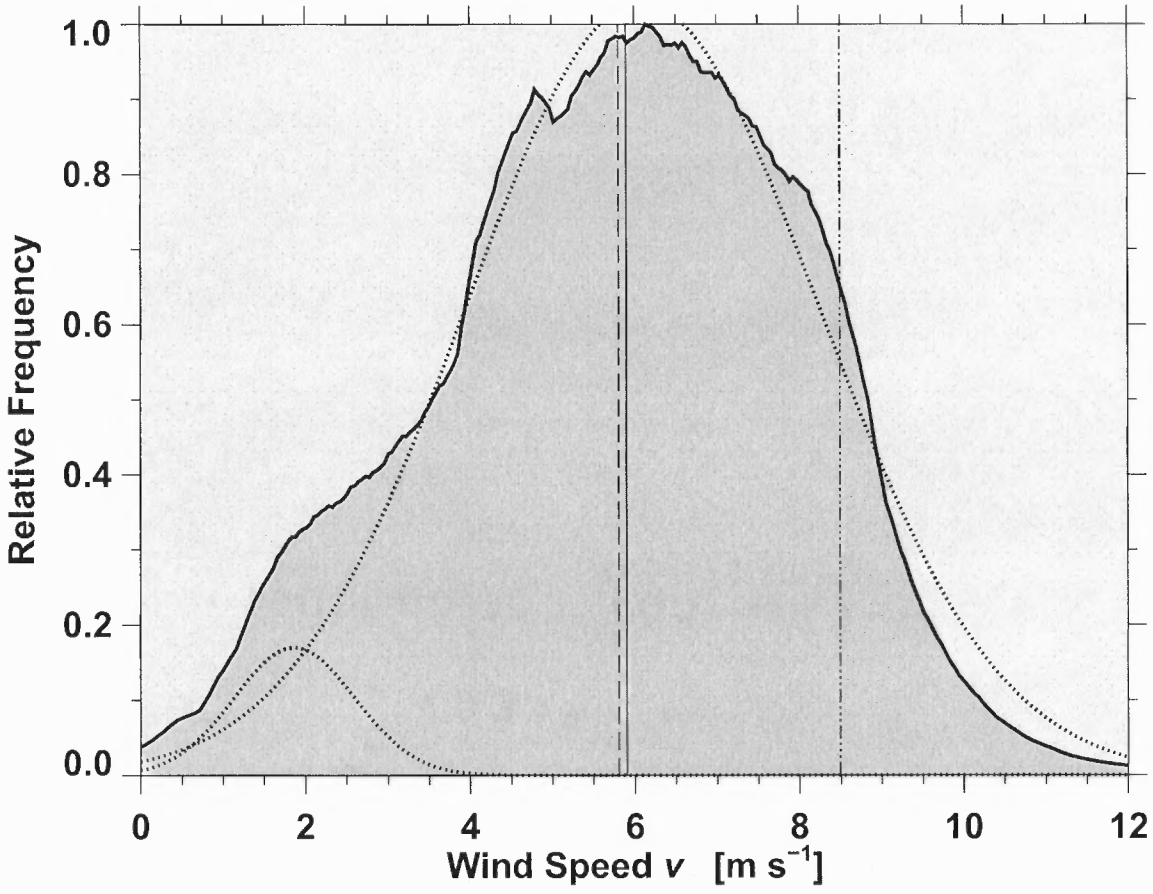

Figure 2.6 Histogram of the wind speed v. The vertical lines represent the mean (solid), median (dashed), and 10th percentile values of the wind speed v, respectively. The dotted curves represent the two normal distributions used to fit the bimodal wind speed profile.

The frequency distribution of the wind speed v is shown in Figure 2.6. The mean, median, and 10th percentile of v are 5.8 m s^{-1}, 5.9 m s^{-1}, and 8.5 m s^{-1}, respectively. The distribution has a bimodal shape with a distinct shoulder on the low wind speed side. Therefore, two Gaussians were fitted to the curve (dotted lines in Figure 2.6) and a low wind speed distribution was obtained with a mean of $\mu = 1.9$ m s^{-1} and a standard deviation of $\sigma = 0.7$ m s^{-1}. The respective values for high wind speeds are $\mu = 6.1$ m s^{-1} and $\sigma = 2.1$ m s^{-1}. The low wind speed distribution encompasses about 5.3% of the total wind speed measurements.

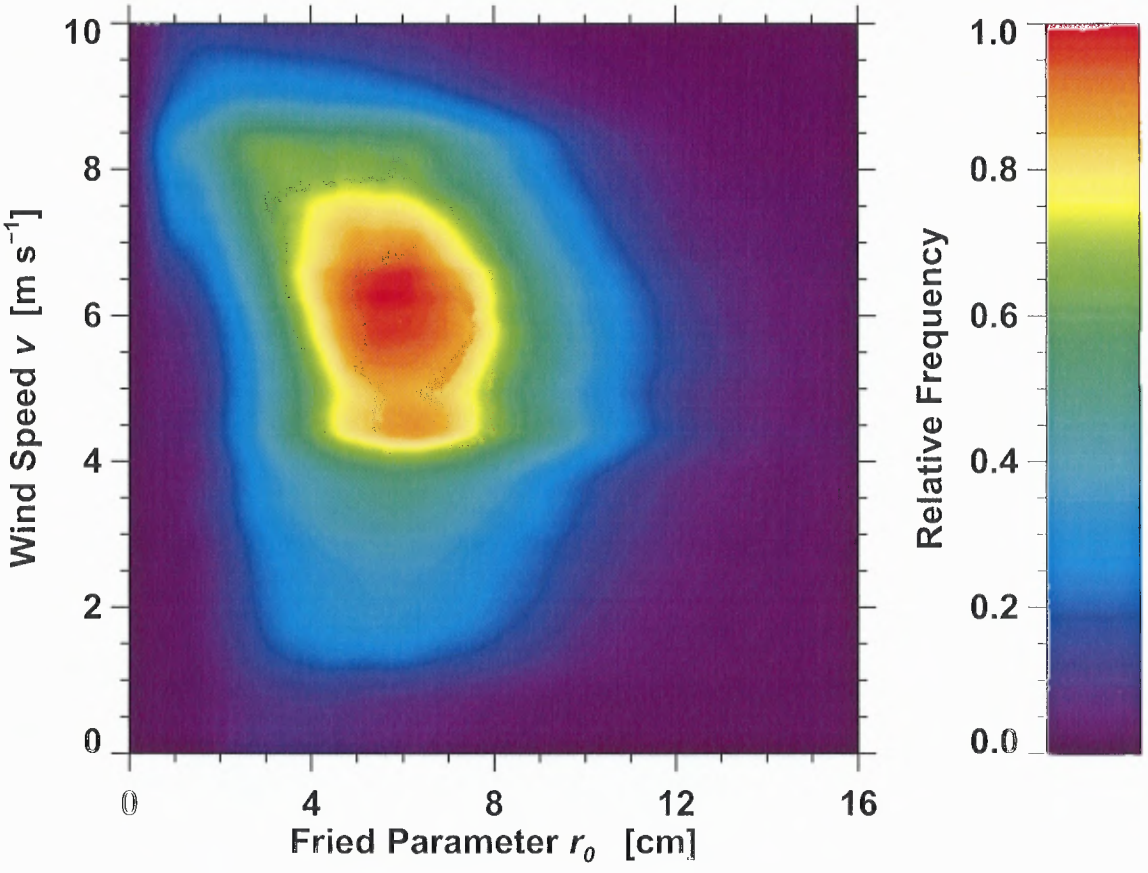

Figure 2.7 Two-dimensional frequency distribution of the Fried parameter r_0 and the wind speed v.

The two-dimensional frequency distribution in Figure 2.7 combines the two most important parameters, wind speed v and Fried parameter r_0, which describe the seeing characteristics at BBSO. The shape of the distribution resembles the letter "D", which indicates an asymmetric distribution towards higher Fried parameters in the most common wind speed regime. Most values are clustered in the range v = 4.0 to 8.0 m s^{-1} and r_0 = 4.0 to 8.0 cm. Good seeing conditions are rarely encountered under low- or high-wind speed conditions. High wind conditions are typically the result of storm systems over the Pacific Ocean traveling southward along the Californian coastline before turning inland to move across the south-western U.S. Occasionally, high winds are associated with Santa Ana winds (Hu and Liu, 2003), which are a product of an inland high pressure system funneling gusty, hot

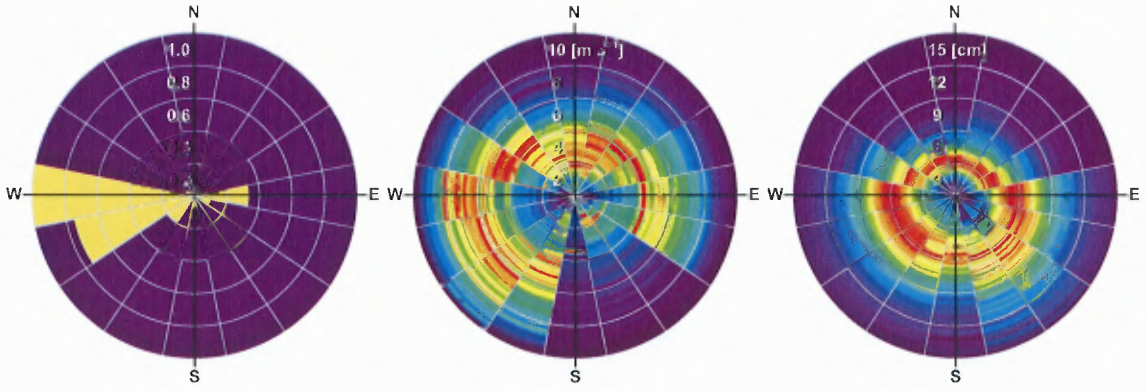

Figure 2.8 *Left.* Polar plot representing the distribution of the wind directions θ at BBSO. *Middle.* Frequency distribution of the wind speed v vs. wind direction θ (grid spacing $\Delta v = 2$ m s^{-1}). *Right.* Frequency distribution of the Fried parameter r_0 vs. wind direction θ (grid spacing $\Delta r_0 = 3$ cm). The distributions were separately scaled for each of the 16 wind direction bins.

desert winds through the canyons and valleys of the San Bernardino Mountains. In the former case, strong turbulence at the altitude of the jet stream will lead to a deterioration of the high-altitude seeing. On the other side of the spectrum, i.e., in the low wind speed regime, the laminar wind flow across the lake surface ceases to exist. As a result heat plumes will rise from the dome and observatory island increasing ground-layer turbulence.

The observations summarized in Figure 2.7 bear also on the NST design. Wind speeds larger than 2.0 m s^{-1} are required to effectively vent the NST dome to avoid dome seeing. However, if the wind speed exceeds 5.0 m s^{-1}, the wind flow through the dome has to be limited to avoid wind buffeting of the open telescope structure. Since this wind speed regime encompasses the best seeing conditions at BBSO, care has to be taken in the thermal control of the dome interior. This requires that dome louvers have to automatically adapt to changing wind conditions (Verdoni and Denker, 2006; Denker and Verdoni, 2006).

One of the most intriguing features of the micro-climate at BBSO is the strong correlation of the daytime wind direction with the east-west orientation of Big Bear Valley. The frequency distribution of the daytime wind directions is shown in the left

panel of Figure 2.8. The length of the pie-shaped segments represents their frequency of occurrence for each of the 16 directions of the compass rose. The prevailing wind directing is West (W: 37%, WSW: 28%, and SW: 7%). In 12% of the measurements, the wind is from the East. The remaining wind directions contribute less than 16%. The origin of the daytime winds are pressure gradients between the coastal Los Angeles basin and the interior regions of the Southern Californian deserts. The valleys of the San Bernardino Mountains then channel these winds, thus, creating the laminar westerly wind flows observed at BBSO. The occasional easterly wind are related to a reversal of the pressure gradient. The resulting strong offshore and downslope winds are commonly referred to as Santa Ana winds (Hu and Liu, 2003), which are characterized by warm temperatures, low relative humidity, low level wind shears and clear skies. The nighttime wind conditions at BBSO are quite different. Cold mountain downslope winds drain into the valley leading to a more uniform distribution of wind directions – with the exception of southerly winds, which rarely occur. Typical wind speeds are about 2.0 m s^{-1} substantially less than during the daytime.

The middle panel of Figure 2.8 displays frequency distributions of the wind speeds for each of the 16 directions on the compass rose. The rainbow color code indicates the number of occurrence with red colors indicating the largest number of occurrences. Each distribution was normalized individually to account for the strongly biased occurrence of the wind directions. The highest wind speeds are encountered for westerly wind directions. The median wind speed is about 7 m s^{-1}. The corresponding median wind speed of about 5 m s^{-1} for easterly winds is substantially less. Since the westerly wind speeds cluster between 4.0 and 8.0 m s^{-1}, sufficiently strong winds are available to flush the ventilated NST dome interior enabling active control of the dome thermal environment.

The right panel of Figure 2.8 follows the same format as the previous panel but displays the frequency distributions of the Fried parameter r_0. The highest values of the Fried parameter (median $r_0 \approx 7.0$ cm) are encountered for westerly winds. The seeing conditions are still good (median $r_0 \approx 6.0$ cm) for East winds, which are often associated with Santa Ana conditions. However, since Santa Ana winds carry large amounts of dust from the desert, good seeing comes at the price of reduced sky clarity. Only if the winds are from the North, the seeing conditions deteriorate to a point (median $r_0 \lesssim 4.0$ cm), where high-resolution solar observations become impossible. North is the only direction, where the air flow is never above the lake surface. Downslope winds from the mountains and the dense pine forest along the north shore are responsible for elevated air turbulence. The strong correlation between wind speed and good seeing conditions is one of the features responsible for the unique seeing profile at BBSO, which allows high-resolution solar observations for extended periods of time from sunrise to sunset (winds from the North occur only in 10% of the time).

2.5.2 Diurnal and Seasonal Variation of the Seeing Conditions

The cool waters of Big Bear Lake tend to suppress the ground-layer seeing typically encountered at mountain and mountain-island sites. This effectively eliminates the deleterious effects of ground heating begining in early morning and experienced at sites without water. The top panel of Figure 2.9 shows the Fried parameter r_0 as a function of time from local noon. The choice of local time as the temporal axis has the advantage to see at one glance the seeing conditions during a typical observing day at BBSO. The shaded background represents the standard deviation of all r_0 values for a given time. The best seeing conditions are typically encountered about two hours before local noon. The convex shape of the temporal seeing profile is quite different from mountain and mountain-island sites, which show a pronounced

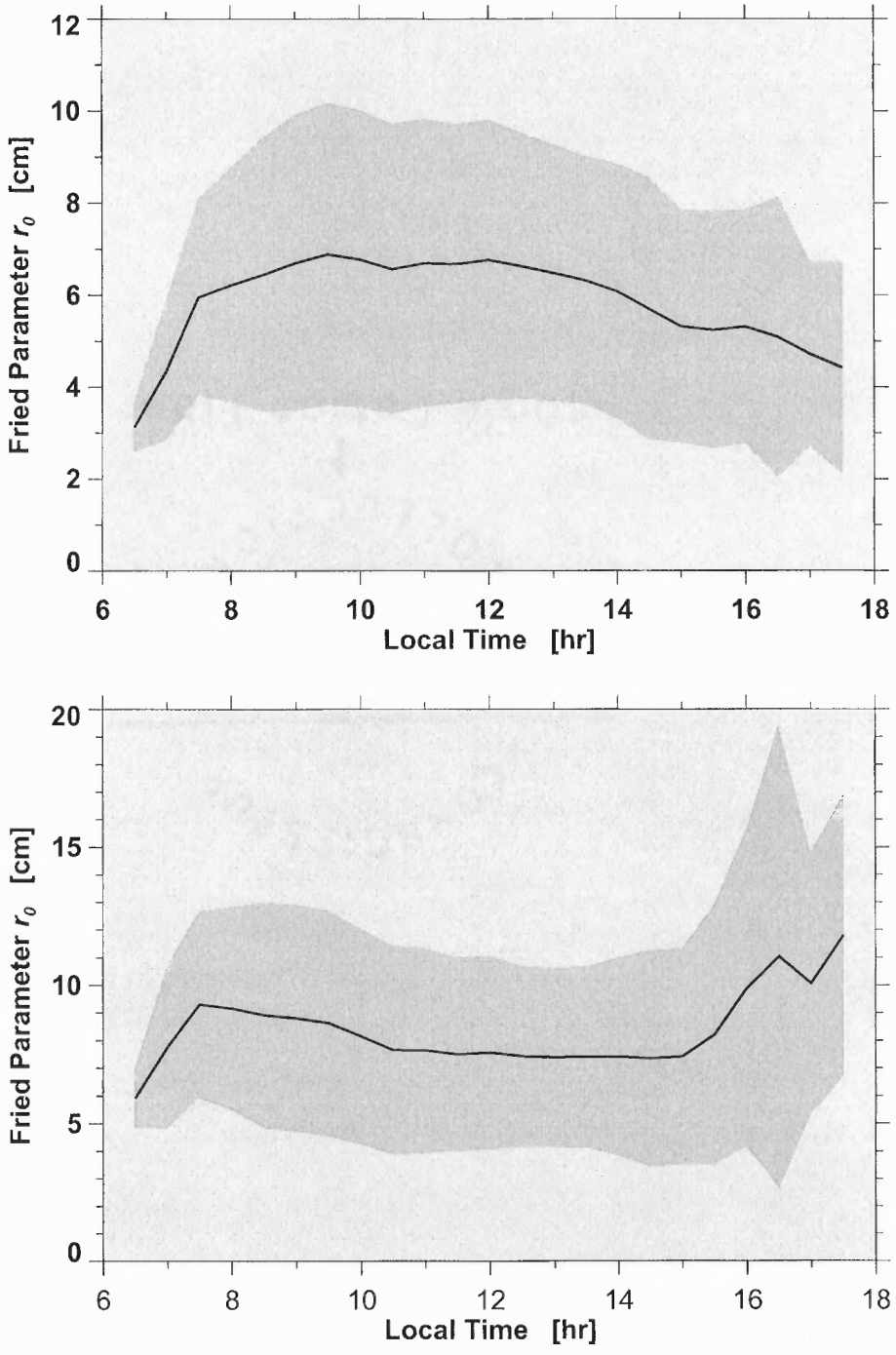

Figure 2.9 *Top.* Average Fried parameter r_0 as a function of time with respect to local noon. *Bottom.* Corresponding air mass corrected temporal behavior of r_0. In both cases, the gray background represents the standard deviation reflecting the range of typically encountered seeing conditions.

maximum early in the morning before ground heating sets in. Considering that observations with solar AO require a Fried parameter $r_0 \gtrsim 7.0$ cm (Rimmele, 2000; Denker *et al.*, 2007), Figure 2.9 clearly indicates that AO corrected observations are possible at BBSO for substantial periods of time from sunrise to sunset.

Even though an air mass corrected Fried parameter is only meaningful in nighttime observations, the air mass corrected temporal behavior of the Fried parameter r_0' (bottom panel of Figure 2.9) still provides some important insight. The time profile is surprisingly flat with typical values of $r_0' \approx 8.0$ cm. The notable exception is in the afternoon at five hours after local noon. A closer inspection of the data reveals that these higher r_0' values originate from a small number of observations in the winter time close to sunset. In these cases, the air mass is large. Thus, the air mass corrected Fried parameter is high. As mentioned in Section 2.3, the BBSO ATST seeing monitor was usually started between 8:00 am and 9:00 am and turned off between 4:00 pm and 6:00 pm local time. Therefore, almost all of the measurements were taken at low air masses. This explains the absence of a lobe with higher r_0 values after sunrise in the bottom panel of Figure 2.9. The slightly larger r_0' values before sunset hint at such a lobe. Note that the statistics for observations outside the range of local noon ± 4 hours are very poor and strongly biased towards afternoon observations in the winter (see Figure 2.4).

Since the lake-site location of BBSO is a unique feature for a solar observatory, the question is posed, if the seeing conditions are related to the length of the line-of-sight that the sunlight traverses across the lake. In a first step, the air mass corrected Fried parameter r_0' as a function of the solar azimuth angle. This curve is very flat with an average r_0' of slightly less than 8.5 cm. In this display, the conspicuous late afternoon spike seen in the bottom panel of Figure 2.9 completely disappears. Note that again the observations are restricted to low air masses due to the operating schedule of the seeing monitor. In a second step, a topographical map

of Big Bear Valley was digitized and the lake surface was. Thus, the line-of-sight length across the lake could easily be computed for any value of the Solar azimuth angle. However, no meaningful correlation between seeing conditions and the Sun's position across the lake was detected. Considering that the worst seeing conditions are encountered for northerly winds, it was concluded that the wind direction is of minor importance for the seeing conditions, as long as it traverses a substantial fraction of water. Under these conditions, the wind flow becomes laminar and the ground-layer seeing is effectively removed.

The nighttime wind regime is characterized by gentle mountain downslope winds with typical wind speeds of less than 2.0 m s^{-1}. Furthermore, large fractions of the night might not show any air motion at all. The downslope winds descend the mountain ridges surrounding Big Bear Lake from any direction with the exception of South. The wind characteristics during the day are quite different as can be seen in Figure 2.10. Beginning at sunrise, the mild winds encountered during the night increase in force until they reach their maximum of about 6.0 m s^{-1} at local noon. Ground heating and the pressure differential between inland desert and coastal areas are the origins of these winds, which will calm again after sunset. Correlated with the increase of wind speed, a rapid decrease of air moisture is observed. The humidity at noon is less than 40% during 60% of the time. The interaction of increasing wind speed and decreasing air mass is one explanation of the larger Fried parameters seen at 10:00 am local time in the top panel of Figure 2.9.

The bar chart in Figure 2.11 depicts the seasonal variations of the wind speed. The dark gray bars represent the mean wind speed for each month. In addition, bars in lighter grays were included to indicate the top 10^{th} and 30^{th} percentiles of the monthly distributions. The difference in wind speed between months are typically less than 2.0 m s^{-1}. The highest wind speeds occur in the summer months, when the

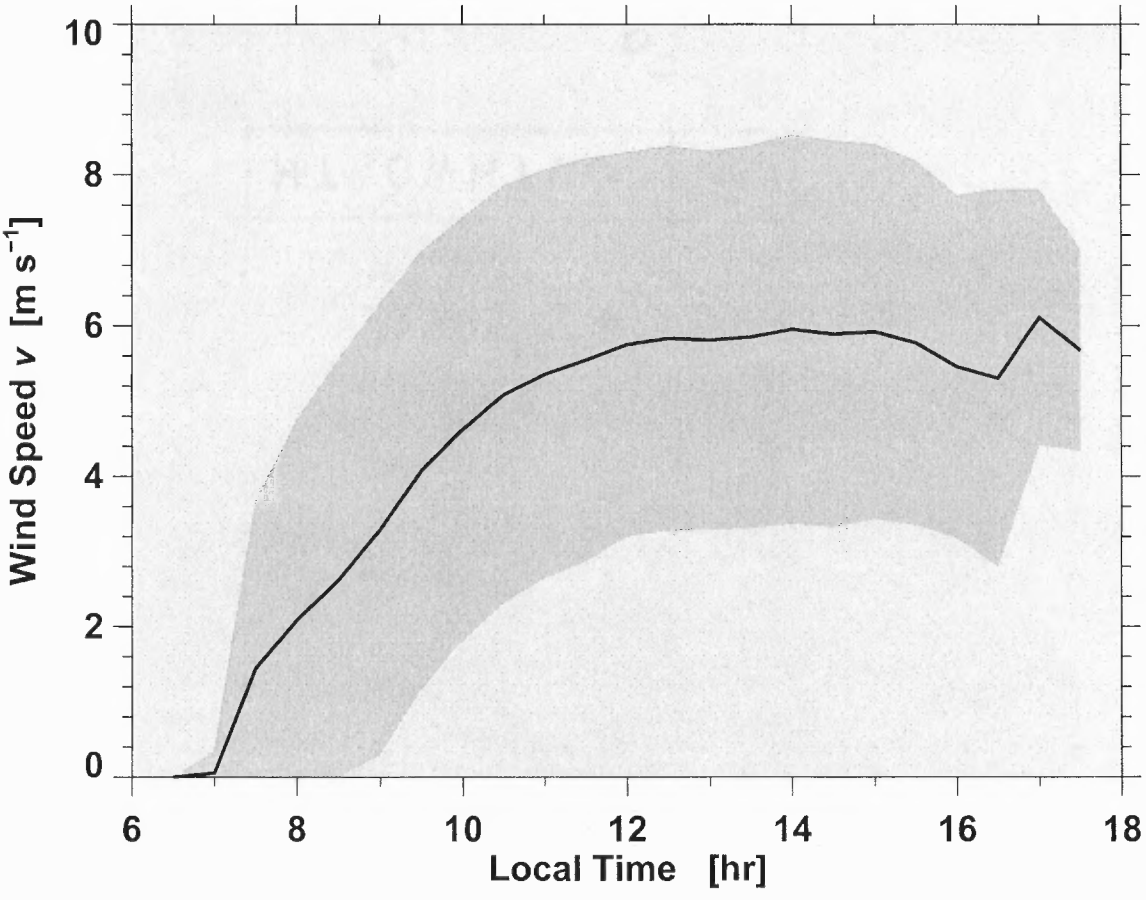

Figure 2.10 Average wind speed as a function of time with respect to local noon. The gray background represents the standard deviation reflecting the range of typically encountered wind conditions.

mean values approach 6.0 m s^{-1}. The wind characteristics for the remaining months are very similar.

The bar chart of the seasonal variation of the Fried parameter r_0 (Figure 2.12) essentially follows the seasonal variation of the wind speeds (Figure 2.11). The best seeing conditions take place in the (late) summer, when the Fried parameter r_0 exceeds 7.0 cm. With the exception of the months of February and April, the mean Fried parameter hovers around 6.0 cm. The winter and early spring season at BBSO is characterized by short but sometimes severe winter storms, which can last several days. Since the ATST site survey covered less than three years, the variance in the mean value and percentiles of r_0 could be related to the small sample, in

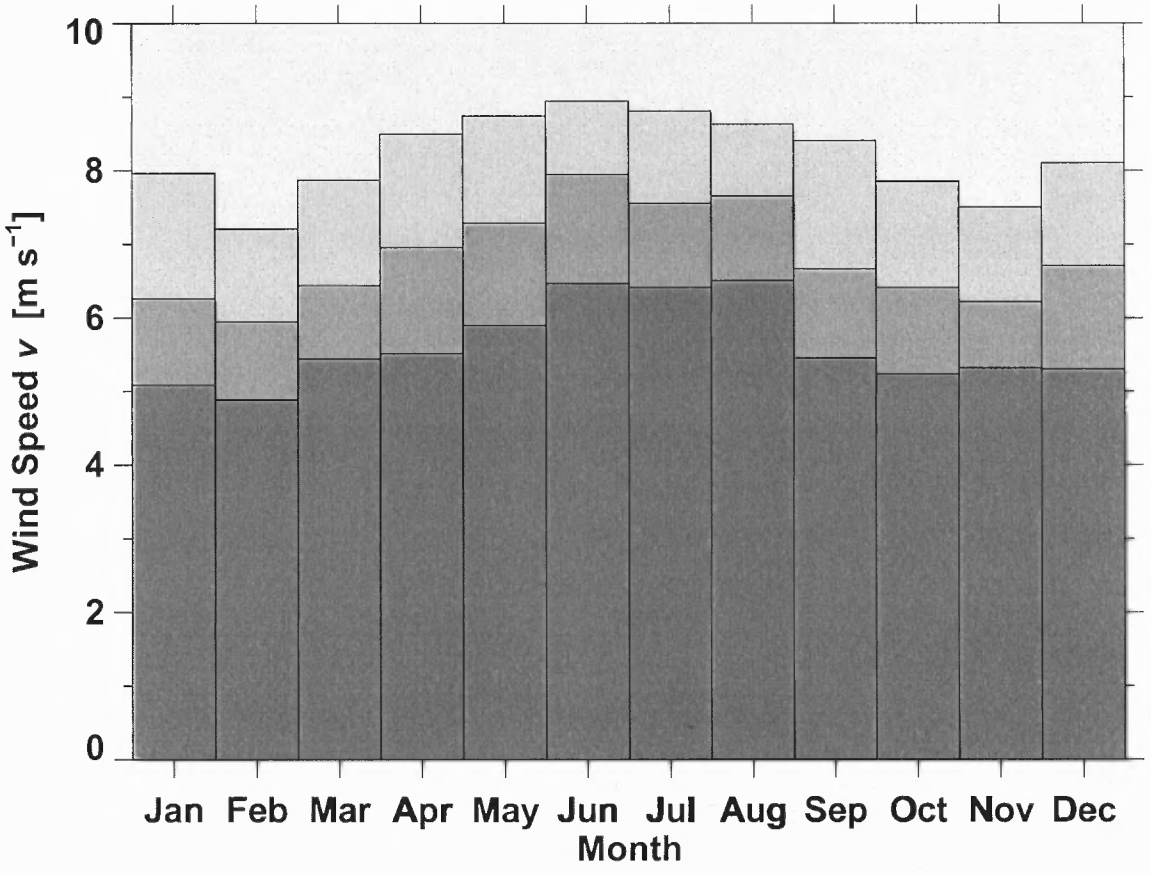

Figure 2.11 Monthly variation of the wind speed v. The average wind speed is shown as dark gray. The lighter grays correspond to the top 10^{th} and 30^{th} percentile of the monthly frequency distributions.

which the winter storms are unevenly distributed. The seasonal variation of the Fried parameter r_0 strongly suggests an all year operation of the observatory, which again makes BBSO a good candidate for synoptic observations and sustained high-resolution observing campaigns.

2.6 Conclusions

The following list provides the major findings and conclusions of this examination of the ATST site survey data.

1. Fried parameters of $r_0 \gtrsim 7.0$ cm are necessary to resolve solar granulation so that the wavefront sensor of an AO system can track on quiet Sun (Rimmele,

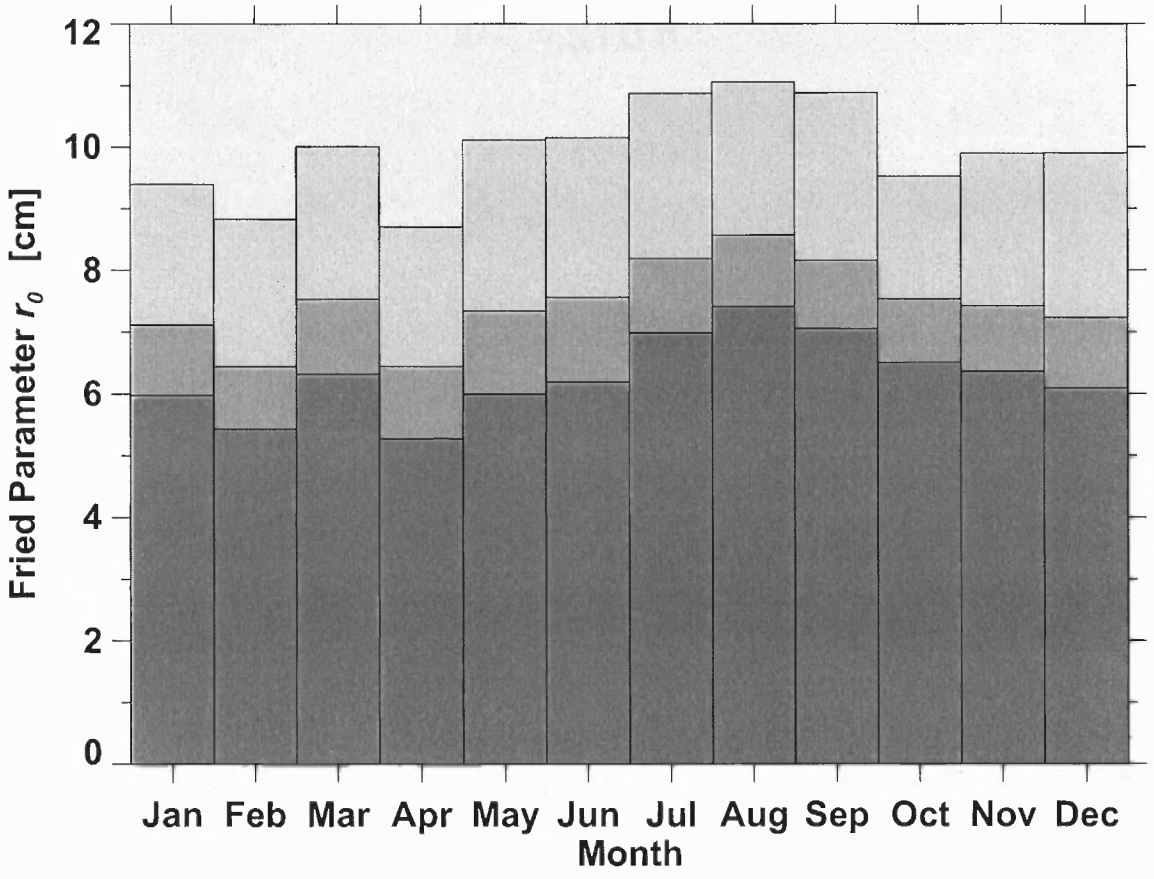

Figure 2.12 Monthly variation of the Fried parameter r_0. The average Fried parameter is shown as dark gray. The lighter grays correspond to the 10^{th} and 30^{th} percentile of the monthly frequency distributions.

2000; Denker *et al.*, 2007). Since the mean Fried parameter is $r_0 = 6.4$ cm, AO-corrected observations can be obtained at BBSO for extended periods of time.

2. The flat seeing profile with good seeing conditions from sunrise to sunset makes BBSO ideally suited for synoptic observations with small telescopes with apertures of less than 25 cm, which do not have an integrated AO system.

3. The seasonal variation of the Fried parameter r_0 indicates that high-resolution observations can be obtained all year round. However, the best seeing conditions take place in the (late) summer.

4. The correlation between wind speed v and Fried parameter r_0 suggests that strong laminar wind flows across the lake are necessary to effectively removed local turbulence responsible for ground-layer seeing. The mediocre seeing conditions related to mountain downslope winds support this finding.
5. The ATST site survey was conducted during a severe drought in Southern California. Big Bear Lake receded from the observing peninsula and exposed much of the lake floor, which gave rise to local turbulence. For this reason, better seeing conditions should be expected for higher lake levels, when the observatory peninsula is tightly surrounded by the lake.
6. Finally, as with the "Caldera Effect" at La Palma, the seeing conditions at BBSO are closely related to local topography and micro-climate. Even though BBSO belongs to the class of mountain-lake sites, the strong influence of local topography and micro-climate leaves the question unanswered, if BBSO is typical representative of that class. Panguitch Lake in Utah was another mountain-lake site included in the first half of the ATST site survey. Comparing both sites might provide important clues on how lakes effectively suppress of ground-layer turbulence and if these results could be generalized to represent an entire class of observing sites. The ATST site survey has provided a wealth of information for some of the major solar observatories in the world to accurately assess these site-specific characteristics.

The ATST site survey provided comprehensive seeing information for a variety of sites, which ultimately led to the selection of Haleakalā, Maui, Hawai'i as the future ATST site. Since many of the major solar observatories were included in this study, the data provides also detailed seeing information for each of the sites, which will be beneficial for the operation of existing telescopes and siting of future instruments. Furthermore, the site survey not only allowed for a rigorous characterization of the

BBSO seeing environment as presented in this study, but also motivated the integration of seeing measurements into the operation of NST (Denker and Verdoni, 2006). Upon completion NST will be engaged in a host of campaign-style solar observing programs consisting of high-resolution spectro-polarimetry and synoptic studies of solar activity (Gallagher *et al.*, 2002; Goode *et al.*, 2003; Denker *et al.*, 2006). To aid in the prioritization and scheduling of these programs, work has already begun incorporating the existing ATST seeing data into future NST operations.

CHAPTER 3

THE NEW SOLAR TELESCOPE

3.1 Overview

NST is an off-axis open-structure Gregorian-style telescope with a 1.6 m aperture. The project is a collaborative effort between BBSO, the Korean Astronomical Observatory (KAO) and the Institute for Astronomy (IfA) at the University of Hawaii. NST replaces the 65 cm vacuum telescope at BBSO and from the start will be engaged in high resolution campaign-style observations of the Sun with an emphasis on small-scale photospheric magneto-convection and chromospheric dynamics. NST will be housed in the existing observatory structure. However, modification of the telescope pier and replacement of the dome was necessary to accommodate NST's larger size and open structure design. As of January 2008, all major contracts for design and fabrication have been made and construction and installation of NST is well underway. In this chapter, an overview of BSSO site characteristics, NST optical design, heat stop assembly, optical support structure (OSS), control systems, and finally active optics, adaptive optics and post-focus instrumentation is presented. Some of these topics are discussed in much greater detail in other chapters of this thesis but the aim here is to present a complete picture of NST and the robustness of the underlying design ideas and their execution.

3.2 Introduction

Resolving the fine structure on the Sun is one of the major drivers in building large aperture solar telescopes. With a clear aperture of 1.6 m at a wavelength of 500 nm the NST will have an angular resolution of approximately 0.065″. This is an angular resolution corresponds to a length of approximately 50 km on the solar surface, which

by no accident is on the order of the cross-section of a single magnetic flux tube – a key ingredient in understanding solar magnetism (Zwaan, 1981). With recent advances in AO, NST joins a growing group of ground-based open-structure solar telescopes, moving beyond the conventional meter-class vacuum telescopes that have been in operation at solar observatories for decades. NST is ideally suited for campaign-style solar observations providing unparalleled spatial and temporal resolution for both active region and quiet sun studies. The telescope will feed facility class post-focus instrumentation that includes BBSO's next generation of magnetographs (Denker *et al.*, 2003a,b; Cao *et al.*, 2006). Telescope operations will also benefit from AO and a Real-Time Image Reconstruction (RTIR) system that employs parallel processing (Denker *et al.*, 2001b, 2005). Both the AO and RTIR systems will be discussed in more detail in Chapter 6.

NST will play an important role as a major contributor in the solar physics community by providing imaging of the Sun with unprecedented spatial resolution. It will be in a key position to contribute data and research with active space-based missions such as the Solar Dynamics Observatory (SDO), Solar TErrestrial RElations Observatory (STEREO) and the SOLAR-B/Hinode mission. The large field-of-view (FOV) magnetic measurements of the Helioseismic and Magnetic Imager (HMI) on board SDO can be complemented with higher resolution magnetic field measurements taken using both of the NST imaging magnetographs. In a similar way NST will complement both STEREO and Hinode observations with higher spatial resolution images and magnetograms. Along with these collaborations the design and construction of NST began with some specific science objectives.

The objectives of NST are (a) high-resolution, high cadence studies of solar activity such as flares, (b) the temporal evolution and sub arc-second structure of the magnetic region where the flare occurred, (c) the study of the dynamics of kilo-Gauss flux tubes, (d) magneto-convection in sunspots and (e) the study of potential heating

Figure 3.1 Big Bear Solar Observatory outfitted with the recently refurbished dome at the end of a 300 m causeway. In the foreground of the image is a small dome housing the earthshine and Hα full-disk telescope.

mechanisms associated with the upper solar atmosphere. All of these objectives require high-angular resolution in order to resolve the fundamental photospheric magnetic structure size which lays at the heart in understanding the mechanisms responsible for transporting energy flux from the photosphere to the upper solar atmospheric layers. Along studies of small-scale magnetic fields, NST will engage in the study of larger concentrations of magnetic flux such as sunspots. By providing high-resolution observations over long periods of time the NST is in a key position to bridge the gap between global and local solar phenomena.

3.3 Site Characteristics

BBSO is located at the end of a 300 m causeway that stretches out from Big Bear Lake's north shore. Figure 3.1 shows the main observatory building, which is outfitted with the new NST dome, at the end of the causeway. The observatory was established in 1969 by California Institute of Technology, after a comprehensive site

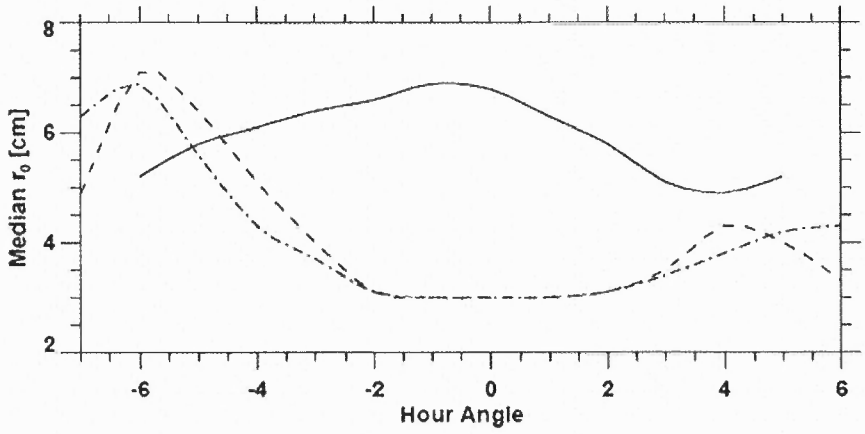

Figure 3.2 Seeing characteristics for three of the sites identified in the ATST site survey suitable for high-resolution solar observations. The x-axis shows the hour angle of the Sun while the y-axis represents the median Fried parameter r_0. The three lines, solid, dashed-dotted and dashed represent BBSO, La Palma, and Haleakalā, respectively (Figure 2 in Denker *et al.* (2006)).

survey had been carried out (Zirin and Mosher, 1988). Big Bear Lake is located at an altitude of approximately 2000 m in the San Bernardino Mountains of Southern California. The lake actively suppresses the ground layer seeing, which coupled with a predominately westerly wind affords BBSO excellent conditions for solar observing. Chapter 2 provides an in depth description of the local seeing characteristics at BBSO. The characterization was based on the analysis of data taken by the SSWG during the search for the best location for the ATST. BBSO benefits from long periods of good seeing (median r_0 greater than 6.0 cm) throughout most of the day, with higher values occurring closer to local noon.

This is a markedly different profile from the high-altitude,volcanic island locations such as La Palma, Canary Islands and Haleakalā, Maui considered in the ATST survey. For these sites the best conditions occur early in the day and then taper off by local noon when the ground-layer seeing begins to dominate. Figure 3.2 shows the seeing characteristics for La Palma (dashed-dotted), Haleakalā (dashed), and BBSO (solid). It is important to note that the height of the SSWG instrument (Beckers,

2001) matches that of the NST primary mirror. Thus, the data collected by the survey had a direct impact on the design of the thermal control of the telescope and dome environment (Verdoni and Denker, 2006). The details of the thermal control for the NST are presented in length in Chapters 4 and 5.

3.4 Optical Design

NST was modeled after the Scatter-free Observatory for Limb Active Regions and Coronae (SOLAR-C) of the University of Hawai'i. SOLAR-C is a 0.5 m off-axis coronagraph funded by the National Aeronautics and Space Administration (NASA) and the Air Force Office for Scientific Research (AFOSR). It is operated by the University of Hawaii on Haleakalā (Kuhn *et al.*, 2003). The development and successful deployment of SOLAR-C has shown that an off-axis design can achieve the required collimation, alignment and scattered light performance required for NST. SOLAR-C also provided insight into solutions of technical issues such as mirror cell support, thermal design, active optical alignment, control and software not only for NST but also for future off-axis open-structure telescopes such as ATST.

Like the SOLAR-C, NST is an off-axis Gregorian-type telescope. The telescope is comprised of four mirrors – a 1.7 m parabolic primary (M1), a 14.5 cm concave ellipsoidal secondary (M2), and two diagonal flat mirrors (M3 and M4). The diagonal flat mirrors M3 and M4 direct the light into the declination and Coudé axis, respectively. The heat stop assembly, explained in the next section, will be placed at the primary focus between M1 and M2. The primary mirror was fabricated from a Zerodur blank. Zerodur, the material of choice for most modern high precision optical applications, has high material homogeneity, sufficiently large operating temperature and low coefficient of thermal expansion ($0.1 \pm 1.0 \times 10^{-7}$ K^{-1}). As stated above the diffraction limit of the telescope in the visible at 500 nm is $0.065''$ with a corresponding near-infrared value of $0.21''$ at 1,600 nm. NST working wavelength

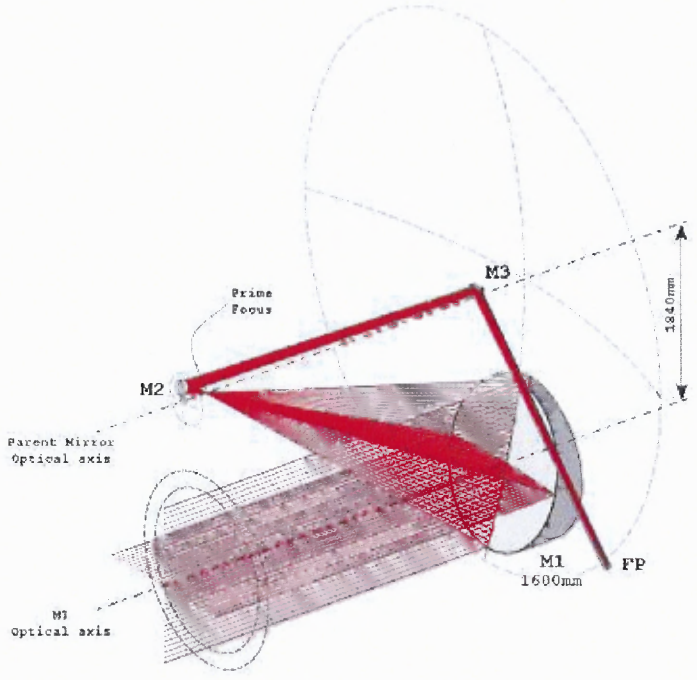

Figure 3.3 NST optical optical layout showing the parent mirrors of both M1 and M2 (courtesy of Roy Coulter).

range will be from 390–1,700 nm. Figure 3.3 shows NST's optical layout. The primary mirror is situated 1.84 m from the optical axis of its 5.3-meter parent mirror. The f-ratio of the M1 parent is $f/0.73$ with the f-number of the primary mirror at 2.4 corresponding to a focal length of 4.1 m. Both M1 and M2 are figured to $\lambda/30$ and $\lambda/15$ respectively with a finishing of 1.0-1.5 nm. The FOV in the optical laboratory will be $180''$. The effective focal length of NST is 83.2 m corresponding to a final focal ratio in the Gregorian focus of $f/52$. For an effective focal length of 83.2 m, the diameter of the secondary image is 73 mm corresponding to a FOV of $3'$ and a plate scale of $2.48''$ mm^{-1}.

The University of Arizona's Steward Observatory Mirror Laboratory (SOML) is developing computer generated hologram (CGH) techniques for use in producing 8.4-meter mirrors for large-scale projects such as the Giant Magellan Telescope (GMT) and the Large Synoptic Survey Telescope (LSST). To test these techniques SOML is using the NST primary as a 1/5 scale project (Martin *et al.*, 2004). Figure 3.4

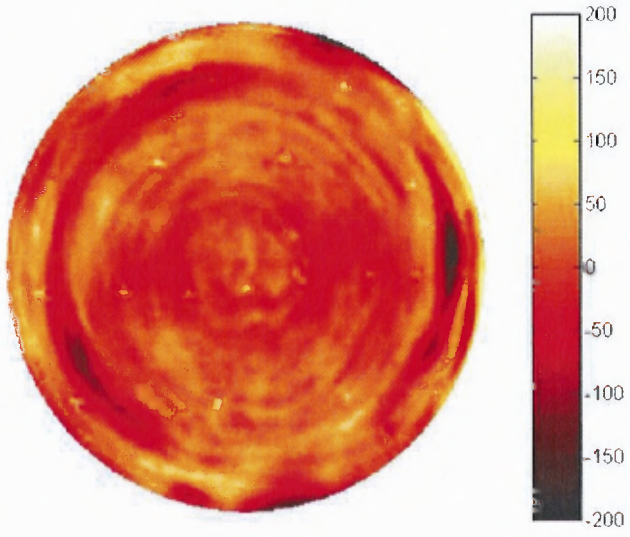

Figure 3.4 The rms-surface error of the NST primary mirror as measured by the SOML in February 2006 (Figure 6 in Denker *et al.* (2006)).

shows the surface errors of M1 as measured in February 2006. At the time of this measurement the rms-surface error was 35 nm – approximately 25 nm off from the 10 nm value required for the NST. To date, the polishing of M1 has reached the expected rms value and the mirror is now headed to Kitt-Peak, Arizona to be aluminized. The fabrication and polishing of M2 was completed by the Space Optics Research Laboratory (SORL). SORL figured two M2 mirrors from the same parent, one of which will be used as a back-up.

One of the benefits of NST's off-axis design is having an unobstructed pupil, which eliminates scattered light and also enhances the AO system performance. Another advantage of the off-axis design is that the prime focus is easily accessible with no obstruction in the light path. The primary mirror will be mounted on a set of 36 actuators, which will compensate for gravity and thermal effects. M2 will be mounted on a hexapod system manufactured by Physik Instrumente, Germany and can be positioned using the system to attain a linear and rotational accuracy of ± 2 μm and ± 10 μrad, respectively. Figure 3.5 shows a CAD rendering of M2 mounted on the hexapod system with the heat stop in place.

Figure 3.5 CAD rendering of the M2 mirror mounted on the Physik Instrumente M-850 hexapod system (light gray) with the heat stop in place (courtesy of Jeff Kuhn).

To help keep the relative alignment of M1 and M2 throughout the observing period, a dedicated wavefront sensor mounted between M2 and M3 will be used. Along with the wavefront sensor, polarization calibration optics, including linear polarizers and wave retarders, will be mounted here as well.

Figure 3.6 shows the general optical layout of the wavefront sensor and the set of polarization calibration optics as they will be mounted between M2 and the optical flat M3. With a beam diameter of 96–98 mm just 400–200 mm before M3, relatively large optical elements with diameters of about 100 mm will be required.

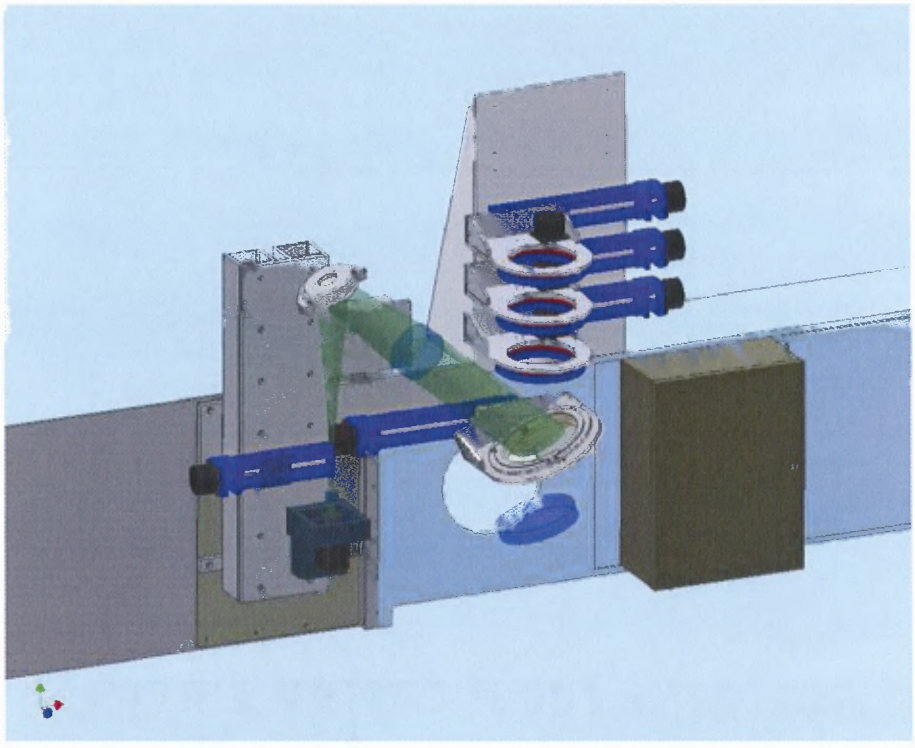

Figure 3.6 CAD rendering showing the general optical layout of the wavefront sensor and the polarization calibration optics (courtesy of Roy Coulter).

3.5 Heat Stop Assembly

The prime focal plane of NST will receive approximately 2,500 W of power giving an irradiance of about 2.5 W mm^{-2} or 2.5 M W m^{-2}. To dissipate this energy, the heat stop shown from two different perspectives in Figure 3.7, which was designed and built in-house at IfA, will be used. IfA developed a similar heat stop for the SOLAR-C telescope so that integration of this component should be relatively seamless. As the light gathering power of solar telescopes increases, the careful implementation of a heat stop becomes a necessity. For the old 65 cm vacuum telescope at BBSO, the heat stop dumped the waste beam in to the dome environment. Doing this for NST would add most of the 2,500 W to the dome environment creating unwanted internal seeing effects. The NST heat stop will absorb rather than reflect a majority of the incident radiation and transfer the heat outside of the dome via a circulating chilled fluid.

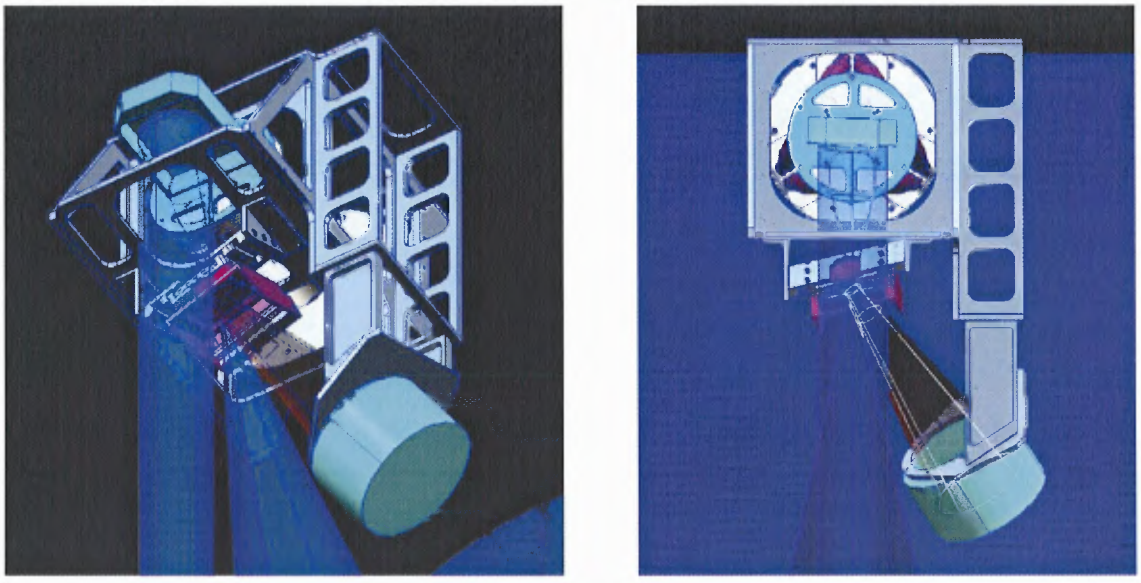

Figure 3.7 CAD rendering showing the NST heat stop from two different perspectives (Figure 7 in Denker *et al.* (2006)).

The designed pointing range of NST is up to 8′ beyond either side of the solar limb. The primary focus geometry is defined by both this pointing range of the telescope and by the folded light paths at the secondary mirror M2. The prime focal surface is shown in Figure 3.8 along with the pointing range of the telescope. The outermost circle with a diameter of 81 mm defines the image zone within which the full solar disk can reside. The reflecting surface of the heat stop will provide a buffer of approximately 10 mm around this. Light that falls outside of this zone will generate a signal triggering a safety measure. Centered on the image zone is the prime focus field stop with a diameter of 3.8 mm represented by the small circle. The three intermediate sized circles represents the full solar image of 36 mm at the prime focal plane, centered and residing at both extremes. The waste light, *i.e.*, light that does not pass through the field stop, is reflected out of the optical path and terminated at a beam dump. The amount of reflected light is negligible and will not contribute to any internal seeing effects.

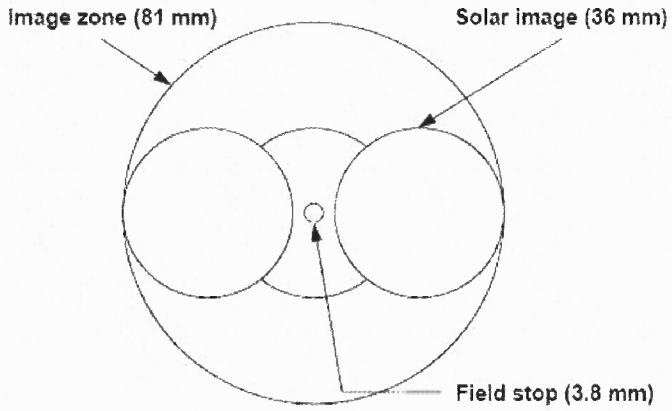

Figure 3.8 Diagram of NST's prime focal plane. The outermost circle represents the area within which the full solar disk can reside (Figure 8 in Denker *et al.* (2006)).

3.6 Optical Support Structure

All major components of the OSS were commissioned by DFM Engineering Inc. of Longmont, Colorado. The company supplied the equatorial mount, primary mirror cell, positioning actuators and mirror supports for M1, telescope tube, control system for OSS, mounts and mirrors for M3 through M5 and the handling equipment for the primary. Figure 3.9 shows a Computer Aided Design (CAD) drawing of NST from two different perspectives with some of the major components labeled. The OSS weighs approximately 8.5 tons, imposing a larger load on the existing telescope pier. In March 2007, the existing telescope pier was demolished and construction of the new pier was finished by July of the same year. The new pier is designed to carry the increased load as well as raising the height of the NST rotational axis to the center of the new dome. Work for the pier and construction was commissioned by NJIT's structural engineering group.

Initial plans for the OSS proposed by DFM consisted of an unbalanced system, designed to account for the telescope pier's weight requirements. A balanced design

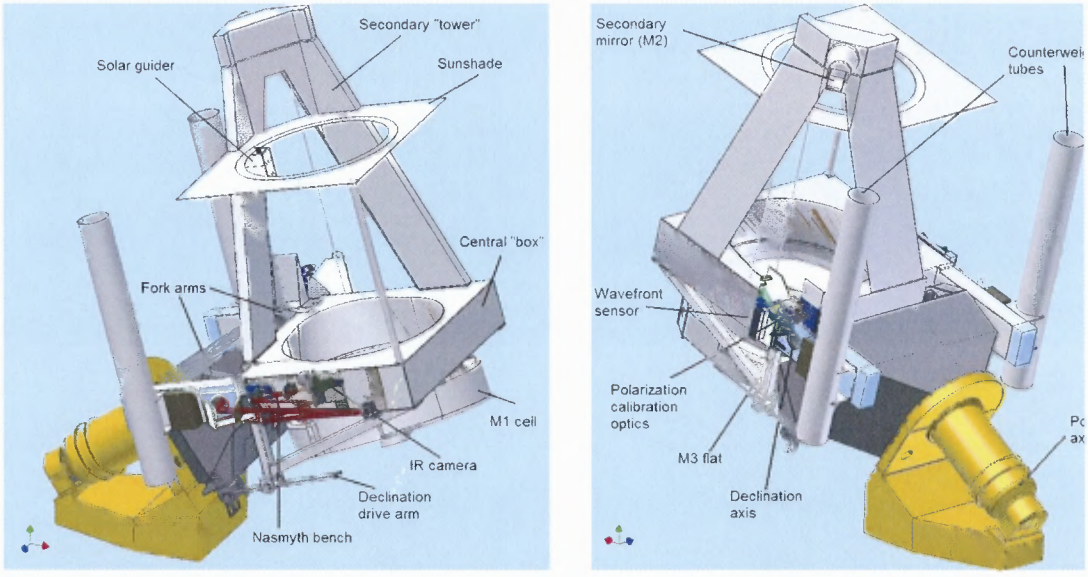

Figure 3.9 CAD renderings of NST from two different perspectives. Not shown in are the heat stop assembly, which is located at the primary focus before M2. Also omitted is the flat Coudé mirror M4, which is positioned at the bottom of the polar axis and serves to direct light down to the optical laboratory (courtesy of Roy Coulter).

would have resulted in an OSS weighing 13 to 18 tons as a result of needing counterweights to balance the cantilever motion of the mirror cell and telescope tube. To counter the unbalanced moments, DFM came up with a Declination drive system (DEC), that consists of a declination drive arm, visible in the left panel of Figure 3.9. The declination drive arm will be capable of supporting the extreme load imparted by the telescope structure. To account for variations in the center of gravity about the right ascension (RA) axis of the telescope, two movable 1/2 ton counter weights (see right panel of Figure 3.9) housed in tubes will be used to compensate the offset. The overall telescope mount design is based off of DFM CCT 1.3 EQ mount with a modified, shortened fork.

The primary mirror cell shown in Figure 3.9 will have an active support consisting of a 36 point axial and six point tangential actuators. The actuators will serve to compensate for changing thermal and gravity conditions. To hold the primary in position, six of the actuators (three axial and three tangential) will be used.

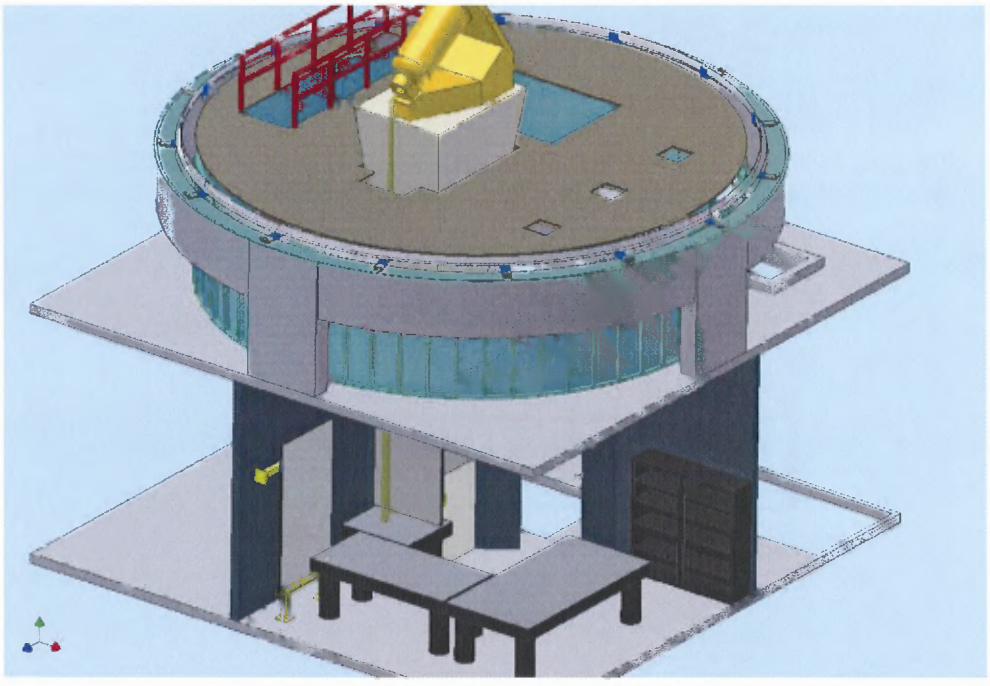

Figure 3.10 Light from the observing deck is directed down through the polar axis of the telescope to the optical laboratory via the Coudé feed (Figure 4 in Denker *et al.* (2006)).

The remaining 33 axial actuators will compensate for unwanted mirror deformities and the remainder of tangential supports will provide small rotational corrections to the primary. The secondary mirror and hexapod mount (shown in greater detail in Figure 3.5) will be attached to the secondary tower along with the solar guider and sunshade. The solar guider, used for pointing control, was developed in-house and consists of a Sigma 70–300 mm zoom lens, which forms a 4 mm solar image on a four-quadrant sensor. The sensor is mounted on a linear micrometer stage allowing positioning of the telescope with sub-arcsecond accuracy. The central box shown in Figure 3.9 will hold the Nasmyth bench, where all operating wavelengths are available, as well as the polarization calibration optics and wavefront sensor. Not visible in Figure 3.9 is M4, which will direct light down to the optical laboratory. Figure 3.10 shows the Coudé feed from the observing deck to the optical laboratory where the post-focus instrumentation is located.

3.7 Control Systems

To monitor and control NST operations a high-level Telescope Control System (TCS) needs to be implemented. The NST TCS, developed in-house by NJIT and BBSO staff and scientists, will provide robust operation of the entire telescope system. The control system will need to be able to provide the following functionality:

Dome operations. All dome movement such as rotation, opening and closing the shutter, tracking the telescope throughout observing time and adjusting dome louvers.

Pointing and Tracking. Track the observing target throughout the required observing period. Correct for target precession and atmospheric and gravity induced distortions.

Active Optics. Control the actuators on the back and sides of the primary mirror to correct for thermal and gravity induced deformities. Supply the necessary adjustments for the alignment of the secondary and primary by controlling the hexapod system.

Thermal Control. The temperature at the primary mirror, heat stop, secondary mirror and various locations throughout the dome will be measured and used to initiate active and passive cooling measures, *i.e.*, dome vents and air knife operation.

Science Instruments. Monitor status and operation of post-focus instruments such as VIM and IRIM

To provide control to these important telescope functions the TCS was designed as a distributed system rather than a monolithic system – with all telescope functionality in one software package (Yang *et al.*, 2006). Figure 3.11 shows the structure of the TCS and the breakdown of the subsystems. TCS is controlled through a head

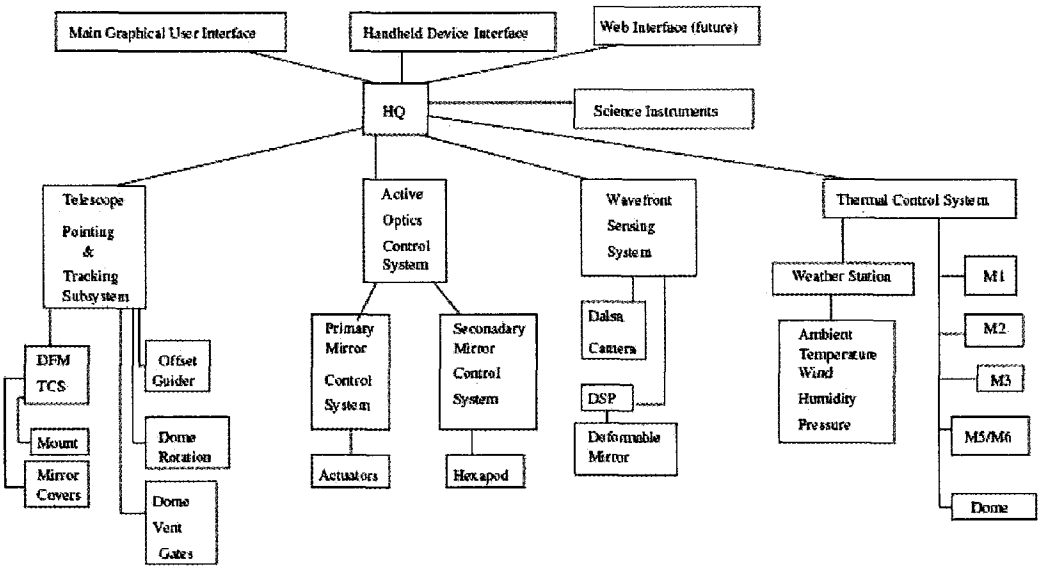

Figure 3.11 NST operations are handled using the TCS. The system shown here is split into multiple subsystems, each providing a a different function (Figure 2 in Varsik and Yang (2006)).

quarter (HQ) computer that receives information from the various subsystems via an ethernet link. The communication interface between all systems in the TCS is handled using the middleware platform Internet Communication Engine (ICE), which the control systems team decided was the most robust and appropriate software for this application. Messaging and information exchange in the TCS is handled using forms written in the eXtensible Markup Language (XML). Each of the major subsystems will have its own control computer and all extensive information on each subsystem will be stored in a database to be used in refining telescope operations. The telescope operators will issue high level commands through a graphical user interface (GUI) – with the most of the low level functionality hidden. However, access to the low level commands is still possible for cases involving subsystem maintenance and failure recovery.

3.8 Post-Focus Instrumentation

NST will benefit from both active and adaptive optics systems. The active optics system includes the relative alignment between M1 and M2 as well as maintaining the surface integrity of M1 in the presence of gravity sagging and thermal induced expansions and contractions. The deformation of the primary due to gravity and thermal variations will occur rather slowly. Therefore, these controls are grouped as active optics even though the primary is adaptive. The active optics system will rely on a dedicated wavefront sensor manufactured by Adaptive Optics Associates (AOA) that is mounted on the OSS. The active alignment uses the DC-component of the wavefront sensor to keep alignment between M1 and M2. The active system will operate in both a closed- and open-loop system.

At the heart of the AO system for NST is a 76 subaperture Shack-Hartman sensor operating in a closed loop with a 97 actuator deformable mirror. Both the Shack-Hartman sensor and deformable mirror are manufactured by Xinetics. The AO system is identical to the system at Dunn Solar Telescope (DST) at National Solar Observatory/Sacramento Peak (NSO/SP), New Mexico (Rimmele *et al.*, 2004). The system uses a 1280×1024 pixel Baja Technologies 10-bit Complex Metal-Oxide Semiconductor (CMOS) camera as a detector. The control software for the system was developed at NSO/SP. Of the 1280×1024 pixels, only 200×200 are read in to ensure a frame rate of 2500 frames s^{-1}. The AO system has been successful in use with the 65 cm telescope at BBSO. However, to accommodate the NST operating wavelengths, the design and development of a 350 actuator system is currently in the works.

Along with the active and adaptive optics systems, NST will have several other post-focus instruments. Two Fabry-Pérot-based imaging magnetographs – the Visible light Imaging Magnetograph (VIM) and the Infra-Red Imaging Magnetograph (IRIM) – will be used for polarimetric studies of the Sun at various wavelengths

in the visible and infrared (Denker *et al.*, 2003a,b; Cao *et al.*, 2006). A fast CCD camera system used for image reconstruction complements the suite of post-focus instruments (Denker *et al.*, 2001a, 2005). Chapter 6 describes in further detail the design, layout and operation of the AO system at BBSO. In Chapters 7 and 8, an in-depth discussion of VIM and the results from a June 2006 observing run are presented, respectively.

This aim of this chapter was to give an overview of the 1.6 m NST project at BBSO. The project is well underway with the majority of components already finished or on their way to completion. Alignment procedures for the telescope will be tested and developed in the coming months as first light nears. The NST project will not only have an impact in its contribution to solar physics, but will also serve as a model for future large-aperture ground-based telescopes.

CHAPTER 4

THE THERMAL CONTROL OF THE NEW SOLAR TELESCOPE AT BIG BEAR SOLAR OBSERVATORY

4.1 Overview

In this chapter the basic design of the THermal Control System (THCS) for the 1.6-meter New Solar Telescope (NST) at the Big Bear Solar Observatory (BBSO), California is presented. The NST is an off-axis Gregorian telescope with an equatorial mount and an open support structure. Since the telescope optics is exposed to the air, it is imperative to control the local/dome seeing, i.e., temperature fluctuations along the exposed optical path have to be minimized. To accomplish this, a THCS is implemented to monitor the dome environment and interact with the louver system of the dome to optimize instrument performance. In addition, an air knife is used to minimize mirror seeing. All system components have to communicate with the Telescope Control System (TCS), a hierarchical system of computers linking the various aspects of the entire telescope system, e.g., the active mirror control, adaptive optics, dome and telescope tracking, weather station, etc. An initial thermal model of the dome environment is presented as well as the first temperature measurements taken in the recently replaced BBSO dome.

4.2 Introduction

Some of the most favorable conditions for solar observations occur at observatories that are situated above the inversion layer and are surrounded by a body of water (Beckers, 2001). BBSO is situated at such a site and is the location for the construction of the NST. The NST is set to replace the existing 65 cm vacuum telescope with a 1.6 m aperture, open support structure, Gregorian-style solar telescope. Upon completion NST will be engaged in campaign style observations of the Sun joining

the next generation of large-aperture, diffraction-limited solar telescopes. Its capability of performing both high-temporal and high-spatial resolution studies of the Sun will enable the NST to engage in a host of scientific studies including, but not limited to, high cadence solar flare dynamics, active region magnetic field evolution and structure as well as upper solar atmosphere heating (Goode *et al.*, 2003). For large-diameter solar telescopes operating at the theoretical diffraction limit, one of the main design issues besides the polishing of the primary, is the development of an advanced THCS (Goode *et al.*, 2003).

The THCS is responsible for reducing the effects of local convection that arise in the dome as well as controlling the temperature of the mirrors to match the ambient temperature. In an effort to accommodate the NST open-structure design, BBSO recently replaced the existing observatory dome with a new 5/8 sphere ventilated dome. Passive flushing of the dome interior is achieved through 14 louvers that are evenly spaced around the perimeter of the dome. The wind characteristics at BBSO (Denker and Verdoni, 2006) is westerly with an average speed of approximately 6 m s^{-1}. This is sufficient for flushing the open structure of telescope reducing some of the deleterious effects of enclosure related seeing on image quality. The ability to make large-aperture solar telescopes with an open design and still operate at the theoretical diffraction limit viable stems from recent advances in solar AO technology (Rimmele *et al.*, 2004). NST will benefit from the recently developed high-order AO system, frame selection and speckle masking technology that has already been implemented using observations with the 65 cm vacuum telescope (Denker *et al.*, 2005).

The open telescope design is not unique to NST, it has been implemented successfully at the DOT on La Palma and is also the choice configuration for other solar telescopes such as GREGOR and the ATST. Along with an open optical support structure both DOT and GREGOR have retractable domes exposing the telescope

optics to the surrounding environment. In the case of DOT the characteristic winds at La Palma effectively suppress thermal plumes associated with local ground heating (Rutten *et al.*, 2004). The open structure of DOT allows for the wind to enter the telescope structure deterring the build up of internal telescope seeing. The proposed ATST at Haleakalā, Maui, Hawaii, will also use an open structure to house its 4 m primary. However, ATST will not use a retractable dome but rather a ventilated and cooled enclosure, that has been designed and optimized using software that applies site survey data to a CAD-generated enclosure model (Dalrymple *et al.*, 2004). An aerodynamic method is applied and the results, coupled with measured wind and temperature data, are combined to give a temperature distribution on the dome surface.

The open structure design of NST will require both passive and active thermal control to reduce enclosure related seeing and ensure high quality diffraction-limited observation (0.07″ at 500 nm). In the following sections, the fundamental characteristics of the NST dome as well as an overview of the THCS are discussed. Along with the dome characteristics, some preliminary temperature tracking data from a 16 point temperature measurement taken in the new dome is presented.

4.3 Dome Design

The newly installed dome at BBSO is a 10 m diameter, 5/8 sphere with an over the top nesting shutter housing a 2 m circular aperture. The dome was manufactured by MFG Ratech and is modelled after the dome constructed for the Southern Astrophysical Research (SOAR) telescope (Teran *et al.*, 2000). The SOAR dome is a 20 m diameter 5/8 sphere, with a similar over the top shutter with windscreen attachment. The exterior is comprised of an insulated fiberglass panel system that is assembled in sections. The dome rotates on a 16 fixed point bogie system allowing

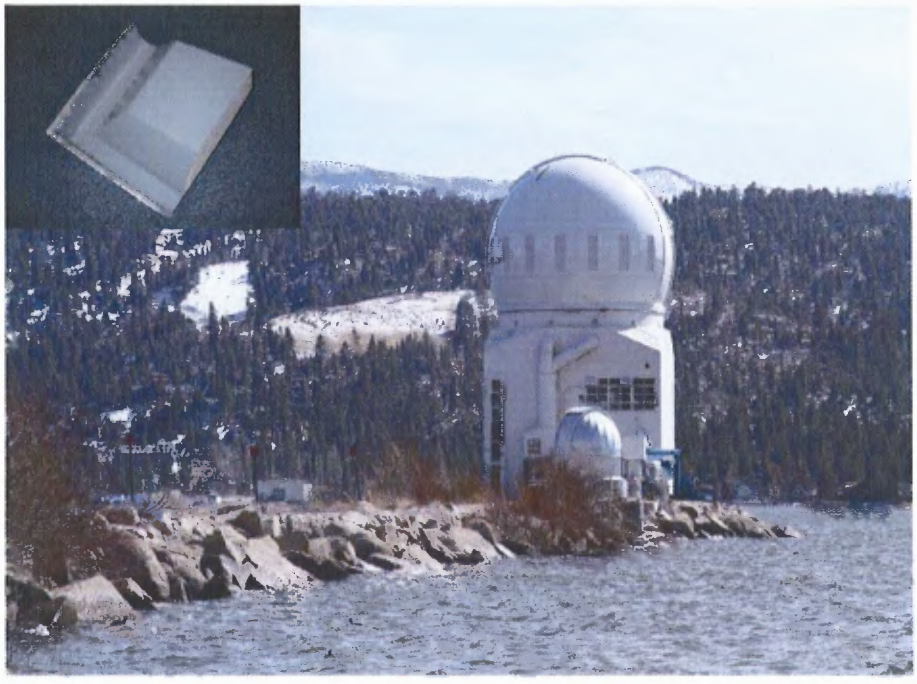

Figure 4.1 Image of new NST dome (MFG Ratech) dome with insert of foam core material

for the dome, shutter and windscreen to track the telescope for maximum protection against prevailing winds.

The spherical shape of the the new dome was a natural fit for NST as it did not require major modification of the existing observatory structure. The spherical shape also lends itself nicely to the dome ventilation system by eliminating the presence of dead air space inside the dome volume (Teran *et al.*, 2000). The dome consists of a metal frame support structure surrounded by white insulated fiberglass panels. The panels are insulated with a special foam core that provides added stability as well as insulation to the dome. Figure 4.1 shows the newly installed NST dome with the recently constructed Earthshine observatory, the inset image shows the foam core insulation. The dome shutter is an over-the-top type shutter that separates the dome into two even sections. Attached to the shutter is a windscreen so that the dome interior is only exposed via the 2 m aperture during observation. The determination of the slit width was based on assembly criteria. Namely, the width of the slit must

be able to accommodate the largest telescope component that would be lowered into the observatory by a crane. The largest component being the support ring for the primary mirror yielded a slit width of 2.5 m to provide suitable clearance during NST installation. Also the slit width must be able to adequately accommodate the primary mirror when it needs to be re-coated. Another consideration for the telescope aperture was the amount of excess sunlight entering the dome, which has to be minimized to avoid heating of the telescope support structure. To determine the minimal aperture diameter, the case of off-pointing the telescope to the solar limb was considered. For a clear aperture of 1.6 m at the telescope primary and assuming a circular aperture roughly 5.5 m above the primary maintaining uniform illumination of the primary would require an aperture diameter of 1.65 m. When one considers the tracking accuracy of the dome and shutter a value of 2.0 m is suitable for the telescope aperture, ignoring in this case the small field angle of the telescope. With the primary mirror being 1.6 m in diameter, an annulus of sunlight 0.2 m in width and an area of roughly 4 m^2 will heat the telescope structure and dome floor. This corresponds to a solar load of roughly 6 kW, which has to be managed by THCS. To measure the solar load, photometers will be mounted on the optical support structure.

Unlike the SOAR dome the NST dome has 14 vent gate assemblies evenly spaced around the perimeter of the dome to allow for wind flushing of the dome interior. The vent gates are constructed of heavy gauge extruded aluminum rated to withstand a wind load of approximately 190 kg m^{-2} or a wind speed of 57 m s^{-1}. The vent dimensions are 0.6 m$\times$1.8 m with a depth of approximately 0.1 m. Each of the vents is outfitted with a damper or set of louvers, which control the amount of air let in and out of the dome. The louver assembly is split into a top and bottom portion that can be opened and closed independently. The dampers will be controlled via the telescope pointing and tracking subsystem and will be activated based on the

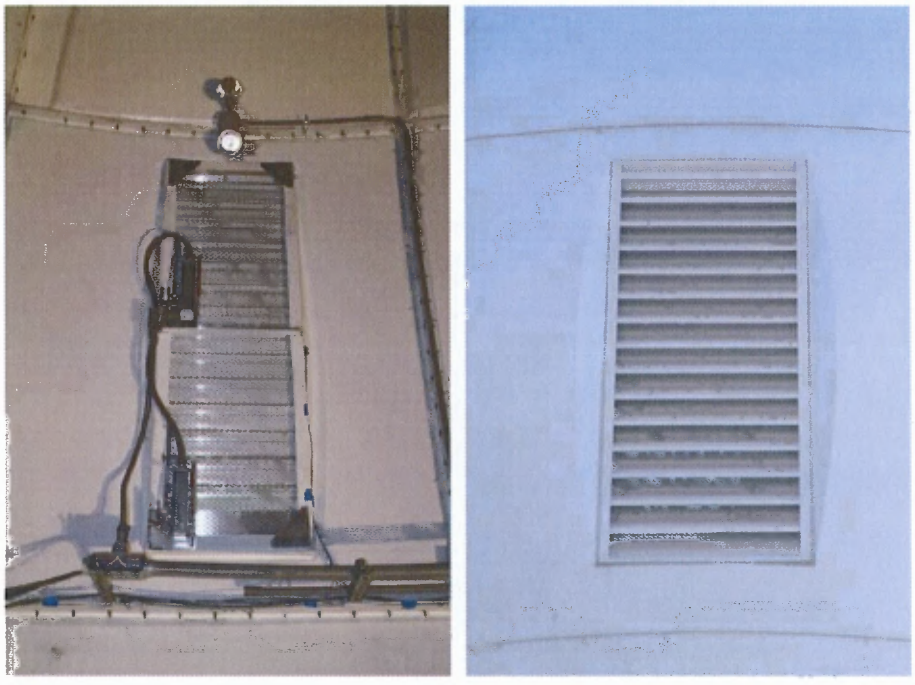

Figure 4.2 From left right the inside and outside of one of the active vent gates.

direction of the wind, measured by a weather station outside the dome, and the distribution of the internal dome temperature as measured by 16 temperature probe units arranged symmetrically throughout the dome interior (Denker *et al.*, 2006). Figure 4.2 shows a picture of the inside and outside of one dome louver. Visible in the figure are the two motors responsible for opening and closing the top and/or bottom portion of the vent louver system.

With a diameter of 10 m the total volume of the dome is approximately 330 m^3. This volume will need to be flushed approximately 20 or more times per hour corresponding to a wind speed of roughly 2 to 3 m s^{-1}. Data taken from the comprehensive ATST site survey shows that the mean wind speed at BBSO is 6 m/s with a wind speed of 9 m s^{-1} occurring 10 percent of the time (Denker and Verdoni, 2006). For cases, where the wind speed is greater than 5 m s^{-1}, the dampers will be used to regulate the flow to the desired amount. In the case, where wind speeds are too low, forced air will be used to generate a flow such that a flushing rate of 30 dome volumes per hour is achieved. In addition, the wind flow can be directed depending on the

louver position to stream across the face of the primary mirror. At astronomical noon, when the mirror face is at its lowest position, it may be useful to only open the bottom portion of the utilized louvers. Currently experiments involving different louver configuration schemes are being explored and will implemented into THCS.

4.4 Thermal Control System

Considerable work has been done to understand and combat seeing and seeing related effects in solar and nighttime telescopes. In their enclosure-seeing report the ATST thermal systems group describe the types of thermal convection that arise in ventilated domes (Dalrymple *et al.*, 2004). For ventilated domes with a passive louver system installed such as in the NST dome, there are several convective effects that lead to enclosure related seeing. The most dominant form is the convection arising from exterior dome heating. There is little that can be done to combat this effect, however natural cooling from moderate to high speed winds can lower the outside dome temperature and reduce the buoyant convection driven plumes due to the heated dome exterior. NST will not implement any active measures to control the natural convection from the dome shell heating such as air conditioning and or shell temperature regulation. The idea is to restrict convection to the *forced regime*, this corresponds to the least impact type seeing in the enclosure (Dalrymple *et al.*, 2004). The NST will have an open telescope design. Therefore, temperature fluctuations along the optical path have the potential to severely limit the telescopes performance. To regulate this effect the NST will require an advanced THCS to ensure that image degradation resulting from thermal convection effects is minimized. The THCS subsystem is part of the hierarchical Telescope Control System (TCS) and will in general, be responsible for all seeing related issues. This involves communication with several seeing related instruments and web services. Figure 4.3 shows the flow chart for NST THCS and all of the related instruments and services . The abbrevi-

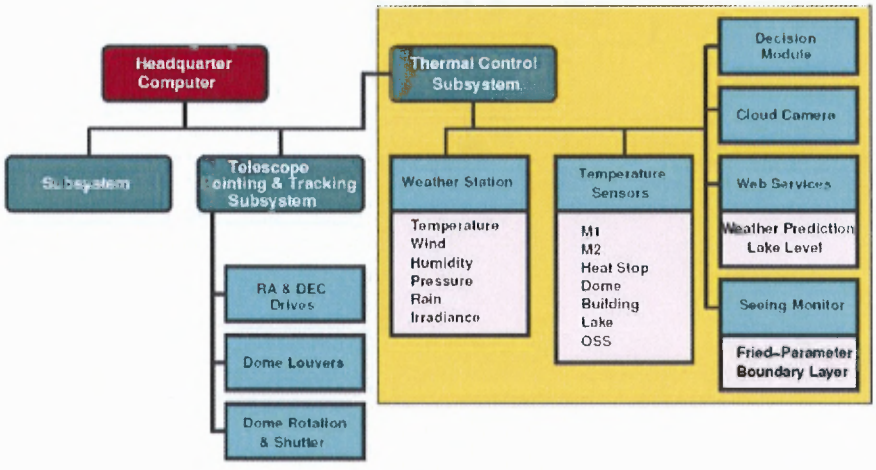

Figure 4.3 Thermal control flow chart for NST.

ations M1, M2, correspond to the primary and secondary mirrors respectively and OSS refers to the Optical Support Structure. Below is a list of these instruments and services accompanied by a brief description of how they will be used in the overall THCS.

Weather Station: Weather data will be collected using a Davis Instruments Vantage Pro2 Plus weather station. This instrument will measure temperature, rain fall, wind speed and wind direction. The unit is equipped with a solar radiation sensor as well as a UV sensor. THCS will use the temperature, wind speed and wind direction data from the weather station to determine the proper louver configuration. This will be performed by comparing the temperature outside (ambient temperature) with the internal temperature of the dome as read by the ethernet/internet tracking thermometer described below.

Web Services: On top of data from local instrumentation, weather data will be collected from online sources before and during daily operations. For instance, forecast data on wind speed and direction at various altitudes as well as other useful environmental related parameters are provided every six hours by the National Center for Environmental Prediction (NCEP, `http://www.ncep.noaa.gov/`). All of the data related to both the thermal control and seeing will be archived in a

single database developed in MySQL. The data will be used in a seeing forecast model allowing the telescope operator to schedule observations that best fit the prevailing seeing conditions. Since the lake level can vary seasonally and during times of drought, a model that calculates the exact length of segments along the line-of-sight that traverses the lake (Denker and Verdoni, 2006). Lake level data is provided by the Big Bear Municipal Water District (BBMWD, `http://www.bbmwd.org/`) and the lake contours have been collected and digitized from various, commercial topographic maps.

Ethernet/Internet Thermometer and Temperature Probes: Temperatures are measured by a TempTrax Model E16 ethernet/internet ready tracking thermometer. This unit can monitor up to 16 temperature probes placed at various positions on throughout the dome interior. It has an accuracy of 0.5° C from −29° C to +49° C with a resolution of 0.1°. The tracking thermometer accepts 16 heavy-duty thermo-resistor based temperature probes that are attached to a 25 m PVC insulated wire cabling. Determining the most effective placement of the probes is currently being studied. Each of the 16 probes will be temporarily mounted at fixed positions on the interior dome surface and the temperatures will be measured for several weeks. Figure 4.4 shows a picture of one of the probes fixed to the inside of the dome via an adhesive cable clip.

Decision Module: The THCS objectives are twofold: (1) gather seeing, climate and environmental data from a variety of sensors, instruments and web resources and (2) assemble these data into information, which can be requested by other subsystems or send requests to these subsystems to perform actions, which will help to optimize the telescope performance. The communication interfaces (Yang *et al.*, 2006) are based on the Internet Communication Engine (Ice) as middleware and the messages are passed between subsystems and a centralized "headquarter" (HQ) computer as ASCII templates written in the eXtensible Mark-up Language

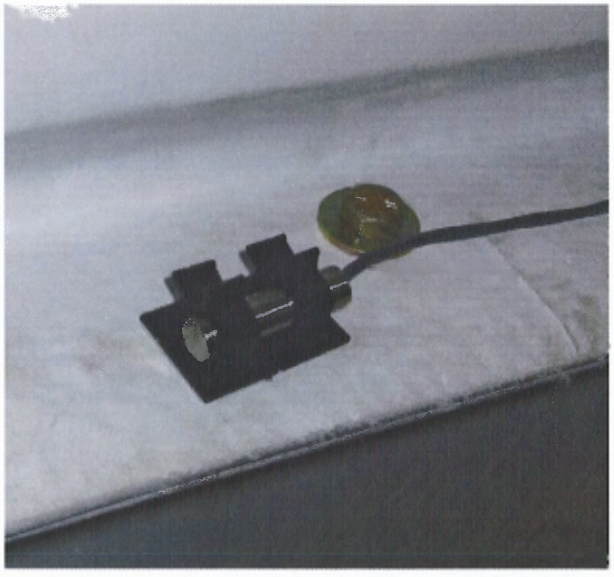

Figure 4.4 TempTrax heavy-duty probe mounted on NST dome interior.

(XML). The decision module builds and updates a three-dimensional temperature model of the temperature profile inside the dome. An adaptive merit function will be used to minimize temperature gradients in the dome and keep the air temperature inside the dome close to the exterior values. The 14 dome louvers and forced air ventilation can be used for this purpose. In addition, air flow and temperature through the M1 and M2 air knifes can be controlled. However, only a very small correlation with the climate and atmospheric seeing conditions in case of the airknifes is expected. Since telescope performance is difficult to quantify without precise information on the prevailing seeing conditions, a seeing monitor has been integrated into THCS (Denker and Verdoni, 2006). One of the seeing monitors used in the ATST site survey was made available by the ATST project (Beckers, 2001; Hill *et al.*, 2004a). This instrument will be mounted on an instrument platform attached to the south wall of the observatory building. The seeing data in connection with NST wavefront sensor and climate data will be integrated in the decision process. All data will be collected in a MySQL database so that a benchmark for optimal thermal control of the dome environment can be established. The decision module

will further provide warnings and error messages in case of instrument failure, e.g., if the coolant temperature of the heat stop exceeds a critical threshold, HQ will be notified and the telescope is brought into a fail safe mode pointing away from the sun to prevent damage.

Cloud Camera: One of the shortcoming of the ATST site survey was the relatively large uncertainty of the clear-time fraction for all sites (e.g., 47% to 71% for BBSO depending on the interpretation of the instrument health status) (Hill *et al.*, 2004a). This motivated the inclusion of an inexpensive, dedicated web camera into THCS. The CCD camera is equipped with a "fish eye" lens and takes images of the entire sky at a cadence of about 5 min. An automated program detects clouds in these images and computes the cloud cover. The temporal evolution of the cloud cover will be archived and becomes part of the seeing forecast model. Long-term measurements of the cloud cover can reliably establish the clear-time fraction. In addition, the observer will receive warning messages, if the cloud cover increases/reaches a certain threshold or rain starts to fall. This warning message relies also on information provided by the weather station's rain sensor.

Seeing Monitor: The Seeing Monitor is comprised of S-DIMM and ShaBar instruments. These instruments were developed for the ATST site survey to measure seeing characteristics and sky brightness at candidate sites (Beckers, 2001; Lin and Penn, 2004). These instruments will be installed at the south side of the observatory on an existing spare instrument platform. Seeing information will also be made available from the by products of speckle masking imaging (Denker and Verdoni, 2006).

4.5 Experiments

In January 2006, the first set of 16 temperature sensors were installed on the interior surface of the fiberglass dome. At this time, the dome structure, skin, and louvers

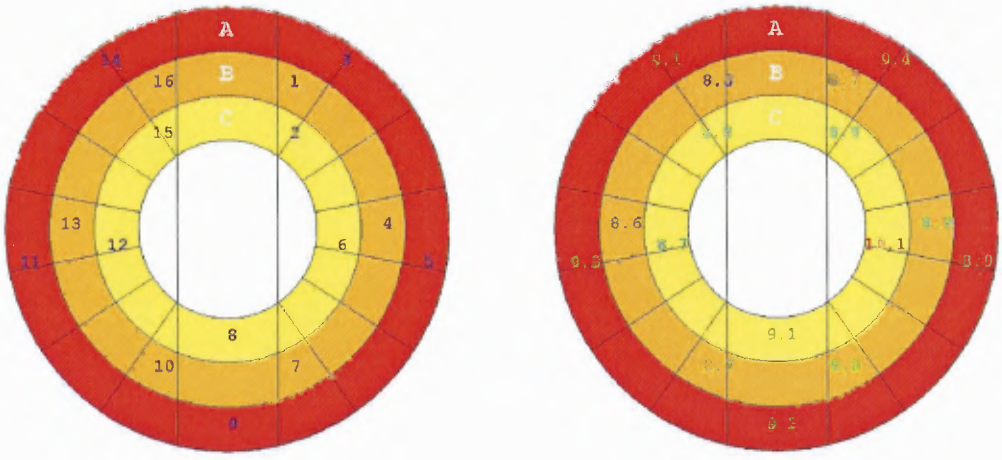

Figure 4.5 Quick-look GUIs of the temperature sensors. (*left*) Location and numbering scheme of the 16 temperature sensor. (*right*) A temperature sample obtained at 18:36:47 UT on February 14, 2006. The rainbow color code corresponds to low (blue) and high (red) temperatures. The rings A, B and C denote increasing heights of the temperature sensors. The entrance aperture (pointed towards North) is at the top of the images.

were already installed. However, the dome drive and shutter motors were not operational. The dome aperture was pointed towards the North to enable access to the construction area inside the dome. Figure 4.5 displays the quick-look graphical user interfaces (GUI), which provides feed-back from the temperature sensors. The left panel of Figure 4.5 shows the location and distribution of the sensors. A denotes the lowest position in the dome, i.e., the middle of the first ring of fiberglass panels. B and C correspond to the middle of the second and third ring, respectively. The B ring is roughly at the height of the primary mirror and contains the dome louvers. The right panel of Figure 4.5 summarizes a set of temperature measurements for all 16 sensors. The temperature differential is encoded in a rainbow color scheme. Temperature measurements were made every 5 s and the GUI is updated at the same time. The telescope operator can thus have an immediate and intuitive feedback of the temperature distribution in the dome interior. The GUI is flexible to allow the

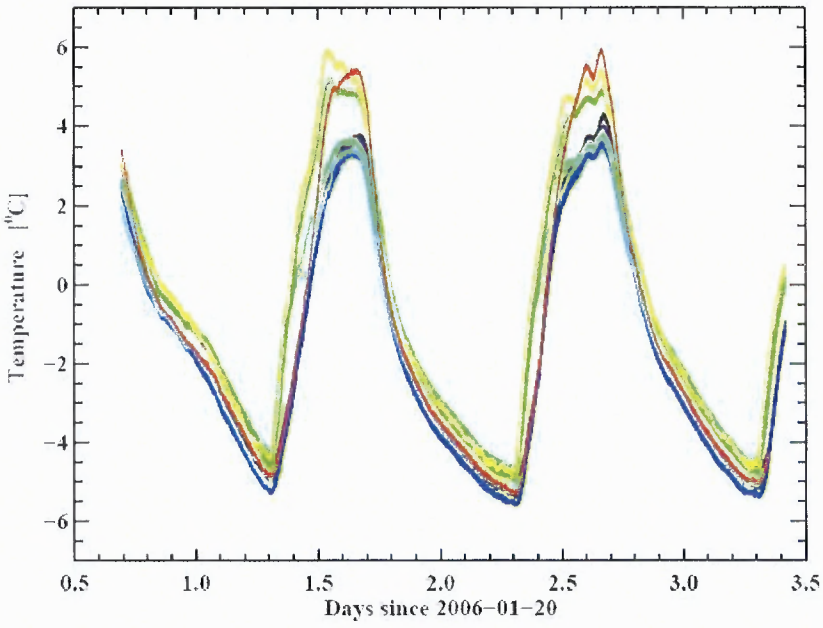

Figure 4.6 Temporal evolution of the temperature profile for selected sensors. The data was obtained at a 5 s cadence during three days in January 2006.

display of other information, e.g., the difference to the exterior temperature or the temperature increase, since the observing started.

4.6 Conclusions

Controlling the dome environment is one of the crucial tasks in the operation of modern solar telescopes with open designs. In this chapter the general ideas of a THCS which will be used with the NST are presented. Preliminary results indicate that strong temperature gradients exists within the dome. Daily temperature changes exceed 10° C during the winter months. The temperature differences between day and night are even larger during the summer month. Thermal studies will be continued once there is full control over all dome functions (by mid-2006). Of particular interest is an exact understanding of the louver settings, which will allow a smooth air flow to be directed towards the primary mirror. Also of interest is combining airknife and wavefront sensing data to determine a proper thermal cooling scheme

for the primary mirror. The NST is assembled and undergoing the first round of alignment test. In the subsequent one-year commissioning phase, integration of the THCS subsystems and instruments will be complete as well as finalizing the decision module.

CHAPTER 5

THE THERMAL ENVIRONMENT OF THE FIBER GLASS DOME FOR THE NEW SOLAR TELESCOPE AT BIG BEAR SOLAR OBSERVATORY

5.1 Overview

The NST is a 1.6-meter off-axis Gregory-type telescope with an equatorial mount and an open optical support structure. To mitigate the temperature fluctuations along the exposed optical path, the effects of local/dome-related seeing have to be minimized. To accomplish this, NST will be housed in a 5/8 sphere fiberglass dome that is outfitted with 14 active vents evenly spaced around its perimeter. The 14 vents house louvers that open and close independently of one another to regulate and direct the passage of air through the dome. In January 2006, 16 thermal probes were installed throughout the dome and the temperature distribution was measured. The measurements confirmed the existence of a strong thermal gradient on the order of 5° C inside the dome. In December 2006, a second set of temperature measurements were made using different louver configurations. In this study, the results of these measurements along with their integration into the THCS and the overall TCS are presented.

5.2 Introduction

Solar telescopes with an aperture larger than 1 m face a variety of challenges, if they want to achieve diffraction-limited resolution. Site selection is of primary concern. In the context of the proposed 4-meter aperture ATST, significant efforts were undertaken to identify the best site(s) for solar observations (Hill *et al.*, 2004a; Socas-Navarro *et al.*, 2005; Verdoni and Denker, 2007). Big Bear Solar Observatory (BBSO) was identified as one of three sites suitable for high-resolution solar

observations. However, the seeing characteristics at BBSO – a mountain-lake site – are quite different (Verdoni and Denker, 2007) from the two other mountain-island sites Haleakalā, Maui, Hawai'i (which was selected as the future ATST site) and Observatorio Roque de los Muchachos on La Palma, Spain. The lake effectively suppresses the ground-layer seeing and very good seeing conditions are encountered from sunrise to sunset. This makes BBSO ideally suited for solar activity monitoring and space weather studies (Gallagher *et al.*, 2002) combining synoptic with high-resolution capabilities. These site characteristics and scientific objectives are exactly what has motivated the design, development and now construction of NST (Goode *et al.*, 2003; Denker *et al.*, 2006).

Since instrument seeing is a severe issue for solar telescopes, most high-resolution solar telescopes were placed inside vacuum tanks. This approach, however, is no longer feasible for apertures larger than 1 m, since the entrance window (or lens) would become too thick in order to withstand the vacuum. Therefore, the next generation of solar telescopes has to rely on "open-designs", i.e., the optical support structure and optics will be exposed to the elements. This in turn requires a good understanding and control of the thermal environment in which the telescope is placed. In a first set of papers (Denker and Verdoni, 2006; Verdoni and Denker, 2006), a description on how to integrate seeing measurements into the NST operations and introduced plans on how to implement the NST THCS. In this study, a discussion in more detail is given on the THCS implementation, the design of the fiberglass dome (a smaller version of the SOAR telescope dome (Teran *et al.*, 2000), a detailed weather record for BBSO, temperature measurements inside the dome under varying observing conditions, and some implications for the thermal control of the primary mirror, which is a 1/5-scale model for the 8.4-meter off-axis segments of the Giant Magellan Telescope's primary mirrors (Martin *et al.*, 2004).


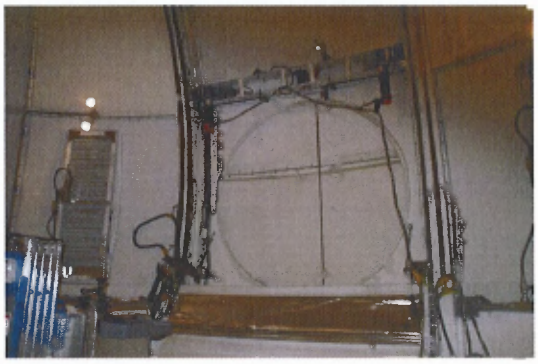

Figure 5.1 *Left.* Image of the new NST dome at BBSO. The smaller dome in the foreground houses the Earthshine and Hα full-disk telescopes. In this image the shutter is closed and the iris is covering the domes 2-meter circular aperture. *Right.* Inside of view of the closed iris and the iris drive motors. The folded windscreen is visible at the bottom of the iris.

5.3 5/8-Sphere Fiberglass Dome

The new NST dome at BBSO is a 10-meter diameter 5/8 sphere with an over-the-top nesting shutter housing a 2-meter circular aperture. The dome was manufactured by MFG Ratech and is modeled after the dome for the SOAR telescope in Cerro Pachon, Chile (Teran *et al.*, 2000). The SOAR dome is approximately twice the size of the NST with a diameter of 20 m. It has a similar over the top shutter with windscreen attachment. However, it does not have the 14 active damped louver assemblies, which are evenly spaced around NST's equator. The exterior of the NST dome is comprised of Fiberglass Reinforced Plastic (FRP) panels that are assembled in three ring sections, which are vertically split into two hemispheres by the dome slit. The sections are supported by two 10-meter diameter steel arch girders that serve as guides for the dome shutter. Both the panels and arches sit on top of a 9.2-meter diameter steel ring beam, which rotates on a 16 fixed-point bogie system allowing the dome, shutter and windscreen to track the telescope for maximum protection against the prevailing winds.

The left panel of Figure 5.1 shows the newly installed NST dome with the aperture pointing to the east. In this image the dome shutter is closed and the iris

covers the 2-meter circular aperture. Housed in the smaller dome in the foreground are the BBSO Earthshine and Hα full-disk telescopes. The right panel of Figure 5.1 depicts an inside view of the closed iris. At the bottom of the aperture panel is the collapsed, foldable wind screen. As the aperture panel raises and lowers, the wind screen unfolds covering the exposed portion of the dome slit. To test the structural integrity of the dome a stress analysis was performed. The analysis was based on the maximum operating snow and ice loading conditions. The conditions call for the dome to retain its structure with a snow depth of 1 m, an average dead load of 97 kg m^{-2} with a peak dead load of 195 kg m^{-2}, and an ice thickness of 0.05 m. A worst case stress analysis was performed with a peak dead load of 195 kg m^{-2} and a 55 m $s^{-}1$ wind acting simultaneously. The result was that the 10 m diameter was in substantial conformance with the manufacturers requirements.

NST's 14 vent gates allow wind flushing of the dome interior. The gates are made of a heavy gauge extruded aluminum, which is rated to withstand a wind load of approximately 190 kg m^{-2}. Each of the vents is 0.6 m $\times$ 1.8 m with a depth of approximately 0.1 m. A damper is attached to each vent, which allows control over the amount and direction of air flow through the dome. The dampers will be activated based on the direction of the wind, measured by a weather station outside the dome, and the temperature gradients inside the dome, measured by 16 temperature probe units arranged symmetrically throughout the dome interior (Denker *et al.*, 2006).

Figure 5.2 gives an image of the inside of the dome showing three vent gate assemblies. The two motors responsible for opening and closing the vent louver system. To eliminate the presence of a thermal gradient inside the dome, the dome volume must be flushed 20 or more times per hour, which requires a wind speed of approximately 2 to 3 m s^{-1}. BBSO benefits from a predominately westerly winds with a mean speed of 6 m s^{-1} (Verdoni and Denker, 2007). With a total dome volume of 330 m^3, this is sufficient to achieve a flushing rate of 30 dome volumes per hour.

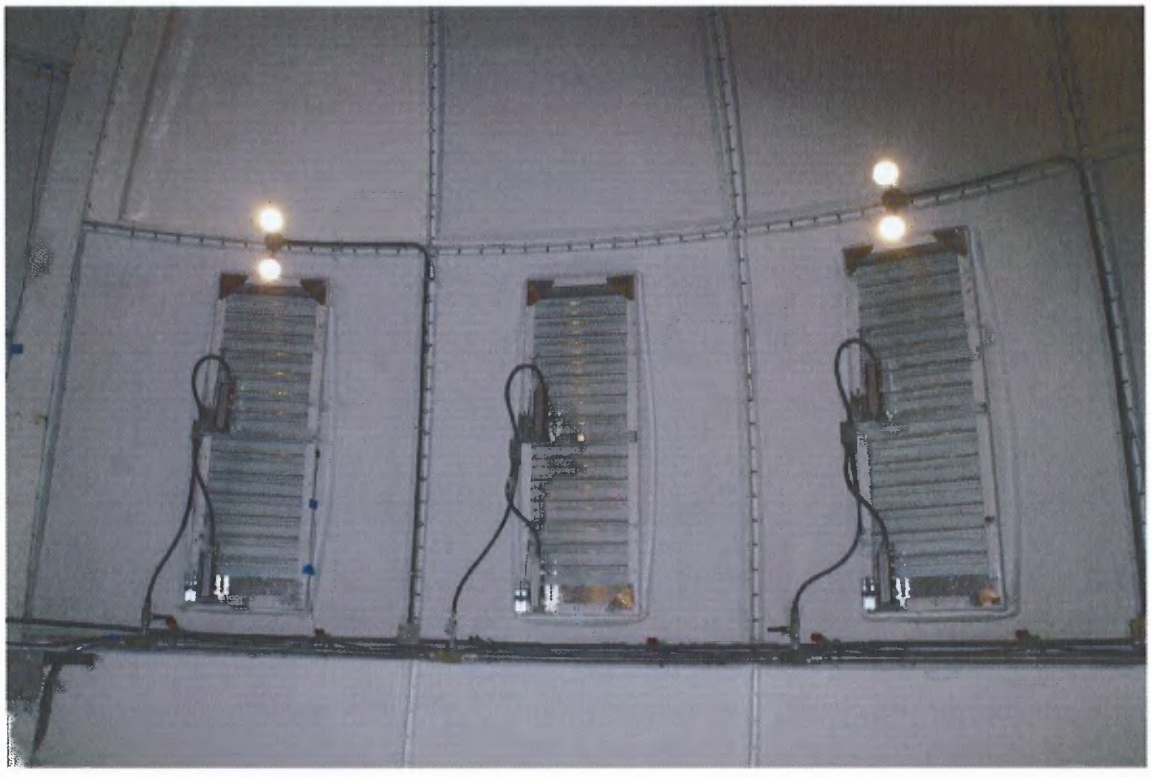

Figure 5.2 The inside of the dome showing three of the active vent gate assemblies. Visible on each of the vents are the two motors that adjust the damper settings.

In January 2006, the first set of 16 temperature sensors were installed on the interior surface of the NST dome. A description of the Temp-Trax temperature monitoring system including the probes and the corresponding control is given in Chapter 4. At the time the temperature probes were installed, dome structure, skin, and louvers were in place. However, the dome drive and shutter motors were not yet operational and as a result opening and closing the louvers was not possible at the time the probes were installed. A schematic of the dome with the louver configuration is shown in Figure 5.3. The labels A, B, and C denote the three levels of the dome from the bottom to the top respectively. The 14 louvers are marked in black by the numbers 1 through 7 on the east and west portions of the dome. In Figure 5.4 the evolution of the temperature inside the dome over a period of five days

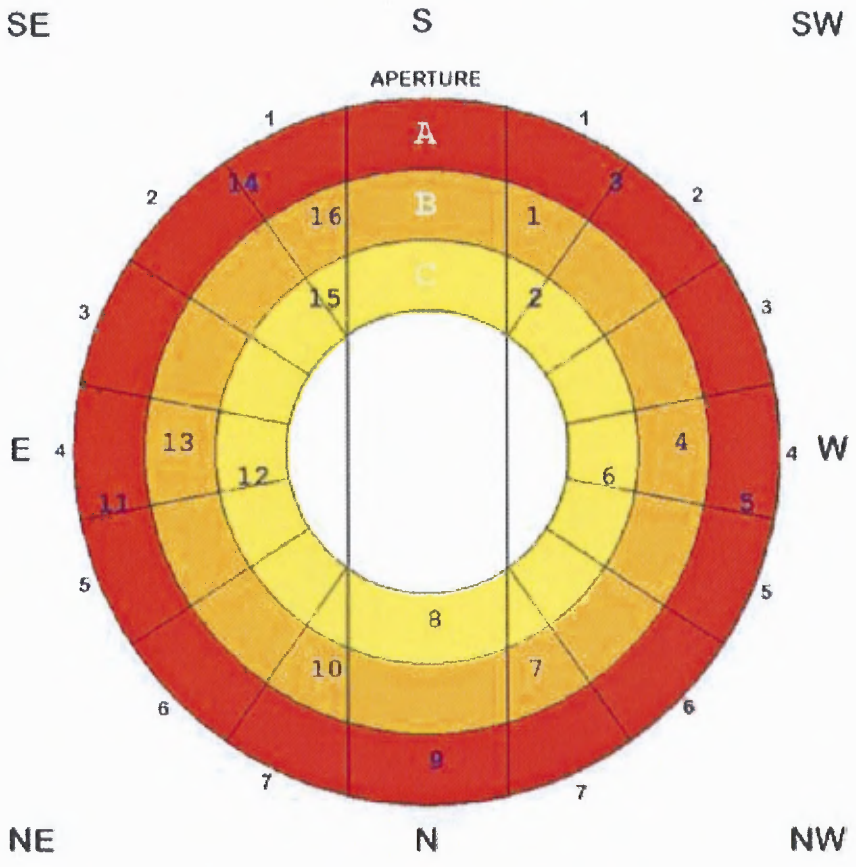

Figure 5.3 Schematic of the dome showing the location of the temperature probes (blue text), louvers (black text), and the orientation of the dome during January and December 2006 temperature probe experiments.

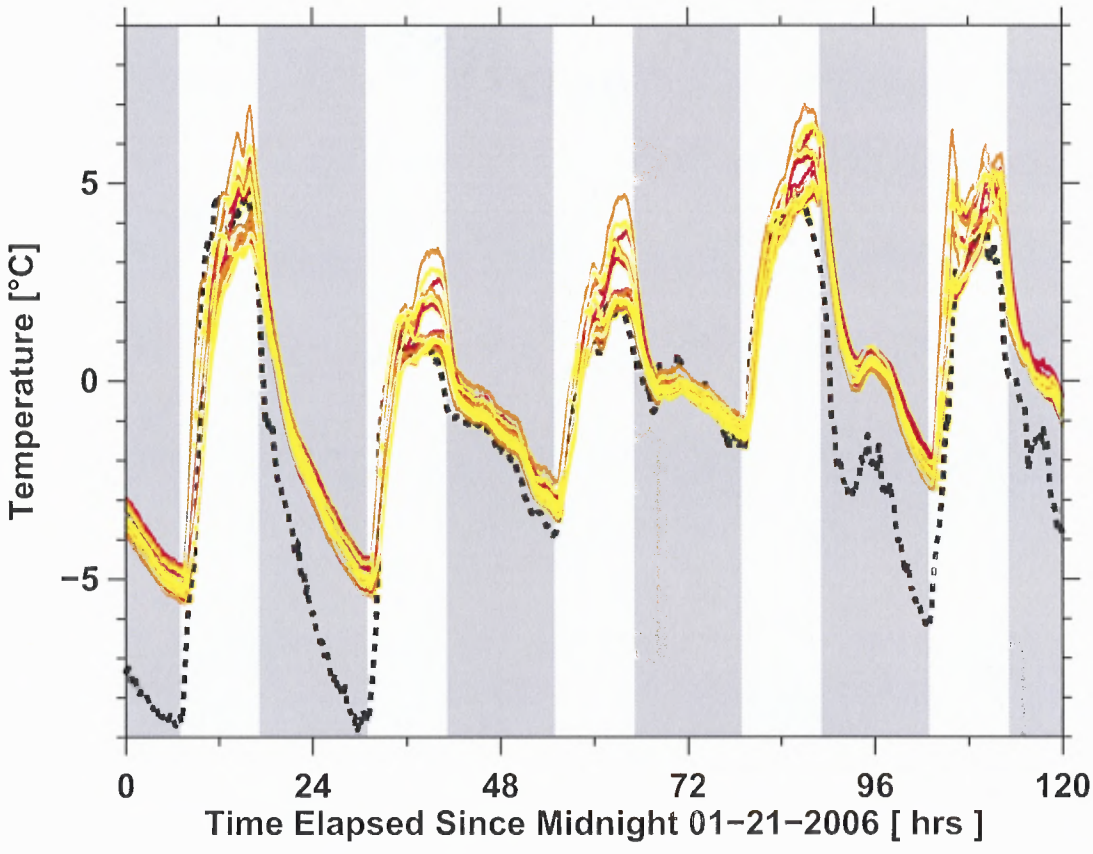

Figure 5.4 The temperature recorded for five days in January 2006. The reddish-orange, orange, and yellow solid lines represent the temperature recorded by probes located at dome levels A, B, and C respectively. The dotted-dashed black line represents the temperature outside recorded by the weather station. The background white and grey panels mark the location of sunrise and sunset respectively.

is shown. All of the louvers were closed and the dome was oriented with its aperture pointing to the south. The reddish-orange, orange, and yellow lines correspond to the probes that are located at dome level A (bottom), B (middle), and C (top) respectively. The dotted-dashed black line indicates the temperature outside the dome measured by the weather station. The temperature measured by each of the probes is plotted over periods of day and night which are represented by the white and dark-grey background panels. The largest difference in temperature read by the probes occurs shortly after local noon and becomes the most pronounced in the

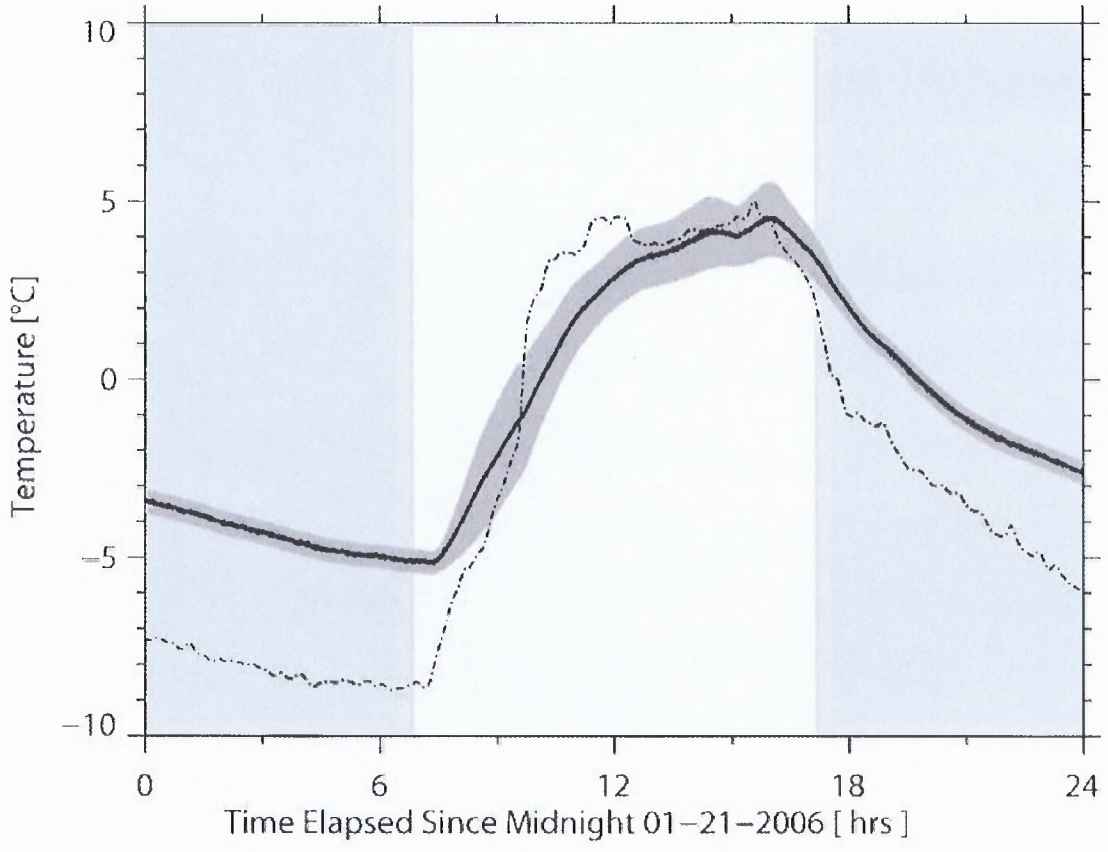

Figure 5.5 The mean temperature (solid black line) of all 16 temperature probes plotted with the standard deviation (dark grey). Sunrise and sunset are represented by the light grey and white background panels respectively.

hours before sunset. Figure 5.5 a closer look at the dome temperature evolution is shown. the mean temperature for all 16 probes (solid black line) plotted with the standard deviation (dark grey). A maximum temperature gradient of 3.3° C (2 σ) occurs at approximately 17:30 UT. It is clear from the plot that during the night the probes come closest to being in thermal equilibrium with each other with a minimum standard deviation of ±0.25° C.

5.3.1 Louver Experiments

In this section, the results of five days of temperature measurements taken while opening and closing the louvers in the dome is discussed. It is important to note

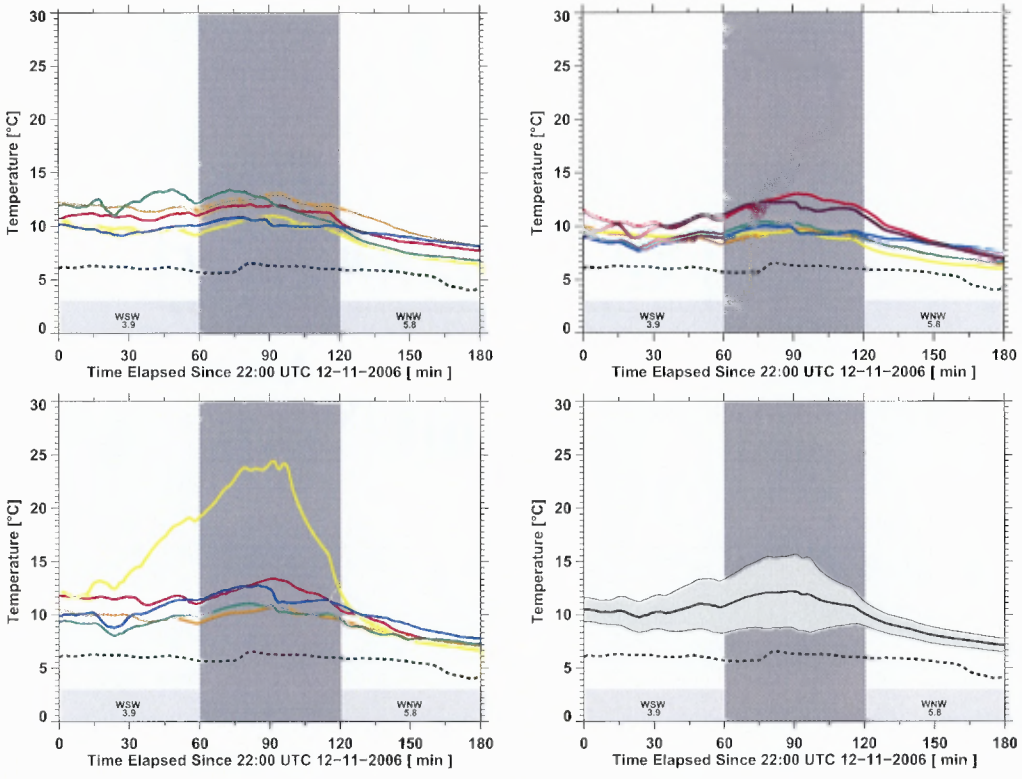

Figure 5.6 2006 December 11, louver experiment.

that the NST was not present in the dome at the time the measurements were made, and that there was a considerable amount of construction traffic moving in and out of the observatory. To develop a realistic understanding of the temperature distribution in the dome, and consequently create an accurate proxy that will determine the louver configuration, the temperature must be measured under normal observation conditions with all systems present. Nonetheless, the five days of temperature measurements with different louver configurations are important in determining if the louvers position has any effect at all on the dome temperature.

By December 2006, control of the dome drive and shutter motors had been integrated into the TCS. The next step was to investigate the effect that louver position (open or closed) has on the internal temperature of the dome. The dome shutter was closed as well as the iris, and the aperture position of the dome was set to point west and remained in that position for the duration of the experiment. Figure 5.6

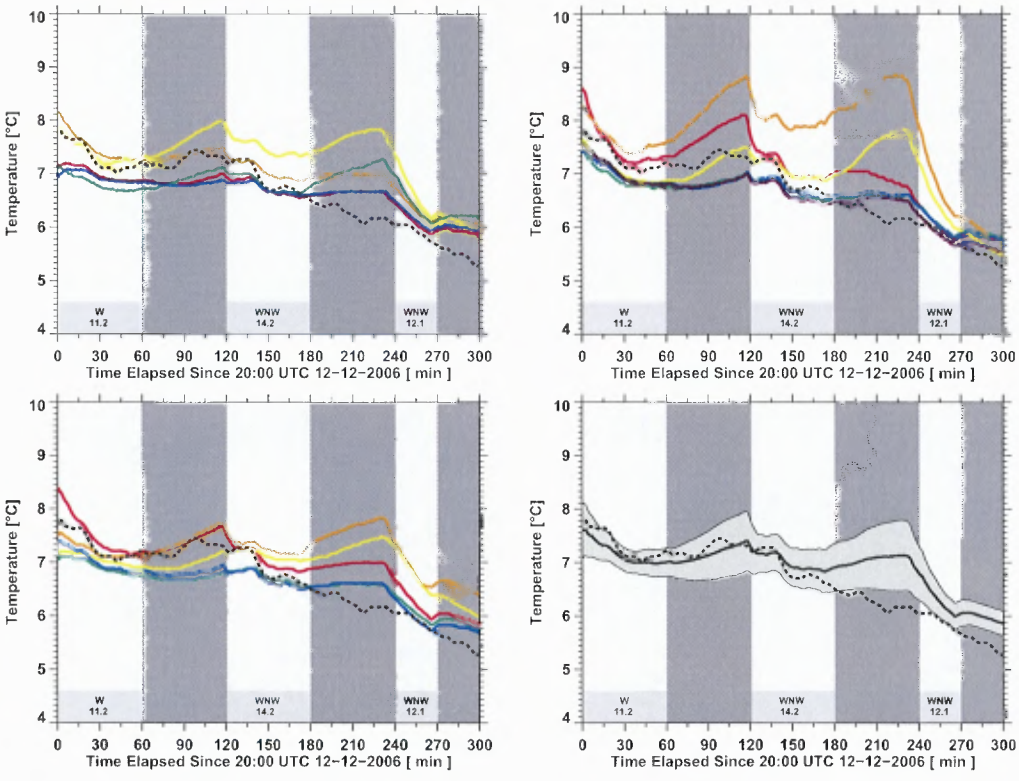

Figure 5.7 2006 December 12, louver experiment.

shows the results of the first louver experiment conducted on 2006 December 11. The y-axis is temperature in degrees Celsius and the x-axis displays the time in minutes. The white and dark grey background panels correspond to all 14 louvers being in an open or closed position, respectively. The dashed black line represents the outside temperature as measured by the weather station and the color lines are the probe temperatures. The average wind speed and wind direction for the times when the louvers are in the open position are given in the light grey box at the bottom of each plot. To get a rough idea of the height distribution of the temperature, a plot of the probes in three groups corresponding to the three levels A, B, and C of dome referring to Figure 5.3 is provided. The probes on level A are represented in the plot on the top left, level B in the top right, level C on the bottom left, and in the bottom right plot the mean temperature for all 16 probes is plotted over the standard deviation. This format is used for Figure 5.6 through Figure 5.10 of this section. On 2006

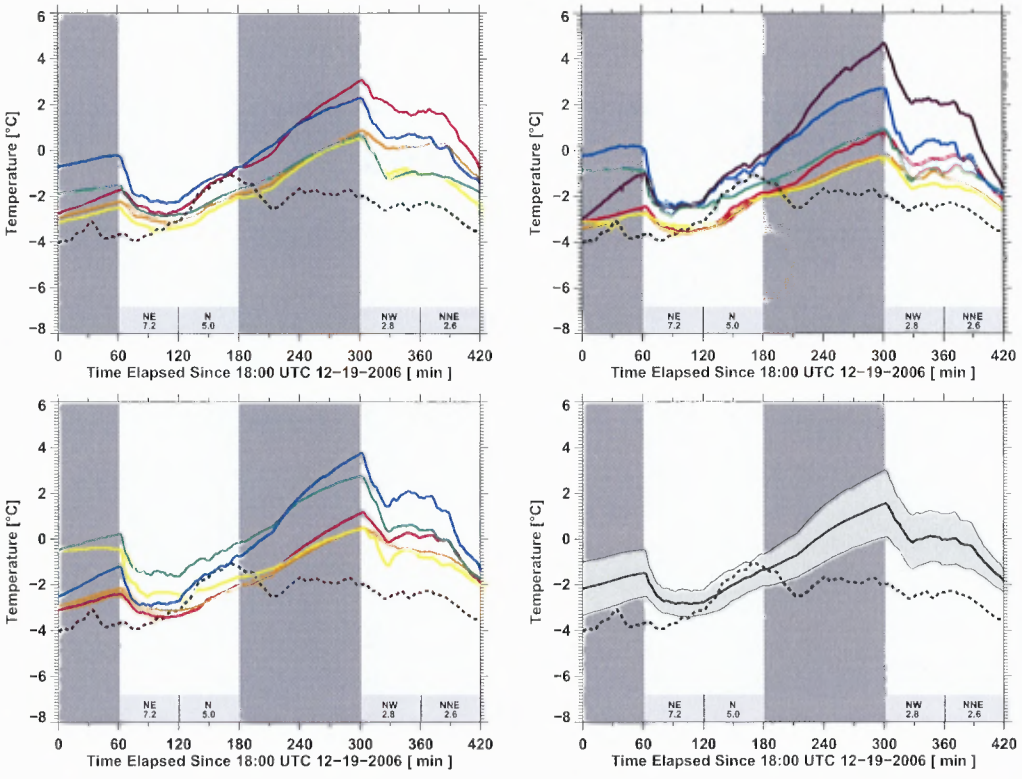

Figure 5.8 2006 December 19, louver experiment.

December 11, starting at 22:00 UT with all of the louvers open the temperature was recorded for a period of three hours. The louvers were kept open for the first hour, closed for the second hour and then opened for the third. A maximum temperature gradient of 7.1° C occurs at 23:35 UT (louvers closed). The outside temperature throughout the period of measurement remained fairly consistent at approximately 6.0° C with a discernable rise in temperature occurring at 23:30 UT. The yellow line corresponding to probe 8 located at level C in the dome measures a noticeable increase in temperature starting around 22:30 UT. This certainly effects the standard deviation which is considered as a crude proxy for the temperature distribution. The spike in temperature recorded by probe 8 could be a result of a number of factors. Most likely is that a worker in the dome was in close proximity to the probe during the time of measurement. That being said, there is only a modest change noticed at all three levels of the dome with respect to the louver configuration. One can note

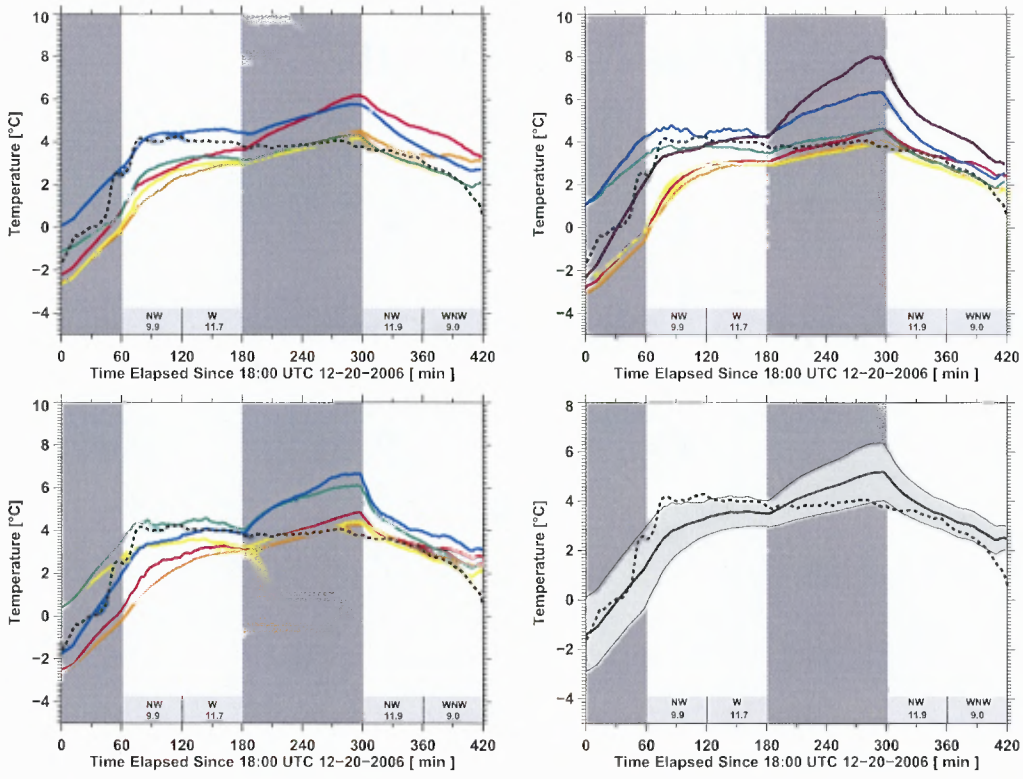

Figure 5.9 2006 December 20, louver experiment.

however that the average wind speed throughout the first hour of the experiment was approximately 2 m s^{-1} below the characteristic wind speed experienced at BBSO. In the final hour of the experiment the average wind speed increased to 6.8 m s^{-1} at which point the thermal gradient decreased. Figure 5.7 shows the results of the temperature measurements made on 2006 December 12,. The louvers were opened and closed in intervals of one hour and average wind speeds through out the period of measurement was considerably higher ($\sim$ 4.67 m s^{-1}) than that of the previous day. The louver position has a more pronounced effect on the dome temperature, with a maximum temperature gradient of 1.4° C occurring at 23:45 UT. It is also evident that the outside temperature until approximately 22:00 UT falls with in (2σ) of the mean dome temperature.

The next set of probe measurements, shown in Figure 5.8 and Figure 5.9, the louvers were opened and closed in intervals of 2 hours. The maximum temperature

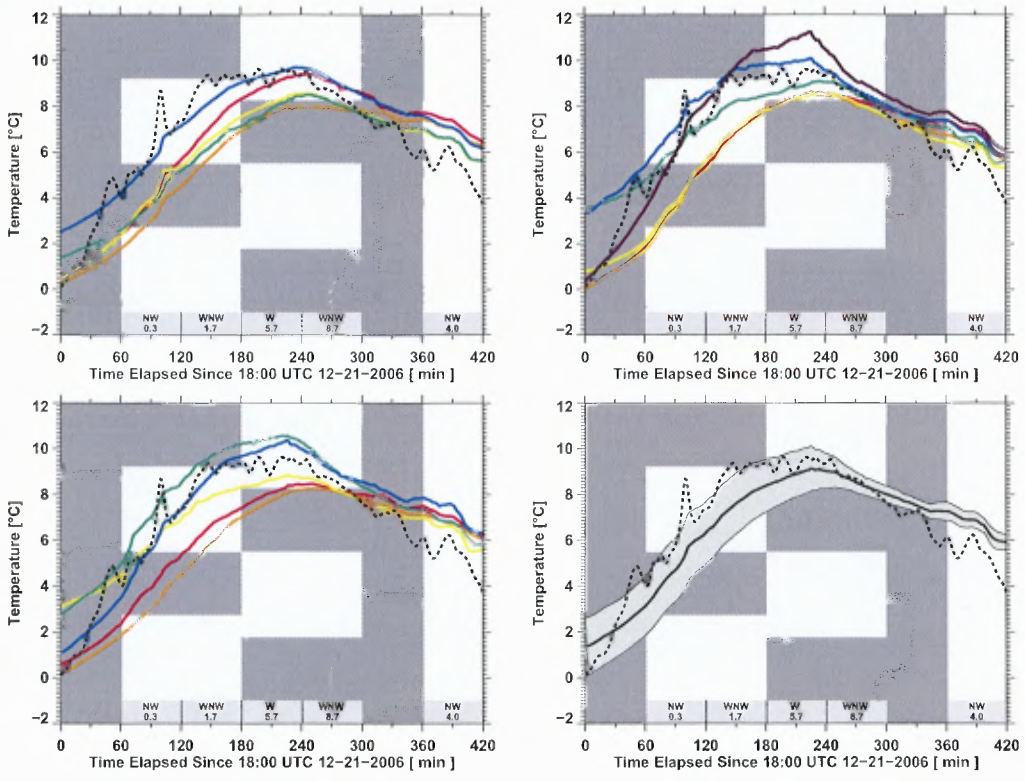

Figure 5.10 2006 December 21, louver experiment.

gradients for 2006 December 19, and 2006 December 20, are 2.9° C and 3.2° C, respectively. They both occur at approximately the same time 23:40 UT. In Figure 5.8 a minimal thermal gradient is seen to occur during the two hours the louvers are first opened. The outside temperature is within (2σ) of the mean dome temperature. There is a clear increase in temperature at 21:00 UT when the louvers are closed. When the louvers are opened again at 24:00 UT the winds speeds have decreased and though the dome temperature decreases it does not reach the value of the outside temperature as it had before 21:00 UT. In Figures 5.9 the dome temperature more or less tracks the outside temperature which could be a resultof high average wind speeds.

On 2006 December 21, the final temperature experiment was conducted. Starting at 18:00 UT all 14 louvers were in the closed position. At 19:00 UT louvers 1 through 4 on the east facing side of the dome and louvers 4 through 7 on the

west facing side (refer to Figure 5.3) of the dome were opened with the remaining louvers closed. At 21:00 UT louvers 4 through 7 on the east facing side of the dome and louvers 1 through 4 on the west facing side of the of the dome were opened with the remaining louvers closed. The wind speeds throughout the measurement period varied considerably, with very low wind speeds (~ 1.0 m s^{-1}) occurring from 19:00 to 21:00 UT and typical wind speeds of (~ 6.0 m s^{-1}) occurring from 21:00 to 23:00 UT. A maximum temperature gradient of 2.9° C occurred at approximately 21:00 UT. Looking at the evolution of the temperature gradient (2σ) throughout the measurement period a discernable reduction is seen to occur when the wind speed increases.

From these experiments it is clear that the position of the louvers (open or closed) has an effect on the temperature inside the dome. However, for an accurate (quantitative) characterization it is imperative that measurements, such as the ones presented here, be made during NST observing periods. It is also clear that the higher the wind speed the faster the internal dome temperature measured at the locations of the 16 probes approaches the outside temperature. More temperature probes need to be installed at strategic locations inside the dome to get a more precise view of the domes internal temperature distribution.

5.4 Meteorological Data

An accurate characterization of the meteorological conditions in the immediate surroundings of an observatory is important for daily and seasonal operations of the telescope. In February 2005, a Vantage Pro2 Plus weather station manufactured by Davis Instruments (`http://www.davisnet.com/`) was installed at BBSO to monitor these conditions. The weather station is outfitted with an integrated suite of meteorological instruments including solar radiation and UV sensors. Temperature and humidity sensors are housed inside a radiation shield for improved accuracy. The

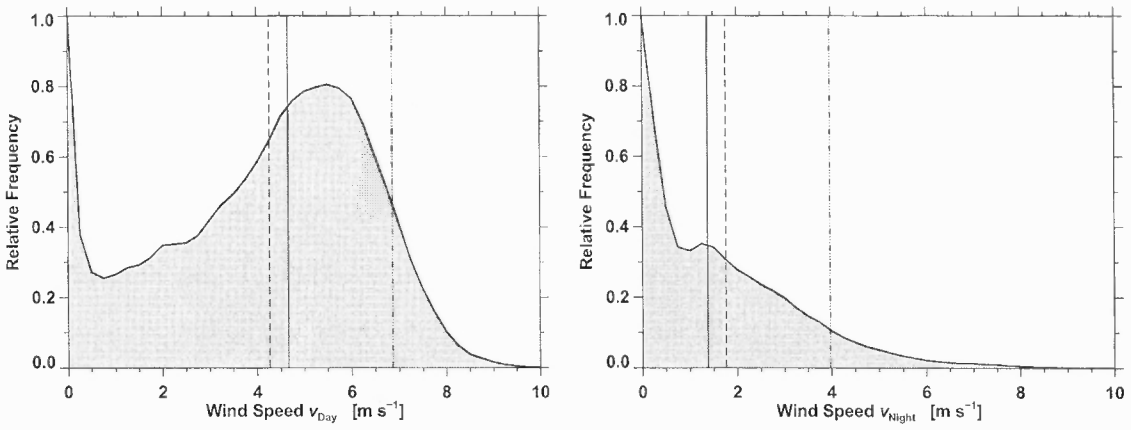

Figure 5.11 Frequency distributions of the wind speeds v_{Day} (*left*) and v_{Night} (*right*). The median, mean, and 10^{th} percentile wind speeds are indicated by solid, dashed, and dashed-dotted vertical lines, respectively.

weather station data presented in this section covers 741 days from 2005 February 28, to 2007 March 10. The data was sampled at a 1-minute cadence with the exception of the first 10 days, when a cadence was 5 min.

The frequency distributions of daytime (*left*) and nighttime (*right*) wind speeds are shown in Figure 5.11. The median wind speed during the daytime is 4.67 m s^{-1} with a mean of 4.27 m s^{-1}. The 10^{th} percentile (6.87 m s^{-1}) of the wind speed distribution was computed to provide an estimate for high wind conditions. During the night, the winds decrease in strength. The median, mean, and 10^{th} percentile wind speeds are 1.38 m s^{-1}, 1.76 m s^{-1}, and 3.97 m s^{-1}, respectively. The median, mean and 10^{th} percentile values for each of the distributions are represented by a solid, dashed, and dashed-dotted vertical line in Figure 5.11. The two wind speed distributions clearly show different characteristics. Much higher velocities are encountered during the daytime with a well-defined maximum between 5.0 and 6.0 m s^{-1}. This maximum is basically absent in the nighttime distribution, where a basically monotonic decrease of the frequency of occurrence with wind speed is found. The physical mechanism behind these discrepancies becomes more apparent in the frequency distribution of the directions (Figure 5.12).

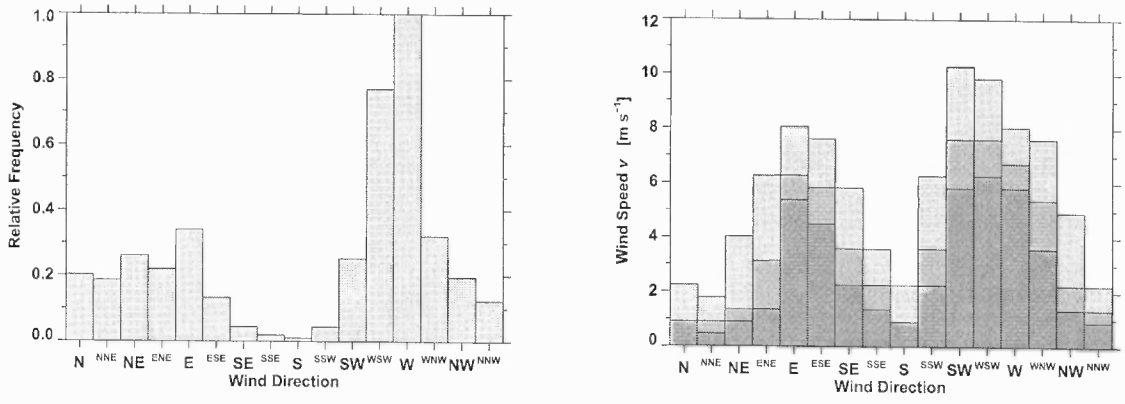

Figure 5.12 *Left.* Frequency distribution of the wind directions. *Right.* The median wind speed as a function of the wind direction is shown as dark gray. The lighter grays correspond to the 10^{th} and 30^{th} percentile of the respective frequency distributions.

The east-west orientation of Big Bear Lake and its mountain location gives rise to a unique distribution of wind directions. The relative frequency distribution of the wind direction is shown in the left panel of Figure 5.14 for the entire data set. The wind directions in the following plots are given on a the compass rose graduated into 16 sector. Immediately apparent is the predominance of westerly wind directions. This westerly wind is a result of gradient in pressure between the Los Angeles basing and the interior regions of the Southern Californian desserts (Verdoni and Denker, 2007). The winds are channeled through the canyons an valleys of the San Bernardino mountains. Since the wind does not encounter any obstruction passing over the cold waters of Big Bear Lake, the observatory island is embedded in almost laminar air flows. The water also provides a "heat sink" effectively suppressing ground-layer seeing. This is the explanation for the very good seeing conditions from sunrise to sunset at BBSO.

A more quantitative picture of the wind speeds as a function of wind direction is presented in the right panel of Figure 5.12. Here, the gray scale corresponds (from dark to light) to the median, 10^{th} and 30^{th} percentile of the frequency distributions, respectively. For a westerly wind a median wind speed of approximately 6.0 m s^{-1} is measured with winds of 8 m s^{-1} or greater occurring 30 percent of the time. For

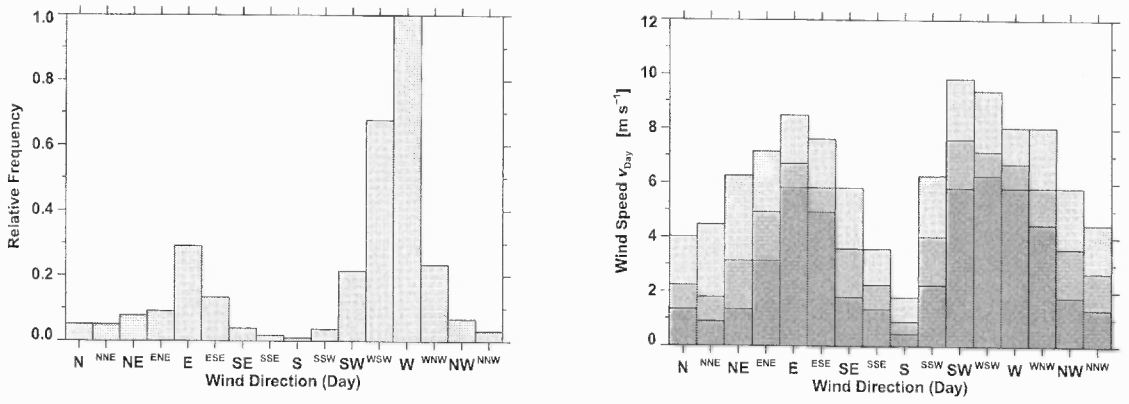

Figure 5.13 Frequency distribution of the daytime wind directions (same format as Figure 5.12).

easterly wind directions, the speeds are comparable to westerly winds. These winds are caused by a reversal of the pressure gradient and are commonly referred to as Santa Ana winds (Hu and Liu, 2003). A detailed discussion of the daytime seeing characteristics at BBSO was presented in an earlier study (Verdoni and Denker, 2007) based on data from the ATST site survey. However, due to the nature of the daytime seeing monitor no nighttime weather data was available. Since nighttime observations might be scheduled for NST and the fact that BBSO has an existing program for Earthshine observations (Montañés-Rodriguez *et al.*, 2005), a presentation of the respective nighttime weather data is also presented in this study. These data also further illustrate the two different observing regimes for day and night (Figures 5.13 and 5.14).

Separating the daytime and nighttime frequency distributions shows an even more pronounced east-west orientation of the winds during the day. It also shows that Santa Ana conditions do not very frequently occur (about 10% of the time). However, even under these conditions the seeing can be very good (Verdoni and Denker, 2007) but the observing conditions suffer from a low sky transparency due to dust carried in from the deserts. The wind speeds are very similar (about 6.0 m s^{-1}) for winds from the East and West (see right panel in Figure 5.13. However, in the the north-south

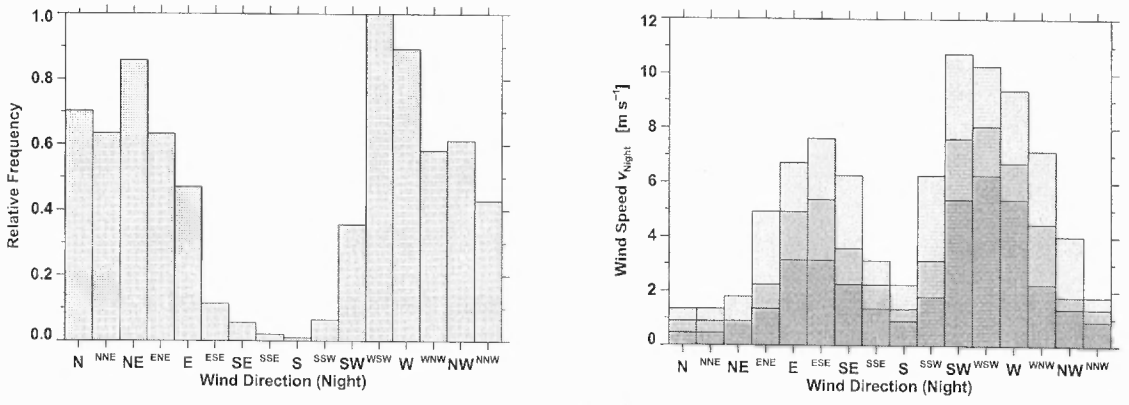

Figure 5.14 Frequency distribution of the nighttime wind directions (same format as Figure 5.12).

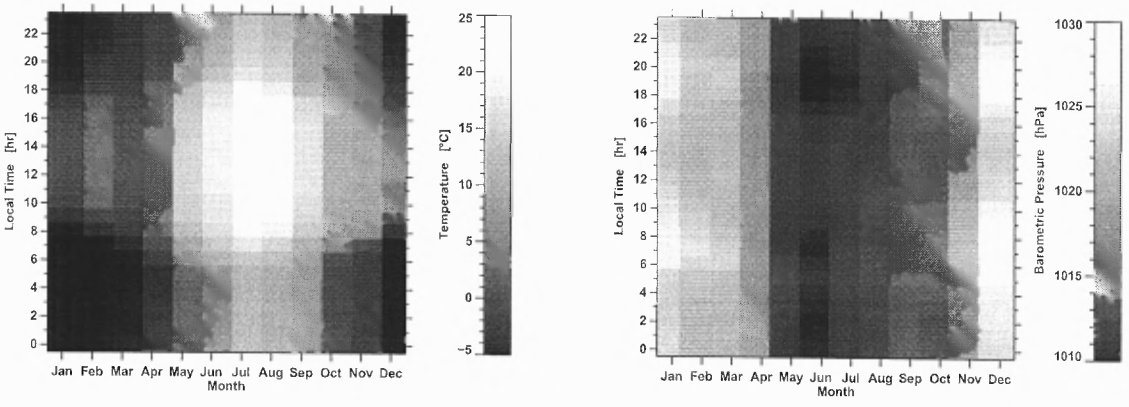

Figure 5.15 *Left.* Seasonal and diurnal variation of median temperature. *Right.* Seasonal and diurnal variation of median barometric pressure.

direction the wind speeds are reduced to about 1.5 m s^{-1}. Figure 5.14 for reveals the nighttime wind regime, which is dominated by mountain down-slope winds. The air that has been heated during the day, now slowly flows down the mountain slope towards the cool surface of the lake. With the exception of the southern mountain slopes, there is no preferential direction for the down-slope winds but the wind speed distribution again follows the east-west orientation of Big Bear Valley. Consulting the wind speed distributions in Figure 5.11, low wind speed times $v < 1.0$ m s^{-1} occur during a significant fraction of time. This happens typically around dusk and dawn, when the change between the daytime and nighttime wind regime takes place.

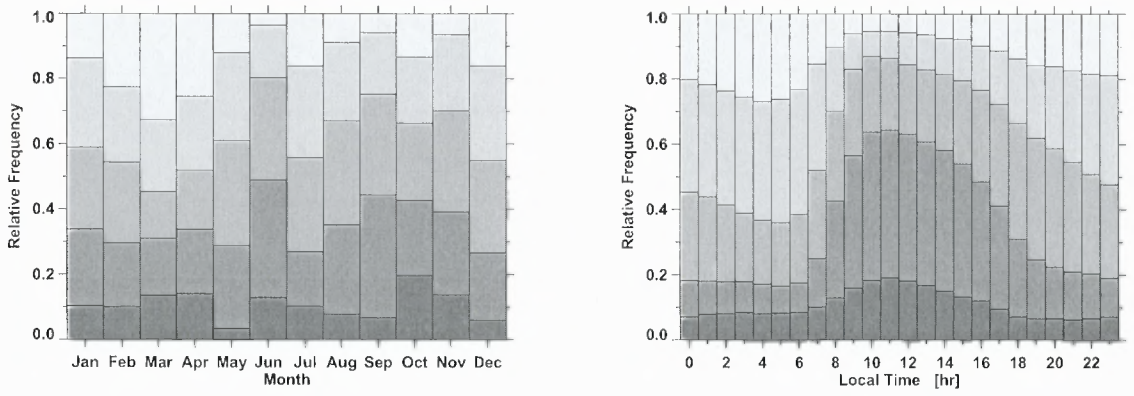

Figure 5.16 *Left.* Seasonal frequency distributions of the humidity. *Right.* Diurnal frequency distributions of the humidity. The gray scale (from dark to bright) corresponds to humidity levels of 20%, 40%, 60%, and 80%.

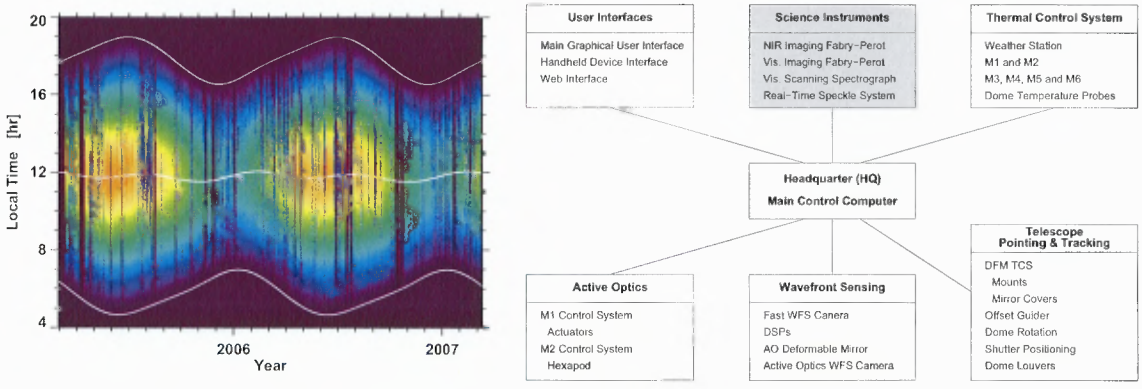

Figure 5.17 *Left.* Diurnal and seasonal variation of the solar radiation spanning the entire data set. The white contour lines refer to sunrise, local noon, and sunset. *Right.* Schematic overview of the main TCS components. The system components of the THCS and Telescope Pointing and Tracking System TPTS, which are responsible for controlling the NST thermal environment, are shown on the right.

In Figure 5.15, the seasonal and diurnal variations of the median temperature (*left*) and median barometric pressure (*right*) are shown as gray scales. The hottest month is July, when median temperatures reach about 25° C. The temperature spread between day and night is also much large during the summer months (about 10° C compared to 7° C in the winter). The warm temperatures in February might be an anomaly, since the data sample presented only covers slightly more than two years. The barometric pressure shown in the right panel of Figure 5.15 is basically inversely proportional to the temperature. The lowest values of the barometric pressure are

measured throughout the summer months. The diurnal variations are more or less negligible. However, a small trend to higher barometric pressure can be observed around dusk and dawn, when transitioning from the daytime to the nighttime wind regime and vice versa. The seasonal trend of the barometric pressure is given by the pressure gradient between the coastal regions of Southern California and the inland deserts.

The seasonal (*left*) and diurnal (*right*) distributions of the humidity are shown in Figure 5.16. The gray scale corresponds (from dark to bright) to humidity levels of 20%, 40%, 60%, and 80%, respectively. The winter months and early spring is the most humid time of the year. Surprisingly, only a weak indication is found (in July) for the monsoon season in July and August. Again, the explanation for this behavior is in the diurnal changes of the humidity. Shortly after sunrise, the air dries out and becomes least humid around local noon. With decreasing solar input in the afternoon, the humidity increases monotonically. This trend continues after sunset. The most humid time is reached just before sunrise. The high humidity during the night and dawn might cause problems for nighttime and Earthshine observations.

The weather station also included a solar radiometer. The left panel of Figure 5.17 displays the diurnal and seasonal variations of the solar radiation from which the CTF was computed. The solar radiation is displayed on a rainbow color scale, where violet corresponds to low light levels and orange/red refers the maximum of the solar radiation at noon in the summer time. Solar ephemeris computations including optical air mass were obtained from the Jet Propulsion Laboratory (JPL) Horizons web page (`http://ssd.jpl.nasa.gov/horizons.cgi`) to aid in the analysisGiorgini *et al.* (1996). The ephemeris data were converted from Universal Time (UT) to Pacific Standard Time (PST, without daylight savings time correction) to match the weather station data. The three white lines (from bottom to top) refer to sunrise, local noon, and sunset, respectively. Especially in the winter and spring,

entire days with low light levels are recorded. These times are during winter storms and when the sky is overcast. The monsoon season is also visible in the left panel of Figure 5.17 during the months of July and August, when the daily radiation traces become spotty about two hours before local noon. During the monsoon the moist air and solar heating can give rise to severe thunderstorms. A threshold of 90% of the instantaneous solar radiation is used to compute the CTF. Since this fractional criterion becomes impractical for elevations lower than 5°, only the CTF is computed for higher elevation angles and this value is extrapolated to the entire data set. The CTF determined from the solar radiation sensor of the weather station is 72.4%. This value agrees well with CTF value from the ATST site survey (71.2%, Hill *et al.*, 2004a) and previous measurements obtained as part of the GONG site survey (70.7%, Hill *et al.*, 1994).

5.5 Thermal Control System

The THCS (Verdoni and Denker, 2006) is part of a distributed computer system, which controls the telescope, dome, AO, and the post-focus instrumentation. The overall system is known as the TCS (Yang *et al.*, 2006). A schematic overview of the TCS is shown in the right panel of Figure 5.17. Use of a distributed system allows for greater flexibility, and ultimately for greater simplicity than a monolithic design would provide. As a consequence, each subsystem within the TCS has only a limited set of tasks to perform.

Overall management of the TCS is carried out by the HQ program running on a dedicated main control computer. HQ collects data from each subsystem for centralized logging and access by the main user GUI systems. Commands are sent from the GUIs to HQ for dispatch to the appropriate TCS system for execution. Each subsystem has an engineering GUI written in Java. In general, C++ and Java are the only languages used in the control system. The object-oriented TCS design

has so far resulted in a successful implementation of all subsystems and significantly shortened the design and development time (Shumko and Yang, 2006). Even though status information is provided by HQ to science instruments, they are currently not considered part of TCS. Instrument designers have to rely on well-defined interfaces implemented in XML to integrate the post-focus instruments in the hierarchical TCS infrastructure.

Communication within TCS is performed by Ethernet, which offers much better performance compared to older RS-232-based implementations and simplifies cabling to the telescope. Ice from ZeroC was chosen as the standard communication protocol/software library. User interaction with all subsystems is handled by a system-wide main GUI, which accesses the subsystems through HQ. The HQ computer is also performing logging and archiving of status information, which is collected in a data base.

All high-level commands are written in XML. Commands, information requests, notifications, or error messages can be sent asynchronously. Fast network connectivity and generally short messages make the overhead of ASCII formatting negligible and does not result in any significant impact on overall performance. Processing of XML messages is trivial, since there are many ready-to-use libraries in both Java and C++. Ice also allows seamless integration various operating systems (e.g., Windows XP and Linux), which are installed on the various subsystem control computers. Subsystems access and control hardware directly or through off-the-shelf Ethernet-based controllers. For example, Galil multi-axis controllers are used with the servo motors for dome rotation and dome shutter operation. Another, example are the TempTrax Model E interfaces for the temperature probes throughout the dome, which communicate via a built-in web server.

While THCS monitors temperatures within TCS, THCS also closely interacts with the Telescope Pointing and Tracking System (TPTS, Varsik and Yang, 2006),

which handles the movement of the telescope and dome. TPTS also provides a wrapper for the telescope mount software provided by the telescope manufacturer DFM Engineering, Inc. One of the TPTS challenges is the alignment of the relatively small dome opening with the optical axis of the telescope. An algorithm is used to find the position required for the dome so that the aperture is in the correct place aligned with the telescope beam, allowing for the offsets between the pivot point of the telescope mount, the center of the telescope light path, and the center of the sphere of the dome. The dome shutter and azimuth drives are then moved so the dome aperture follows the position of the light path during the day. TPTS also controls the dome louvers.

The primary THCS objective is to provide a stable environment for NST's main optical components, which are located inside an open telescope support structure. Therefore, the temperature of the optical support structure and primary and secondary mirrors has to be closely monitored. The surface of the primary mirror can be actively cooled by regulating the air flow and temperature by using a fan driven heat exchanger. The fan will provide a laminar flow across the mirror surface, thus avoiding the rise of turbulent eddies from the sunlit mirror surface. The only way to keep the temperature of the telescope structure and other optical components close to ambient is to effectively ventilate the dome and limit the amount of sunlight entering through the dome aperture by making it as small as possible. The radius of the dome aperture is only 20 cm larger than that of the primary mirror. To accomplish the first task, THCS automatically sends commands to operate the 14 dome louvers through TPTS to adjust to variable wind speeds and directions during the observing day. Real-time information from a weather station and from a network of temperature probes inside the dome are used in a decision module (Denker and Verdoni, 2006; Verdoni and Denker, 2006), which sends the appropriate adjustments through HQ to the dome louvers.

5.6 Thermal Control of the Primary Mirror

The thermal control of the primary mirror relies on two different mechanisms: the air inside the dome has to track the outside temperature and an air knife that directs a laminar flow of air across the Sun-facing primary mirror surface. Assuming that the passive ventilation through the the louvers minimizes interior temperature gradients and reduces internal dome seeing, sample temperature profiles can be used for winter, spring, and summer to evaluate the thermal properties of the primary mirror under realistic observing conditions.

Sample profiles for the four seasons are shown in the left panel of Figure 5.18. These samples were created by averaging all available temperature profiles for the respective seasons. The general shape of all profiles is roughly the same. A fast monotonic temperature rise after sunrise, which reaches a plateau about two hours before local noon. At this time, laminar wind flow across the lake and the lake acting as a heat reservoir balance solar heating and an equilibrium is reached. This plateau persists for up to 10 hours in the summer but lasts only about six hours in the winter. This region of little or no change is not an artifact of the averaging procedure but can also be found in individual daily temperature profiles. Exceptions are days with extended cloud cover. However, since BBSO has more than 300 sunny days per year, cloudy or rainy days only leave an negligible imprint on the averaged seasonal profiles. In the late afternoon and early evening radiative cooling begins, once the Sun sets behind the mountains to the West of the observatory, reaching the coolest temperatures just before sunrise. Typical temperature spreads between day and night are 7.3 K, 9.4 K, 10.3 K, and 9.0 K for winter, spring, summer, and autumn, respectively.

In the right panel of Figure 5.18, two temperature profiles (dashed-triple-dotted curves) for winter (gray) and summer (black) are used to illustrate how the Zerodur primary responds to changes of the ambient temperature (dashed curve). Even

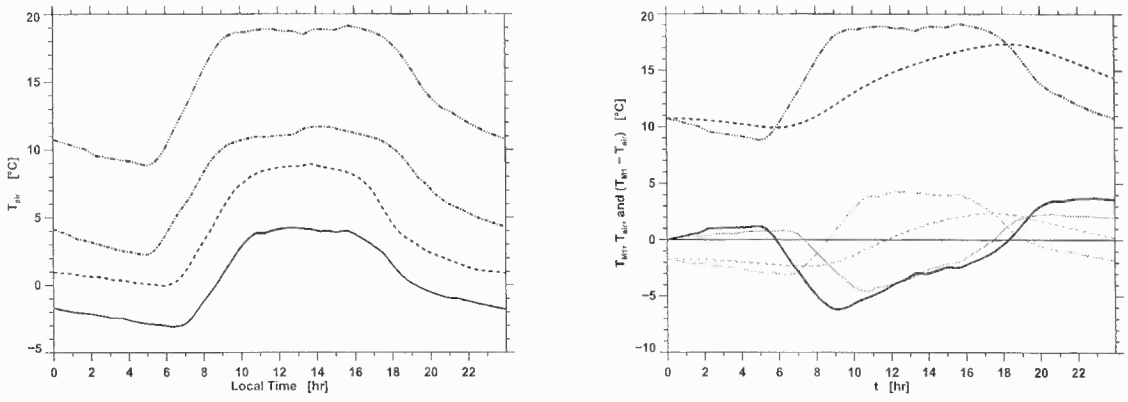

Figure 5.18 *Left.* Average daily temperature profiles for winter (solid), spring (dashed-dotted), summer (dashed-triple-dotted), and autumn (dashed). *Right.* M1 response (dashed) to ambient air temperature variation (dashed-triple-dotted) during the summer (black) and winter (gray) considering convective heat exchange only. Initially (at midnight), M1 and ambient air temperature are the same. Their temperature differences are given by the solid curves.

without direct exposure to sunlight, the thermal inertia of primary mirror leads to a rapid departure from the ambient temperature. Once the temperature difference exceeds about ± 1 K, mirror seeing becomes an issue and severely limits the performance of a (solar) telescope.

In this introductory example, it is assumed that M1 and the surrounding air had the same temperature at midnight. M1 then slowly follows the cooling trend of the ambient air until about sunrise. In fact, it remains within the allowed 1 K temperature envelope for about 1/2 to 1 hour (summer/winter). This agrees with experience gained at older (non-evacuated) solar telescopes, where observations with diffraction-limited quality have been reported for short time periods just after exposing the primary to sunlight. Of course, once these telescopes and their optics heated up, the image quality rapidly deteriorated. The temperature difference between the primary mirror and ambient air $T_{\mathrm{M1}} - T_{\mathrm{air}}$ exceeds the desired 1 K envelope for most of the observing day. In the morning, M1 is cooler by up to 6 K in the summer and 4 K in the winter, respectively. In the late afternoon, the temperature difference reverses sign and reaches values of 4 K in the summer and 2 K in the winter, respectively.

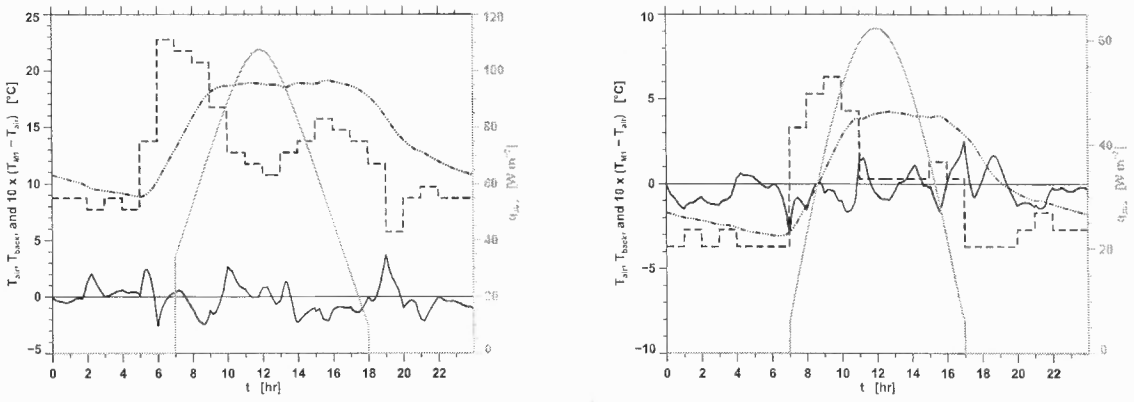

Figure 5.19 *Left.* Lump capacity model of the primary mirror M1 with realistic temperature profile $T_{\rm air}$ (dashed-triple-dotted) and absorbed solar radiation $q_{\rm abs}$ (solid gray) during the summer months. The air temperature $T_{\rm back}$ (dashed) to convectively cool the backside of M1 is changed every hour in multiples of 1 °C to minimize the temperature difference $T_{\rm air} - T_{\rm M1}$ (solid black). The temperature difference has been stretched by a factor of 10 to enhance the visibility of small-scale temperature variations. *Right.* Data for winter months (same labeling as in left panel).

As expected, these effects are smaller in the winter than in the summer. The lag of the time-delayed M1 response is about 4 to 6 hours and fine-structures of the air temperature profile are smoothed out. Importantly, M1 now carries excess heat into the next observing day, which would make maintaining the temperature difference in the range of ± 1 K even more difficult. In the following, a more realistic scenario is discussed, adding solar heating and active cooling of the primary mirror to the model.

Starting with the average temperature profiles for summer and winter (see Figure 5.19), realistic values for the absorbed solar radiation $q_{\rm abs}$ are added to the lump capacity model. It is assumed that the observing day starts at 7:00 am local time in the morning and ends at 6:00 pm in the summer and 5:00 pm in the winter (daylight savings time was not taken into account). Furthermore, the observing days were completely sunny with no cloud cover. In principle, both radiation and convection could be used as cooling/heating mechanisms for the primary mirror M1. Since both mechanisms follow the same formal implementation in the M1 lump

capacity model, only convective air cooling/heating of M1 is discussed here. In addition, radiative cooling/heating would require a heat exchanger in close proximity to M1, which is not possible in the tight confines of the M1 support, which houses the actuators for the M1 active optics.

Changing the air temperature T_{back} only every hour in multiples of 1°C, results in the ability to keep the primary mirror within a few tenth of degree Celsius of the ambient air temperature T_{air}. The rapid rise of the ambient air temperature in the morning requires warming M1 by blowing heated air on the backside. Solar loading by itself is not sufficient to bring M1 fast enough to the desired temperature. The early morning presents therefore the greatest challenge for controlling the M1 thermal environment. Since the backside air temperature T_{back} is almost 15 °C warmer than the ambient air temperature T_{air}, it is essential the backside of the primary mirror cell is tightly sealed to avoid an exchange of air. A similar but inverted control challenge exists in the late afternoon, when M1 has to be cooled to follow the ambient air temperature. However, the temperature differentials are not as severe. As expected, the control requirements are much more relaxed in the winter time, since the day/night temperature difference are much smaller and so is the solar loading. If a predictive model of the daytime temperature exists, the thermal control of the primary mirror becomes feasible. This is certainly the case for sunny days. However, on partially cloudy days daytime temperature predictions become a challenge and it might not be possible to keep M1 within the ±1°C operating envelope. On the other hand, the large clear time fraction at BBSO with more than 300 sunny days, allows to keep the primary mirror within the temperature margins for most of the time.

One concern of the non-isotropic M1 heating/cooling is that the primary mirror can become distorted as a result of thermal gradients. This distortion is proportional to the coefficient of thermal expansion (CTE) of the mirror material. The CTE of

Zerodur is $\alpha = 0.00 \pm 0.10 \times 10^{-6}$ K^{-1} from 0°– 50° C. The major effect is a dominant axial thermal gradient resulting primarily in a focus error, which can be compensated by changing the distance between the primary mirror and the secondary mirror assembly, which is mounted on a hexapod. However, the actual thermal deformation of the primary mirror will be more complex. This deformation has to be monitored by a dedicated wavefront sensor, which also measures the slowly varying gravitational mirror deformations. These data are fed to a control loop of the mirror support system Yang (2006). The AO support of the primary mirror consists of 36 actuators in three concentric circles (6, 12, and 18 actuators at r_i = 21.8 cm, 49.1 cm, and 75.1 cm, respectively). Any residual gravitational or thermal deformations of the primary mirror, which cannot be corrected by active optics, have to be compensated by NST's AO system, which is based on the existing BBSO AO system for the now obsolete 65 cm vacuum reflector (Denker *et al.*, 2007).

5.7 Conclusions

Controlling the thermal environment of the next generation of solar telescopes will be a major challenge considering the necessarily "open-design" of solar telescopes breaking the 1-meter aperture barrier. The results of some initial studies to characterize the BBSO site characteristics and the dome environment in which the future NST will operate are presented here. The time-delayed response of NST's 10-cm thick Zerodur primary mirror to changes of the ambient temperature requires a detailed understanding of its thermal environment and active measures to keep the mirror as close to the ambient temperature as possible. For example, daily temperature predictions become important to determine the optimal temperature of the primary mirror in the morning. An adaptive scheme to operate the dome louvers has to be developed, which equalizes the air temperature inside and outside of the dome, while avoiding wind-shake problems of the optical support structure, especially for the

exposed outrigger that carries the secondary mirror assembly. The work presented here has shown that NST can achieve its expected performance, even in the challenging daytime thermal environment. However, the results of the studies presented here have to be confirmed and refined in the engineering first-light phase, which is expected to begin in early 2009. Commissioning of NST (first-light) is expected about 12 months later.

CHAPTER 6

OVERVIEW OF HIGH-ORDER ADAPTIVE OPTICS, AND SPECKLE MASKING RECONSTRUCTION FOR THE NEW SOLAR TELESCOPE

6.1 Overview

The open structure design of NST requires that careful attention is given to the identification and remediation of local and dome related seeing. With favorable site conditions at BBSO and an advanced THCS, the NST is poised to achieve diffraction-limited observations of the Sun. To achieve its full potential, 0.065″ resolution at 500 nm, NST will need to employ a high-order AO system along with frame selection and a sophisticated post-facto image reconstruction technique. In Denker *et al.* (2005), the combination of these three techniques were successfully employed to generate high quality images of solar active region NOAA 10486 taken with the DST at NSO/SP. Shortly after the DST images were acquired, BBSO was equipped with its own AO system in January 2004 Denker *et al.* (2007). In this section an overview of the AO system at BBSO is presented as well as a more generalized discussion of frame selection and SMI.

6.2 Introduction

Modern large-aperture, ground-based solar telescopes have played and will continue to play a pivotal role in advancing the scientific communities understanding of the Sun. The need for large-aperture telescopes results from the fact that many of the science drivers in solar physics today require high spatial resolution and light gathering power particularly for spectropolarimetric observations. One example would be to obtain direct observational evidence of the proposed kilogauss flux tube. This would require the ability to achieve sustained diffraction limited observations with a

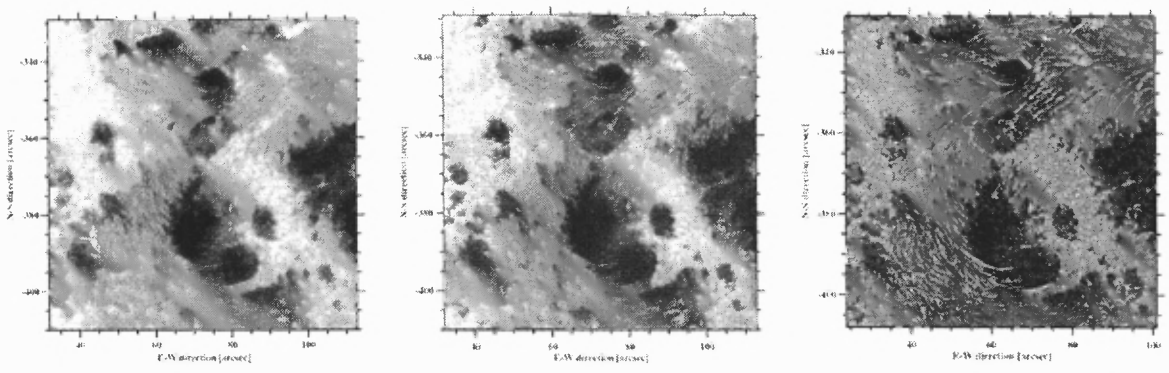

Figure 6.1 Shown from left to right are, the *long-exposure* image, the *short-exposure* reference image, and the reconstructed image of active region NOAA 10486. The reconstructed image is a result of high-order AO, frame selection and SMI Denker *et al.* (2005).

resolution of 50 to 100 km on the solar surface. Such an image scale requires that modern solar observatories implement some form of image correction, either *in-situ* or *post-facto.*

In Denker *et al.* (2005) examples of both in-situ and post-facto image correction are given. Corrections that are in-situ would include implementation of correlation tracking, spot tracking, and AO. Whereas *post-facto* image correction could consist of reconstruction techniques such as phase diversity, speckle deconvolution, speckle holography and SMI. Denker *et al.* (2005) takes this further separating the process of image reconstructions in two categories. The first would be a near *real-time* implementation of post-facto reconstructions using parallel processors as laid out in Denker *et al.* (2001b). The second would consist of a combination of both in-situ and post-facto techniques, which has successfully been shown by Scharmer *et al.* (2002), where both AO and Joint Phase-Diverse Speckle Methods were used. For NST, implementation of both post-facto and in-situ techniques will be employed. This will specifically include AO, frame selection, and SMI. The AO system at BBSO was successfully developed and deployed in January of 2004 for the 65-cm cm telescope Denker *et al.* (2007). Figure 6.1 is a testament to the reconstructive ability

of both post-facto and in-situ techniques. Figure 6.1 is a composite of three images depicting active region NOAA 10486 as observed using the DST on 2003 October 29. NOAA 10486 was one of three active regions responsible for major solar flare activity including an X28 flare on 2003 November 4, the largest flare recorded to date. In Chapter 8, images of a quiet Sun region at disk center utilizing the same reconstruction methods are presented. The left most panel in Figure 6.1 shows the average of 100 *short-exposure* (400 ms) images. This is called a *long-exposure* image. The middle panel of Figure 6.1 shows one of the short-exposure images. This image has the highest granular rms-contrast and is used in computing both image and differential image motion. The third panel in Figure 6.1 shows the result of AO, frame selection and SMI. In the following sections of this chapter a generalized overview of these methods are provided in more detail.

6.3 Adaptive Optics

In Beckers (1993) AO is defined as the removal of atmospheric distortions from a wave-front using an optical component that introduces a controllable counter wave-front distortion which follows the spatial and temporal evolution of Earth's atmosphere. The general objective of an AO system is three fold: first to measure perturbations of a given light beam, second to extract from these measurements a correction signal, and third to apply this signal to an *active* optical element such as a deformable mirror (Stix, 1989). The goal of AO for astronomical applications is to produce a restored wave-front void of a majority of the perturbations induced by Earth's atmosphere. Early AO systems were considered mainly for night time observations and considerable efforts have been spent to develop AO systems for night time observatories. Beckers (1993) credits Horace W. Babcock as one of the first to consider using an adaptive system to compensate for atmospheric effects. In his 1953 paper, Babcock (1953) states that *compensation for atmospheric induced seeing and for mirror*

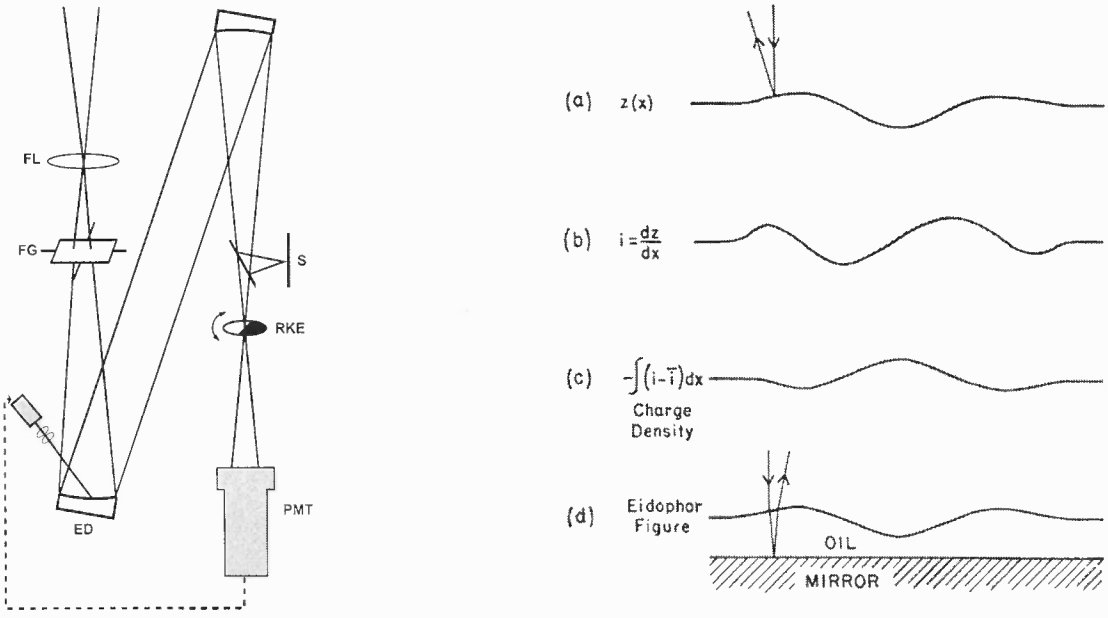

Figure 6.2 *Left.* The left most panel of this figure shows a proof of concept AO set-up as presented in Babcock (1953). *Right.*The right hand side of this figure shows how the modulated electron beam driving signal would be derived. Both of these images are taken from Babcock (1953).

imperfections could be achieved if the means of measuring the deviation of rays from all parts of the mirror could be done continually. This information he explains, would then be fed back to "correct locally" the inherent imperfections in the optical image that result from imperfections in the mirror as well as from atmospheric induced seeing Babcock (1953).

In his paper Babcock describes a set of knife-edge photographs taken using the 200 inch mirror of the Hale telescopes. The photographs taken using a Leica camera were intended not to understand how to correct for atmospheric effects, but to measure accurately deviations in the finishing of the 200-inch Hale mirror at Palomar Observatory. Nonetheless, the images given in Bowen (1950) show the effects of the atmosphere presenting itself as an erratic series of light and dark schlieren patterns passing rapidly across the image of the mirror. Babcock postulates that these atmospheric effects could be removed by placing a ray-controlling element in the conjugate image plane of the primary (Babcock, 1953). Segmented deformable mirrors were not

a technological realization at that time so Babcock suggested the use of an Eidophor, a mirror coated with a thin layer of oil. The oil, acting as the surface of the mirror, in the presence of an applied voltage would deform to a desired shape via electrostatic forces. The inclusion of the Eidophor, deployed as a feed-back element, in knife-edge schlieren imaging system could in effect measure and correct for atmospheric seeing.

The set up proposed by Babcock is shown in left panel of Figure 6.2. Light from the telescope is collected by a Field lens (FL) and passes through a fast guiding set-up (FG) used to keep the instrument centered on the star. The light is then reflected from an Eidophor (ED) and brought to a focus on a rotating knife-edge (RKE) instrument. The knife edge forms a schlieren image onto a detector, in this case a photomultipier tube (PMT). The signal received by the PMT is then used to modulate a signal that drives an electron beam which in turn creates the desired mirror shape (Babcock, 1953). The left panel Figure 6.2 shows the full field being imaged by lens (F) onto the Eidophor. The Eidophor reflects the light to a concave mirror that that focuses the light onto a rotating knife-edge. The light is then imaged on a photocathode tube which delivers an electronically integrated signal that serves to modulate the intensity of the electron beam of the Eidophor (Babcock, 1953).

Babcock went as far as to invent an electronic integration method to be used. The right panel of Figure 6.2 shows the proposed derivation of the Eidophor electron beam signal. Deviations from a perfect image are detected from one scan of the objective image. Figure 6.2a shows a single trace of the signal from the objective, with x denoting the linear distance along the surface of the mirror. These deviations are represented by $z(x)$ which is a function of the distance along the surface of the objective mirror. The intensity of the knife edge image of the trace is differentiated and integrated to give the charge density which is used to drive the electron beam of the Eidophor. The right panel of Figure 6.2 shows the current that is acquired by integrating the intensity in $z(x)$. The system proposed by Babcock is essentially

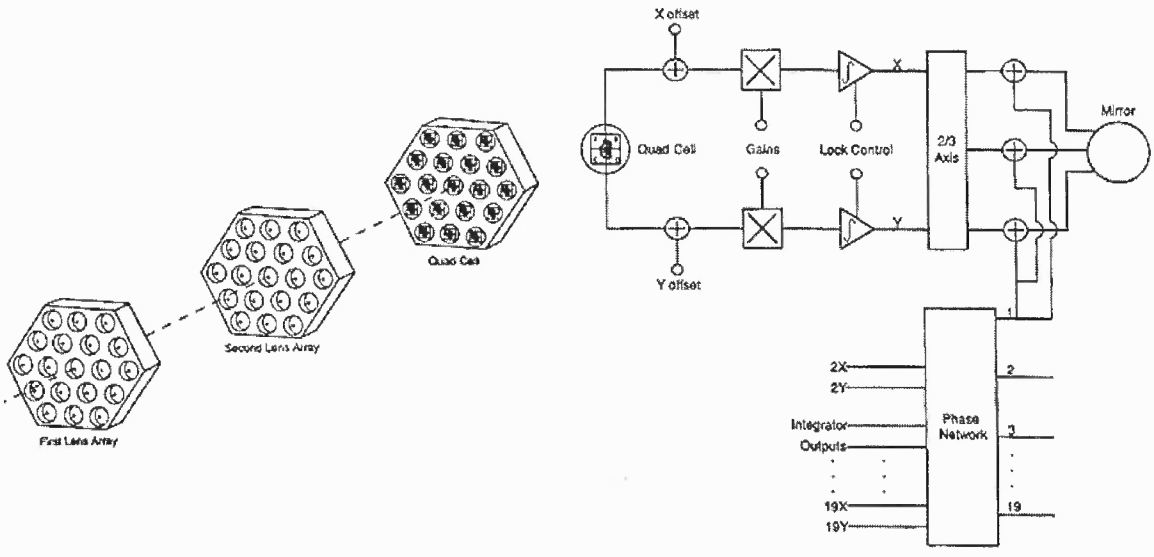

Figure 6.3 *Left.* Two lenslet arrays and their alignment with the 19 element quad cell. *Right.* Servo-loop for each of the 19 mirror segments. Both figures are from Acton and Smithson (1992)

a proof of concept for the first generation of modern AO. These basic principles of AO presented in Babcock (1953) have been expanded upon and are currently being used in AO design. The first solar AO system, developed almost forty years after Babcock's 1953 paper, is credited to John Hardy (Hardy, 1981). The system consisted of a 21-actuator deformable mirror and a shearing interferometer to detect and determine wavelength abberations.

The initial system, installed at NSO/SP for use with the 76-cm DST, used small-scale solar features such as pores as wave-front sensor targets. The system was successful, however showed only a modest improvement in image quality and worked over a relatively small area of the image. By 1991, D.S. Acton and R.C. Smith had developed a 19-segment adaptive mirror system also deployed at the DST. The system worked in the visible part of the spectrum, improved image resolution by approximately 9 times in 3″ seeing conditions, and provided correction over a 30″ diameter FOV (Acton and Smithson, 1992). To measure the wave-front error

a Shack-Hartman wave-front sensor (SHWFS) consisting of two 19-element lenslet arrays that image a high contrast solar feature onto an array of 19 quad cells. Each quad cell is linked to a single mirror segment in a servo-loop control configuration as shown in Figure 6.3. The quad cell is a photo-detector that is divided into four equal square regions. The feature of interest, a solar pore, is centered on the quad cell and an error signal is computed by taking the differences in intensity between different quadrants. Generating the error signals, Δx and Δy, is carried out by taking the difference between the left and right quadrant cells for Δx and the top and bottom quadrant cells for Δy. The signals are digitally integrated and used to drive the x and y-components of the mirror tilt. Figure 6.3 shows both the lenslet arrays, quad cell and servoloop block diagram.

The limiting factor of the system was that it used pores or other small-scale high contrast solar features to lock the system, greatly restricting the range of scientific applications. To overcome this limitation the quad cell based SHWFS was replaced with a correlating SHWFS. In Rimmele *et al.* (1999), a correlating SHWFS solar AO system is described. The principle of operation for the correlating SHWFS is described in Rimmele and Radick (1998). This type of AO system is currently in use at the DST and subsequently has been successfully built and implemented at BBSO Denker *et al.* (2007). The system is very similar to the one presented in Acton and Smithson (1992), with one of the key differences being the use of a correlating SHWFS rather than the quadcell. A correlating SHWFS works by calculating the cross-correlation between a selected subaperture image (reference) and the remaining subaperture images. In the current DST and BBSO AO system, there are a total of 76 subaperture images. The expression for the cross-correlation function is given as

$$CC(\Delta_i) = \sum\sum I_M(\vec{x}) \times I_R(\vec{x} + \Delta_i), \tag{6.1}$$

where $I_R(\vec{x})$ is the reference subaperture image, selected based on it having the highest rms-contrast Rimmele and Radick (1998). $I_M(\vec{x})$ and Δ_i are the remaining

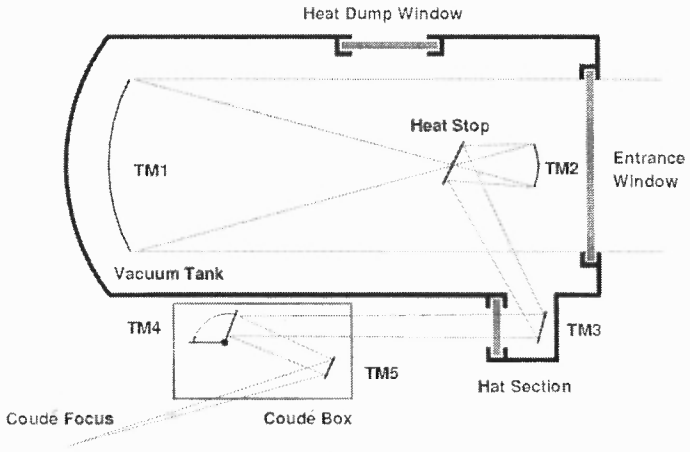

Figure 6.4 Optical schematic of the old BBSO 65-cm telescope (Denker *et al.*, 2007).

subaperture images and pixel shifts between $I_R(\vec{x})$ and $I_M(\vec{x})$, respectively. The maximum of the cross-correlation is located and the displacement necessary to correct the wave-front tilt is determined. The result of the cross-correlation yields a tilt vector map which is used in a modal reconstruction algorithm to determine the driving signals for the shape of the deformable mirror.

The correlating SHWFS system can be used with parallel processing, greatly expediting the computational time. The system can also use, under good seeing conditions, granulation to lock, expanding the range of scientific studies to include quiet Sun regions. In January 2004, under an National Science Foundation NSF grant, BBSO was outfitted with a high-order AO system built as part of a collaborative project with NSO/SP. The main components of this AO system, called *AO-76*, consist of a 76 subaperture SHWFS, a 97-actuator deformable mirror and a digital signal processor system (Denker *et al.*, 2007). The BBSO implementation of AO-76 as it was developed in 2004 is for the most part identical to the set-up at NSO/SP, the main difference being changes in optical design to accommodate the 65-cm BBSO telescope. Figure 6.4 shows an optical schematic of the old 65-cm telescope, which is a vacuum Gregory coudé reflecting telescope with an effective f-ratio of $f/50$. In the coudé focus the plate scale is $6.3''$ mm^{-1}. A 60 mm diameter pupil image is formed

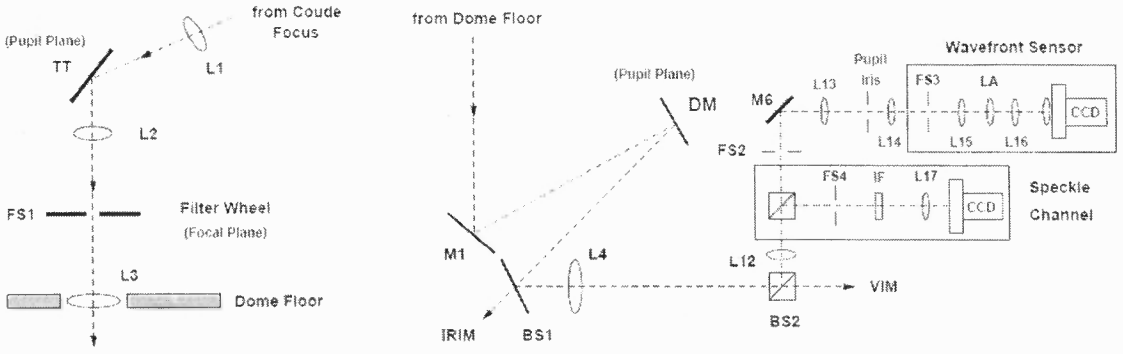

Figure 6.5 Optical schematic of the old 65-cm BBSO telescope in the panel on the left. On the right is the layout of the light path from the coudé focus to the dome floor (Denker *et al.*, 2007).

near a folding mirror (TM3) by a 0.23 m focal length elliptical secondary mirror. The optical support structure of the 65-cm telescope is such that the support truss for the elliptical secondary is close enough to the entrance window of that is casts a sharp shadow in the pupil image. The coudé optics consist of two flat mirrors (TM4 and TM5). These two folding mirrors serve to reflect the light down the right ascension axis of the telescope providing a stationary image for post-focus instrumentation. Modification to the existing coudé optics was necessary to resolve a persistent pupil wobble issue that was resulting in an unstable beam, unsuitable for the AO system.

The problem was resolved by replacing the existing TM4 and TM5 mirrors and mounting the fixed mirror TM5 to a actuator so that it could be dynamically adjusted for the pupil wander. Figure 6.5 shows an optical schematic of the light path from the coudé focus of the old 65 cm telescope down through the dome floor to the AO system and other post focus instrumentation located in BBSO's coudé laboratory. The left most panel of Figure 6.5 shows the light path from the coudé box to a lens (L1) that reimages the light to form the second pupil image of the system on to a tip-tilt mirror (TT). Lens L2 images the Sun at the filter wheel position where there are slots for the targets, grids, pinhole and adjustable iris. Lens L3 forms a third pupil

on the deformable mirror (DM). The infrared portion of the beam is sent to IRIM by means of a dichroic beam splitter (BS1). A 10/90 beam splitter (BS2) directs the smaller fraction of the light to the speckle channel and wave-front sensing optics. The remaining light is sent to the post-focus instrument VIM described in more detail in Chapter 7. The speckle channel is responsible for taking the high cadence speckle images that are subsequently used in the SMI post-facto image restoration. A 50/50 beam splitter serves to send equal portions of light to the speckle channel and the correlating SHWFS. The 76-element lenslet ($f \sim 24$ mm) array is placed in the pupil plane and is responsible for imaging the given portion of solar surface onto the CCD. The CCD camera used in the correlating SHWFS set-up is a custom-built 1280×1024 pixel CMOS camera with a 400 μs read-out time and an acquisition rate of ~ 2500 frames s^{-1}.

Like the DST AO system mentioned above, BBSO's AO-76 uses a two part control system to link the WFS and the deformable mirror. The first part consists of a real-time processor based on a parallel architecture and the second a graphical user interface allowing the user to customize AO operations, such as the allotted number of pixels used per subaperture on the CCD. The real-time processing unit computes both Δx and Δy with subpixel accuracy using the cross-correlation function given above in Equation 6.6. The wave-front reconstruction is accomplished via a board of 40 off-the-shelf Digital Signal Processor (DSP) units. Each DSP unit is responsible for processing two subaperture images whose sizes can be selected as 16×16 or 20×20 pixels.

The success of AO-76 at BBSO has been documented by the high quality of solar images produced throughout numerous observing runs. It is by that measure that AO-76 is the impetus for the development of a new AO system for NST. For NST the AO system will need to successfully operate over the NST's principal observing wavelength range from 0.4 μm in the visible to 1.7 μm in the infrared. The system

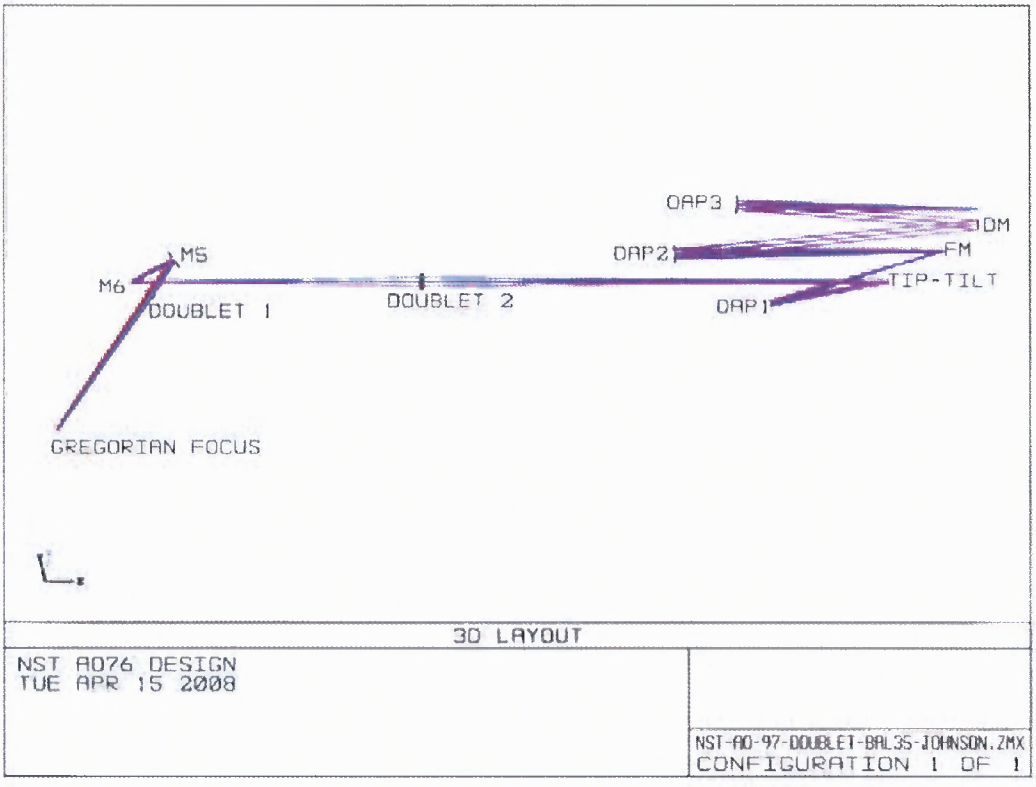

Figure 6.6 Optical layout for AO-76 for NST. Figure courtesy of Nicolas Gorceix, BBSO optical engineer.

will be based on the architecture of AO-76, however plans to upgrade the system to include higher order corrections over a larger area are in development. Figure 6.6 shows the optical layout that will integrate AO-76 with NST. The design will utilize off-the-shelf optical components and was developed in an effort to minimize chromatic abberations. Mirrors M5 and M6 are both flat folding mirrors that will feed light from the Gregorian focus of the telescope. The two refractive elements of the design are the two doublet lenses (doublet 1 and doublet 2), that serve to relay light to the tip-tilt mirror. Mirrors OAP 1-3 are off-axis powered mirrors and DM is the 97-actuator deformable mirror. Currently, collaborative plans between NJIT, NSO/SP and Kiepenheuer-Institut fr Sonnenphysik KIS are in development to build a 300

degree-of-freedom AO system called AO-308, based on the AO-76 architecture, for the NST. The plan is two part: the first being the design and implementation of AO-308 and the second is to include a Multi-Conjugate Adaptive Optics (MCAO) system into the operation of NST. MCAO corrects over a larger area than traditional AO. With an NST FOV of 180″ diameter, AO correction over a larger area will be necessary to optimize observations.

6.4 Frame Selection

Frame selection (Scharmer *et al.*, 2002) is a technique that is used to select an image based on a given set of criteria. The criterium is usually the rms-contrast of the image and this method is used quite often in solar broad-band observations. In Denker *et al.* (2005), high-spatial resolution images were obtained using frame selection in combination with AO and SMI. Frame selection works by taking short-exposure images with a high speed camera and selecting the images that contain a solar feature of choice with the highest rms-contrast. In the case of quiet Sun observations, such as those presented in Chapter 8, the contrast of granulation is used in the frame selection algorithm. To illustrate the implementation of frame selection for this section reference is made to the set of solar observations presented in Denker *et al.* (2005). For this set solar active region NOAA 10486 was observed using two distinct channels.

In the first channel data was acquired in the near-infrared ($\lambda = 1,560 \pm 5$ nm) with a 1024 × 1024 pixel CMOS camera. The second channel or 'speckle channel' was observed in the green continuum using a 1024 × 1024 pixel high-speed CCD camera. The images used in the frame selection algorithm were taken using the speckle channel. From 15:28 to 17:28 UT, 102 sequences consisting of 100 short-exposure (4 ms) images each were taken. The 100 short-exposure images were selected from an initial set of 200 based on the granular rms-contrast of a small

region in the FOV. The set of more than 10,000 short-exposure images were then used in SMI to further enhance the image quality. An example of one of the frame-selected images is shown in the central panel of Figure 6.1. The image shown in Figure 6.1 is the one with the highest granular rms-contrast out of the 200 images taken in that sequence. The representation of the frame selection method presented in Denker *et al.* (2005) can be executed in real-time. In Denker *et al.* (2001b), the methodology for a near-real-time image processing technique is presented. The process boasts image reconstruction of 1024×1024 pixel images with a 1-minute cadence. For the set of observations presented in Denker *et al.* (2005) and in Chapter 8, the data were saved on the hard-drive of the speckle PC and subsequently transferred to a DLT tape drive.

6.5 Speckle Masking Imaging

SMI is a post-facto image restoration method that can be applied to sequences of short-exposure time-series of the Sun. Used with AO, this method further enhances the ability to beat the seeing limit and approach the diffraction limit of the telescope. SMI and image restoration in general is only valid for a portion of the total image. This portion, called the *isoplanatic patch*, is the region over which the wavefront abberations are constant within the seeing correlation time-scale. The size of the isoplanatic patch varies depending on the wavelength ($\sim \lambda^{6/5}$). For observations in the visible portion of the spectrum a typical patch size is on the order of $5''$, whereas in the infrared it is around $20''$ (Stix, Stix, 1989). The exposure time for each image should be less than the time scale of the atmospheric refractive index fluctuations. These fluctuations occur on timescales of a few tens of milliseconds, a short exposure time of 5–10 ms is sufficient and well with in the range of acceptable values. Furthermore the time between two sequences has to be shorter than the evolution time scale of solar photospheric fine structure. The SMI process starts

out with standard data calibration such as applying the flat field and average dark images to the data set. After preprocessing the data a reference image is selected from within the sequence. It is selected based on the highest value of the granular rms-contrast. This image is then used to remove the image displacement from all of the other images within that sequence. Differential image motion is removed in a similar manner but this time the displacement is corrected for image files with sizes of the isoplanatic patch. The aligned images are then used in the SMI method. The goal is to separately reconstruct the Fourier phase and amplitude for the set of images, bring them together in the Fourier domain, apply an amplitude correction taking into account the seeing conditions, and then use the inverse Fourier Transform to generate the reconstructed image. The method begins with the Fourier transform representation of the imaging equation given as

$$F(\mathbf{q}) = F_0(\mathbf{q})S(\mathbf{q}), \tag{6.2}$$

where the bold letter $\mathbf{q}$ indicates a two-dimensional spatial frequency, F and F_0 are the observed and the object Fourier transformed intensity distributions, respectively. The index i refers to the number of images in the sequence. Taking the absolute values of each side and dividing by $\langle|S(\mathbf{q})|^2\rangle$ yeilds,

$$|F_0(\mathbf{q})|^2 = \frac{\langle|F_i(\mathbf{q})|^2\rangle}{\langle|S(\mathbf{q})|^2\rangle}, \tag{6.3}$$

an expression for the Fourier transform of the objects intensity Labeyrie (1970). This is often referred to as the *power spectrum* of the object. Here $\langle$ and $\rangle$ represent an ensemble average. The numerator is the average power spectrum of Fourier transformed images and the denominator is the *speckle transfer function* (STF). Assuming a Kolmogorov spectrum for the atmospheric turbulence, Korff (1973) obtained an asymptotic closed form solution for representing the short-exposure transfer function. This expression is only a function of the Fried parameter r_0. To determine the Fried parameter the spectral ratio technique is used. This method includes all

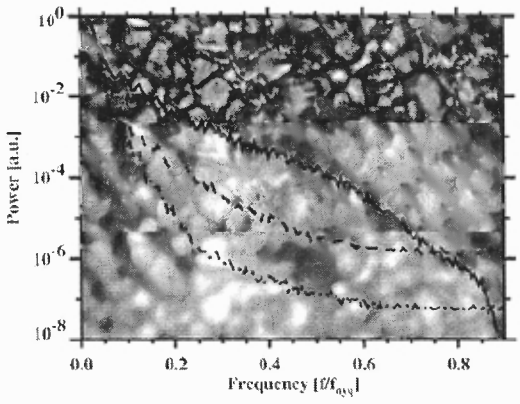

Figure 6.7 Power spectra ordered from highest to lowest for a speckle reconstruction, short and long-exposure image (Denker *et al.*, 2005).

contributions to the seeing from all layers of the turbulent Earth atmosphere and is presented in von der Luehe (1984). The spectral ratio is defined as

$$\varepsilon(\mathbf{q}) = \frac{|\langle F_i(\mathbf{q})\rangle|^2}{\langle |F_i(\mathbf{q})|^2\rangle} = \frac{|F_0(\mathbf{q})|^2}{|F_0(\mathbf{q})|^2} \frac{|\langle S_i(\mathbf{q})\rangle|^2}{\langle |S_i(\mathbf{q})|^2\rangle}, \tag{6.4}$$

where $|\langle S_i(\mathbf{q})\rangle|^2$ and $\langle |S_i(\mathbf{q})|^2\rangle$ are the long and short-exposure transfer functions. The two-dimensional spatial frequency $\mathbf{q}$ is normalized with respect to the system cutoff frequency f_c as

$$\mathbf{q} = (\, q_1 q_2 \,) = \frac{1}{f_c} \overline{f}, \tag{6.5}$$

where f_c is defined as $f_c = D/\lambda R$ von der Luehe (1984). The cutoff frequency is determined by the observing wavelength λ, the telescope diameter D and the focal length R of the system. The long-exposure transfer function is presented in Fried (1966) and like the short-exposure transfer function, it is a function only of r_0. The Fried parameter is measured by comparing the observed spectral ratios with theoretically tabulated values of the long and short-exposure STFs. The choice of a good STF is paramount for accurate, photometrically reliable results. In general, the theoretical STFs presented in Fried (1966) and Korff (1973) were derived without AO correction accounted for. Taking into account the diminishing contrast with distance from the AO lock-point a semi-empirical STF is used. The photometric accuracy of

speckle interferometry using AO-corrected data is presented in Wöger *et al.* (2008). The average power spectra generated from 90 one-dimensional intensity scans across a purely granular region is shown in Figure 6.7. All three of the spectra plotted in Figure 6.7 were normalized to the Nyquist frequency. Figure 6.7 clearly shows that the solid line, representing the power spectrum of a speckle reconstruction, is the highest. This is followed by the short-exposure image shown as the dashed line. With the proper choice of the STF in hand, the Fourier amplitudes can be calculated using Equation 6.3. To complete the image restoration, the Fourier phases need to be calculated. Two methods are commonly used to determine the Fourier phases. In Knox and Thompson (1974) a method to recover the phase information of an object by averaging the cross spectrum is presented for the one-dimensional case. The method can be easily extended for a 2-D image. The Knox-Thompson method involves computing the autocorrelation of Equation 6.2. The average cross spectrum as presented is given as

$$\langle F(\mathbf{q_1})F^*(\mathbf{q_2})\rangle = F_0(\mathbf{q_1})F_0^*(\mathbf{q_2})\langle S(\mathbf{q_1})S^*(\mathbf{q_2})\rangle. \tag{6.6}$$

For $\mathbf{q_1} - \mathbf{q_2} < r_0/\lambda$, the phase of the average observed cross spectrum is in close approximation with the phase of the average object cross spectrum. By measuring the complex correlation between points in the Fourier transform of the image, a phase difference between the points under consideration can be determined. Using iterative methods, the phase of the object is constructed by summing the phase differences between the origin and a point in the Fourier transformed image plane. After combining the object Fourier phases and amplitudes (described by the method above), an inverse Fourier transform gives the reconstructed image. SMI is an extension of the method presented in Knox and Thompson (1974). However, it uses a triple correlation or bispectrum to recover the phase information Stix (1989). The method used in Denker *et al.* (2006) and in the reconstructions shown in Chapter 8 of this thesis are based on the SMI method presented in Weigelt (1977). The triple correlation is

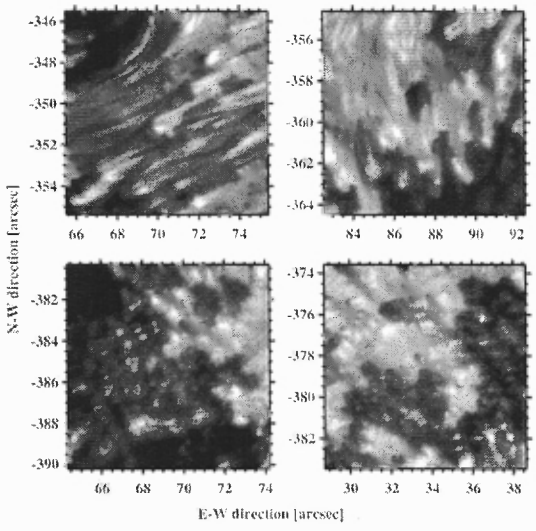

Figure 6.8 SMI clearly enhances the fine structure contents technique visible in this image, e.g., small-scale penumbral structures (Denker *et al.*, 2005).

defined as

$$\langle F^3(\mathbf{q_1}, \mathbf{q_2})\rangle = F_0^3(\mathbf{q_1}, \mathbf{q_2})\langle S(\mathbf{q_1})S^*(\mathbf{q_2})\rangle, \tag{6.7}$$

where $\langle S(\mathbf{q_1})S^*(\mathbf{q_2})\rangle$ is the speckle masking transfer function (SMTF). Once the phase information is known along with the Fourier amplitudes, the inverse Fourier transform yields a mosaic of reconstructed subimages. Figure 6.8 shows the result of applying the SMI technique.

CHAPTER 7

THE VISIBLE-LIGHT IMAGING MAGNETOGRAPH

7.1 Overview

As one of the dedicated post-focus instruments for NST, VIM will provide high temporal and spatial resolution two-dimensional spectro-polarimetric measurements of the Sun. More precise and accurate measurements of photospheric and chromospheric vector flows and vector magnetic fields are thus possible, making the study of solar activity more complete. In this chapter a summary of VIM is presented as well as a calibration method for the set of two LCVRs used for VIM's operation as a spectropolarimeter. A detailed account of observing runs made throughout 2006 and 2007 will be covered as well as the presentation of the first Stokes-V Magnetograms acquired using VIM. Along with the aforementioned material, an outline of future improvements for VIM are discussed.

7.2 Introduction

A two-dimensional imaging spectropolarimeter is an instrument that operates as a spectrograph with the addition of a set of polarization analyzing optics such as LCVRs. In general, this type of instrument is capable of imaging the Sun at various wavelengths for every spatial point in the FOV. Combined with AO and post-facto image reconstruction techniques as discussed in Chapter 6, detailed studies of small-scale magnetic features on the Sun are made possible. Unlike traditional line-of-sight measurements this two-dimensional imaging spectropolarimeter is capable of measuring both the magnitude and direction of the magnetic field. As a consequence of these types of measurements, important physical parameters on the Sun can be determined. One such example is the electric current density. By measuring the

photospheric vector flow and magnetic field one can calculate, using the induction equation, the vertical component of the electric current density. In Li *et al.* (2009), measurement of the transverse magnetic field strength $B_\perp$, the vertical field component B_z, and the magnetic azimuth ϕ were made using the Imaging Vector Magnetograph (IVM) at Mees Solar Observatory (MSO) in Haleakala, Maui. Using a modified form of Amperes law, the absolute value of the vertical component of the current density $|J_z|$ was calculated for active region NOAA 10030. Knowledge of the current density is important because it is thought to play a role in coronal heating (Mickey *et al.*, 1996), one of the major unsolved mysteries of solar physics. Many other examples can be given that support the role for this class of instrument as a permanent installation at current and future solar observatories.

NST will employ the use of two two-dimensional imaging spectropolarimeters, i.e. IRIM and VIM. These instruments will be used as dedicated post-focus instruments replacing the successful Digital Vector Magnetogram (DVM) previously in use at BBSO Spirock *et al.* (2001). VIM will cover the visible portion of the solar spectrum from 550 nm to 700 nm. IRIM will provide infra-red coverage from 1.0 μm to 1.6 μm. Both VIM and IRIM can operate in one of four distinct observing modes (Denker *et al.*, 2003a): pure spectrometer mode (full spectral profile, absence of polarization optics), polarimeter mode (full spectral profile including polarization optics), Doppler mode (selected spectral profile points) and photometric mode (single spectral point). For the purposes of this chapter, only the spectrometer mode and polarimeter mode configurations for VIM are considered. In the following sections, a summary of VIM is provided with emphasis on the calibration method for the two LCVRs. Also presented are the first polarimetric observations using VIM from a 2007 July 15 observing run at NSO/SP.

7.3 Instrument Description

VIM is a Fábry-Perot based filtergraph instrument whose design is geared towards the study of active region dynamics. VIM is first described in Denker *et al.* (2003a) along with its counterpart IRIM. Figure 7.1 shows the optical set-up of VIM and IRIM for the BBSO 65 cm vacuum telescope. VIM is shown in Figure 7.1 configured in its spectrometer mode. Light from the coudé box is directed to lens (L1) which forms a pupil image at the tip-tilt mirror (TT). Lens L2 images the Sun at the filter wheel position which is located at the field stop (FS). The filter wheel has slots for the targets, grids, pinhole and an adjustable iris. Lens L3 forms a second pupil image on the deformable mirror (DM). The infrared portion of the beam is sent to IRIM by means of a dichroic beam splitter (BS1). A 10/90 beam splitter (BS2) directs the smaller fraction of the light to the speckle channel and wave-front sensing optics, the larger fraction of light is sent to VIM. The interference pre-filter (IPF) and Fabry-Pérot interferometer (FPI) serve as the wavelength selecting optical elements of VIM. The detector is a 1024×1024 pixel high-speed charge-coupled device (CCD) camera manufactured by DALSA corporation. It has a 12-bit digitization with a pixel size of $14 \times 14 \mu$m.

The camera can operate in full resolution mode (1k×1k pixel) with a maximum frame rate of 60 frames per second. With 2×2 binning selected, the maximum frame rate is 110 frames per second. An external signal converter was developed to allow for the ability to set custom exposure times and synchronize exposures with the FPI. The signal converter is connected to the camera's TTL trigger-in port. Exposure times between 3 ms and 850 ms can be set through the control computer. The control computer sends a signal to the signal converter box which generates a TTL signal that is sent to the camera. Table 7.1 lists VIM's characteristic parameters as they were for the 65 cm BBSO vacuum reflector now replaced by NST. VIM uses a ICOS FPI system that consists of a ET70FS-1024 series II fused silica etalon with CS100

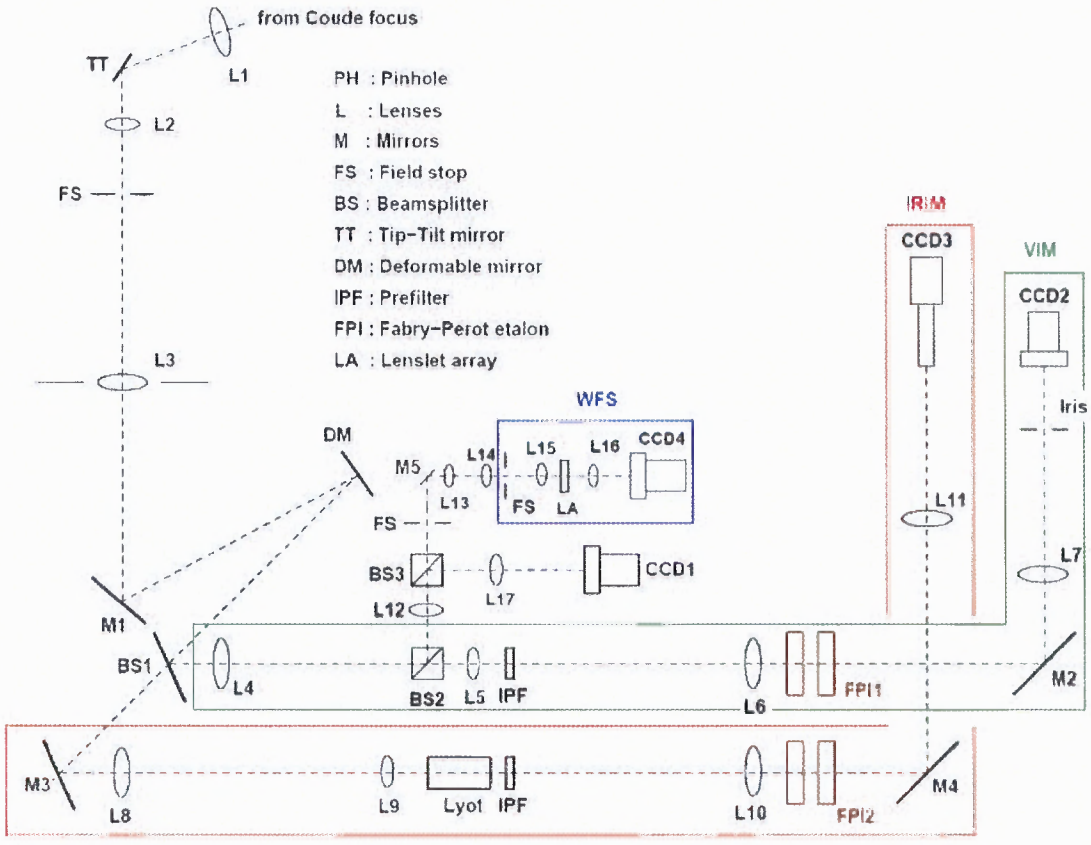

Figure 7.1 Schematic layout showing the optical set-up of VIM and IRIM in the coudé laboratory of the 65 cm vacuum reflector at BBSO.

controllers that adjust FPI plate separation. VIM has an image scale s whose value is close to the telescope's diffraction limit. For NST the value of s will be smaller than that of the 65 cm $\sim 0.065''$, which is close to the NST diffraction limit. The FPI is capable of scanning through a given line profile with a wavelength step $\delta\lambda$ of 1.2 pm. It has a spectral resolution $\lambda/\delta\lambda$ of 87,500. With a plate separation d of 496 μm, the free spectral range $\Delta\lambda$ of the etalon is 0.40 nm at 589.0 nm. In general, the small free spectral range of FPI etalons requires selective prefiltering. To do so, a two-cavity interference filter (IF) with a full-width-at-half-maximum (FWHM) of 0.3 nm is used. The wavelengths of the three prefilters are given in Table 7.1 for the Fe I, Na D_2 and Hα spectral lines. The reflectivity R and absorptivity A of the FPI are 0.968 and 3.4×10^{-3}, respectively. Aside from alignment, VIM's operation is fully controllable

Table 7.1 VIM Characteristic Parameters

Parameter	Design Specifications
FOV	$80'' \times 80''$
Image Scale s	$0.18''\text{pixel}^{-1}$
Diffraction Limit α	$0.19''$ @ 589.0 nm
Plate Separation d	496 μm
Reflectivity R	0.968
Absorption A	3.4×10^{-3}
Wavelength Increment $\delta\lambda$	1.2 pm
Resolving Power $\lambda/\delta\lambda$	87,500
Operating Wavelength λ	Fe I 630.15 nm
	Na D_2 589.00 nm
	Hα 656.28 nm
Free Spectral Range $\Delta\lambda$	0.40 nm

through the FPI control computer. Figure 7.2 is a schematic of the VIM control system. A Graphical User Interface (GUI) allows the user to set various parameters. The software is responsible for synchronizing the following tasks: telescope control computer communication, data acquisition and storage, etalon cavity spacing, and polarization optics control.

7.4 Etalon Characteristics

In Denker and Tritschler (2005) the characterization and the method for calibrating the ET70FS-1024 series II etalon is presented. An important factor that needs to be considered when working with an FPI based instrument is plate parallelism. The method for maintaining and quantifying the plate parallelism is explained using Zernike polynomials to quantify etalon plate characteristics and establish the relationship between the piezo-electric actuator voltage and parallelism of the plates. The technique was developed and implemented on the ICOS etalon used in VIM. Figure 7.3 shows a sketch of the optical set-up used in the experiment. A 20 mW

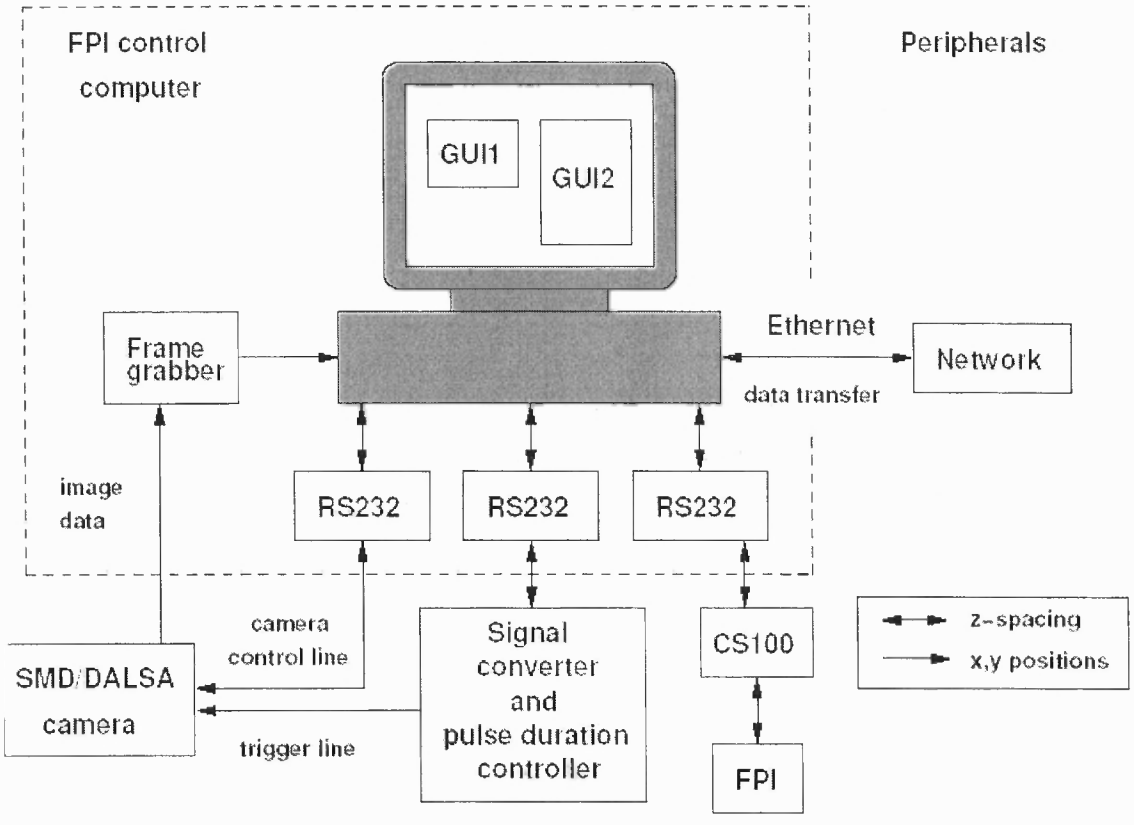

Figure 7.2 Block diagram of the control system for VIM (Figure 1 in Shumko *et al.* (2005).

(632.8 nm) HeNe laser is used as a light source. A 10 μm pinhole spatial filter (SF) and 90 mm diameter custom acromat (A1) collimate the beam passing through the etalon plates. A second acromat (A2) images the first etalon plate on a Dalsa CCD camera. The etalon plates are coated for the wavelength range from 510 nm to 660 nm with a plate flatness of $\lambda/136$. In general FPIs provide excellent light throughput with transmission between 70% to 90% making them a good fit for photon-starved polarimetric measurements. Figure 7.4, shows the etalon coating curves as a function of wavelength. The maximum or peak transmission $\tau_{\max}$ of the etalon is computed using the absorption A and reflectivity R curves using,

$$\tau_{\max} = \left[1 - \frac{A}{1-R}\right]^2. \tag{7.1}$$

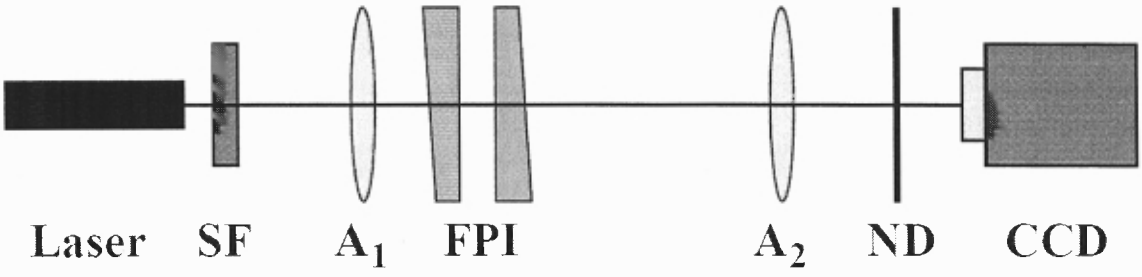

Figure 7.3 Optical set-up for determining the plate parallelism for the VIM's Fabry-Pérot etalon (Figure 2 in Denker and Tritschler (2005)).

The ratio of the separation of adjacent transmission maxima to the half-width, known as the finesse of the etalon F, is calculated using manufacturer specifications with the expression,

$$F = \left[\frac{(1-R)^2}{R\pi^2} + \frac{4}{p^2}\right]^{-\frac{1}{2}}, \tag{7.2}$$

where p is the plate flatness error specified by the manufacturer. In Figure 7.5 the transmission profile for the etalon is shown on the left for 4000 wavelength steps. The free spectral range (distance between neighboring transmission maxima) of 0.40 nm is clearly visible. A free spectral range of 0.40 nm corresponds to 670±1 steps. The full scanning range of the Fábry-Perot etalon is 2.47 nm corresponding to six transmission peaks. On the right hand side of Figure 7.5 is a close up of a single transmission peak. The peak is approximately 9.6±0.4 steps FWHM. The orange curve overlay is a best fit, represented with an Airy function given as

$$\frac{I}{I_0} = \tau_{\max}\left[1 + \frac{(4R)}{(1-R)^2}\sin^2\frac{\delta}{2}\right]^{-1}. \tag{7.3}$$

For an angle of incidence θ and the path difference between two successive beam fractions $\Delta = 2\,n\,d\,\cos(\theta)$, the phase difference δ is

$$\delta = \frac{4\,\pi\,n\,d\,\cos\,\theta}{\lambda}. \tag{7.4}$$

The measurements used to align the etalon plates are done by determining the root-mean-square (rms) variation of the wavelength shift $\lambda_{0,\mathrm{rms}}$. To do this, a range of 0.05 V was manually scanned on the CS100 controller for both the x- and y-direction.

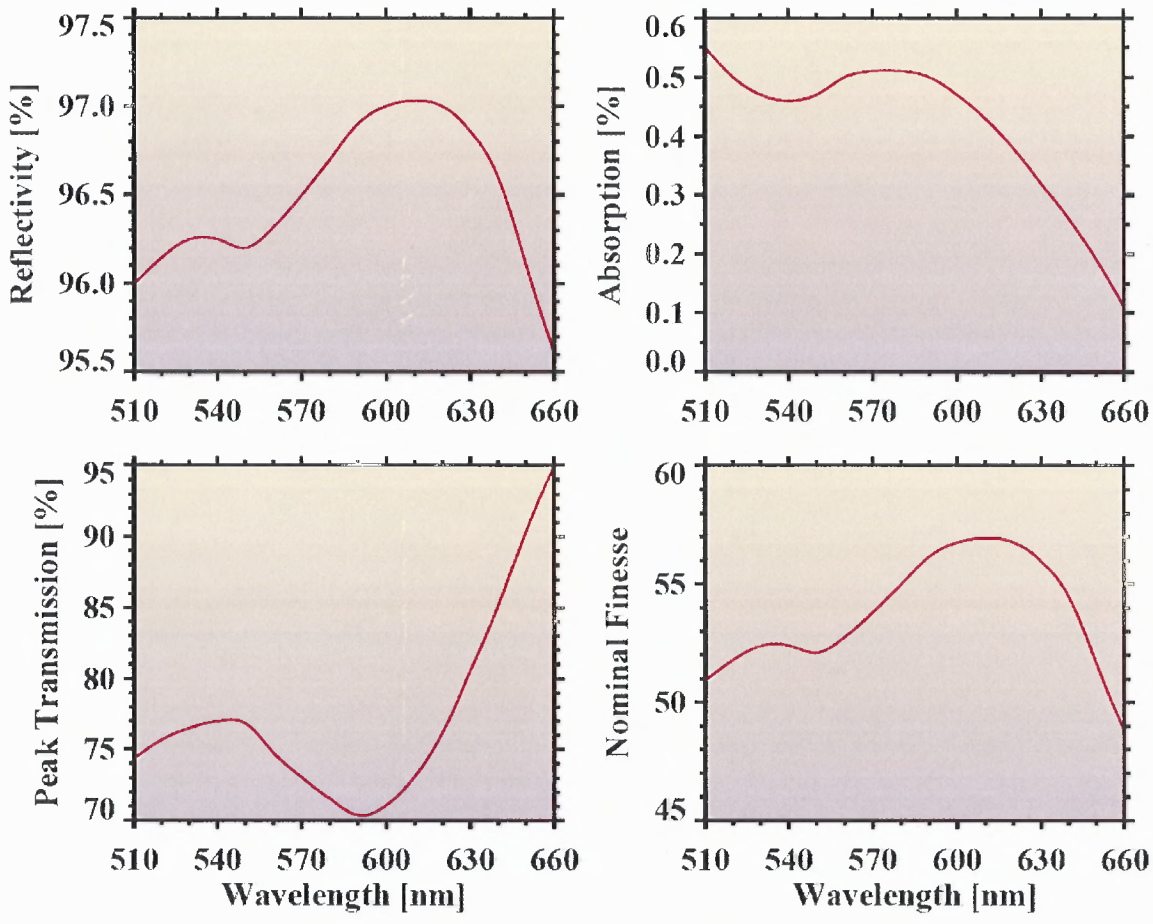

Figure 7.4 The wavelength dependence for the etalon coating is shown. Clockwise from top left: Reflectivity R), Absorption A, Peak Transmission $\tau_{\max}$, and the Nominal Finesse F (Figure 1 in Denker and Tritschler (2005)).

Fifteen data points were taken and a 2^{nd} order polynomial fit was used. Figure 7.6 shows the results of the measurement. The minimum λ_0 for both the x- and y-direction was determined, giving the voltage settings for parallel etalon plates. In an effort to refine the aforementioned method and create the prospect for an automated plate parallelism calibration procedure, Zernike polynomials are used to model the characteristics of the etalon plates. Measurements of the wavelength shift across the FOV are made and the coefficients of a Zernike polynomial fit are determined.

The Zernike coefficients corresponding to the tip-tilt of the etalon plates are compared with the x- and y-voltages corresponding to a minimum $\lambda_{0,\text{rms}}$ and an analytical relationship is formed. Figure 7.7 shows the results of the coefficient

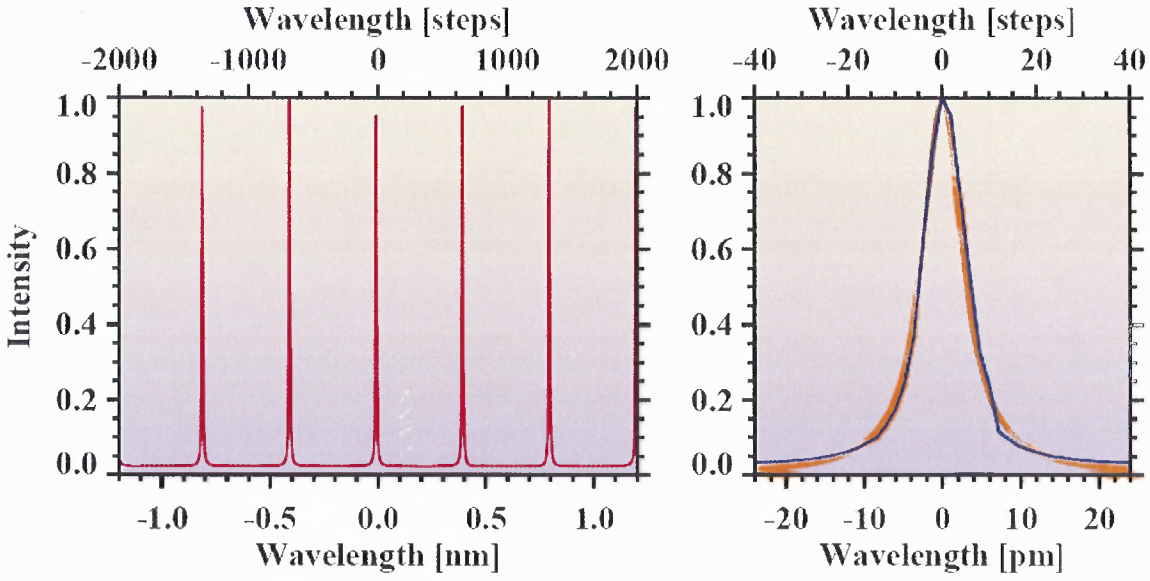

Figure 7.5 The transmission curve for the etalon is shown on the left. The distance between neighboring peaks is the free spectral range $\Delta\lambda$. A close up of a single transmission peak (blue curve) is shown on the right, the orange curve is a best fit Airy function (Figure 3 in Denker and Tritschler (2005)).

comparison described above. The result of this method is that the calibration curves shown in Figure 7.6 need only be measured once and subsequently the correct voltage settings can be determined from just one wavelength shift measurement.

7.5 Pre-Filter Calibration

On 2006 June 3, VIM was packed and transported from the coudé optical laboratory at BBSO to NSO/SP, NM. The objective of the observing run was two-fold: to calibrate the three IFs using the horizontal spectrograph (HST) at the DST, and to make observations using VIM configured in spectrometer mode. In this section, the filter calibration method is discussed. The method was applied to all three interference prefilters used for VIM. The goal is to determine the average transmission profiles for all three of VIM's IFs.

A simplified optical setup for the three-filter calibration is shown in Figure 7.8. A 780 mm lens (L1) serves to feed light into the HST. The slit of HST is set to

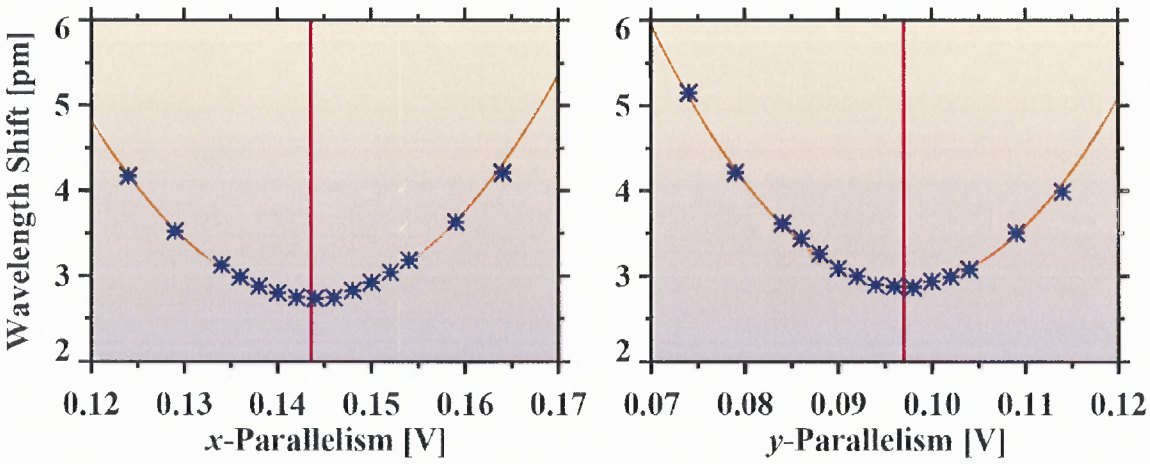

Figure 7.6 Plot of the rms-wavelength shift as a function of piezo-electric voltage. In each plot, blue asterisks mark the measurement points and the orange curve is a polynomial fit. The voltage minimum is marked by the vertical red line (Figure 6 in Denker and Tritschler (2005)).

a width of 40 μm. Inside of the HST (not shown) light is folded 90° by a 75 mm mirror through a collimating lens. Collimated light exits the HST and is dispersed using the NSO-316 (316 lines/mm) Milton Roy blazed grating. Lenses L2, L3 and L4 are 3 m focal length lenses that focus the three relevant dispersed orders from the grating onto three cameras (CCD1, CCD2 and CCD3). The interference filters (IF1, IF2 and IF3) are mounted on precision 360° rotation stages. A shutter (S) is placed in front of each of the filter mounts and a neutral density filter (not shown) is placed behind each to avoid image saturation.

Currently, VIM can operate using one of three two-cavity Barr Associates narrow-band IFs: Hα (IF1) 656.33±0.3 nm, Fe I (IF2) 630.25±0.3 nm and Na D_2 (IF3) 588.99±0.3 nm. The DST was pointed at a quiet Sun region located at disk center. The seeing conditions were good throughout the observing run and the AO system was turned off. The filters were rotated on the stage in increments of 0.5° and for each rotation a set of 64 exposures was taken. Also for each rotation setting a set of 64 flat field exposures was taken. After all the filter rotations were made a set of 64 dark field exposures were taken.

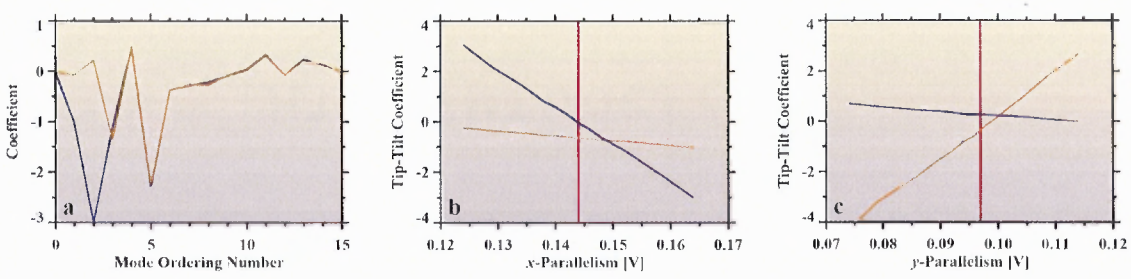

Figure 7.7 Zernike polynomial fit for aligned and misaligned etalon plates represented by the orange and blue curves respectively (*left*). (*middle* and *right*) Tip-tilt coefficients as a function of the applied x and y piezo-electric voltage in orange and blue, respectively (Figure 10 in Denker and Tritschler (2005)).

This process was repeated for all three of the IFs. Figure 7.9a through Figure 7.9f show the spectra and transmission profiles for the Fe I 630.15 nm interference filter with a rotation angles from 0.0° to +2.5° in increments of 0.5°. Flat field and dark frame corrections were applied to the data. The flat field image contains spectral information. To obtain a uniform flat field each row of pixels in the flat field image was divided by the computed average spectrum. Figure 7.10 shows the normalized transmission intensity for the average observed spectrum (thin black curve), the solar atlas spectrum (light gray curve), and the transmission profile for the 0.0° position of the Fe I 630.15 nm interference filter.

The transmission profile for the Fe I 630.15 nm interference filter at various rotation angles is shown in Figure 7.11. As the filter is shifted from normal incidence to oblique, the spectrum is shifted towards the blue. This is evident in Figure 7.11 as the incidence angle increases from normal (0.0°, red) to oblique (+3.5°, blue). After the pre-filter calibration, VIM was configured to operate in spectrometer mode and observations of both quiet Sun and active region were carried out for the remainder of the observing run. A summary and analysis of the observations of a quiet Sun region near disk center are presented in Chapter 8.

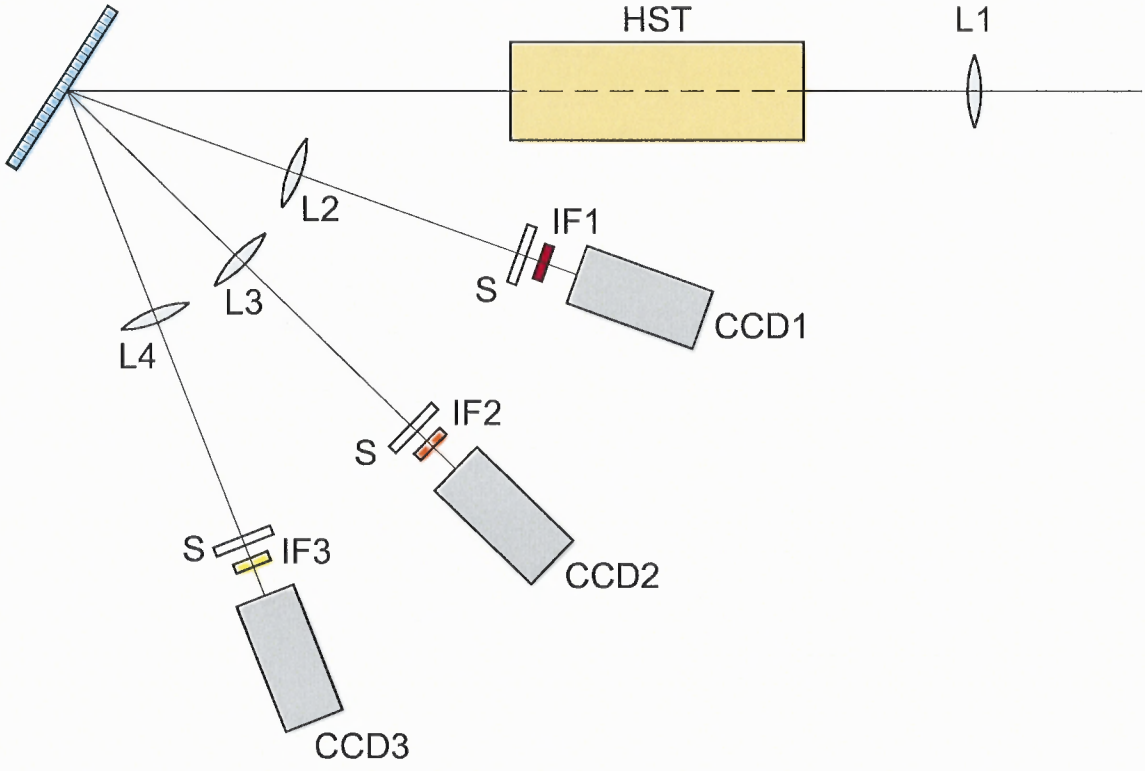

Figure 7.8 Schematic of the optical set-up for the filter calibration experiment carried out on 2006 June 3, at NSO/SP.

7.6 Polarization Optics and Calibration

The components and configuration of the polarization module used in VIM is based on BBSO's DVMG presented in Spirock *et al.* (2001). The DVMG system used two LCVRs to measure polarization and obtain the full Stokes vector. The DVMG calibration technique employed the use of a $\lambda/4$ wave plate at the Ca I 610.3 nm absorption line. To apply this technique for VIM required the purchase of three new $\lambda/4$ wave plates, one for each of VIM's interference filters. Therefore, the substantial cost and feasibility was too prohibitive and a new calibration method was needed. The calibration method used for the Telecentric Etalon Solar Spectrometer (TESOS) full Stokes polarimeter proved to be a good model on which to base our a calibration technique for VIM on (Kentischer *et al.*, 1998). The method uses only narrow-band interference filters to map the wavelength dependence of the LCVRs so no new components were necessary. In this section the calibration procedure for the LCVRs

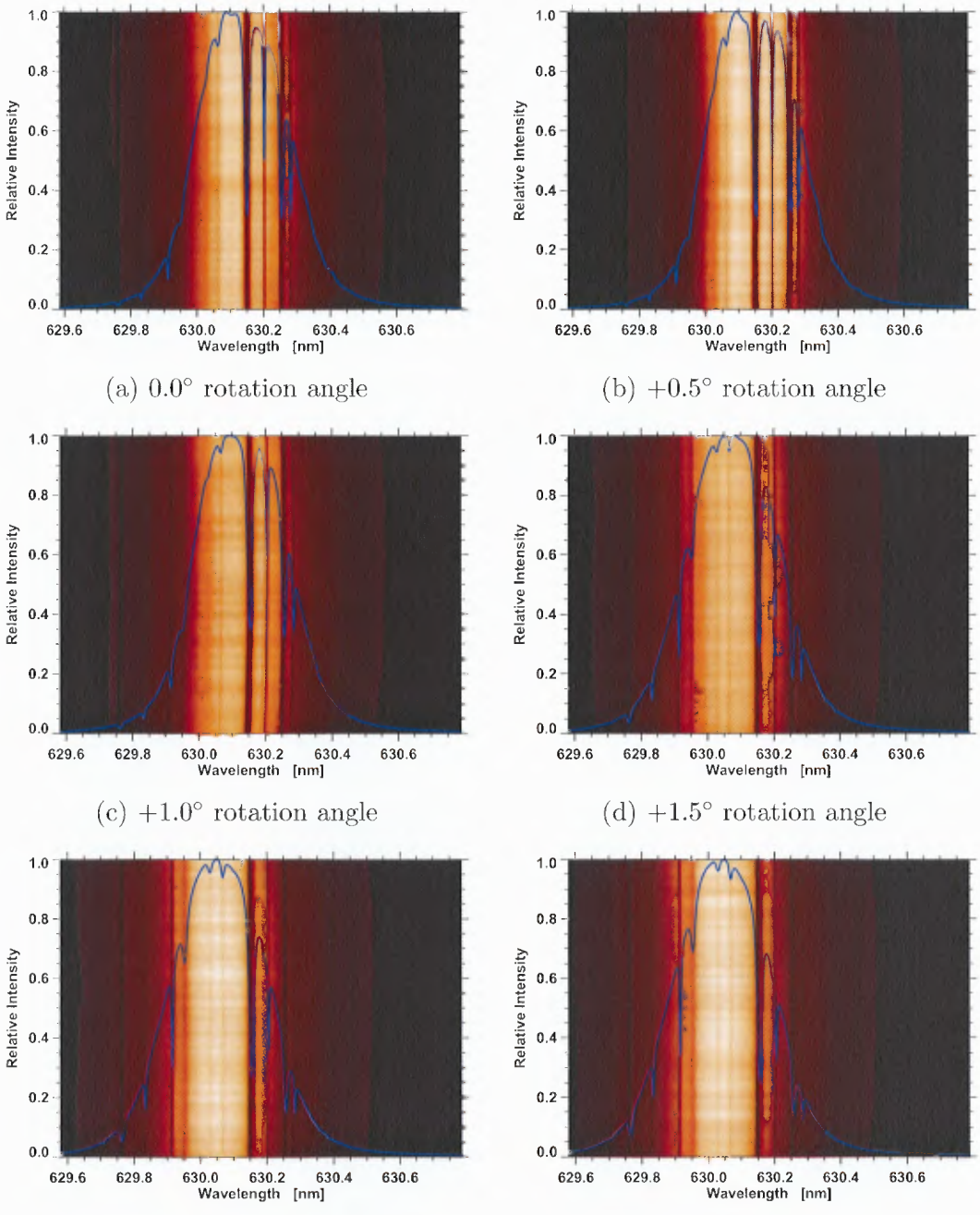

(a) 0.0° rotation angle

(b) +0.5° rotation angle

(c) +1.0° rotation angle

(d) +1.5° rotation angle

(e) +2.0° rotation angle

(f) +2.5° rotation angle

Figure 7.9 Fe I 630.15 nm IF transmission profiles and spectra.

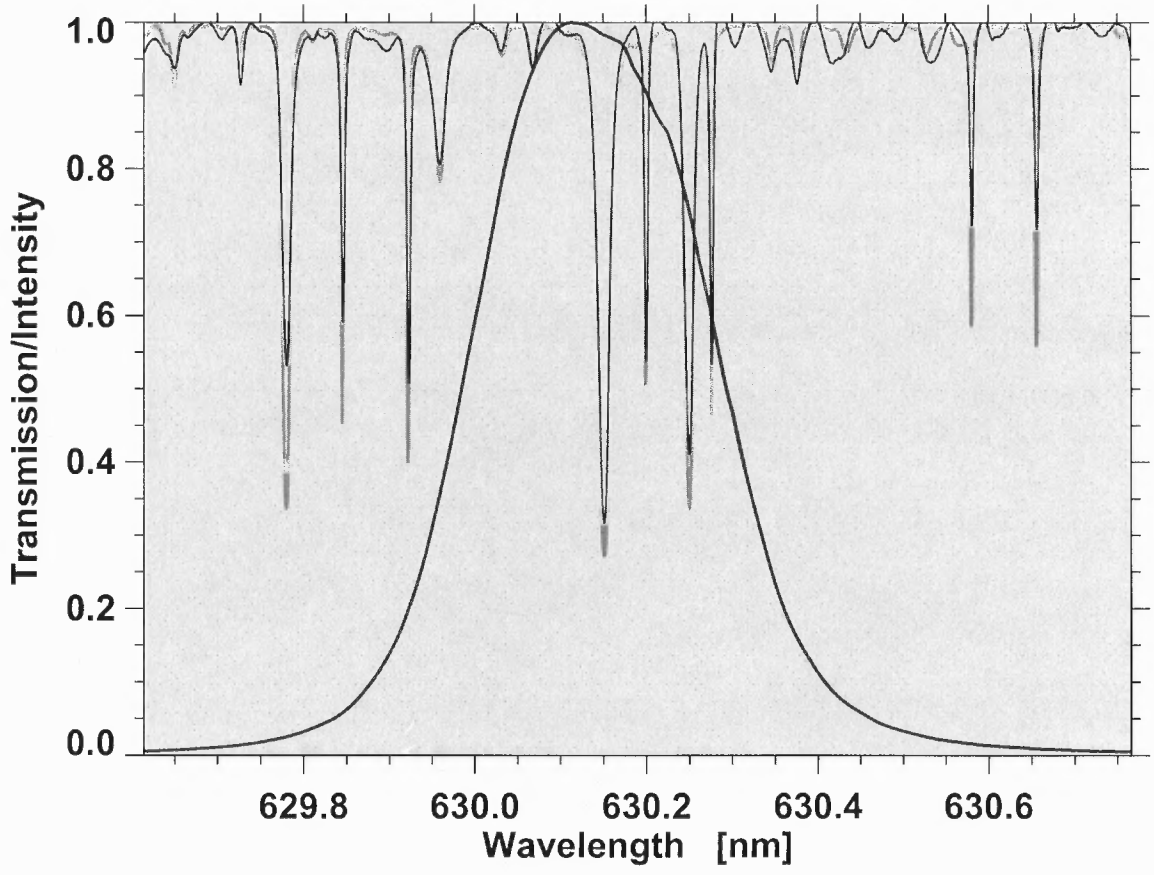

Figure 7.10 Plot of the transmission intensity as a function of wavelength for the average observed spectrum (thin black curve), solar atlas spectrum (light gray curve), and transmission profile (thick black curve) for the Fe I interference filter at 0.0°.

is presented. The derivation of the retardance as a function of voltage for the two LCVRs at each of the three wavelength settings, Fe I 630.3 nm, Na D_2 589.0 nm and Hα 656.3 nm is determined. Figure 7.12 shows the optical set-up used in calibrating the LCVR.

The light source for the calibration is a StockerYale ImageLite Model 20 halogen lamp outfitted with a 12 mm diameter fiber bundle (FB). Care was taken to center the FB on the optical axis of the set-up. Light from the FB is collimated using two acromat lenses L_1 and L_2, with focal lengths $f_1 = 450$ mm and $f_2 = 450$ mm, respectively. A field stop FS serves to minimize stray light caused by the relatively large exit angle of the FB. A 95/5 beam splitter BS directs 95% of the light through

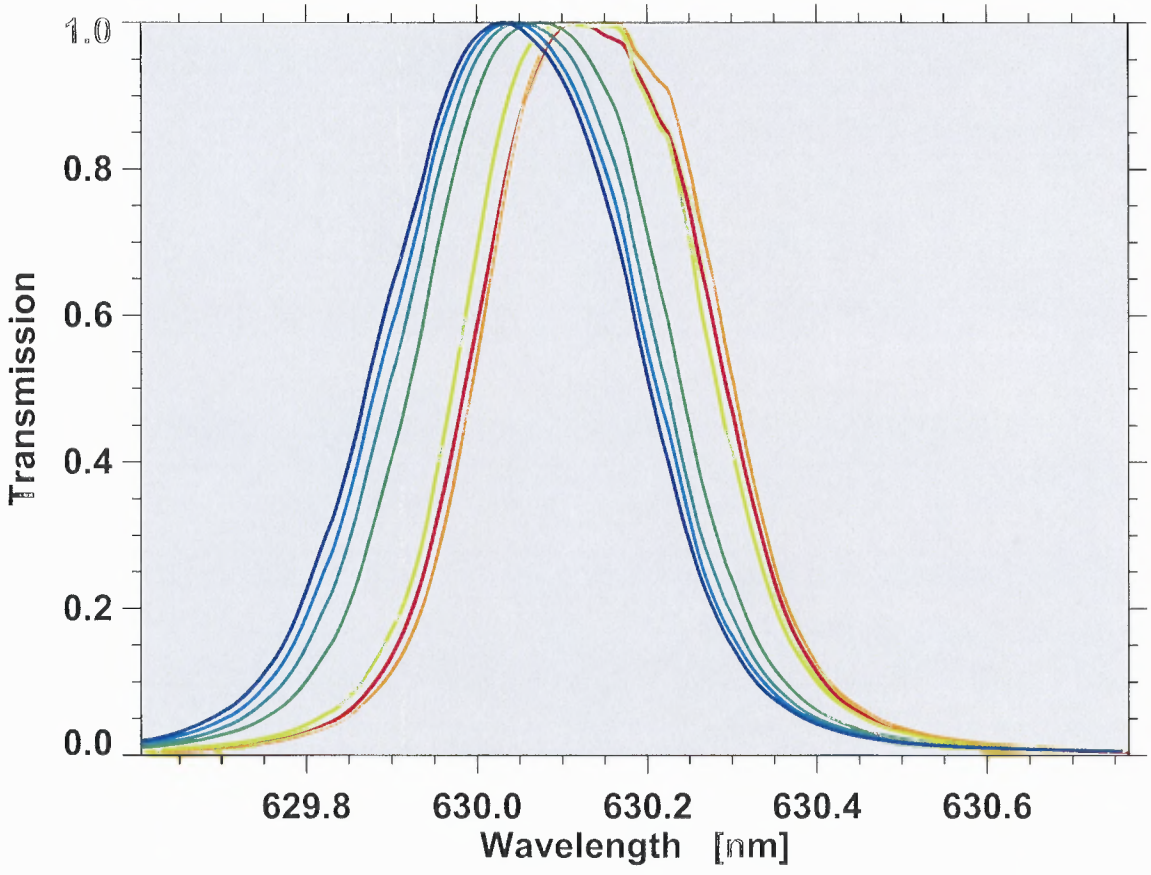

Figure 7.11 Transmission profiles for the Fe I filter at various angles from 0.0° (red) to +3.5° (blue) in increments of 0.5°.

the calibration channel and 5% through the reference channel. A folding mirror M reflects the 5% towards the CCD and a third acromat L_3 with a focal length $f_3 = 500$ mm focuses the light onto a portion of the CCD chip. To keep the intensities of the calibration and reference channel the same at the CCD, a neutral density filter (NG) with 2 mm was inserted in the reference channel. The calibration channel consists of the two linear polarizers (LP) and the LCVR. The two linear polarizers are Meadowlark Optics Model No. DPM-200-VIS1 coated to work in the 400–700 nm range. The two LCVRs are Meadowlark Optics Model No. LRC-300-VIS also for use in the 400–700 nm range. The calibration procedure is done for one LCVR at a time. Both the LCVRs and LPs were mounted on rotation stages with 2° and 1° resolution respectively. The operating temperature of both LCVRs is 30°

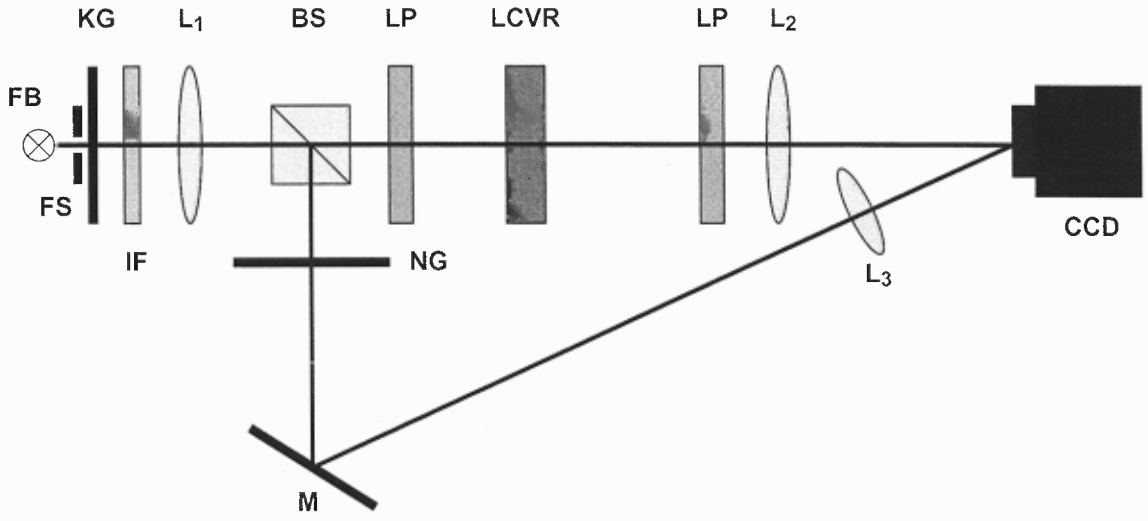

Figure 7.12 Optical set-up to the test the polarization optics. FB: fiber optics bundle, FS: field stop, KG: UV-blocker, BS: 95/5%, L_1 through L_3: acromats, LP: linear polarizer, LCVR: liquid crystal variable retarder, M: folding mirror, NG: neutral density filter, and CCD: CCD camera.

C. Meadowlark Optics liquid crystal digital interface D1040-TSO controllers and power supplies for the temperature stabilization were used throughout the course of the measurement. The detector is a 1024×1024 pixel Dalsa 1M30 CCD set for operation in a 2×2 binning mode producing 512×512 pixel images. The calibration data were obtained from 2006 August 17, through 2006 August 21, in the coudé optical laboratory at BBSO. Figure 7.13 shows a typical image frame acquired. The large circular region in the center of the image is the intensity of the fiber bundle. The "blotchy" looking intensity pattern is a result of both individual fiber quality and uneven illumination by the source. The smaller, relatively uniform, bright circular region in the lower right corner of Figure 7.13 is the reference channel. The masked brighter region in both the calibration and reference channel images is the area used to compute the mean intensities.

7.6.1 Light Source Intensity Variations

An issue when calibrating LCVRs is finding a stable light source. Intensity variations of less than 10^{-3} are needed to carry out calibration measurements. However, light

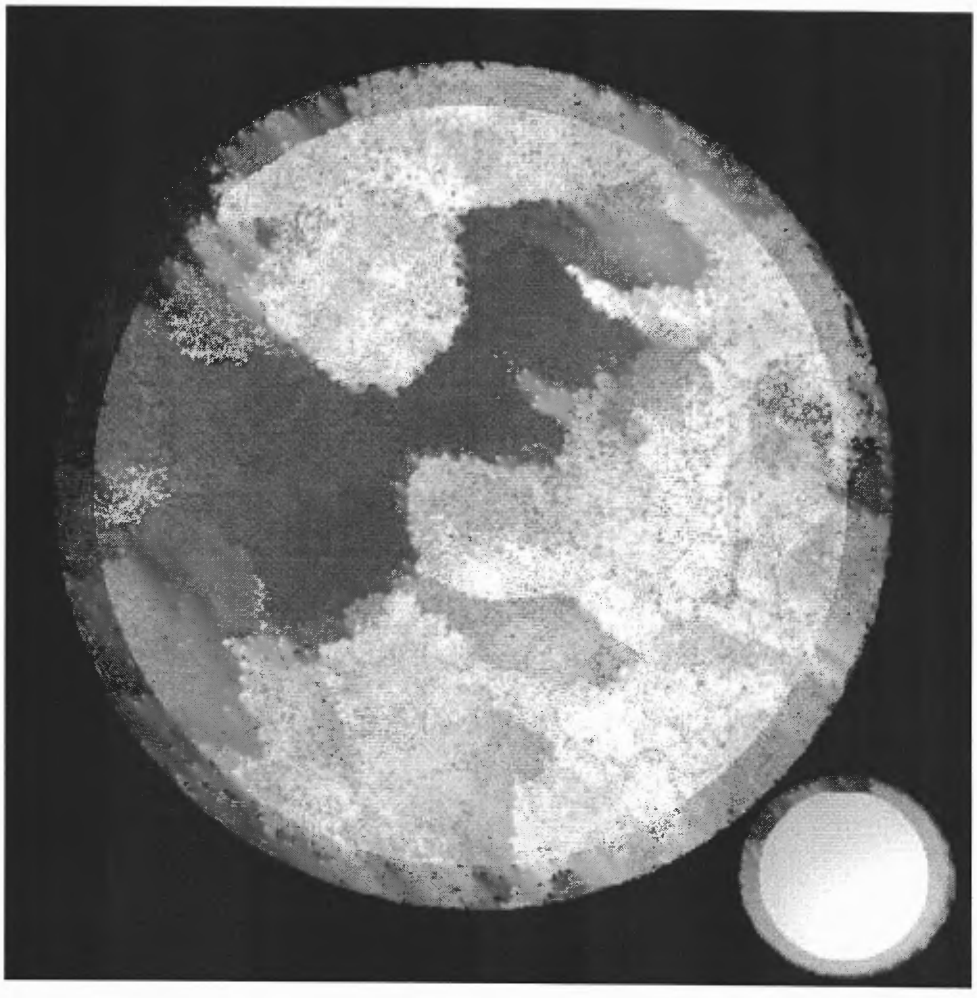

Figure 7.13 Image of the reference channel (lower right corner) and fiber optics bundle. The outlined brighter regions in both the fiber and the reference were used to compute the mean intensities.

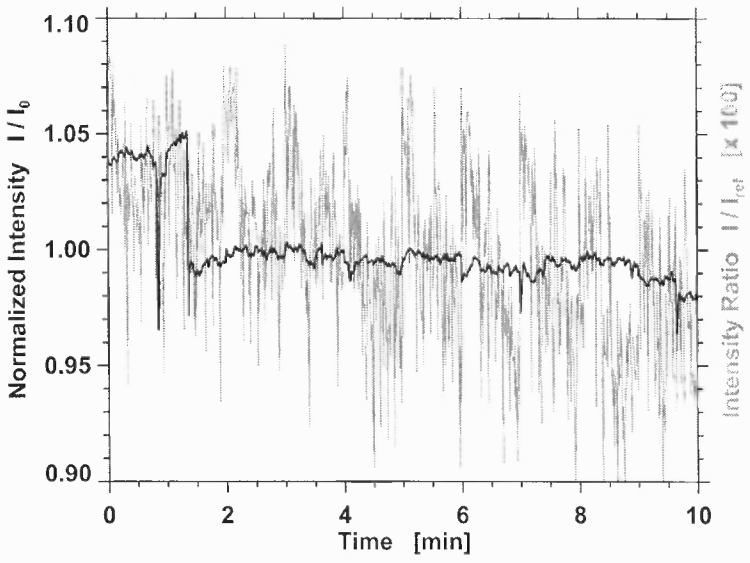

Figure 7.14 The intensity variation of the StockerYale light source over a 10-minute period. The black curve shows the uncorrected light level variations and the gray curve shows the corrected. The gray curve has been multiplied by 100 to show sufficient detail.

sources with this criteria are difficult to find. To illustrate the effect, Figure 7.14 shows the intensity variation over a 10 minute period for the light source. The variations are likely a result of the varying output of the power grid as well as the power consuming devices such as the air conditioning system. Visible in Figure 7.14 is a jump exceeding 5% as well as smaller 1% variations.

To minimize the effect of the light source intensity variations, a differential measurement technique is implemented, by directing 5% of the light via BS along a reference channel and imaging it on a small portion of the CCD. Reference measurements are then made simultaneously and with the same exposure times as the calibration. The result of this differential measurement is shown by the gray curve in Figure 7.14, where the stability has improved by a factor of 50. To show the variation more clearly the intensity ratio I/I_0 was multiplied by a factor of 100. The corrected signal has no discernable jumps, exhibiting only a small drift during the

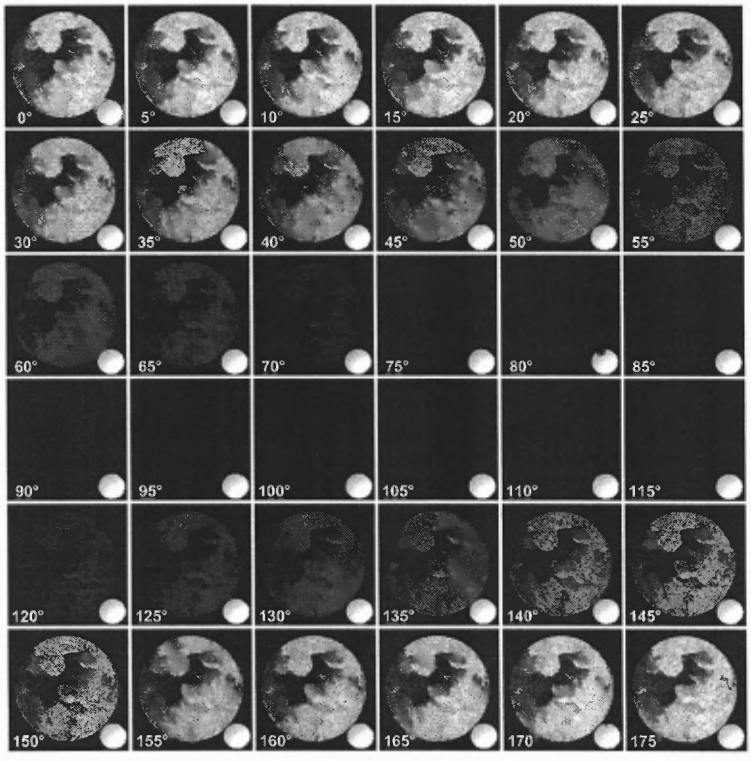

Figure 7.15 Average intensity as a function of the rotation angle of the second linear polarizer.

10-minute period. The improvement in stability of the intensity signal of the light source is sufficient to proceed with determining the retardance measurement.

7.6.2 Calibration Procedure

At least one hour before making any measurement, the light source and LCVRs heaters were powered on. The first step of the calibration procedure is to determine the parallel ($\parallel$) and perpendicular ($\perp$) alignment of the two LPs. The first polarizer remains at a fixed position with its axis in the vertical position (clearly marked by the manufacturer) while the second is turned from 0° to 180° in increments of 5°. An 80 ms exposure time was used for all measurements performed in the calibration. This exposure time is similar to the one that VIM uses during regular operation. At each position 10 images are taken and averaged. Figure 7.15 shows the scanning

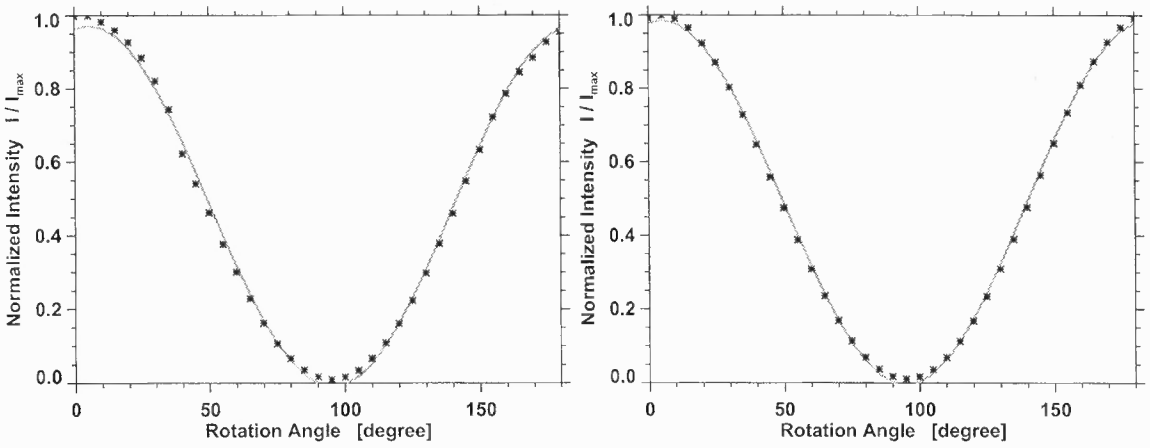

Figure 7.16 Transmission vs. rotation angle between two linear polarizers with out light level corrections (*left*) and with (*right*). The transmission maximum in the uncorrected case (*left*) occurs at 5.3° ($\chi^2 = 3.2 \times 10^{-4}$). For the corrected case (*right*) the maximum occurs at 4.9° ($\chi^2 = 1.2 \times 10^{-4}$).

sequence for the second linear polarizer. The transmission profile for the averaged intensities as a function of rotation angle is shown in Figure 7.16. A non-linear least squares sine-function fit

$$I(\theta) = a_0 \sin(2\theta + a_1) + a_2, \tag{7.5}$$

with fitting parameters a_0, a_1, and a_2 is used to determine the parallel orientation angle $\theta_{\|} = 4.9°$. The fitting parameter a_1 is used to determine the value of $\theta_{\|}$ which is with respect to an arbitrary zero point for which the polarizers are parallel to each other. Figure 7.16 also illustrates the effect of making differential measurements, evident through visual inspection and the χ^2-statistics. The second part of the calibration procedure involves the alignment of the fast axis of the LCVR at a 45° angle with respect to the axis of the first linear polarizer. The polarizers are kept in the parallel position and the fast axis that is marked on the LCVR housing is aligned to the zero position. A range of ±10° is scanned in increments of 2° around the zero position. At each rotation position of the LCVR, 201 measurements are made at voltages from 0 V to 10 V in increments of 50 mV. At each position 10 frames are

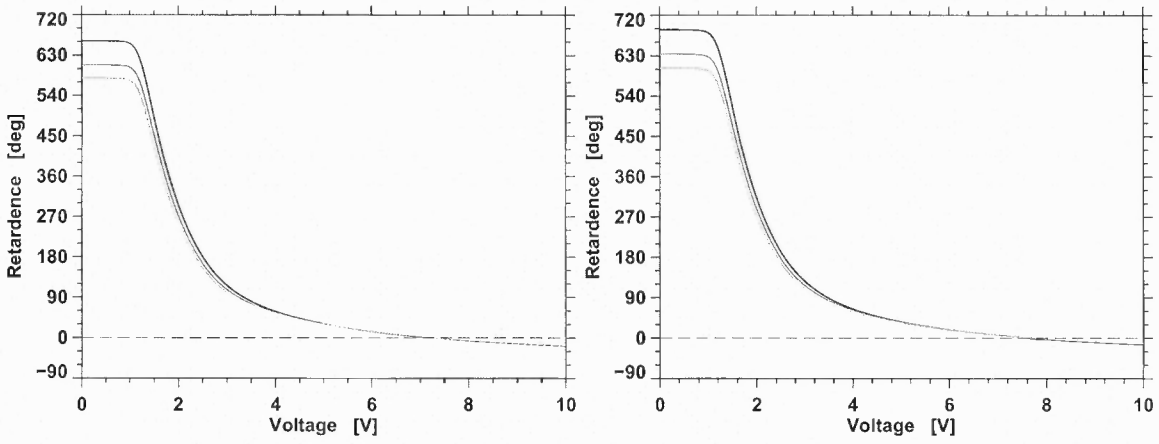

Figure 7.17 The retardance (deg) as a function of applied voltage (V) for Meadowlark Optics LCVR1 (left) and LCVR2 (right) measured with Fe I (gray), Na D_2 (black) and Hα (light gray) interference filters.

averaged. To ensure there was enough time for the LCVR to reach the retardance value, a 100 ms delay was introduced before changing the voltage.

The objective is to find the angle α that corresponds to a minimum in the $I_{\parallel}$ transmission profile. To determine α a parabola-fit was applied to the minima. The resulting α for both LCVR1 and LCVR2 is $\alpha_1 = 146°$ and $\alpha_2 = 304°$. With these values the set-up is aligned and the retardance measurements for all three IFs can be made. The expression for the retardance is

$$\delta = \arccos\left(\frac{I_{\parallel} - I_{\perp}}{I_{\parallel} + I_{\perp}}\right), \tag{7.6}$$

where $I_{\parallel}$ is the intensity of light as function of voltage for parallel linear polarizers and $I_{\perp}$ for perpendicular (crossed) linear polarizers. Figure 7.17 shows the retardance as a function of the applied voltage for Meadowlark Optics LCVR1 and LCVR2 measured with each of the Barr Associates narrow-band interference filters. The retardance as a function of applied voltage for the Fe I 630.25 nm filter is shown in gray, the Na D_2 588.99 nm in black and Hα 656.33 nm in light gray. With the retardances in hand the final step is to determine the voltage settings where the LCVRs act as a glass plate (0° and 360°), a $\lambda/4$ wave plate (90°), and a $\lambda/2$ wave plate (180°). The retardance curves were mapped to a equidistantly spaced grid with a resolution of

Table 7.2 Retardance Settings LCVR No. 1

Retardance	Voltage		
	Na D_2 588.99 nm	Fe I 630.25 nm	Hα 656.33 nm
360°	1794 mV	1714 mV	1665 mV
180°	2488 mV	2397 mV	2342 mV
90°	3321 mV	3216 mV	3147 mV
0°	7233 mV	7309 mV	7281 mV

Table 7.3 Retardance Settings LCVR No. 2

Retardance	Voltage		
	Na D_2 588.99 nm	Fe I 630.25 nm	Hα 656.33 nm
360°	1843 mV	1763 mV	1714 mV
180°	2559 mV	2468 mV	2410 mV
90°	3452 mV	3358 mV	3286 mV
0°	7582 mV	7790 mV	7750 mV

1 mV using linear interpolation and the respective retardance settings were read out. Table 7.2 lists the retardance voltages for LCVR1 and LCVR2.

7.7 Polarimetric Observations with VIM

With the polarization module for VIM calibrated by the end of summer 2006 and BBSO in the midst of upgrading the observatory dome for NST, VIM was packed up and transported to NSO/SP for a December 2006 observing run. The purpose was to obtain polarimetric measurements with VIM using the DST. The seeing conditions at Sacramento Peak throughout the winter months can be quite poor, and fluctuating light levels plagued all attempts at making sensitive polarimetric measurements. VIM was left at NSO/SP and a observing proposal was submitted and accepted for July 2007 at NSOSP. On 2007 July 15, the first successful polarimetric measurements were made with VIM. Figure 7.18 shows the optical set-up for the July 2007 NSO/SP observing run. A speckle channel was included in the set-up to

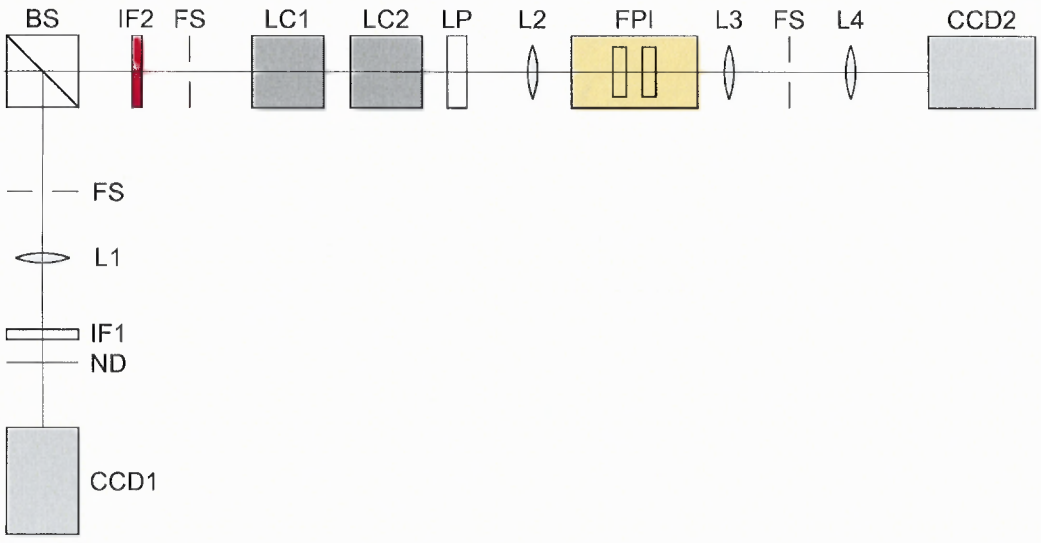

Figure 7.18 Optical set-up for July 2007 observing run. BS: 95/5% beam splitter, FS: field stop, ND: neutral density filter, L_1 through L_4: acromats, LP: linear polarizer, LC1, LC2: liquid crystal variable retarders, FPI: Fabry-Pérot Interferometer, IF1, IF2: narrow band interference filter, CCD1, CCD2: CCD cameras.

make simultaneous white light observations to be used later for speckle restoration. A 95/5% beam splitter (BS) is used to deliver 5% of the light to the speckle channel and the remainder to VIM. The Fe I 630.25 nm filter IF2 was used for the observations. The polarization module consisting of both liquid crystals LC1 and LC2, and a linear polarizer LP were placed after IF2. The Fabry-Pérot Interferometer FPI is mounted in a telecentric configuration using acromats (L2, L3, and L4). The objective was to measure a Stokes V/I signal. VIM was operated in the magnetograph mode, scanning only four wavelength points in the blue wing of the Fe I absorption line. An exposure time of 150 ms was used to make a total of 460 data sets (Stokes $I+V$ and $I-V$) with a cadence of 4.7 s.

The data was taken from 15:20 to 15:50 UT, spanning a time period of 30 min. A "rough estimate" of the Stokes V/I signal is shown in Figure 7.19 for a region of the Sun located at 6.9° S and 28.6° W. The term "rough estimate" refers to operating VIM in the "magnetograph mode", where only four wavelength points in the Fe I line wing are analyzed. The signal to noise ratio (S/N) was enhanced by averaging over

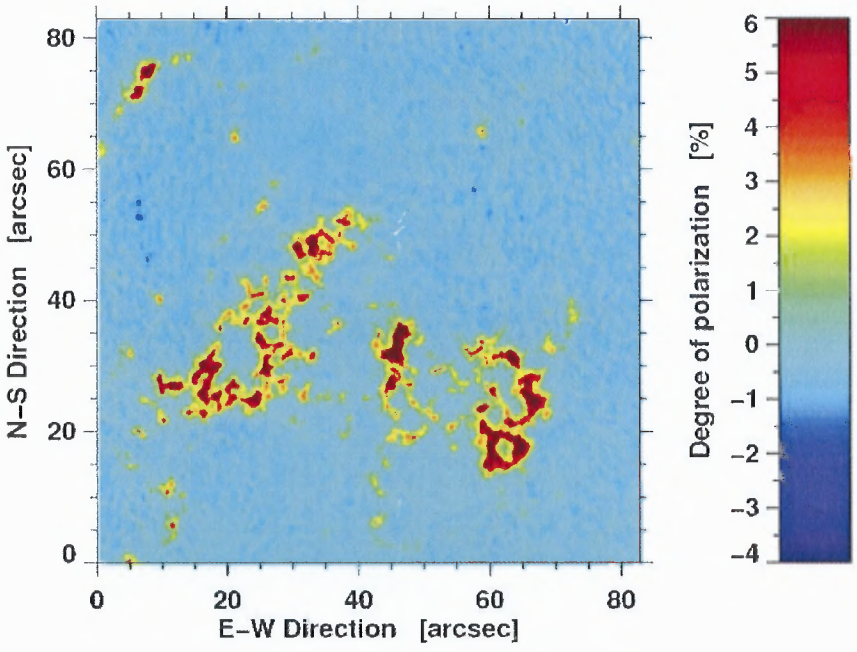

Figure 7.19 Stokes V/I in blue wing of Fe I 630.15 nm line.

a 2 minute time period . The results are promising, however further calibration is necessary. For instance, for a Fabry-Pérot etalon mounted in a telecentric configuration the central wavelength λ_0 is a function of the FOV. Figure 7.20 shows a map of the wavelength shift over the $80'' \times 80''$. A shift of 5.0 pm is measured which is on the order of VIMs bandpass at the Fe I line. The effects of the shift can be seen as artifacts at the east and west sides of the magnetogram in Figure 7.19.

7.8 Conclusion

In this chapter VIM is described as well as some of the more important calibration procedures that are necessary to implement when observing using VIM. The first calibration discussed is a procedure for determining and controlling the plate parallelism of the etalon. For the ICOS Fabry-Pérot etalon used by VIM, Denker and Tritschler (2005) measured a peak-to-valley wavelength shift of 12.9 pm at 632.8 nm across the central 50 mm of the FOV due to unparallel plates. To resolve the effect that plate parallelism has on both wavelength and finesse, Denker and Tritschler

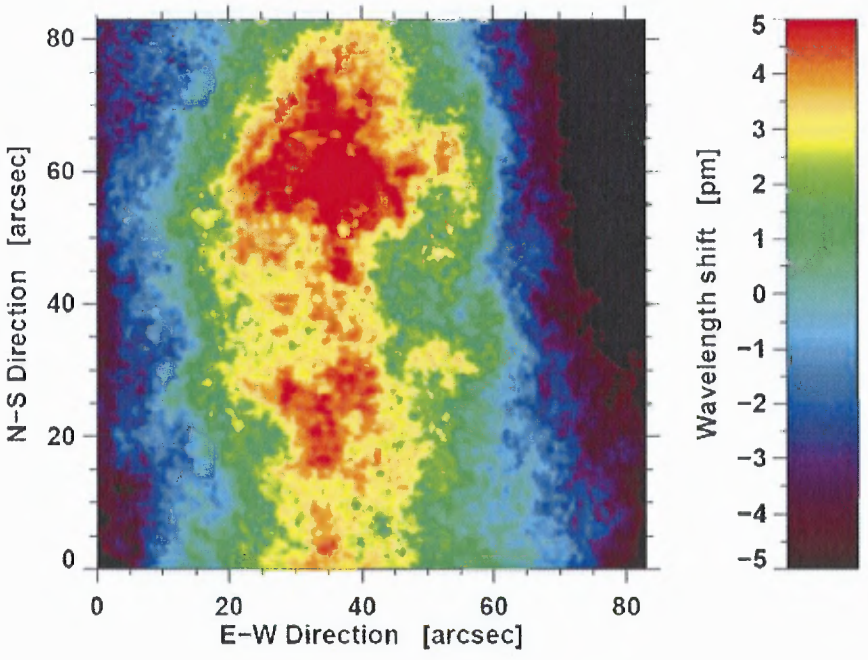

Figure 7.20 Central wavelength shift map of the Fabry-Pérot etalon.

(2005) presents a procedure that relates the coefficients of Zernike polynomials to the x and y voltages of the piezo-electric actuators that control plate separation. Along with plate parallelism, it is necessary to know the transmission profile of the IFs as a function of rotation angle in order to center the spectral line on the pass band of the filter. Using the HST at the DST the average transmission profile was determined for each of the three IFs for different rotation angles. It was found that as the filter is rotated from normal to oblique incidence, the spectrum is shifted towards the blue. The final calibration procedure that presented in this chapter is the measurement of the retardance vs. voltage curves for the two LCVRs used for VIMs operation as a spectropolarimeter.

The goals of modern, two-dimensional spectroscopic and polarimetric instruments are to provide observations of the Sun with high spatial, spectral and temporal resolution. These three conditions must be met to help further current understanding of feature morphology, heights of formation, and dynamics of small-scale magnetic fields in the solar atmosphere. VIM is a Fabry-Pérot based imaging magnetograph

instrument that possesses all of the aforementioned characteristics. The primary role of VIM as a dedicated post-focus instrument for NST will be the study of active region evolution and space-weather forecasting. However, it is equally well suited for quiet Sun observations such as the ones presented in Chapter 8. Successful observations using VIM have also been presented in Denker *et al.* (2008), where VIM was used in the spectrometer mode to study the characteristics of bright penumbral grains in an active region.

CHAPTER 8
QUIET SUN OBSERVATIONS OF THE CHROMOSPHERE

8.1 Overview

The quiet Sun shows a multitude of magnetic fine structures, in both the photosphere and chromosphere. To discern among different structural elements, observations with high spatial, spectral and temporal resolution are required. On 2006 June 11, near-simultaneous broad-band continuum (600 nm) and narrow-band spectroscopic (Hα λ656.28 nm and NaD_2 λ588.99 nm) data were acquired of a supergranular cell in a quiet region near Sun center using the Dunn Solar Telescope (DST) at the National Solar Observatory/Sacramento Peak (NSOSP). The time-series of broad-band continuum data were restored using the speckle masking technique (Weigelt, 1977) to achieve almost diffraction-limited resolution across the entire ($83'' \times 83''$) field-of-view. The narrow-band spectroscopic data were acquired using a Fabry-Pérot based two-dimensional imaging magnetograph instrument called the Visible-light Imaging Magnetograph (VIM). At the time these observations were made, the polarization module for VIM was in the process of being calibrated (see Chapter 7) and as a result the data presented here were acquired using VIM configured as a spectrometer.

In a first step the data sets and the reduction techniques used are described. The results of the broad-band and narrow-band data are then combined to study the dynamic upflow events that are observed to occur throughout the cell interior and boundaries. The results presented in Lee *et al.* (2000) are confirmed using the Hα data and an attempt to find a similar signature of these events in NaD_2 which is formed at a lower height in the solar atmosphere. While upflow events have been observed in Hα, this is the first time that a study has been made to identify upflow events in their early stages of development using NaD_2 observations.

8.2 Introduction

In this section the current model of the quiet solar atmosphere is reviewed, in an effort to set the stage for the observations that follow. By observing emission that originates from different altitudes in the Sun's atmosphere (i.e. 600 nm, Hα 656.28 nm and Na D_2 588.99 nm) one may develop a better sense of how the atmosphere is composed vertically. In a simple sense, it may be said that different solar absorption lines are *formed* at different heights in the Suns atmosphere. The formation heights of various solar atmospheric absorption lines are determined by both observations and numerical radiative-transfer-based simulations of which there are many (an excellent review of solar atmospheric models is presented in Rutten 2007). Based on current atmospheric models, one cannot accurately say that the line in which the Sun is observed at is formed at a precise altitude in the atmosphere. A safer assumption would be to prescribe a range of heights to the formation of a given absorption line. This is the assumption that is taken throughout the rest of the chapter particularly when upflow events and the heights in the solar atmosphere at which they potentially exist are discussed.

The quiet solar atmosphere is generally considered to be composed of three layers, the photosphere, chromosphere and corona. When taken as a whole, the atmosphere is riddled by complex interactions of competing physical processes, such as convection, conduction, magnetic fields and of course radiation (Wedemeyer-Böhm *et al.*, 2009). Together these processes create a complex framework in which the observer and theorist must come to agreement. In the dense photosphere, hydrodynamic forces dominate, where the ratio of gas pressure to magnetic pressure (plasma β) is greater than one. It is in observations of the photosphere that the emergent granular pattern is seen as a result of the overshooting convective motion from below. The situation is reversed in the case of the chromosphere, where β is less than one and magnetohydrodynamic (MHD) forces dominate. The transition from the photo-

sphere to the chromosphere can be thought of as a transition that marks the onset of the magnetic-field-dominated region of the solar atmosphere (Uitenbroek, 2004). Though there is an inherent difference between the photosphere and chromosphere in terms of the dominant forces that are present, the two atmospheric layers should not be thought of as independent of one another.

The magnetic fields that create the rich and complex structure visible in narrow-band observations, taken in one of the strong chromospheric absorption lines (Hα, Ca), originate as emergent flux in the photosphere. Through advection by large-scale convective flows, the emergent flux gathers at the boundaries of supergranular cells where on-disk features such as mottles/fibrils (spicules at the limb) outline the observed magnetic network. Figure 8.1 (Figure 16 in Wedemeyer-Böhm *et al.* (2009)) shows a relatively simplified schematic of the structure of the quiet solar atmosphere, which is based on numerical simulation and observations. Wedemeyer-Böhm *et al.* (2009) organize the atmosphere in terms of two different domains, the "canopy" and "sub-canopy", named for the way in which the magnetic field extends over the internetwork (IN). The canopy consists of large-scale magnetic fields that are rooted at the network boundaries with field strengths on the order of kG, while the sub-canopy is dominated by a ubiquitous magnetic carpet of weak fields with a mean field strength of approximately 2 G (Title and Schrijver, 1998). Stratified within the canopy and sub-canopy domains are the constituent layers of the solar atmosphere, the photosphere, and the chromosphere. The chromosphere is represented most clearly through the large-scale magnetic structures that form the canopy domain, namely spicules.

The photosphere on the other hand can be thought of, according to Wedemeyer-Böhm *et al.* (2009) and Rutten (2007), as consisting of three layers: the lower photosphere, middle photosphere, and upper photosphere. Granulation is the signature feature in the the lower and middle photosphere, the dynamics of which are a result of

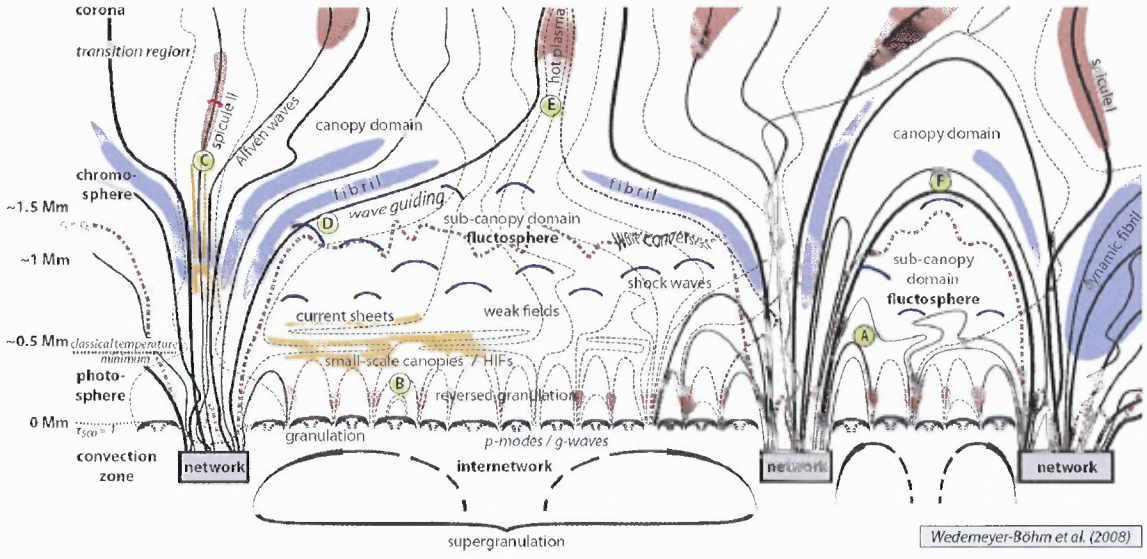

Figure 8.1 A schematic showing a simplified view of the quiet Suns atmospheric structure. The scale on the left of the figure gives the approximate heights of the atmosphere layers. (Figure 16 in Wedemeyer-Böhm *et al.* (2009)).

a host of underlying convective effects. The upper photosphere sits approximately at 500 km above the surface at the location of the temperature minimum. The upper layer of the photosphere sits below the fluctosphere (or clapotisphere), an atmospheric region that is characterized by weak fields whose dynamics are determined by acoustic wave interference that originates in the low photosphere (Rutten, 2007). Acoustic wave generation can be attributed to convective overshoot, exploding granules, and solar p-mode oscillations. Evidence for acoustic waves in the solar atmosphere was first presented in the early 1960's when Leighton *et al.* (1962) measured brightness fluctuations in Na D_1 observations with 5 oscillation periods. Acoustic waves interact in a complex fashion with local magnetic field lines that exist in a cavity such as the sub-canopy.

The picture of the solar atmosphere, greatly simplified in the explanation given in this section, is one of interacting phenomena that are invariably coupled from the photosphere up to the corona. Summarizing the results presented by Wedemeyer-Böhm *et al.* (2009): The photosphere ($\sim$ 0–500 km) is the layer that sits on top

of the convection zone, and can be thought of as having a lower, middle and upper portion. The fluctosphere ($\sim$ 500–1500 km) located within the sub-canopy domain, is a region of variable density, dominated by shock waves. The chromosphere ($\sim$ 1500 km; transition region) is the upper most layer of the solar atmosphere, sitting in the canopy domain with the predominant visible features being spicules.

The atmospheric features that are the focus of this chapter are the transient features called Hα upflows. The name Hα upflows, first given in Chae *et al.* (1998), comes from the signature blue shift that these features present in Hα line profiles. Upflows occur both in the IN and along the network boundaries with average Doppler velocities of approximately 5 km s^{-1} (Lee *et al.*, 2000). The formation of these features is thought to be a result of magnetic reconnection that is associated with converging network-internetwork magnetic dipoles. In Wang *et al.* (1998), observational evidence was presented showing the correspondence between upflows (called Hα – 1.0 Å jets at the time) and UV explosive events.

The upflow features presented in Wang *et al.* (1998) occurred primarily at the network-internetwork boundary which was determined by the good spatial agreement seen after co-aligning BBSO magnetographs and Hα time sequences. Shortly after, Chae *et al.* (1998) presented the results of a study using Hα spectrograph data and Solar and Heliospheric Observatory (SOHO) / Solar Ultraviolet Measurements of Emitted Radiation (SUMER) data. The results of the study conducted by Chae *et al.* (1998) confirmed the link between upflows and UV explosive events, and showed the existence of upflows not only at the network-internetwork boundary but within the cell as well. In an attempt to explain the link between observed flux cancelation, Hα upflows, and UV explosive events, Chae (1999) presented a two-step magnetic reconnection model.

The model starts with the formation of a small magnetic island formed by flux pile up as a result of slowly occurring magnetic reconnection in the photosphere.

When a critical flux is reached the magnetic island becomes unstable and moves either up or down from its equilibrium position. An island that moves up into higher layers does so with increasing velocity and it begins to expand. At this point the island is observed as an upflow feature in Hα. The second reconnection occurs when the upward moving island comes into contact with overlying magnetic field lines, creating a current sheet. Cool material is then injected from the expanding island into the overlying field lines where the material is heated and accelerated. The accelerated material is what is observed in the UV, and is interpreted as an explosive event.

Upflow events are part of a large group of jet-like phenomena (thought to occur through magnetic reconnection) that are observed throughout the upper atmospheric layers of the Sun. However, it is difficult to distinguish between them and to pinpoint the precise role they may play in supplying the required mass and energy necessary to explain the hot corona and other of the Sun's physical characteristics. In a recent article by Heggland *et al.* (2009), a numerical simulation was presented giving the observational signatures of magnetic reconnection caused by waves. In this study Heggland *et al.* (2009) mentions the correspondence between the intervals in which explosive events occur and wave modes produced by the granulation. Numerical simulations of this type, paired with multi-wavelength observations of high spatial and temporal resolution, could close the gaps that exist between observation and theory. In the following section a description of the observations that were made using the DST at NSO/SP on 2006 June 11, centered on a network region at disk center are discussed.

8.3 Observations

On 2006 June 11, a quiet Sun region located near Sun center (N4.4°, W1.6°) was observed using the DST at NSO/SP. The seeing conditions throughout the period of

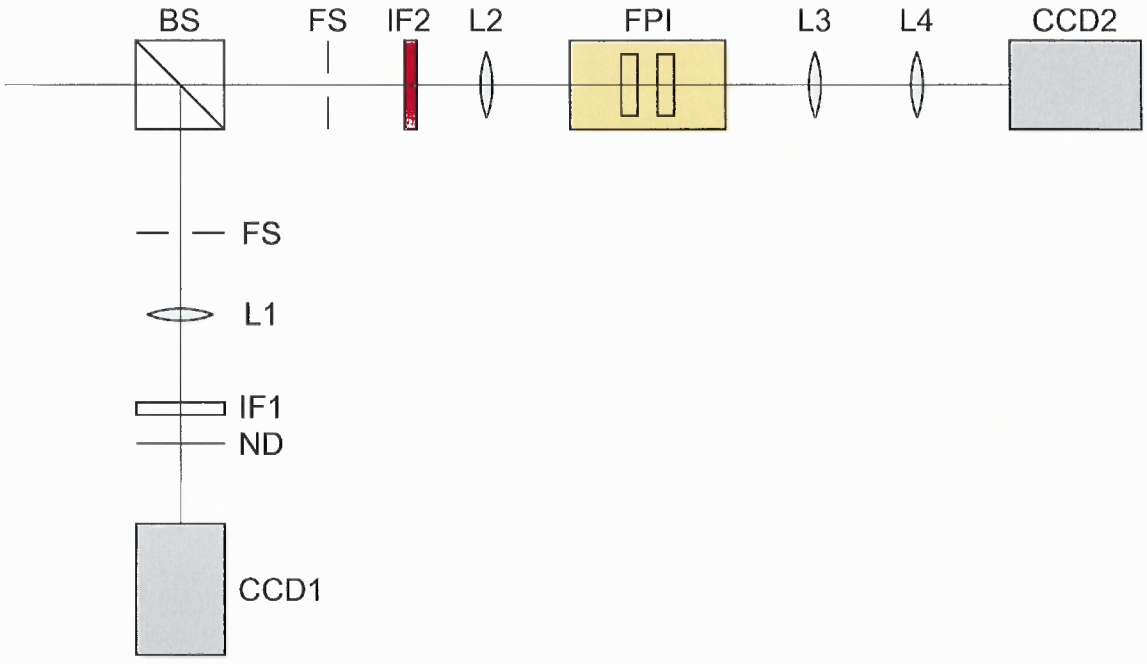

Figure 8.2 Optical set-up; 95/5% beam splitter (BS), field stop (FS), interference filters (IF1 and IF2), acromat lenses (L1–L4), Fábry-Perot Interferometer (FPI), neutral density filter (ND), and cameras (CCD1 and CCD2)

observation varied from excellent to poor. During times of good seeing the NSO/SP high-order Adaptive Optics (AO) system was deployed successfully. At the time, a pair of active regions, NOAA 10892 and NOAA 10893 were present on the Sun. Active region NOAA 10893 located at South 66″ and West −43″ was closest to disk center. A study of NOAA 10892 using data reduction techniques identical to the ones presented here is given in Denker *et al.* (2008). Figure 8.2 shows an optical schematic of the setup used for observations.

The data were acquired in two distinct channels: a narrow-band spectroscopic channel consisting of VIM, and a broad-band *speckle-channel* using a fast CCD camera for speckle imaging. A beamsplitting cube BS transmits 95% of the incident light to the narrow-band channel and reflects 5% to the speckle channel. In the narrow-band channel the pupil image at FS is focused by a 3000 mm acromat lens L2 to a point between the plates of a Fabry-Pérot etalon FPI. The FPI is arranged in a telecentric configuration which minimizes transmittance variations across the

Table 8.1 VIM Characteristics

Parameter	Specifications
Field-of-View FOV	$85.3'' \times 85.3''$
Image scale s	$0.17''$ pixel^{-1}
Bandpass $\delta\lambda$	7.2 pm
FPI wavelength coverage	550–700 nm
IF filters	656.28 nm $\pm$.015 nm
	588.99 nm $\pm$.015 nm
Wavelength points (Hα)	80
Wavelength points (Na D_2)	85
FPI step (λ/step)	2.4 pm @ 656.28 nm
	2.15 pm @ 588.99 nm
Free Spectral Range $\Delta\lambda$	0.4 nm
Spectral Resolution ($\lambda/\delta\lambda$)	87,500 @ 656.28 nm
	81,791 @ 588.99 nm
Exposure Time Δt	40 ms

FOV. The drawback to a telecentric configuration is that the spectral resolution of the observations is slightly reduced by spurious artificial Doppler signals due to the wavelength dependence of the FPI transmission across the FOV. Corrections for such effects are omitted for the reasons presented in Krieg *et al.* (1999), who cited negligible wavelength variations of approximately -16 mÅ in the raw data using a setup very similar to the one in Figure 8.2.

After passing through the FPI, light is collimated by $f3 = 800$ mm L3 and $f4 = 250$ mm L4-a pair of acromat lenses- and re-imaged onto a 512×512 pixel camera CCD2. The narrow-band (3 Å) interference filter IF2 is placed close to the pupil image at FS, set before the FPI. At this point in the optical path the light is collimated. In the speckle channel a 600 nm broad-band ($\pm$5 nm) filter IF1 is used in combination with a 1024×1024 pixel high-speed CCD camera CCD1. Light passes through the pupil stop FS and is imaged on CCD1 using a 1000 mm acromat lens L1. A neutral density filter ND is placed after IF1 to attenuate the light, so that

Table 8.2 Speckle Characteristics

Parameter	Specifications
Field-of-View FOV	$83.1'' \times 83.1''$
Image scale s	$0.08''$ pixel^{-1}
IF filter	600 nm $\pm$5 nm
Exposure Time Δt	4 ms

Table 8.3 Table of Observations

Set	Instrument	λ (nm)	Time (UT)	Cadence (s)
Ia	VIM	656.28	14:12–14:24	12
	Speckle	600	14:12–14:24	30
Ib	VIM	656.28	14:24–14:41	30
	Speckle	600	14:25–14:42	30
II	VIM	656.28	14:43–15:12	30
	Speckle	600	14:43–15:12	30
III	VIM	588.99	15:20–15:50	30
	Speckle	600	15:20–15:50	30
IV	VIM	588.99	15:51–16:21	30
	Speckle	600	15:52–16:22	30

image saturation is avoided. A description of the instrument characteristics for the observations are given in Table 8.1 and Table 8.2.

A total of four sets of data were acquired from 14:12–16:21 UT. Table 8.3 lists the individual times for each of the four data sets. The first set, listed in the Table 8.3, is comprised of two subsets. Subset Ia was taken with the FPI configured to one frame per step (resulting in a 12-s cadence), and so finished sooner than the corresponding speckle set. The FPI was quickly reconfigured through the software to acquire five frames per step (subset Ib) and finished with the first speckle set. In the remaining three sets of data the FPI was configured to take five frames per step. The first two sets were acquired in Hα and for the remaining two (III and IV) the filter was switched and observations were made in Na D_2. It is important to note

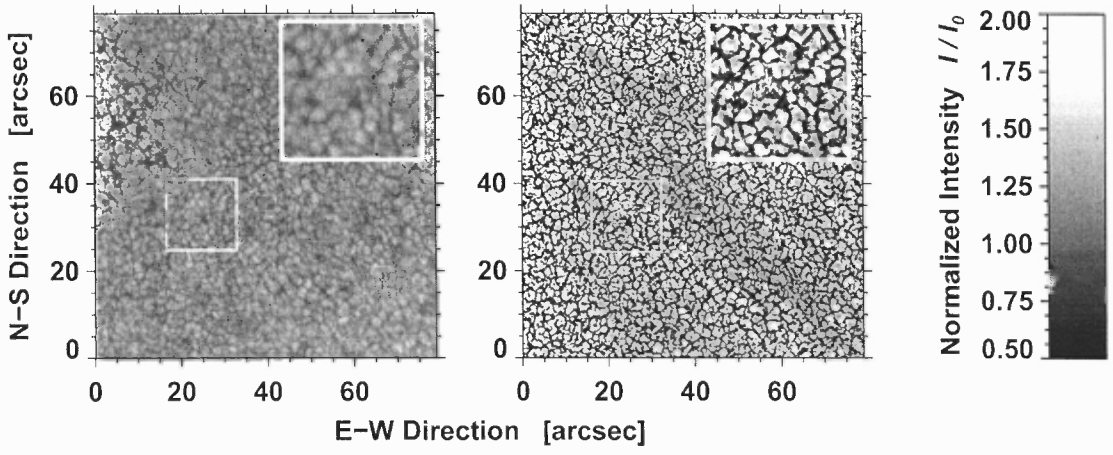

Figure 8.3 (*left*) AO-corrected image acquired at 14:16 UT before speckle masking imaging (SMI) was applied.(*right*) Same image after SMI was applied. The inset in each of the images gives a close up view the 16″× 16″outlined region. Solar filigree are visible in between the lanes that separate the granules.

that both CCD1 and CCD2 are controlled with separate computers, as a result the data were acquired in a *near-simultaneous* fashion, as the synchronization of both instruments occurs within a few seconds (∼20±5 s) of each other.

8.3.1 Broad-band Data

In the speckle-channel, bursts of 4 ms (short exposure) images were acquired with a 30-s cadence. The FOV for the broad-band images is 83.1″× 83.1″, resulting in an image scale of 0.08″ pixel^{-1}. In line with the review of modern image correction methods presented in Chapter 6, AO, frame selection, and speckle masking imaging (SMI) were applied to all four sets of the broad-band data. The data reduction methods for the broad-band data are identical to the ones presented in Denker *et al.* (2008). Figure 8.3 gives an example of one of the broad-band images with (*right*) and without (*left*) SMI applied. The image was acquired in the first data set at 14:16 UT during a period of excellent seeing. The granular rms contrast for the uncorrected image is ≈5.5±0.7%. The inset (16″× 16″) in the upper right corner of both images in Figure 8.3 provides a closer look at the enhancement of image

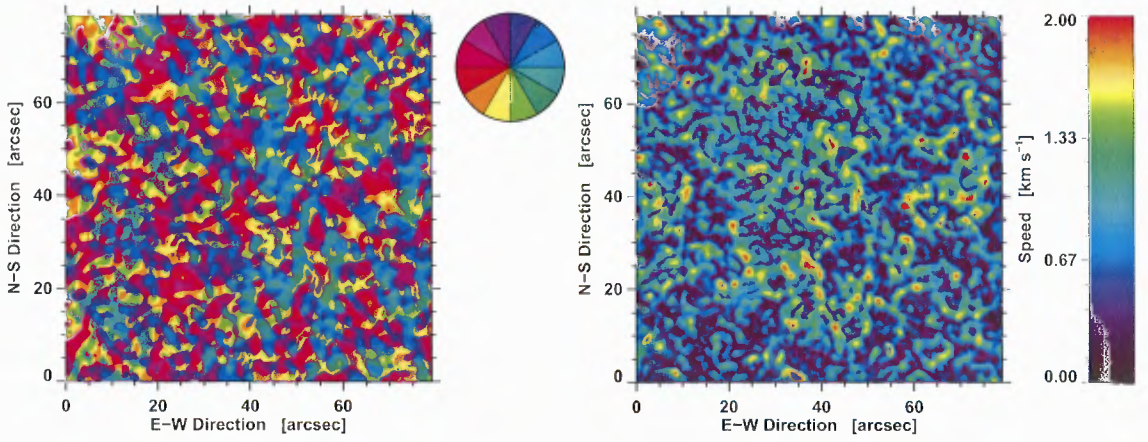

Figure 8.4 The LCT derived flow direction (*left*) averaged over a 30 minute period and the corresponding flow speed (*right*).

quality after SMI is applied. The result of SMI was a total of 240 reconstructions (60 in each set). For each set the horizontal proper motions (flows) were determined using local correlation tracking (LCT, November and Simon, 1988). LCT methods use the change in contrast in consecutive images in the time series to determine the direction and magnitude of the photospheric flow. Before the LCT algorithm was applied, preprocessing was necessary. Alignment of the images was carried out by matching the reconstructed images to a reference image in the same set. Differential image motion was removed using a destretching algorithm and seeing effects and solar oscillations were removed using a subsonic filter. After preprocessing LCT techniques were applied to determine the proper motion of the granulation in the reconstructed image sequences.

The results of LCT are shown in Figure 8.4. The flow direction and speed from the reconstructed broad-band data in set I are shown on the left and right respectively. In the flow speed map, horizontal speeds in excess of ~ 1.5 km s^{-1} are seen scattered throughout the FOV. The color compass to the right of the flow direction map indicates the direction of horizontal proper motions. Divergent regions in the flow direction map are located by matching the sequence of colors in the compass, taken in a clockwise direction, to a region in the map. Convergent flows can be

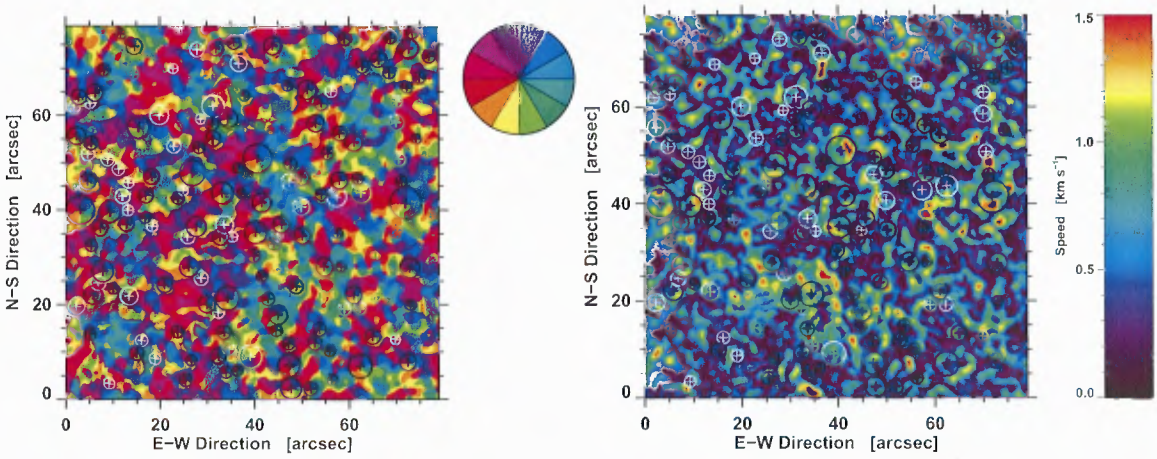

Figure 8.5 Locations of divergent and convergent regions superimposed on the (*left*) flow direction and (*right*) speed map. White circles correspond to convergent regions and the black circles to divergent.

identified by rotating the color compass counter-clockwise 180° and identifying the resulting color sequence in the direction map. An iterative algorithm to determine the locations of the divergent and convergent flows in the direction map was applied. For each location a circle, whose radius is proportional to the degree that the convergent or divergent flow is coherent, is prescribed outlining the region. In Figure 8.5 the locations of the convergent (white circles)and divergent (black circles) flows are plotted over the direction and speed maps of Figure 8.4. In the direction map, circles with large radii correspond to regions where there is a larger coherent convergent or divergent flow. In the flow speed map, these same regions usually contain flows with large horizontal flow speeds (~ 1.5 km s^{-1}).

For this study, a qualitative interpretation of the outlined flow regions is taken and a more rigorous and quantitative study is left for future work. In the following section the locations of the flow centers are used to investigate a possible relation between upflow occurrence in the chromosphere with average photospheric proper motion.

8.3.2 Narrow-band Data

For each broad-band set, a set of narrow-band images was acquired. The FOV for the spectroscopic observations is $85.3'' \times 85.3''$ corresponding to an image scale of $0.17''$ pixel^{-1}. Referring to Table 8.3, image sets I and II were taken in Hα and III and IV in Na D_2. VIM, like all 2-D imaging spectrometers, measures a spectrum at every location in the FOV. For Hα, 80 wavelength points were scanned with a spacing of 2.4 pm covering a range of $\sim$192.0 pm. A spacing of 2.15 pm was used for Na D_2, but 85 wavelength points were scanned resulting in a slightly smaller range of $\sim$183.0 pm. Taking 5 images per wavelength point resulted in 400 (Hα) and 425 (Na D_2) images per scan with a 30 second cadence to match the broad-band sequence. The image with the highest contrast was selected from the five frames for each point in the scan. Calibration images were acquired for both of the filters and were used in the data reduction: Flat fields, dark frames, target frames used to correct for the different scales and displacements between the narrow and broad-band images.

In all, the narrow-band observations consist of 275 scans of the same quiet Sun region, 155 in Hα and 120 in Na D_2 giving a total of more than 22,000 images. All of the images in the set were run through an iterative data reduction program, and were later sorted, selecting the scans that were acquired during the times of the best seeing. The data reduction process began with subtraction of an average dark frame from each image in the scan. From the flat field scans, taken for each filter, the gain table for the CCD at each wavelength point was obtained. The frame at each wavelength point was then divided by its corresponding gain table. Image motion was corrected and a common FOV was determined.

The tilt and shift of the line profile was determined and applied the data. The final step in the data reduction process was to fit the average line profiles for Hα and Na D_2 to the associated line profiles from a the Kitt Peak FTS-Spectral-Atlas Kurucz *et al.* (1984). The average flat field line profile is divided by a gaussian

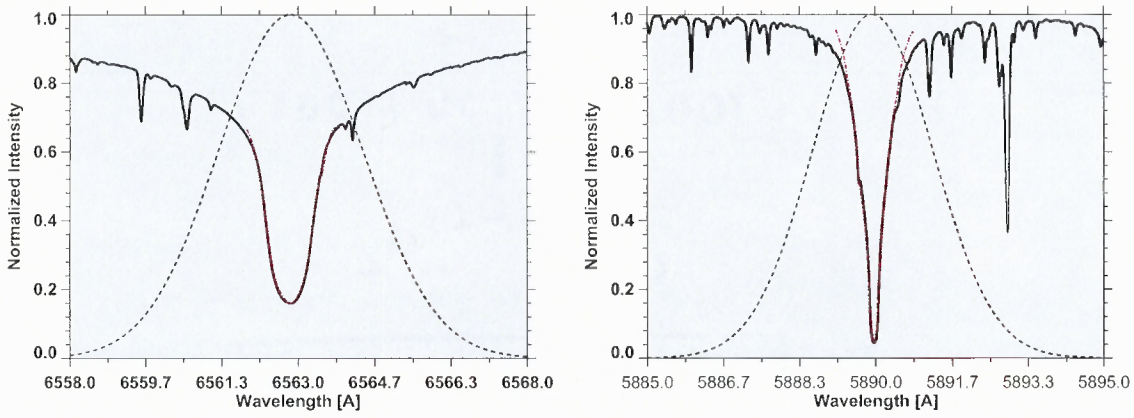

Figure 8.6 (*left*) Hα average line profile (red dash-dot). Solar atlas (black solid). Gaussian approximation of the interference filter transmission profile (black dashed). (*right*) Same plot for Na D_2.

approximation of the corresponding interference filter transmission profile and then choose points in both the atlas and average profile that corresponded to the same wavelength position. It is assumed that the intensity and wavelength difference between the average profile and the atlas is the same for all points in the line and a linear fit is used to independently determine their values. Figure 8.6 shows the atlas profile (black line), average corrected profile (red dash-dotted line) and the gaussian approximation to the filter transmission profile (black dash) for Hα (*left*) and Na D_2 (*right*). The linear fit routine returns the χ^2-square value as a metric for determining the goodness of fit. The standard deviations of the points in the average line profile and the FPI wavelength variation discussed above from Krieg *et al.* (1999) are used as errors for the linear fit routine. The resulting χ^2 values are 0.87 and 0.92 for Hα and Na D_2 respectively.

With the approximate wavelength positions and intensity values determined, the data can be scaled accordingly and calculations of the Doppler velocity can be carried out with more certainty. A sample scan in Hα taken at 14:16 UT (corresponding to the best speckle image in Figure 8.3) for eight wavelength positions in steps of ± 0.2 Å around line center is shown in Figure 8.7. As line center is approached

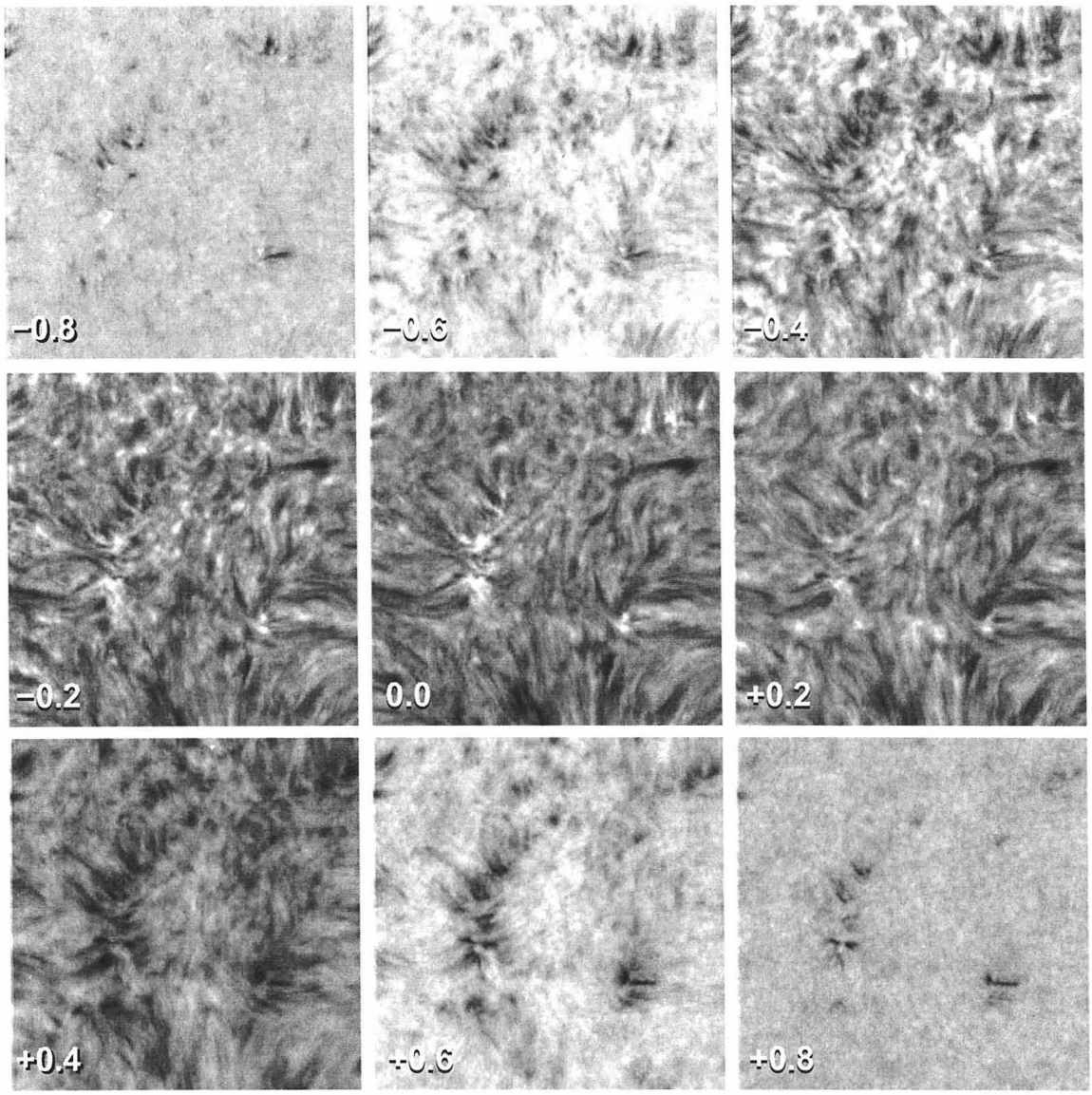

Figure 8.7 Hα line scan taken at 14:16 UT in steps of 0.2 Å around line center. The scan is nearly simultaneous with the best speckle image from that set.

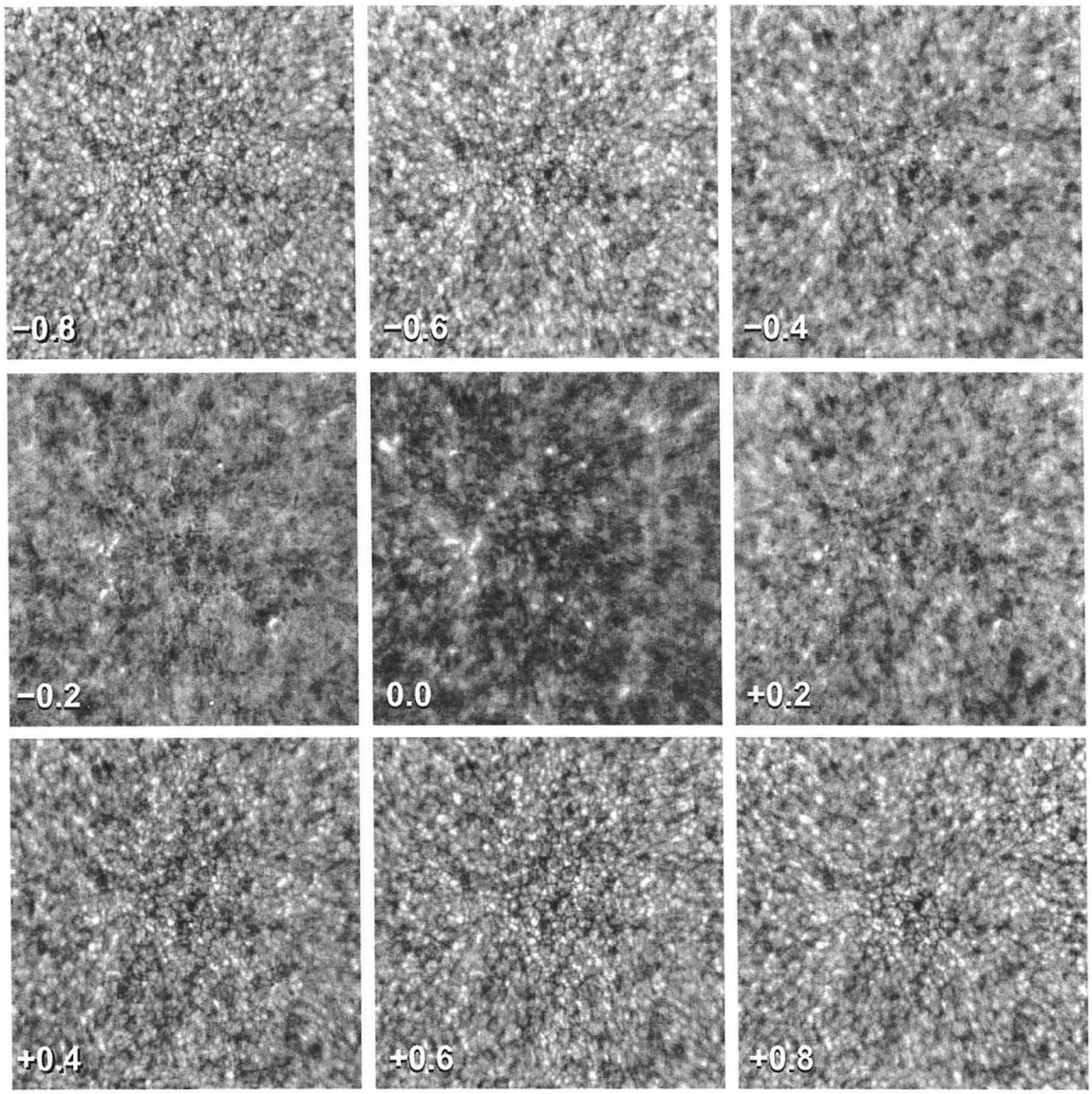

Figure 8.8 $\mathrm{Na\,D_2}$ scan taken at 15:23 UT shown in steps of 0.2 Å around line center.

from either the blue or red wing, the distribution of magnetic structures outlining a supergranular cell becomes more evident. Of particular interest are the presence of small scale features within the cell interior. The figure small scale features that are seen in the blue wing (-0.6 Å) throughout the cell interior are not present in the corresponding position in the red wing (+0.6 Å). These features are the locations of upflow regions as characterized in Lee *et al.* (2000).

In Figure 8.8, a sample scan in Na D_2 is shown. Here the rich magnetic structure of the upper chromosphere is not evident as the formation height for sodium spans a lower range of altitudes. The width of the sodium absorption line is considerably more narrow than that of the broad Hα line. At $\pm$0.4 Å around line center, the distinctive pattern of the granulation is clearly visible. It is not until $\pm$0.2 Å around line center that higher layers of the upper photosphere are seen. Small scale features appear throughout the IN and network boundary. In the following section one such region is identified along with it's corresponding line profile.

8.4 Results

In Lee *et al.* (2000) Hα upflow regions were identified using Dopplergrams. The Dopplergrams were constructed by subtracting the Hα +0.6 Å red line wing image from the $-$0.6 Å blue wing image. Upflow event features were identified as having a rounded and or "clumpy" spatial profile thus distinguishing them from the more elongated mottles and fibrils. Along with having a distinguishing spatial profile, Lee *et al.* (2000) found that upflow event features also have a characteristic blueshifted spectral profile that distinguishes them from mottles.

Two types of profiles were found for upflow features both at the network boundaries and within the IN. The first type is called type I upflow events, and they are found to have line profiles that are broadened in the blue wing of the line profile but remain fixed in the red wing when compared to the average quiet Sun profile. Type

I events were primarily found at the network boundaries. The second type of upflow event is called type II or dark grains. Dark grains are primarily found within the IN. Type II events show emission in the red, appearing to be shifted towards the blue when compared to the average quiet Sun line profile.

Identifying upflow regions was performed in a similar fashion to the one presented in Lee *et al.* (2000). However, a method for constructing Dopplergrams different than the one presented in Lee *et al.* (2000) is used. Two different techniques are used to derive the Dopplergrams used for this study. The first is a line bisector technique that calculates the bisector of the line profile at an intensity threshold defined by $I = I_0/\exp(1)$, where I_0 represents the continuum intensity of the quiet Sun. The Doppler map derived using this technique reflects contributions from all points in the line profile and is heavily influenced by points in the line wing that represent lower altitudes. In this study a Doppler map of this kind is called a Doppler line wing map, and is distinguished from the second type of Doppler map, the Doppler core map. The Doppler core map consists of line core velocities that are derived by making a parabola fit to spectral points approximately ± 10 pm (for Hα) around the line center.

Figure 8.9 shows an example of two Doppler line wing maps from a scan acquired at 14:50:30 UT in Hα (*left*) and at 15:25:01 UT in Na D$_2$ (*right*). For both maps, positive shifts correspond to downflows (yellow to white) and negative to upflows (blue to black). One can see that regions of strong downflows outline the supergranular cell boundary, with the intermittent appearance of strong upflow regions (this most evident in the Hα Doppler line wing map). In Na D$_2$ Doppler line wing maps, the situation is presented in much the same way, strong downflow regions roughly outline the network boundary, with the presence of a few strong upflow regions persisting between the downflows. A granular pattern strongly presents itself in the Na D$_2$ Doppler line wing map which reflects the line wing contribution to the

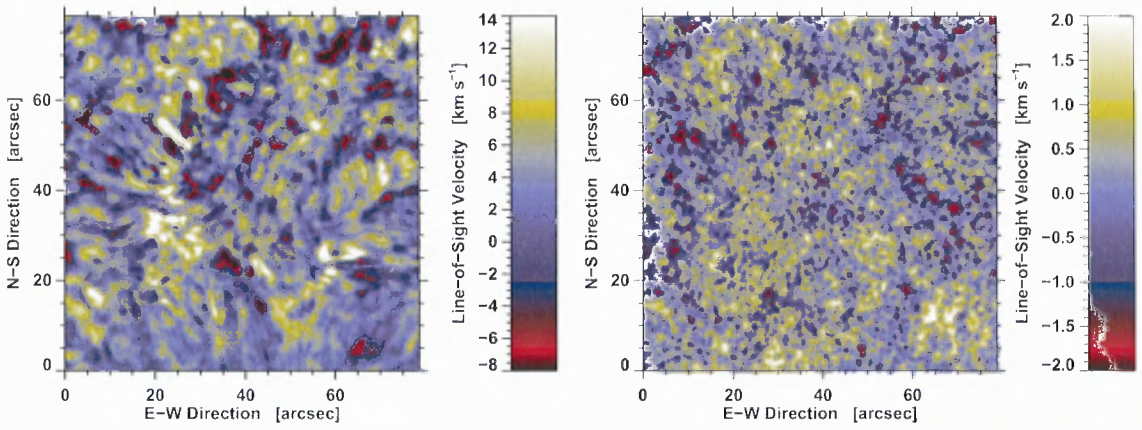

Figure 8.9 (*left*) Hα line of sight Doppler velocity map derived from reduced data acquired at 14:15:30 UT. Negative values correspond to upflows and positive to downflows. The maximum and minimum Doppler velocities are ≈ -7.47 km s^{-1} and $\approx +13$ km s^{-1}, respectively. (*right*) Na D$_2$ line of sight velocity map from a scan acquired at 15:25:02 UT. The maximum and minimum Doppler velocities are ≈ -2.0 km s^{-1} and $\approx +2.5$ km s^{-1}, respectively.

Doppler velocity. For the Hα Doppler map in Figure 8.9, the maximum upflow and downflow velocities recorded are ≈ -7.47 km s^{-1} and $\approx +13$ km s^{-1}, respectively. Na D$_2$ shows Doppler velocities that are smaller than the ones in Hα, with maximum upflow and downflow velocities ≈ -2.0 km s^{-1} and $\approx +2.5$ km s^{-1}, respectively. This is not surprising given that Doppler shift is proportional to $m^{-1/2}$, where m is the atomic mass. One would expect that sodium, with an atomic mass $\approx$21 times heavier than that of hydrogen, would have a less broad Doppler profile and hence smaller Doppler velocities. The Doppler velocities quoted above came from features that were found close to the IN-facing side of the network boundary. Upflow structures are also found inside the IN in both Hα and Na D$_2$.

Two such examples are given in Figure 8.10 and Figure 8.11. In Figure 8.10 the black circled region at the center of the Hα Doppler line wing map (*left*) and its corresponding line profile (*right*) are shown. The black asterisk line corresponds to the profile of the absorption feature and the solid black line the average quiet Sun line profile. A Doppler shift of ≈ -6 km s^{-1} was measured for this feature.

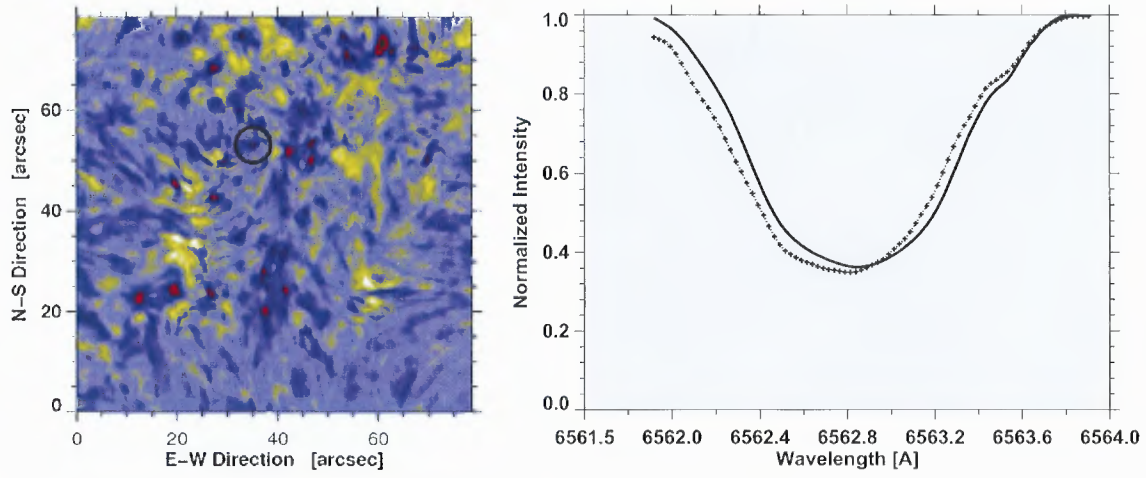

Figure 8.10 (*left*) Hα Doppler line wing map with upflow feature (black circle) and the corresponding (*right*) spectral profile (black asterisk) plotted over the average profile (black line).

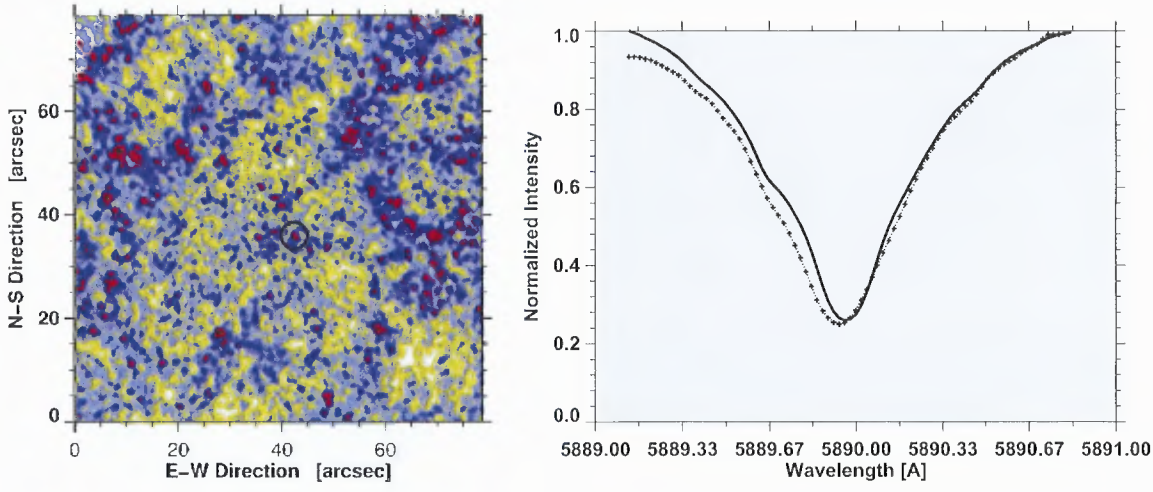

Figure 8.11 (*left*) Na D_2 Doppler line wing map with upflow feature (black circle) and the corresponding (*right*) spectral profile (black asterisk) plotted over the average profile (black line).

A blue-shifted profile of this kind is indicative of the type II upflow event or dark grain described above. As stated above, dark grains are primarily found within the IN. A type I upflow profile is shown in the right hand panel of Figure 8.11. This feature (black circle), was found close to the center of the IN in the Na D_2 Doppler line wing map. This feature has a Doppler velocity of ≈ -2 km s^{-1} and shows a characteristic type I blue wing broadening and a fixed red wing showing a slight absorption compared to the average profile.

In all, five upflow features were identified in Hα Doppler line wing maps for a 1.5 minute time-series (14:12:01–14:13:37 UT) from set Ia. Four of the five upflow features could be classified as type II upflows and were located both within and in close proximity to the IN boundary. The remaining feature was of type I and was located near the IN boundary. The average Doppler velocity of the five features was $\approx -5.5 \pm 1.2$ km s^{-1}. Five features were also identified in Na D_2, from a 4 minute time-series (15:23:12–15:27:28 UT) consisting of scans acquired in set III. For the five upflow features identified in the Na D_2 Doppler line wing map, all were of type I and were located both within and close to the IN boundary. The average Doppler velocity found for the five Na D_2 features was $\approx -2.3 \pm 0.3$ km s^{-1}. It is important to note that measurements, in Na D_2, of the line-of-sight (LOS) Doppler velocities of granular motion presented in Krieg *et al.* (1999) are on the order of ≈ -2 km s^{-1}. With this in mind it is difficult to say that the features that are identified as upflows in the Na D_2 Doppler line wing maps are indeed upflow features of the type presented in Lee *et al.* (2000).

However, it is also noted that granular lifetimes are on the order of ≈ 6 min Stix (1989), whereas upflow events have lifetimes on the order of 1–1.5 min. By examining both the spectral and temporal characteristics of upflow features observed in Na D_2 Doppler line wing maps, a more definitive conclusion could be reached regarding the ability to distinguish nascent upflow events from granular motion. A rigorous study

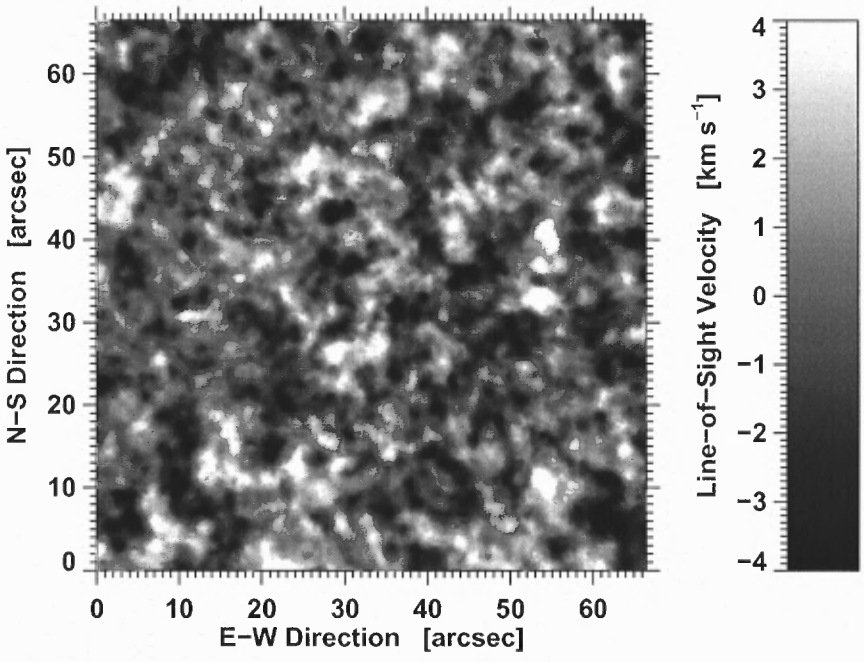

Figure 8.12 Na D_2 line of sight Doppler core velocity map from a scan acquired at 15:27:28 UT. The maximum and minimum Doppler velocities are ≈-3.5 km s^{-1} and ≈+4.5 km s^{-1}, respectively.

of the temporal evolution of upflow events observed in Na D_2 is left for future work and the focus in this chapter is primarily on the identification of upflow events.

One possible solution to the problem of distinguishing between upflow events observed in Doppler maps and granular upflows is to look higher in the atmosphere by looking at velocity contributions closer to the line core. The study of granular velocities presented in Krieg *et al.* (1999) gives a geometrical height of formation for the Doppler velocity signal of 50–200 km. The Dopplergrams presented in Krieg *et al.* (1999) were constructed by combining −500 mÅ and −600 mÅ blue wing images, with +500 mÅ and +600 mÅ red wing images. The Na D_2 line core has a geometrical height of formation between 200 km and 800 km Uitenbroek (2004). Attention can now be turned toward the Doppler core maps in a search for upflow signatures. Figure 8.12 shows a Doppler core map derived from a scan acquired at 15:27:28 UT. It is evident that the signature from the granulation is not nearly as pronounced as it is in the Doppler line wing maps. For the Doppler core maps

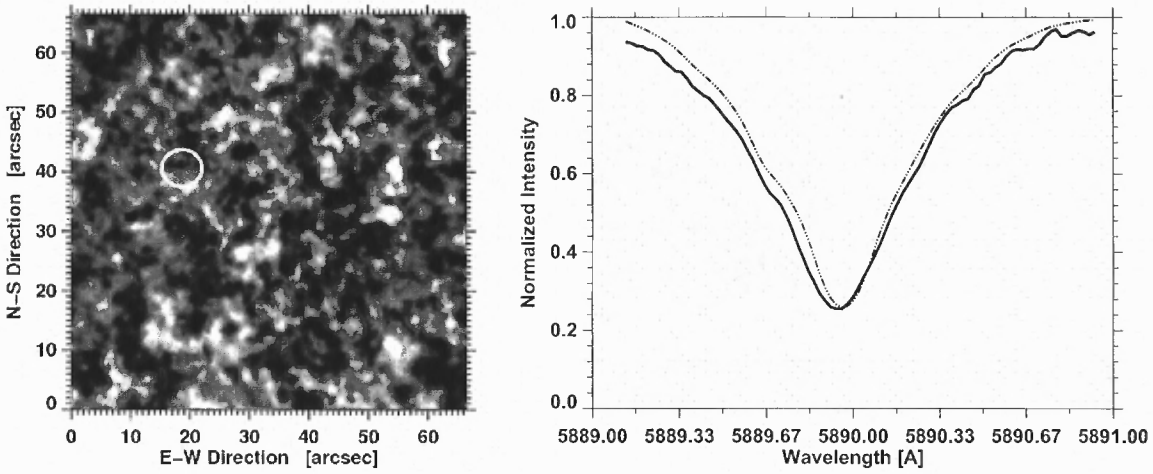

Figure 8.13 (*left*) Na D_2 Doppler core map from a scan acquired at 15:27:28 UT with an upflow feature (white circle) and the corresponding (*right*) spectral profile (black solid line) plotted over the average profile (dark grey dashed line).

five features are identified (different than the ones identified in the Doppler line wing maps) all appearing in the same 4 minute time-series from 15:23:12–15:27:28 UT. An example of one such feature and the corresponding line profile is shown in Figure 8.13. The profile for this feature is characteristic of a type I upflow event however, there is a small amount of absorption evident in the red wing. The LOS Doppler core velocity is measured to be ≈ -3.2 km s^{-1}. The average velocity of the five features is $\approx -2.8 \pm 0.4$ km s^{-1}, which is slightly larger than the average velocity values recorded in the Doppler line wing maps.

Along with the spectral characteristics, the position of upflows with respect to the divergent and convergent centers derived from LCT is presented. The two step reconnection model given in Chae (1999) suggests that upflow events exist at points where slow magnetic reconnection in and at the network boundaries occur. This has been further verified by studies showing the coincidence between flux cancelation at the photosphere and UV transition region jets. Without magnetic field data it is difficult to establish a spatial relationship between upflows and photospheric features. However, an attempt is made here by examining the co-alignment of Na D_2 and Hα

Doppler maps with the underlying flow direction. Before aligning the two fields, the narrow-band images had to be scaled and shifted with respect to the broad-band images. Using the target frames the necessary scaling factor and pixel shift between the CCD1 and CCD2 were determined.

The corrections were applied and the result is shown in Figure 8.14. In both the left and right panels of Figure 8.14, black circles with black cross hairs correspond to divergent flows and black circles with white cross hairs correspond to convergent flows. Diverging motions corresponding to emerging bipoles, seem to preferentially occur in the cell interior. It is difficult to say whether or not positive Doppler shifts are related to either divergent or convergent flows or if negative Doppler shifts have a preferential underlying flow direction at least in Hα. In Na D_2 however there seems to be a correspondence between downflows with convergent regions and upflows with divergent regions. Convergent regions seem to coincide with the location of downflows seen in the Doppler map. Since Na D_2 forms in the middle and upper photosphere at heights of 50–200 km it is relatively safe to assume that convergent horizontal flows are centered on the intergranular lanes which show up as downflows in the Na D_2 Doppler map. Upflows in the Doppler map seem to be in agreement with the location of divergent horizontal flows.

Another characteristic of upflows are their lifetimes. Figure 8.15 and Figure 8.16 show a time sequence of Doppler maps for Hα and Na D_2 respectively. Upflows are shown in red and black, and downflows in yellow and white. The Hα time sequence of Doppler maps presented in Figure 8.15 was derived from subset Ia where the narrow-band scans were acquired with a 12 s cadence. The figure shows a 1.5 min time series from 14:12:01–14:13:37 UT. Let it be clear that no attempts are made here to determine the precise lifetimes of upflows but instead these figures are used as an illustration to show the dynamical nature of these features as well as make a statement about the how the lifetimes might be used as a distinguishing charac-

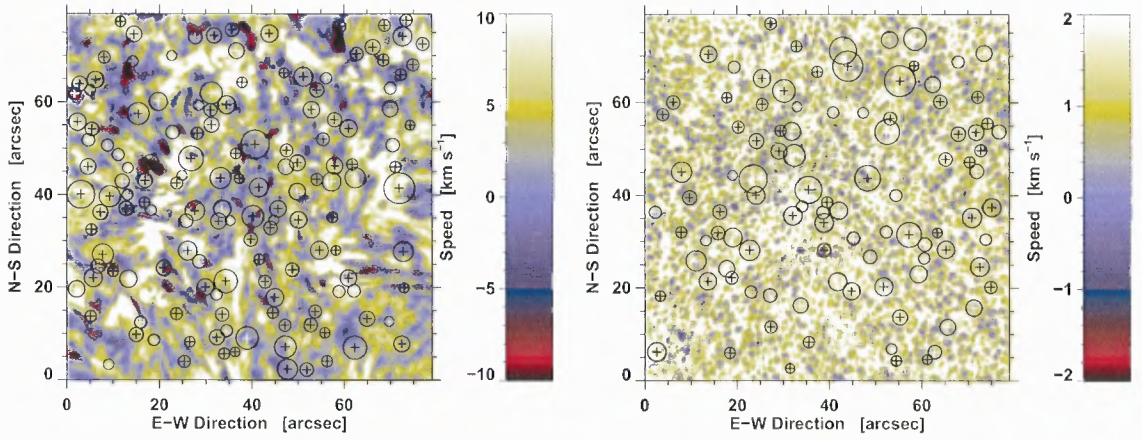

Figure 8.14 (*left*) Scaled Hα Doppler velocity map with position of divergent (black circles black crosshairs) and convergent (black circles white crosshairs) co-aligned. (*right*) Scaled Na D$_2$ Doppler velocity map showing the same.

teristic. Several strong upflow regions are visible both on and within the network boundaries. Features that are located along the network boundaries appear larger in size and have lifetimes that are longer than the smaller size shorter lifetime IN features. The time sequence of Na D$_2$ Doppler maps presented in Figure 8.16 were derived from the reduced data in set III. The figure shows a 4 minute time sequence from 15:23:12–15:27:28 UT, acquired with a 30 s cadence. Here a picture similar to the one in Figure 8.15 is seen. With mean granulation lifetimes on the order of 6 minutes and the frequent appearance and disappearance of upflows in the sodium Doppler map, it is quite possible that the upflows that are observed to occur in Na D$_2$ are associated with the same magnetic reconnection events that are proposed to be the source of Hα upflow events.

8.5 Conclusion

In this chapter the work carried out by Chae *et al.* (1998) and Lee *et al.* (2000) is expanded upon by using broad-band 600 nm and narrow-band Na D$_2$ 588.99 nm and Hα 656.28 nm data to study the behavior and characteristics of upflow events at different heights in the solar atmosphere. In the context of the two-step reconnection

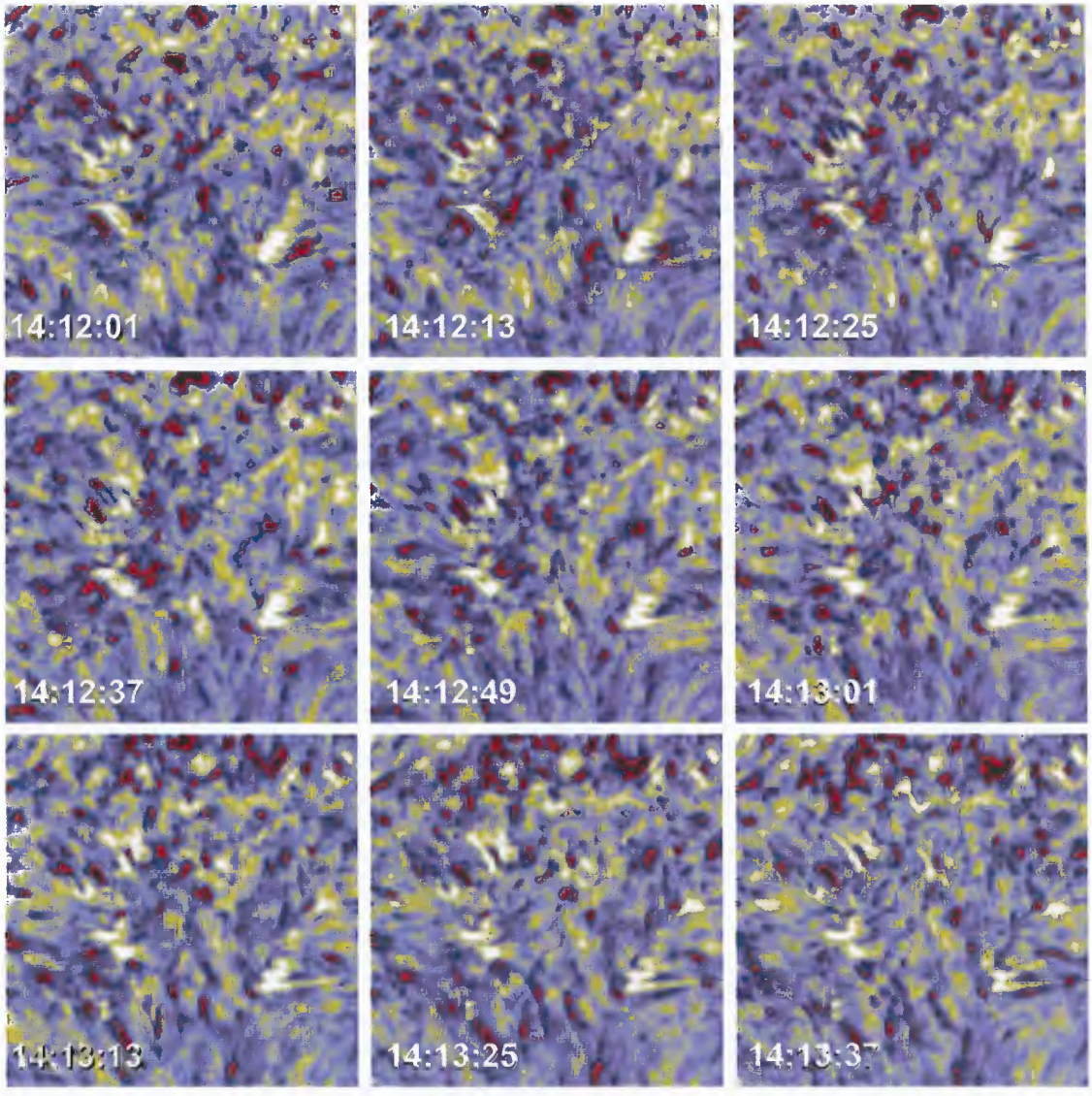

Figure 8.15 Time sequence (14:12:01–14:13:37 UT) of Hα Doppler velocity maps.

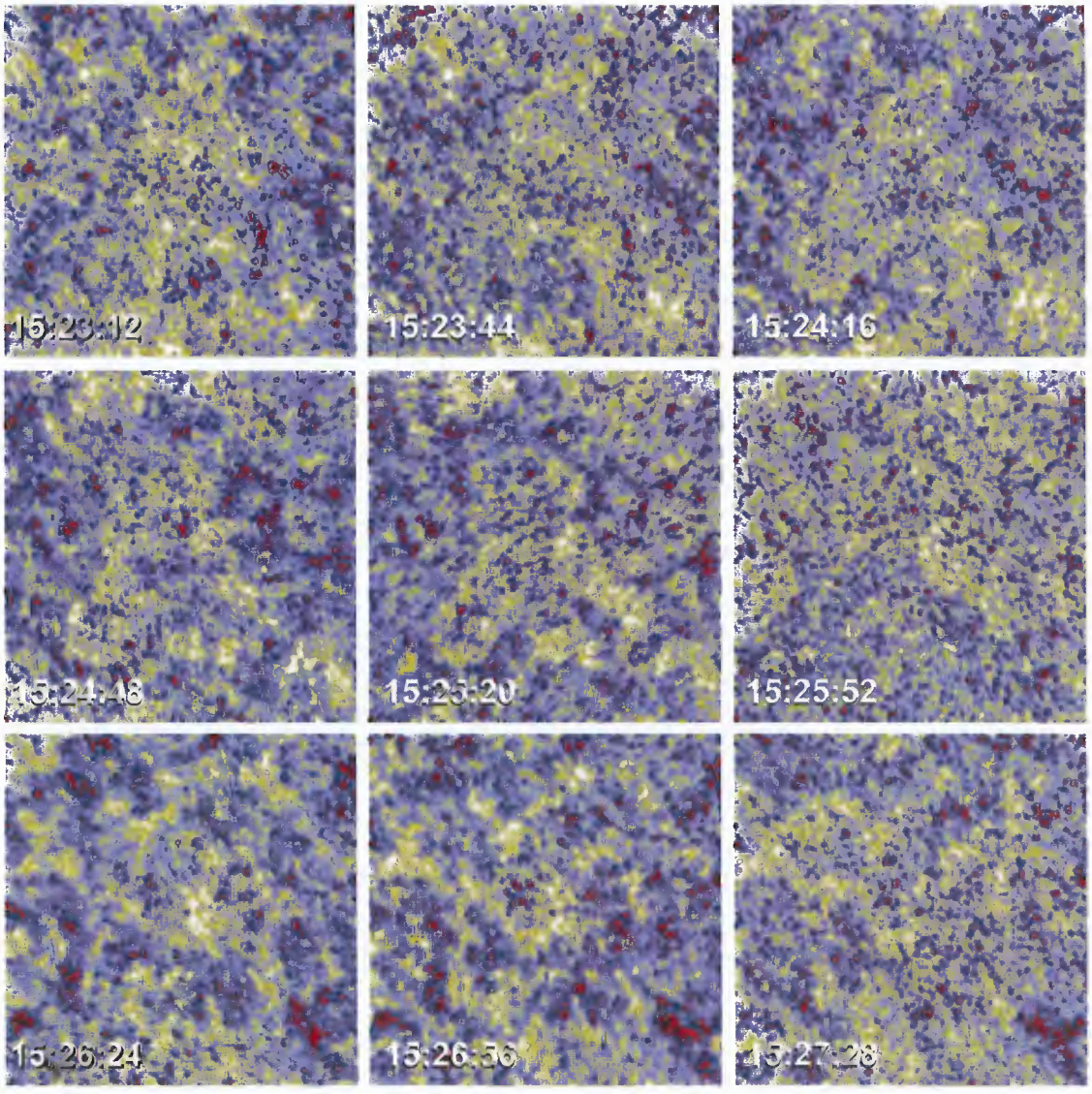

Figure 8.16 Time sequence (15:23:12–15:27:28 UT) of Na D_2 Doppler velocity maps.

model presented in Chae (1999), of particular interest is the question of where and how upflow events begin and evolve.

To begin to answer this, low chromosphere and photosphere observations using Na D_2 data are used to search for the early stages of upflow development. The line wing and line core Doppler velocities in Na D_2 are found to be approximately one half the velocities measured in Hα . An average Doppler line wing velocity for five upflow features in Hα of $\approx -5.5 \pm 1.2$ km s^{-1} is found. This is in line with the Doppler velocities presented in Lee *et al.* (2000). In Na D_2, using Doppler line wing maps and Doppler core maps upflows with velocities on the order of $\approx -2.3 \pm 0.3$ km s^{-1} and $\approx -2.8 \pm 0.4$ km s^{-1} are observed for line wing and line core Doppler velocities respectively. The smaller velocities observed for upflow features in Na D_2 could be the result of the sodium atom's larger atomic mass or, in the context of the two-step reconnection model, a look at the early stages of the rising magnetic island as it passes through the denser layers of the photosphere and lower chromosphere.

To make any sort of conclusive statements about the nascent stages of upflow evolution, further analysis is necessary. A sample size of five features is not enough to generate reliable statistics and efforts are currently underway to automate the identification of upflow features in both Doppler line wing and core maps for all data sets. With the automated identification of features, careful tracking of the temporal evolution of these events will be possible in both Na D_2 and Hα. This will be particularly useful in Na D_2 where the velocity signal from the granulation is dominant, and knowledge of the feature lifetimes would allow one to distinguish upflows from granulation.

CHAPTER 9

SUMMARY AND CLOSING REMARKS

From its nuclear core to the outer reaches of the heliosphere, the Sun supplies the scientific community with a steady stream of both fundamental and complex questions related to all areas of physics. From the perspective of the modern observer, the enormous variety of solar instrumentation that exists today is a reflection of the successful attempts that have been made to provide answers to some of these questions. In this thesis the emphasis is on the active role that ground-based solar observatories play by providing what are some of the necessary components needed to make high-resolution observations of the Sun.

The first component discussed is the choice of a proper location for the observatory. Using four years of meteorological and seeing data acquired during the site survey for the 4 m Advanced Technology Solar Telescope (ATST), provide a statistical analysis of the data with particular interest in the seeing characteristics at a mountain lake-site observatory, its relation to the local environment and climate, and the implications for the 1.6-meter New Solar Telescope (NST) currently in operation at Big Bear Solar Observatory (BBSO). Prevailing westerly winds with average speeds of 6 m s^{-1} will provide the necessary cooling needed to maintain temperatures and remove thermal gradients inside the observatory dome. Analysis of the seeing conditions show excellent windows for high resolution observations from sunrise to sunset making BBSO an ideal site for both synoptic and campaign style solar observations.

Following the detailed analysis of the site and seeing characteristics, a brief overview is given of the NST in an effort to seamlessly segue into the preliminary design of the NST THermal Control System (THCS). The open structure design of

NST requires that temperatures inside the dome be in equilibrium with the outside so as to minimize the effects of convective currents around the telescope structure. Measurement of the temperature inside the dome using 16 thermal probes confirmed the existence of a strong thermal gradient on the order of 5° Celsius inside the dome. Passive measures are used to flush the air in the dome by using 14 active vents housing louvers that open and close independently of one another to regulate and direct the passage of air through the dome. Temperature tests were carried out while simultaneously opening and closing the louvers, showing that the louvers do affect the internal dome temperature. However, further experiments with the telescope present and operating under normal observing conditions are necessary to arrive at an optimum algorithm for opening and closing the louvers.

The NST will benefit from a host of new and hold post focus instrumentation. One of instruments is a two-dimensional imaging spectro-polarimeter called the Visible-light Imaging Magnetograph (VIM). VIM will provide high temporal and spatial resolution two-dimensional spectro-polarimetric measurements of the Sun, making the study of solar activity more complete. In Chapter 7 VIM is summarized and a calibration method for the set of two Liquid Crystals (LC) used for VIM's operation as a spectropolarimeter is provided. In July 2007, using the calibrated polarization module, the first Stokes-V Magnetograms using VIM were obtained.

In Chapter 8 near-simultaneous narrow-band and broad-band observations are presented of a quiet Sun region at disk center using VIM and a speckle camera. Data sets of this type provide a wealth of information pertaining to the structure, dynamics, and coupling of the different layers of the Solar atmosphere. The purpose of this chapter, keeping within the context of this thesis, is to provide the reader with an application of high-resolution observations of the Sun using upflow events as an example. Using line wing Doppler maps, upflow events with velocities on the order of ≈ -8 km s^{-1} in Hα, and ≈ -2 km s^{-1} in Na D$_2$ are found. The line profiles

associated with upflows seen in Hα are characteristic of both type I and type II (dark grain) upflow events, while the upflows observed in Na D_2 are characteristic only of type I. This the first step of an in-depth study of upflow features at lower geometric heights in the solar atmosphere.

REFERENCES

Acton, D. S., Smithson, R. C., Jun. 1992: *Solar Imaging with a Segmented Adaptive Mirror.* Applied Optics **31**, 3161–3169.

Babcock, H. W., Oct. 1953: *The Possibility of Compensating Astronomical Seeing.* Publications of the Astronomical Society of the Pacific **65**, 229–236.

Beckers, J. M., 1993: *Adaptive Optics for Astronomy - Principles, Performance, and Applications.* Annual Review of Astronomy and Astrophysics **31**, 13–62.

Beckers, J. M., 2001: *A Seeing Monitor for Solar and Other Extended Object Observations.* Experimental Astronomy **12**, 1–20.

Bowen, I. S., 1950: *Final Adjustments and Tests of the Hale Telescope.* Publications of the Astronomical Society of the Pacific **62**, 91–97.

Bradley, E. S., Roberts, Jr., L. C., Bradford, L. W., Skinner, M. A., Nahrstedt, D. A., Waterson, M. F., Kuhn, J. R., 2006: *Characterization of Meteorological and Seeing Conditions at Haleakala.* Publications of the Astronomical Society of the Pacific **118**, 172–182.

Brandt, P. N., Wöhl, H., 1982: *Solar Site-Testing Campaign of JOSO on the Canary Islands in 1979* **109**, 77–89.

Cao, W., Jing, J., Ma, J., Xu, Y., Wang, H., Goode, P. R., 2006: *Diffraction-Limited Polarimetry from the Infrared Imaging Magnetograph at Big Bear Solar Observatory.* Publications of the Astronomical Society of the Pacific **118**, 838–844.

Centeno, R., Socas-Navarro, H., Lites, B., Kubo, M., Frank, Z., Shine, R., Tarbell, T., Title, A., Ichimoto, K., Tsuneta, S., Katsukawa, Y., Suematsu, Y., Shimizu, T., Nagata, S., Sep. 2007: *Emergence of Small-Scale Magnetic Loops in the Quiet-Sun Internetwork.* The Astrophysical Journal **666**, L137–L140.

Chae, J., 1999: *Small-Scale Magnetic Reconnection in the Quiet Sun.* in: High Resolution Solar Physics: Theory, Observations, and Techniques, Astronomical Society of the Pacific Conference Series **183** 375–382.

Chae, J., Wang, H., Lee, C.-Y., Goode, P. R., Schuhle, U., Sep. 1998: *Chromospheric Upflow Events Associated with Transition Region Explosive Events.* The Astrophysical Journal **504**, L123–L126.

Dalrymple, N. E., Oschmann, J. M., Hubbard, R. P., 2004: *ATST Enclosure: Seeing Performance, Thermal Modeling, and Error Budgets.* in: Modeling and Systems Engineering for Astronomy 497–507.

Denker, C., Didkovsky, L., Ma, J., Shumko, S., Varsik, J., Wang, J., Wang, H., Goode, P. R., 2003a: *Imaging Magnetographs for High-Resolution Solar Observations in the Visible and Near-Infrared Wavelength Region.* Astronomical Notes **324**, 332–333.

Denker, C., Goode, P. R., Ren, D., Saadeghvaziri, M. A., Verdoni, A. P., Wang, H., Yang, G., Abramenko, V., Cao, W., Coulter, R., Fear, R., Nenow, J., Shoumko, S., Spirock, T. J., Varsik, J. R., Chae, J., Kuhn, J. R., Moon, Y., Park, Y. D., Tritschler, A., 2006: *Progress on the 1.6-Meter New Solar Telescope at Big Bear Solar Observatory.* in: Stepp, L. M. (ed.), Ground-Based and Airborne Telescopes, Proceedings of SPIE **6267** 62670–62682.

Denker, C., Ma, J., Wang, J., Didkovsky, L. V., Varsik, J. R., Wang, H., Goode, P. R., 2003b: *IRIM: An Imaging Magnetograph for High-Resolution Solar Observations in the Near-Infrared.* in: Innovative Telescopes and Instrumentation for Solar Astrophysics, Proceedings of SPIE **4853** 223–234.

Denker, C., Mascarinas, D., Xu, Y., Cao, W., Yang, G., Wang, H., Goode, P. R., Rimmele, T., 2005: *High-Spatial Resolution Imaging Combining High-Order Adaptive Optics, Frame Selection, and Speckle Masking Reconstruction.* Solar Physics **227**, 217–230.

Denker, C., Spirock, T., Varsik, J. R., Chae, J., Marquette, W. H., Wang, H., Goode, P. R., 2001a: *Dynamics of Quiet Sun Magnetic Fields.* in: Sigwarth, M. (ed.), Advanced Solar Polarimetry – Theory, Observation, and Instrumentation, Astronomical Society of the Pacific Conference Series **236** 463–470.

Denker, C., Tritschler, A., 2005: *Measuring and Maintaining the Plate Parallelism of Fabry-Pérot Etalons.* Publications of the Astronomical Society of the Pacific **117**, 1435–1444.

Denker, C., Tritschler, A., Deng, N., 2008: *High-Resolution Observations Of Extremely Bright Penumbral Grains.* Astronomical Notes **329**, 773–779.

Denker, C., Tritschler, A., Rimmele, T. R., Richards, K., Hegwer, S. L., Wöger, F., 2007: *Adaptive Optics at the Big Bear Solar Observatory: Instrument Description and First Observations.* Publications of the Astronomical Society of the Pacific **119**, 170–182.

Denker, C., Verdoni, A. P., 2006: *Integrating Seeing Measurements into the Operations of Solar Telescopes.* in: Stepp, L. M. (ed.), Ground-Based and Airborne Telescopes, Proceedings of SPIE **6267** 62670L.

Denker, C., Yang, G., Wang, H., 2001b: *Near Real-Time Image Reconstruction.* Solar Physics **202**, 63–70.

Fried, D. L., 1966: *Optical Resolution Through a Randomly Inhomogeneous Medium for Very Long and Very Short Exposures.* Journal of the Optical Society of America **56**, 1372–1379.

Fried, D. L., Mevers, G. E., 1974: *Evaluation of r_0 for Propagation Down Through the Atmosphere.* Applied Optics **13**, 2620–2622.

Gallagher, P. T., Denker, C., Yurchyshyn, V., Spirock, T., Qiu, J., Wang, H., Goode, P. R., 2002: *Solar Activity Monitoring and Forecasting Capabilities at Big Bear Solar Observatory.* Annales Geophysicae **20**, 1105–1115.

Giorgini, J. D., Yeomans, D. K., Chamberlin, A. B., Chodas, P. W., Jacobson, R. A., Keesey, M. S., Lieske, J. H., Ostro, S. J., Standish, E. M., Wimberly, R. N., 1996: *JPL's On-Line Solar System Data Service.* in: Bulletin of the American Astronomical Society, Bulletin of the American Astronomical Society **28** 1158.

Goode, P. R., Denker, C., Didkovsky, L. I., Kuhn, J. R., Wang, H., 2003: *1.6-Meter Solar Telescope in Big Bear - The NST.* Journal of the Korean Astronomical Society **36**, 125–133.

Goode, P. R., Wang, H., Marquette, W. H., Denker, C., 2000: *Measuring Seeing from Solar Scintillometry and the Spectral Ratio Technique.* Solar Physics **195**, 421–431.

Hale, G. E., 1905: *A Study of the Conditions for Solar Research at Mount Wilson, California.* The Astrophysical Journal **21**, 124–155.

Hanson, P. J., Weltzin, J. F., 2000: *Drought Disturbance from Climate Change: Response of United States Forests.* Science of the Total Environment **262**, 205–220.

Hardy, J., Mar. 1981: *Solar Isoplanatic Patch Measurements.* in: Dunn, R. B. (ed.), Solar instrumentation: What's next? 421–433.

Heggland, L., De Pontieu, B., Hansteen, V. H., Feb. 2009: *Observational Signatures of Simulated Reconnection Events in the Solar Chromosphere and Transition Region.* Submitted to The Astrophysical Journal.

Hill, F., Beckers, J., Brandt, P., Briggs, J., Brown, T., Brown, W., Collados, M., Denker, C., Fletcher, S., Hegwer, S., Horst, T., Komsa, M., Kuhn, J., Lecinski, A., Lin, H., Oncley, S., Penn, M., Radick, R., Rimmele, T., Socas-Navarro, H., Streander, K., 2006: *Site Testing for the Advanced Technology Solar Telescope.* in: Stepp, L. M. (ed.), Ground-Based and Airborne Telescopes, Proceedings of SPIE **6267** 62671T.

Hill, F., Beckers, J., Brandt, P., Briggs, J., Brown, T., Brown, W., Collados, M., Denker, C., Fletcher, S., Hegwer, S., Horst, T., Komsa, M., Kuhn, J., Lecinski, A., Lin, H., Oncley, S., Penn, M., Rimmele, T. R., Socas-Navarro, H., Streander, K., 2004a: *Solar Site Testing for the Advanced Technology Solar Telescope.* in: Oschmann, J. M. (ed.), Ground-Based Telescopes, Proceedings of SPIE **5489** 122–129.

Hill, F., Beckers, J., Brown, T., Collados, M., Denker, C., Kuhn, J., Penn, M., Socas-Navarro, H., Soltau, D., Streander, K., 2004b: *ATST Site Survey Working Group Final Report.* ATST Project Document **21**.

Hill, F., Fischer, G., Forgach, S., Grier, J., Leibacher, J. W., Jones, H. P., Jones, P. B., Kupke, R., Stebbins, R. T., Clay, D. W., 1994: *The Global Oscillation Network Group Site Survey, 2: Results.* Solar Physics **152**, 351–379.

Hu, H., Liu, W. T., 2003: *Oceanic Thermal and Biological Responses to Santa Ana Winds.* Geophysical Research Letters **30**, 50–1.

Keil, S., Oschmann, J. M., Rimmele, T. R., Hubbard, R., Warner, M., Price, R., Dalrymple, N., Goodrich, B., Hegwer, S., Hill, F., Wagner, J., 2004: *Advanced Technology Solar Telescope: Conceptual Design and Status.* in: Oschmann, J. M. (ed.), Ground-Based Telescopes, Proceedings of SPIE **5489** 625–637.

Kentischer, T. J., Schmidt, W., Sigwarth, M., Uexkuell, M. V., Dec. 1998: *TESOS, a Double Fabry-Perot Instrument for Solar Spectroscopy* **340**, 569–578.

Knox, K. T., Thompson, B. J., Oct. 1974: *Recovery of Images from Atmospherically Degraded Short-Exposure Photographs.* The Astrophysical Journal **193**, L45–L48.

Korff, D., 1973: *Analysis of a Method for Obtaining Near Diffraction Limited Information in the Presence of Atmospheric Turbulence.* Journal of the Optical Society of America **63**, 971–980.

Krieg, J., Wunnenberg, M., Kneer, F., Koschinsky, M., Ritter, C., Mar. 1999: *Height Variation of the Solar Granulation* **343**, 983–989.

Kuhn, J. R., Coulter, R., Lin, H., Mickey, D. L., 2003: *The SOLARC Off-Axis Coronagraph.* in: Keil, S. L., Avakyan, S. V. (eds.), Innovative Telescopes and Instrumentation for Solar Astrophysics., Proceedings of the Society of Photo-Optical Instrumentation Engineers **4853** 318–326.

Kurucz, R. L., Furenlid, I., Brault, J., Testerman, L., 1984: Solar flux atlas from 296 to 1300 nm.

Labeyrie, A., May 1970: *Attainment of Diffraction Limited Resolution in Large Telescopes by Fourier Analysing Speckle Patterns in Star Images* **6**, 85–87.

Lee, C.-Y., Chae, J., Wang, H., Dec. 2000: *Dynamical Characteristics of Small-Scale Hα Upflow Events on the Quiet Sun.* The Astrophysical Journal **545**, 1124–1134.

Leighton, R. B., Noyes, R. W., Simon, G. W., Mar. 1962: *Velocity Fields in the Solar Atmosphere. I. Preliminary Report.* The Astrophysical Journal **135**, 474–499.

Li, J., van Ballegooijen, A. A., Mickey, D., Feb. 2009: *Vector Magnetic Fields and Electric Currents from the Imaging Vector Magnetograph.* The Astrophysical Journal **692**, 1543–1560.

Lin, H., Penn, M. J., 2004: *The Advanced Technology Solar Telescope Site Survey Sky Brightness Monitor.* Publications of the Astronomical Society of the Pacific **116**, 652–666.

Liu, Z., Beckers, J. M., 2001: *Comparative Solar Seeing and Scintillation Studies at the Fuxian Lake Solar Station.* Solar Physics **198**, 197–209.

Martin, H. M., Burge, J. H., Cuerden, B., Miller, S. M., Smith, B., Zhao, C., 2004: *Manufacture of 8.4-m Off-Axis Segments: A 1/5-Scale Demonstration.* in: Optical Fabrication, Metrology, and Material Advancements for Telescopes, Proceedings of SPIE **5494** 62–70.

Mickey, D. L., Canfield, R. C., Labonte, B. J., Leka, K. D., Waterson, M. F., Weber, H. M., 1996: *The Imaging Vector Magnetograph at Haleakala.* Solar Physics **168**, 229–250.

Montañés-Rodriguez, P., Pallé, E., Goode, P. R., Hickey, J., Koonin, S. E., 2005: *Globally Integrated Measurements of the Earth's Visible Spectral Albedo.* The Astrophysical Journal **629**, 1175–1182.

November, L. J., Simon, G. W., 1988: *Precise proper-motion measurement of solar granulation.* apj **333**, 427–442.

Rimmele, T., Dunn, R., Richards, K., Radick, R., 1999: *Solar Adaptive Optics at the National Solar Observatory.* in: Rimmele, T. R., Balasubramaniam, K. S., Radick, R. R. (eds.), High Resolution Solar Physics: Theory, Observations, and Techniques, Astronomical Society of the Pacific Conference Series **183** 222–230.

Rimmele, T. R., 2000: *Solar Adaptive Optics.* in: Wizinowich, P. L. (ed.), Adaptive Optical Systems Technology, Proceedings of SPIE **4007** 218–231.

Rimmele, T. R., Keil, S., Wagner, J., Dalrymple, N., Goodrich, B., Hansen, E., Hill, F., Hubbard, R., Phelps, L., Richards, K., Warner, M., 2005: *Advanced Technology Solar Telescope: A Progress Report.* in: Fineschi, S., Viereck, R. A. (eds.), Solar Physics and Space Weather Instrumentation, Proceedings of SPIE **5901** 41–51.

Rimmele, T. R., Radick, R. R., Sep. 1998: *Deconvolving Solar Images Using a Shack-Hartmann Wavefront Sensor.* in: Bonaccini, D., Tyson, R. K. (eds.), Adaptive Optical System Technologies, Proceedings of the Society of Photo-Optical Instrumentation Engineers **3353** 1014–1021.

Rimmele, T. R., Richards, K., Hegwer, S., Fletcher, S., Gregory, S., Moretto, G., Didkovsky, L. V., Denker, C., Dolgushin, A., Goode, P. R., Langlois, M., Marino, J., Marquette, W., 2004: *First Results from the NSO/NJIT Solar Adaptive Optics System.* in: Fineschi, S., Gummin, M. A. (eds.), Telescopes and Instrumentation for Solar Astrophysics, Proceedings of SPIE **5171** 179–186.

Rutten, R. J., May 2007: *Observing the Solar Chromosphere.* in: The Physics of Chromospheric Plasmas, Astronomical Society of the Pacific Conference Series **368** 27–49.

Rutten, R. J., Hammerschlag, R. H., Bettonvil, F. C. M., Sütterlin, P., de Wijn, A. G., 2004: *DOT Tomography of the Solar Atmosphere. I. Telescope Summary and Program Definition.* Astronomy and Astrophysics **413**, 1183–1189.

Sarazin, M., Roddier, F., 1990: *The ESO Differential Image Motion Monitor* **227**, 294–300.

Scharmer, G. B., Gudiksen, B. V., Kiselman, D., Löfdahl, M. G., Rouppe van der Voort, L. H. M., Nov. 2002: *Dark Cores in Sunspot Penumbral Filaments.* Nature **420**, 151–153.

Shumko, S., Abramenko, V., Denker, C., Goode, P., Tritschler, A., Varsik, J., 2005: *The Visible–Light Magnetograph at the Big Bear Solar Observatory: Hardware and Software.* in: Shopbell, P., Britton, M., Ebert, R. (eds.), Astronomical Data Analysis Software and Systems XIV, Astronomical Society of the Pacific Conference Series **347** 509–513.

Shumko, S., Yang, G., 2006: *Object-Oriented Communications for the NST's Telescope Control System: Design and Implementation.* in: Lewis, H., Bridger, A. (eds.), Advanced Software and Control for Astronomy, Proceedings of SPIE **6274** 62741Q.

Socas-Navarro, H., Beckers, J., Brandt, P., Briggs, J., Brown, T., Brown, W., Collados, M., Denker, C., Fletcher, S., Hegwer, S., Hill, F., Horst, T., Komsa, M., Kuhn, J., Lecinski, A., Lin, H., Oncley, S., Penn, M., Rimmele, T., Streander, K., 2005: *Solar Site Survey for the Advanced Technology Solar Telescope. I. Analysis of the Seeing Data.* Publications of the Astronomical Society of the Pacific **117**, 1296–1305.

Spirock, T., Denker, C., Chen, H., Chae, J., Qiu, J., Varsik, J., Wang, H., Goode, P. R., Marquette, W., 2001: *The Big Bear Solar Observatory's Digital Vector Magnetograph.* in: Sigwarth, M. (ed.), Advanced Solar Polarimetry – Theory, Observation, and Instrumentation, Astronomical Society of the Pacific Conference Series **236** 65–72.

Stix, M., 1989: The Sun. An Introduction. Astronomy and Astrophysics Library, Berlin: Springer, 1989.

Teran, J. U., Porter, D. S., Hileman, E. A., Neff, D. H., 2000: *Unique Dome Design for the SOAR Telescope Project.* in: Sebring, T. A., Andersen, T. (eds.), Telescope Structures, Enclosures, Controls, Assembly/Integration/Validation, and Commissioning, Proceedings of SPIE **4004** 155–163.

Title, A. M., Schrijver, C. J., 1998: *The Sun's Magnetic Carpet.* in: Donahue, R. A., Bookbinder, J. A. (eds.), Cool Stars, Stellar Systems, and the Sun, Astronomical Society of the Pacific Conference Series **154** 345–360.

Uitenbroek, H., 2004: *Observational Aspects of Waves in the Chromosphere.* in: Lacoste, H. (ed.), SOHO 13 Waves, Oscillations and Small-Scale Transients Events in the Solar Atmosphere: Joint View from SOHO and TRACE, ESA Special Publication **547** 107–117.

Varsik, J. R., Yang, G., 2006: *Design of a Telescope Pointing and Tracking Subsystem for the Big Bear Solar Observatory New Solar Telescope.* in: Advanced Software and Control for Astronomy, Proceedings of SPIE **6274** 62741T.

Verdoni, A. P., Denker, C., 2006: *The Thermal Control Systems of the New Solar Telescope at Big Bear Solar Observatory.* in: Stepp, L. M. (ed.), Ground-Based and Airborne Telescopes, Proceedings of SPIE **6267** 62670M.

Verdoni, A. P., Denker, C., 2007: *The Local Seeing Environment at Big Bear Solar Observatory.* Publications of the Astronomical Society of the Pacific **119**, 793–804.

Verdoni, A. P., Denker, C., Varsik, J. R., Shumko, S., Nenow, J., Coulter, R., Sep. 2007: *The Thermal Environment of the Fiber Glass Dome for the New Solar Telescope at Big Bear Solar Observatory.* in: Solar Physics and Space Weather Instrumentation II, Proceedings of the Society of Photo-Optical Instrumentation Engineers **6689**.

Vernin, J., Munoz-Tunon, C., 1994: *Optical Seeing at La Palma Observatory. 2: Intensive Site Testing Campaign at the Nordic Optical Telescope* **284**, 311–318.

von der Luehe, O., May 1984: *Estimating Fried's Parameter from a Time Series of an Arbitrary Resolved Object Imaged Through Atmospheric Turbulence.* Journal of the Optical Society of America A **1**, 510–519.

Wagner, J., Rimmele, T. R., Keil, S., Barr, J., Dalrymple, N., Ditsler, J., Goodrich, B., Hansen, E., Hegwer, S., Hill, F., Hubbard, R., Phelps, L., Price, R., Richards, K., Warner, M., 2006: *Advanced Technology Solar Telescope: A Progress Report.* in: Stepp, L. M. (ed.), Ground-based and Airborne Telescopes, Proceedings of SPIE **6267** 626709.

Wang, H., Johannesson, A., Stage, M., Lee, C., Zirin, H., 1998: *Study of Hα Jets on the Quiet Sun.* **178**, 55–69.

Wedemeyer-Böhm, S., Lagg, A., Nordlund, Å., 2009: *Coupling from the Photosphere to the Chromosphere and the Corona.* SSR **144**, 317–350.

Weigelt, G. P., Apr. 1977: *Modified Astronomical Speckle Interferometry 'Speckle Masking'.* Optics Communications **21**, 55–59.

Wöger, F., von der Lühe, O., Reardon, K., Sep. 2008: *Speckle Interferometry with Adaptive Optics Corrected Solar Data* **488**, 375–381.

Woodhouse, C. A., 2004: *A Paleo Perspective on Hydroclimatic Variability in the Western United States.* Aquatic Science **66**, 346–356.

Yang, G., 2006: *Design and Implementation of the Primary and Secondary Mirror Control System for NST.* in: Lewis, H., Bridger, A. (eds.), Advanced Software and Control for Astronomy, Proceedings of SPIE **6274** 62740Z.

Yang, G., Varsik, J. R., Shumko, S., Denker, C., Choi, S., Verdoni, A. P., Wang, H., 2006: *The Telescope Control System of the New Solar Telescope at Big Bear Solar Observatory.* in: Lewis, H., Bridger, A. (eds.), Advanced Software and Control for Astronomy, Proceedings of SPIE **6274** 62741Y.

Zirin, H., Mosher, J. M., 1988: *The Caltech Solar Site Survey, 1965-1967.* Solar Physics **115**, 183–201.

Zwaan, C., 1981: *Solar magnetic structure and the solar activity cycle review of observational data.* in: The Sun as a Star 163–179.